Response of Earthquakes to Transient Stresses, in Laboratory and Nature

Thesis by
Krittanon Sirorattanakul

In Partial Fulfillment of the Requirements for the
Degree of
Ph.D. in Geophysics

CALIFORNIA INSTITUTE OF TECHNOLOGY
Pasadena, California

2024
Defended May 6, 2024

Krittanon Sirorattanakul
ORCID: 0000-0003-2310-8447

All models are wrong, but some are useful.
— George E. P. Box, 1960

There is no such thing as a perfect result, only perfect intentions.
— Kulapant Pimsamarn, 2010

ACKNOWLEDGEMENTS

Never have I dreamed of attending a world-renowned institution like Caltech and doing a PhD. My journey has greatly benefited from many mentors, colleagues, and friends I have met over the past few years. This thesis work would not have been possible without the support from the following individuals (which, of course, is still a non-exhaustive list).

First and foremost, I sincerely express my deepest gratitude to my two incredible advisors, Jean-Philippe Avouac and Ares Rosakis, who taught me and are still teaching me how to be a scientist (and engineer). From the first day that I met Jean-Philippe, I could feel his genuine excitement in understanding the natural worlds (including Martian). Throughout my PhD journey, Jean-Phillippe has taught me to identify important science questions and to use creativity to tackle them. Life is short and it would be wasteful to work on non-important problems. The time in the field (through the Ge121 class, which I took once and TA'd once) with him was very valuable. I am always excited to hear about his stories from fieldwork in the Himalayas. Ares, on the other hand, has taught me to think like an engineer. His creativity in problem-solving, especially related to laboratory experiments, is unparalleled. With some rather simple advice from him, many of my experiments magically worked. Both of my advisors were extremely supportive of the research direction that I wanted to pursue and gave me plenty of flexibility to explore my creativity. Being advised by both a scientist and engineer, and an observational geophysicist and an experimentalist, the best of both worlds, has given me a unique view of research, which I will continue to carry throughout my career.

I am also extremely grateful to the rest of my committee members: Nadia Lapusta, Zachary Ross, and Zhongwen Zhan. Nadia, thank you for all your excitement about my laboratory measurements. Your insights as a modeler have allowed us to interpret them and enhance our understanding of the natural laws. Every meeting with you is extremely valuable, as I can feel that you always give 100% to your students. I am also grateful for all the life advice that you have given me. Zach, thank you for initiating the project on the Westmorland swarm, which has become Chapter 4 of my thesis. It is the longest, the most comprehensive, and possibly my proudest work during my PhD. Zhongwen, thank you for agreeing to be the chair of my committee. In all of the committee meetings, you always asked great questions and gave valuable feedback.

There are two other mentors and friends who have had made a significant impact on my PhD journey. Mateo Acosta is a colleague, a mentor, and a friend who I probably have the most science discussions with during my PhD journey, almost on a daily basis. I especially enjoyed our time together in the lab, making experiments much more fun regardless of how tedious they were. He is also a walking encyclopedia who can always point me to relevant articles. Vito Rubino is a mentor who taught me most of the things I know about experiments. My interactions with him have allowed me to slowly accumulate skillsets related to experiments, which cannot be easily taught.

My research is a collaborative effort that would have not been possible without my co-authors: Stacy Larochelle, Attilio Lattanzi, Mostafa Khoshmanesh, Elizabeth Cochran, John Wilding, Yuexin Li, Stephen Bourne, and Jan van Elk; computer codes that were given to me (either directly or indirectly) and were written by the following individuals: Adriano Gualandi, Thomas Ader, Sylvain Michel, Kyungjae Im, Kejie Chen, Sylvain Barbot, Andrew Kositsky; the science discussions with research group members (that have not yet being mentioned): Marcello Gori, Qiuyi (Bing) Li, Jonathan Smith, Luca Dal Zilio, Guanli Wang, Hojjat Kaveh, Taeho Kim, Samson Marty; the specimens manufacturing and logistics related to experiments: Ali Kiani, Petros Arakelian; and help from admins at Caltech: Lisa Christiansen, Julie Lee, Donna Mojadehi, Donna Mireles, Kimberly Baker-Gatchalian, Dalia De Ita Perez, and Sandi Parra.

My experience at Caltech has also been enriched by the existence of the Center for Geomechanics and Mitigation of Geohazards (GMG). The interactions with industry members allowed me to gain a better understanding of the applications of our research. This led to two internships with Chevron that exposed me to an alternative industry career choice. During the internships, I learned a lot from my mentors Zijun Fang and Yunhui Tan, and my supervisor Peggy Rijken.

Besides research, Caltech has also allowed me to go on numerous field trips, enhancing my understanding of the geological wonders. Claire Bucholz, Madeline Lewis, and Juliet Ryan-Davis, thank you for the 18 days in the Sierra Nevada. Michael Lamb, Alistair Hayden, and Gen Li, thank you for the trip to the Wax Lake delta in Louisiana. Joseph Kirschvink, thank you for the nine iterations of Ge136 trips that I have gone to, from Grand Canyon to Big Sur, and a virtual one. Paul Asimow, thank you for leading enrichment trips to Iceland and Hawaii. Rob Clayton and Mark Simons, thank you for the geophysics field course.

Above all, I would not be here today without the encouragement and support from my past mentors. From my undergraduate at Lehigh University, thank you, Anne Meltzer, for introducing me to earthquake sciences (especially "slow-slip" events, which I strive to understand); thank you, Joshua Pepper, for providing me with my first research experience leading up to my first peer-reviewed publication, thank you H. Daniel Ou-Yang for the science discussions after the weekly physics colloquium and for supporting me to attend my first conference. Prior to this, I am indebted to my mentors from Thailand. Prinya Putthapiban, thank you for teaching me geology. Kulapant Pimsamarn, thank you for teaching me physics and providing me with wisdom that has become the guideline of my life: “There is no such thing as a perfect result, only perfect intentions.”

Now, on a personal note, I thank all of my friends, who make my PhD journey less stressful. Carl Swindle and Ruolin Deng, thank you for being my best friends during my PhD time and for all our camping trips, from the forests in the Sierra Nevada to the deserts in the Mojave. All the fun things we did together will become stories to be reminiscing of in the future. Chloe Daudon, Samson Marty, Kyungjae Im, Hadrien Meyer, Ojashvi Rautela, Oliver Stephenson, Zhe Jia, Minyan Zhong, thank you for sharing the office space with me at some point during my PhD. Shuo Cao, Zitong (Jerry) Wang, Guanli Wang, Yijian Zhou, Yuexin Li, Guannan Dong, thank you for playing badminton with me three times a week (although some of you may not have shown up that often). Emily Miaou, thank you for our boba chats and occasional squash (and, of course, the opportunity to be involved in the Science Olympiad and inspire new generations of scientists). Adriana Piña Paez, Surjyendu Bhattacharjee, Shirui Peng, Phelan Yu, thank you for the dinner outings. Yida Li, Tobias Koehne, thank you for being in my cohort and sharing the PhD journey with me from the beginning to the end. Kyungjae Im, Yongsoo Park, Qiuyi (Bing) Li, Yu-Fang Hsu, Kelian Dascher-Cousineau, Alba Rodríguez Padilla, thank you for hanging out with me during various conferences. Pitchayawee Kittitananuvong, Boontigan Kuhasubpasin, Ronnakrit Rattanasriampaipong, Patcharaporn Maneerat, thank you for being a supportive Thai Earth Scientist community away from home.

Lastly, this journey would not be possible without my partner and supportive family members. Yunyun (Winnie) Gu, thank you for always being there for me and listening to me rambling about science. Mom (Piyaporn Sirorattanakul) and Dad (Dissapong Sirorattanakul), thank you for supporting my decision to study abroad, and I hope I have made you proud.

ABSTRACT

Earthquake rates are known to fluctuate with time according to the changing state of stress in the Earth's crust. Studying the response of earthquakes to transient stresses provides a unique insight into the mechanisms controlling the earthquake nucleation process. Common sources of transient stresses include stress changes from fault slip during large earthquakes, spontaneous slow fault slip, fluid pressure diffusion, seasonal changes of water mass and snowpacks related to hydrological cycles, tidal stresses from changes of gravitational forces of the Sun and the Moon, and anthropogenic fluid injection and extraction related to geoenergy production. In this thesis, we first start in the laboratory-scale fault and conduct friction experiments to enhance our understanding of the underlying friction laws used for modeling earthquakes. We find that the traditional view of Coulomb friction, which postulates that there exists a threshold shear force called "static friction," below which the frictional interface remains stationary, is incorrect. Our measurements have shown that such an interface is still sliding, albeit with extremely small decaying slip rates down to 10^{-12} m/s. This is consistent with a more recently developed friction law, which describes friction as dependent on slip rate and the state of the interface, e.g., time since the last earthquake. Next, we move beyond the laboratory and study natural faults. In one example, we study the response of earthquakes to transient stress induced by a spontaneous slow fault slip event that preceded the earthquake swarm sequence by approximately half a day. In another example, we study the response of earthquakes to seasonal stress perturbations as a result of seasonal changes in groundwater mass and snowpack between wet and dry seasons, using California as a case study. In both examples, we find that earthquake nucleation is not an instantaneous process. Rather the earthquake rates lag after the stress rates. Such behavior cannot be described by Coulomb friction but can be quantitatively explained by the rate- and state-dependent friction. In the final example, we document bursts of fast propagating swarms of induced earthquakes at the Groningen gas field in the Netherlands. While transient stress must exist to drive the sequence, we cannot explicitly quantify the sources. Overall, our work provides key insights into the earthquake nucleation process, allowing us to better understand how to model the response of earthquakes to transient stress, including earthquakes that are induced by anthropogenic activities related to geoenergy production.

PUBLISHED CONTENT AND CONTRIBUTIONS

Chapter 2 is under review as:

K. Sirorattanakul, S. Larochelle, V. Rubino, N. Lapusta, and A. J. Rosakis. Sliding and healing of frictional interfaces that appear stationary.

N.L., A.J.R., and V.R. conceived the study. K.S. and V.R. designed the experiments. K.S. performed the measurements. K.S. and S.L. analyzed the data. All authors contributed to the interpretation and edited the manuscript.

Chapter 3 is to be submitted as:

K. Sirorattanakul, V. Rubino, A. Lattanzi, and A. J. Rosakis. Experimental quantification of ultraslow slip rate of shear interfaces using digital image correlation.

K.S., V.R., A.J.R. conceived the study. KS and VR designed the experiments. K.S. performed the measurements, analyzed the data, prepared all figures, and drafted the manuscript. K.S. and A.L. perform uncertainty analysis using simulated experiments. V.R. and A.J.R. supervised the project. All authors contributed to the interpretation and edited the manuscript.

Chapter 4 is published as:

K. Sirorattanakul, Z. E. Ross, M. Khoshmanesh, E. S. Cochran, M. Acosta, and J.-P. Avouac. The 2020 Westmorland, California earthquake swarm as aftershocks of a slow slip event sustained by fluid flow. *Journal of Geophysical Research: Solid Earth*, 127(11):e2022JB024693, 2022. doi: 10.1029/2022JB024693.

K.S. performed the data analysis and modeling, prepared all figures, and drafted the manuscript. Z.E.R. and E.S.C. generated the seismicity catalog, M.K. generated the InSAR results, J.P.A. supervised the data analysis and modeling and the manuscript preparation. All authors contributed to the interpretation and edited the manuscript.

Chapter 5 is to be submitted as:

K. Sirorattanakul, and J.-P. Avouac. Earthquake nucleation process revealed by modulation of seismicity rate in California driven by tectonic, hydrological, and tidal loading.

K.S. performed the data analysis, prepared all figures, and drafted the manuscript. J.P.A. supervised the data analysis and manuscript preparation.

Chapter 6 is under review as:

K. Sirorattanakul, J. D. Wilding, M. Acosta, Y. Li, Z. E. Ross, S. J. Bourne, J. van Elk, and J.-P. Avouac. Bursts of fast propagating swarms of induced earthquakes at the Groningen gas field.

K.S. performed the data analysis, prepared all figures, and drafted the manuscript. J.D.W. and Z.E.R. generated the seismicity catalog. M.A. and Y.L. modeled the compaction. J.P.A. supervised the data analysis and manuscript preparation. All authors contributed to the interpretation and edited the manuscript.

TABLE OF CONTENTS

LIST OF ILLUSTRATIONS

LIST OF TABLES

Number *Page*

Chapter 1

INTRODUCTION

Faults are pre-existing fractures that are prevalent in the Earth's crust. When they are pushed by tectonic forces, the rigid plates on the two sides of the faults can abruptly slide past one another, resulting in an earthquake. Even though the first-order physics controlling the earthquakes is conceptually simple, applications to the real-world are not straightforward. The stress state, the frictional parameters, and the geometry of the faults at depth are typically unknown, making earthquake forecasting an extremely challenging task. The unresolved fundamental questions in earthquake science can generally be divided into three main categories, as follows:

1. How do earthquakes start? What drives and sustains an earthquake sequence?
2. Once an earthquake has started, what determines the size of the largest earthquake?
3. What controls the ground shaking resulting from earthquakes?

In this thesis, I focus on the first question and study the process governing earthquake nucleation. In regions where faults are subjected to constant stress rates, such as the long-term tectonic loading, the earthquake rates are expected to be constant in time, depending only on the stress rate. Upon interactions with transient stress perturbations, the earthquake rates are expected to be modulated accordingly. While these transient stresses make forecasting earthquake rates difficult, studying the amount and timing of the responses of earthquakes to transient stresses provides a unique opportunity to probe the earthquake nucleation process and provide insights into the triggering mechanisms and the stress state of the faults.

In this introductory chapter, I first review the common sources of transient stresses and discuss a workflow that can be used to model them. This review is meant to be an introductory material for non-specialists and is not meant to be exhaustive. As I point out throughout the review, readers are advised to consult more comprehensive papers. This chapter is then concluded by outlining and summarizing the content of the remaining chapters of the thesis.

1.1 Common sources of transient crustal stresses

1.1.1 Static stress changes from large earthquakes

The most common source of transient stresses in the Earth's crust is the permanent static stress changes due to rapid fault slip during a large earthquake (King et al., 1994). Areas immediately surrounding the slipping regions experience stress drop as faults release elastic strain energy. On the contrary, areas close to the terminus of the slipping region experience increasing stress (Figure 1.1a). These stress changes typically range from 0.1 – 10 MPa and are the main drivers of the aftershock sequences following a large earthquake (Dieterich, 1994, Stein, 1999). According to "Båth's law", the largest of these aftershocks are usually about 1.2 magnitude unit lower than the mainshock (Richter, 1958). Furthermore, the aftershock rates $n(t)$ are known to follow a power law decay, referred to as the Omori-Utsu law of aftershocks (Omori, 1894, Utsu, 1961), as follows:

$$n(t) = \frac{k}{(c+t)^p} \tag{1.1}$$

where k, c and p are empirical constants of the law, and generally, $p \sim 1$.

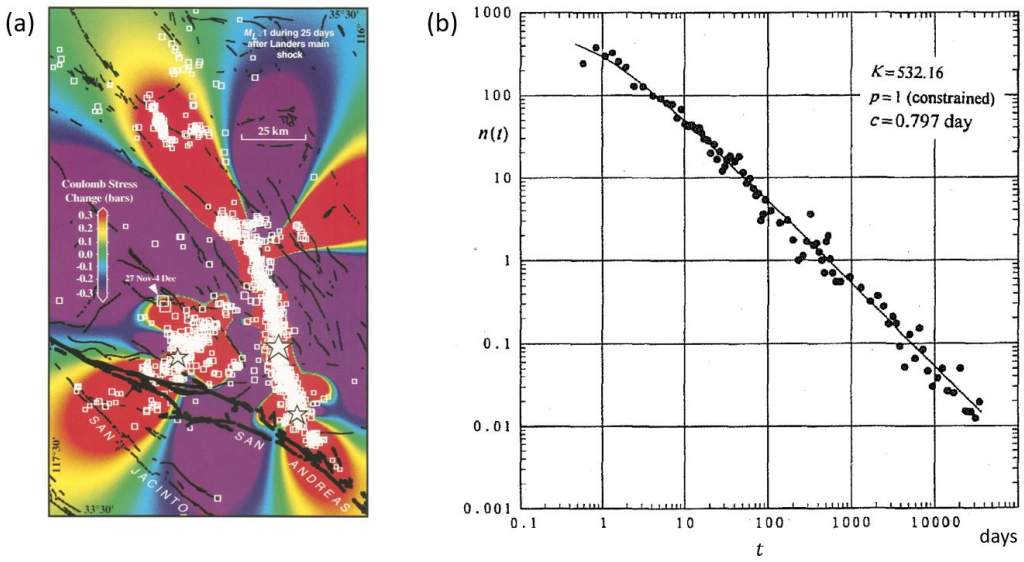

Figure 1.1: Static stress changes from large earthquakes drive aftershocks. (a) Coulomb stress changes following the 1992 M7.4 Landers, California earthquake, taken from King et al. (1994). (b) The rates of aftershocks following the 1891 M8 Nobi, Japan earthquake, modified from Utsu et al. (1995).

The Omori-Utsu law is one of the most well-constrained statistical properties of earthquakes. Following the 1891 M8 Nobi, Japan earthquake, the decay of aftershock rates follow the Omori-Utsu law, even after 100 years (Utsu et al., 1995, Figure 1.1b). However, the underlying mechanisms that produce such behaviors are still debated. Since aftershocks do not all occur immediately after the mainshock, there must be some underlying mechanisms governing the delay in aftershocks triggering. One potential explanation is that faults need finite time to accelerate toward failure, and hence, earthquake nucleation is not instantaneous. To capture such effect, rate- and state-dependent friction law (Section 1.3.2) can be used and the Omori-Utsu law can be reproduced (Dieterich, 1994, 2007, Section 1.3.4). Alternatively, post-seismic stress relaxation after the mainshock in the form of slow fault slip known as "afterslip" (Helmstetter and Shaw, 2009, Perfettini and Avouac, 2004, Perfettini et al., 2018, Section 1.1.3) or fluid diffusion following a sudden change of pore fluid pressure due to static stress change from the mainshock (Miller, 2020) could also lead to delayed triggering and could potentially explain the Omori-Utsu law.

For a more comprehensive review of static stress changes, Omori-Utsu law, and modeling aftershocks, the readers can consult King (2007), Utsu et al. (1995), and Hardebeck et al. (2024), respectively.

1.1.2 Dynamic stress changes from large earthquakes

In addition to the static stress changes, earthquakes also generate elastic waves that propagate through the Earth's crust, creating transient crustal stresses at a distant location that can dynamically trigger earthquake events. It has been estimated that between 15 - 60% of aftershocks may be dynamically triggered (Hardebeck and Harris, 2022, van der Elst and Brodsky, 2021). The causal links between the events are typically established using the travel time of the elastic waves. An example of such dynamic triggering is shown in Figure 1.2. The broadband record is dominated by the long-period waves that were emitted from a distant earthquake. The high-pass filtered version, on the other hand, only keeps high-frequency energy, which must originate near the seismometers as attenuations in the Earth's crust will first filter out the high-frequency energy. As a result, the individual events shown in the high-frequency records are the dynamically triggered events.

In comparison to the static stress changes, these dynamic stress changes are typically smaller on the order of 0.1 – 10 kPa. While these are much smaller than the ambient stress acting on the faults, when considering a large population of faults, there

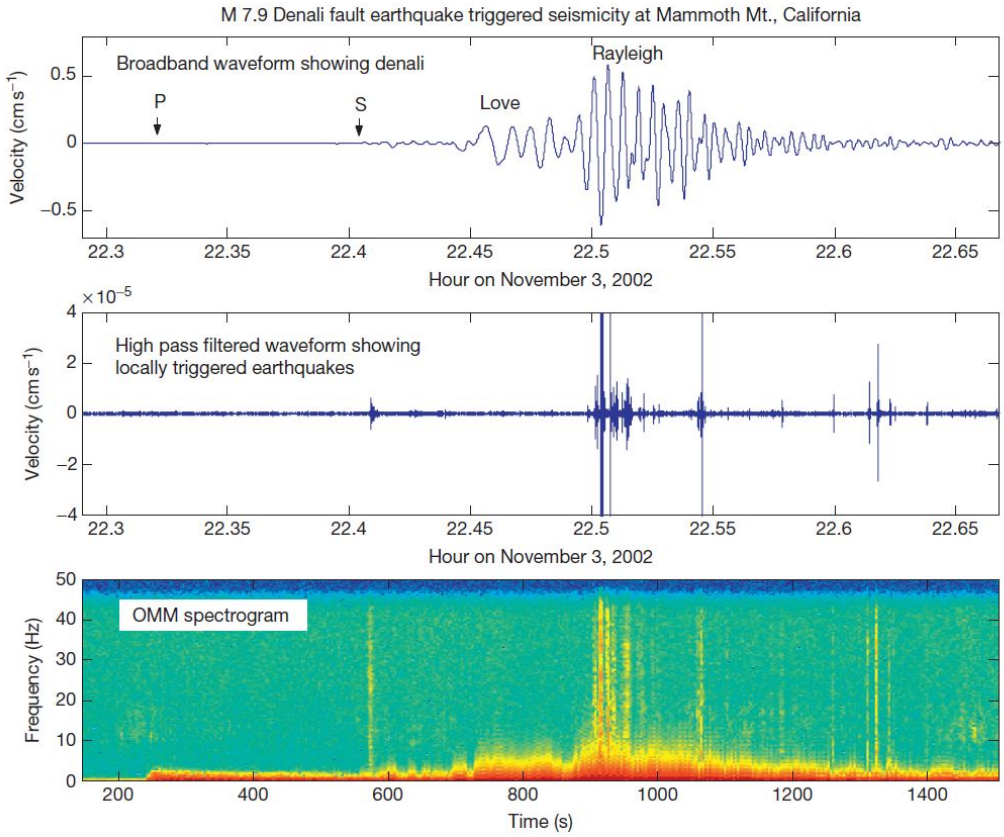

Figure 1.2: Examples of dynamically triggered earthquakes following the 2002 M7.9 Denali, Alaska earthquake at Mammoth Mountain, California. The top panel shows a seismogram recorded at station OMM following the Denali earthquake. The middle panel shows the high-pass filtered waveform revealing locally triggered earthquakes (with clear P- and S-wave arrivals if zoomed in) that are synchronized with individual surface wave packets. The bottom panel shows the spectrogram of the recorded data. Figure is taken from Hill and Prejean (2015).

must exist some fraction that is very close to failure and can be triggered with small perturbations (Brodsky and Van Der Elst, 2014). On the other hand, direct triggering cannot explain why some dynamically triggered events persist for weeks after the passage of the seismic waves. Other mechanisms, such as permeability enhancement following dynamic stress changes (Brodsky et al., 2003, Elkhoury et al., 2006), can potentially contribute to delayed triggering.

For a more comprehensive review of dynamic triggering, the readers can consult Brodsky and Van Der Elst (2014) and Hill and Prejean (2015).

1.1.3 Postseismic deformation

Large earthquakes instantly deform the Earth's crust. Following the earthquakes, the Earth's crust continues to deform in the form of "postseismic" deformation and exhibit time-dependent stress changes. Postseismic deformation can occur in various forms. The most common one is the slow fault slip or "afterslip" occurring on the same or adjacent fault planes (Benioff, 1951, Marone et al., 1991, Perfettini and Avouac, 2004, Perfettini et al., 2018). The accumulated slip typically increases as a logarithmic of time and can be explained by the healing effect of the rate- and state-dependent friction laws (Marone et al., 1991, Perfettini and Avouac, 2004). Healing is later discussed in Section 1.3.3 and thoroughly studied in Chapters 2 and 3 of this thesis. Another common form of postseismic deformation is the ductile flow of the mantle in the form of "viscoelastic relaxation." The characteristic timescale of viscoelastic relaxation is related to mantle viscosity and is expected to be longer than the timescale of afterslip (Khazaradze et al., 2002). In many cases, both afterslip and viscoelastic relaxation can co-exist (Freed et al., 2006). Overall, postseismic deformation can induce considerable transient crustal stresses in the order of 1 – 100 kPa.

For a more comprehensive review, the readers can consult Perfettini and Avouac (2004) and Avouac (2015).

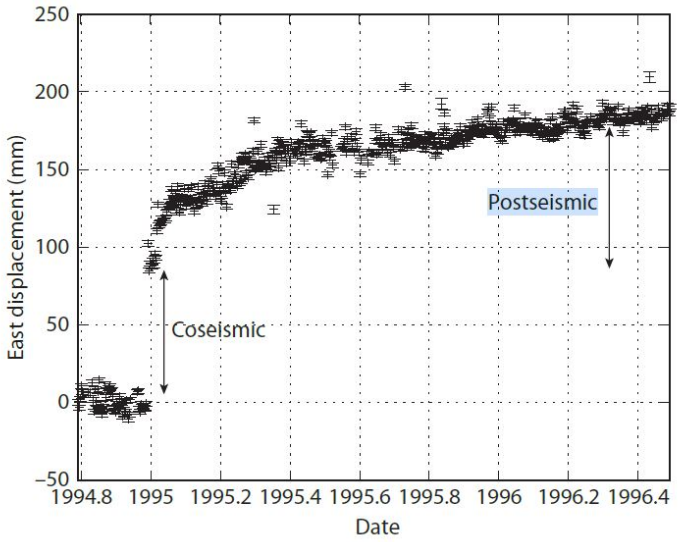

Figure 1.3: Example of postseismic deformation following the 1994 M7.7 Sanriku-Haruka-Oki, Japan earthquake. Figure is taken from Segall (2010).

1.1.4 Spontaneous slow-slip events and fluid flow

Faults do not need to slip rapidly. They can also slide slowly without producing any elastic waves in the form of creep (Bürgmann, 2018, Chen and Bürgmann, 2017, Harris, 2017, Li et al., 2023). Occasionally, creep can accelerate, resulting in spontaneous "slow-slip events" (Ide et al., 2007, Peng and Gomberg, 2010). Slow-slip events are often associated with fluid flow, though laboratory experiments have been able to reproduce slow-slip events without fluid flow (Leeman et al., 2016).

Slow-slip events produce stress changes in the order of 1 – 100 kPa and can result in a "swarm" sequence (Lohman and McGuire, 2007, Sirorattanakul et al., 2022b). In contrast to a typical mainshock-aftershock sequence, a swarm occurs as a burst of small-magnitude earthquakes without a clearly identifiable mainshock (Mogi, 1963). One spectacular example of a slow-slip-driven swarm is the 2012 Brawley, California earthquake swarm (Wei et al., 2015). Fluid injection related to geothermal energy production first induced a slow-slip event on a normal fault, which produced transient stress that drove the subsequent swarm sequence (Figure 1.4).

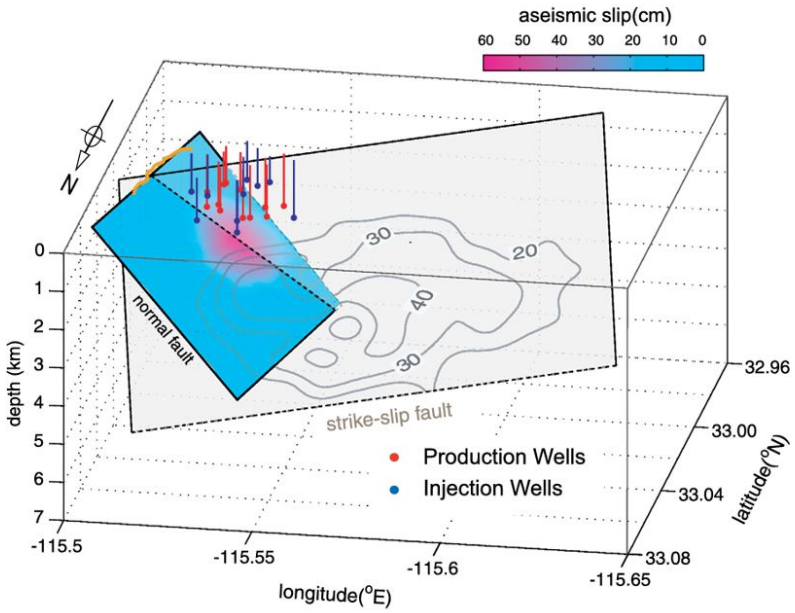

Figure 1.4: Example of a slow-slip driven sequence. Injection activities associated to the Brawley geothermal field induced a slow-slip event on a normal fault, which subsequently triggerred M_w 4.7 earthquake on an adjacent strike-slip fault and drove the 2012 Brawley, California earthquake swarm. Figure is taken from Wei et al. (2015).

In this thesis, we discuss two other examples of swarms. In Chapter 4, we discuss the 2020 Westmorland, California swarm, which we interpreted to be driven primarily by a spontaneously slow-slip event and sustained by fluid flow. In Chapter 6, we discuss swarms in the Groningen gas field, which are most likely driven by fast propagating slow-slip events.

For a more comprehensive review of earthquake swarms, the readers can consult references in the introduction of Chapter 4 of this thesis.

1.1.5 Hydrological loading and poroelastic effects

The levels of groundwater and snowpack can drastically change between the wet and dry seasons. These changes cause seasonal transient stress in the Earth's crust through two major mechanisms (Figure 1.5). First, the changes in seasonal water storage induce a direct change in surface loading due to its weights, modifying the stress state of the faults at a deeper depth (Boussinesq, 1878, Chanard et al., 2014). Second, changes in water storage alter the pore fluid pressure and consequently, deform the surrounding bulk materials through poroelasticity (Wang, 2000). As an analogy, a sponge inflates as it dries up and compacts as it is soaked in the water. Surface loading typically occurs over a regional scale (Amos et al., 2014, Johnson et al., 2017b), while the poroelastic responses are typically confined within aquifers and sedimentary basins (Kang and Knight, 2023, Larochelle et al., 2022).

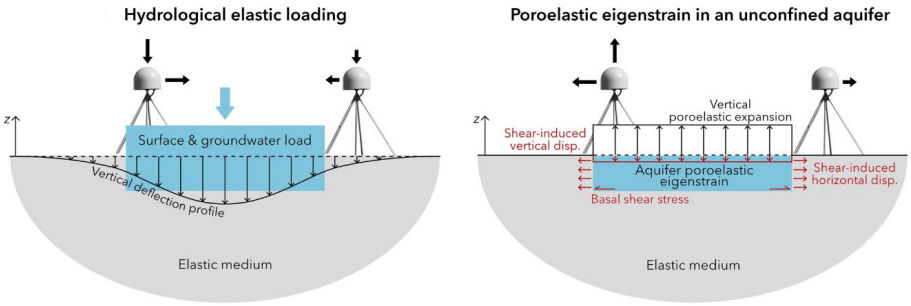

Figure 1.5: Transient stresses due to hydrology. (Left) Added water mass causes subsidence and horizontal motion toward the added load. (Right) Added water mass increases pore fluid pressure causing poroelastic expansion. Figure is taken from Larochelle et al. (2022).

Hydrological surface load induces stress changes in the order of kPa. While this is a small value in comparison to stress drop during an earthquake event, it has been documented to significantly modulate the earthquake rates in several regions around the world, including the Himalayas (Bettinelli et al., 2008, Bollinger et al., 2007),

California (Dutilleul et al., 2015, Johnson et al., 2017b), New Madrid Seismic Zone (Craig et al., 2017), East African rift (Xue et al., 2020), and Lake Biwa in Japan (Xue et al., 2021). Poroelastic stress changes are typically smaller, but they can also modulate earthquake rates in the induced seismicity context (Acosta et al., 2023). In Chapter 5 of this thesis, we explore the response of earthquakes to hydrological surface loading, focusing on California.

For a more comprehensive review of hydrological-driven seismicity, the readers can consult Bürgmann et al. (2023).

1.1.6 Solid Earth tides

Changes in the gravitational pull between the Earth, the Sun, and the Moon cause transient tidal stresses that are a superposition of harmonic perturbations with a dominant period of 12.4 hr (Agnew, 2007). The tidal forces stretch and compress the solid Earth itself but also change the water levels in the oceans. The amplitude of tidal stress is approximately 1 – 10 kPa, which is the same order of magnitude as hydrological surface loading and is generally well-constrained by existing models (Figure 1.6). While there exist studies that document the response of earthquake rates to tidal stress, the modulation amplitudes are often much smaller than the response to the seasonal surface loading (Bucholc and Steacy, 2016, Cochran et al., 2004, Vidale et al., 1998, Wang et al., 2022, Wilcock, 2001). These observations suggest that the response of earthquakes to periodic loading is dependent on the period (Ader et al., 2014).

For a more comprehensive review of Earth tides, the readers can consult Agnew (2007).

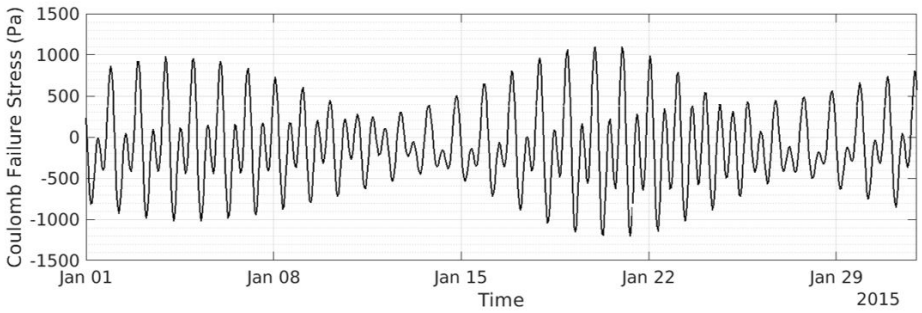

Figure 1.6: Amplitudes of Coulomb stress changes induced by the solid Earth tides. Figure is taken from Sirorattanakul et al. (2022b)

1.1.7 Anthropogenic fluid injection or extraction

Not all transient crustal stresses are natural. Due to the demands for energy, humans have exploited geoenergy resources and significantly modified the state of the subsurface reservoir in the process through the injection and extraction of gas and other fluids. These operations can result in pressure drops as large as tens of MPa and produce up to 1 MPa of stress changes (Figure 1.7). Even though geoenergy sites are generally located in a tectonically quiet area where faults are typically not critically stressed, these stress changes are quite significant and can induce earthquakes (Moein et al., 2023). The stress perturbations can be in the form of direct pressure changes (Cesca et al., 2021, Hennings et al., 2021, Hubbert and Rubey, 1959, Nur and Booker, 1972, Shapiro et al., 1997, Stokes et al., 2023) or through poroelastic deformation (Acosta et al., 2023, Goebel et al., 2017, Li et al., 2021, Segall, 1989, Segall and Lu, 2015, Zhai et al., 2019). Since the stress perturbations due to anthropogenic activities are generally better constrained than natural transient stresses, the study of the response of earthquake rates to anthropogenic fluid injection or extraction provides another unique opportunity to study the earthquake nucleation process. In this thesis, we explore a case study of induced seismicity in Chapter 6.

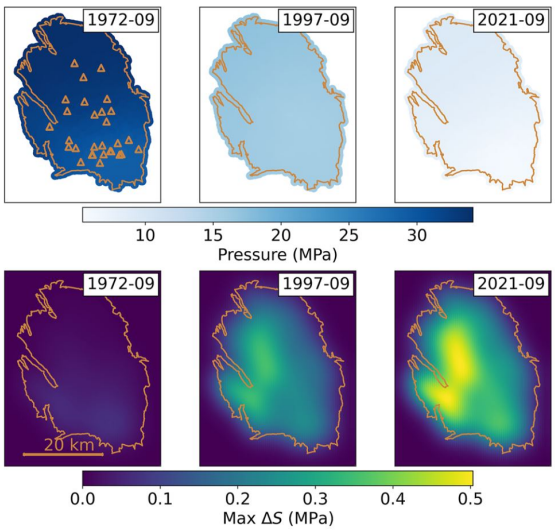

Figure 1.7: Pressure and Coulomb stress change ΔS as a result of gas extraction in the Groningen gas field in the Netherlands. Figure is taken from Acosta et al. (2023)

For a more comprehensive review of induced seismicity, the readers can consult the following articles: Atkinson et al. (2020), Ellsworth (2013), Grigoli et al. (2017), Keranen and Weingarten (2018), Moein et al. (2023), Wu et al. (2022).

1.2 Determining transient stresses with geodetic methods

These transient crustal stresses cannot be directly measured, but rather have to be inferred through modeling. Because the crust is elastic, these stresses produce strains resulting in measurable surface deformations. Geodetic techniques are often utilized to measure such deformations (Bürgmann and Thatcher, 2013), including the following:

- **GPS/GNSS** (Global Position System / Global Navigation Satellite System) stations are used to measure the relative displacement of a point on Earth's surface by trilateration its position with respect to a fleet of orbiting satellites. Handheld GPS or those in the phone can have a precision of tens of meters. These permanent GPS stations, however, can resolve displacement in order of millimeters. While it can provide a continuous record of ground displacements, each station can only measure displacement at one location. For a more comprehensive review, the readers can consult Blewitt (2015).

- **InSAR** (Interferometric Synthetic Aperture Radar) is a technique used to measure phase changes between successive radar images. The shift in the ground would change the travel times between the ground and the satellite resulting in phase changes. InSAR can resolve movements in order of centimeters. In comparison to GPS, InSAR covers a much larger region, but its temporal resolution is limited to when the satellite orbits over the same region, which is typically 2 weeks. The displacements resolved are also limited to the direction of the line-of-sight between the ground and the satellite. For a more comprehensive review, the readers can consult Simons and Rosen (2015).

- **Optical satellite images** can also be used to measure displacements through the usage of image correlation techniques to track movements of features observed on the Earth's surface (Leprince et al., 2007). This technique only produces horizontal displacements and can resolve displacements in order of only tens of centimeters. However, optical satellite images are routinely acquired and are more widely available than InSAR. For a more comprehensive review, the readers can consult Avouac and Leprince (2015).

- **Gravity measurements** from the GRACE (Gravity Recovery and Climate Experiment) and its follow-on mission can be used to track the movement of groundwater and ice mass which dominates seasonal changes in gravity. The measurements are conducted through a pair of satellites, in which the

distances between them change due to changes in the gravity field. For a more comprehensive review, the readers can consult Wahr (2007).

- **Creepmeter** is an instrument that can be used to quantify fault slip. Typically, two monuments are placed on the different sides of a fault, separating over a distance, typically about 30 meters apart, with a wire connecting them. The displacements of the wire are interpreted as fault slips. For a more comprehensive review, the readers can consult Bilham et al. (2004).

- **Strainmeter** is an instrument that is typically placed in a borehole at a depth of a few hundred meters, which can continuously measure strains with precision of up to one part per billion through the changes of borehole diameter. For a more comprehensive review, the readers can consult Agnew (1986).

- **Tiltmeter** is an instrument that can measure the changes in the ground tilt with respect to the horizontal direction. They are typically used to monitor the volcanoes. For a more comprehensive review, the readers can consult Agnew (1986).

By modeling the surface deformations, one can infer the properties of the sources of stress perturbations. With proper determination and quantification of the sources, one can use physics-based forward models to determine transient stresses in the Earth's crust (Boussinesq, 1878, Chanard et al., 2014, Larochelle et al., 2022, Okada, 1985, 1992). However, these sources are often mixed, making source determination a non-trivial task. One method that can be used to separate out the contributions from the different sources to the measure deformations is to use a blind source separation technique such as the Independent Component Analysis (ICA), which we used in Chapter 4 of this thesis. These methods are first developed to tackle the "cocktail party problem," in which speakers are placed around the cocktail party to isolate a sound of interest from a mixture of various speeches and noises in social settings. By assuming that each person has a unique speech, which is independent of others, we can separate out these sources by trying to maximize the statistical independence between the signals' probability density function (Choudrey and Roberts, 2003). This technique has been successfully applied to GPS and InSAR data (Gualandi and Liu, 2021, Gualandi et al., 2016, 2020, Larochelle et al., 2018, Michel et al., 2019, Sirorattanakul et al., 2022b).

1.3 Modeling the response of earthquakes to transient stresses

1.3.1 Coulomb instantaneous failure model

The simplest model of earthquakes is based on force balances. A fault will slide if the shear stress τ_0 approaches the shear strength (or the shear resistance) of the fault τ_{res}, given by:

$$\tau_{\text{res}} = f_{\text{static}}(\sigma_0 - P) \tag{1.2}$$

where f_{static} is the static friction coefficient, σ_0 is the normal stress acting on the fault (compression positive), and P is the pore fluid pressure. This failure criterion is widely used in the mechanics of granular media and soils and is typically referred to as the "Coulomb failure criterion." While Charles Augustin Coulomb has conducted numerous experiments leading to his seminal work on friction (Coulomb, 1773, 1821), the idea that friction depends on compressive stress was developed much earlier by Guillaume Amontons (Amontons, 1699). For a more comprehensive review of the earlier work in friction theory, the readers can consult Dowson (1979) and Popova and Popov (2015).

Based on the Coulomb failure criterion, to make a fault slide, one can either increase the driving shear stress τ_0 or decrease the shear strength of the fault by either decreasing normal stress σ_0 or increasing pore fluid pressure P. To quantify whether changes in the stress state push a fault toward failure, we can utilize a metric ΔS, referred to as the "Coulomb stress change," defined as follows (King et al., 1994):

$$\Delta S = \Delta\tau_0 - f_{\text{static}}(\Delta\sigma_0 - \Delta P) \tag{1.3}$$

where $\Delta\tau_0$ is shear stress change, $\Delta\sigma_0$ is normal stress change, and ΔP is pore fluid pressure change. For most rocks, $f_{\text{static}} \sim 0.6$. To account for poroelastic deformation, one can replace the f_{static} by $f_{\text{static}}(1 - B)$ where B is the Skemptons coefficient (King et al., 1994). For most faults, $f_{\text{static}}(1 - B) \sim 0.4$.

The response of a fault to a constant stress rate $\dot{S}$ under the Coulomb failure criterion is illustrated in Figure 1.8. As we push the fault, we continuously increase the friction coefficient f, defined as the ratio of shear to normal stress (τ/σ). As the friction coefficient f reaches its static threshold f_s, the fault instantaneously slides, and the friction coefficient suddenly reduces to its dynamic value f_d as the fault experiences a release of strain energy. As we continue to push the fault, the friction coefficient

slowly increases again until it reaches the static value and repeats the process. In this model, the earthquake rate $R(t)$ is proportional to the stress rate $\dot{S}(t)$, and can be written as follows:

$$\frac{R(t)}{r} = \frac{\dot{S}(t)}{\dot{S}_0} \tag{1.4}$$

where r is the background seismicity rate occurring at the background stress rate ($\dot{S}_0$). The Coulomb instantaneous failure model cannot explain the different slip rates on the fault as the model is bimodal (stationary vs. rapid sliding). It also does not provide any mechanism for delayed triggering and, therefore, cannot explain the widely observed Omori-Utsu law of aftershocks without introducing other complexities such as afterslip or fluid diffusion (Section 1.1.1).

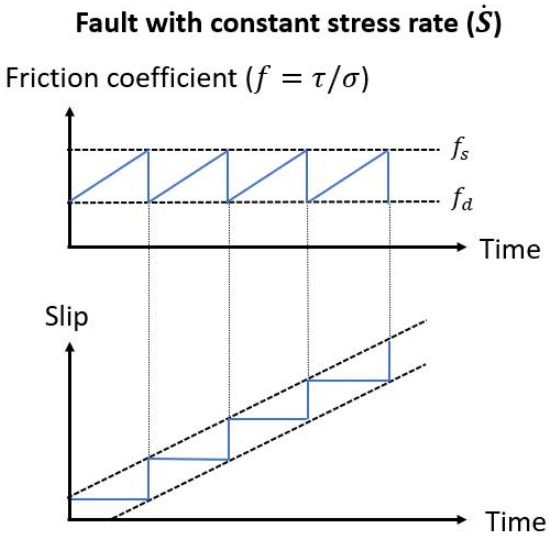

Figure 1.8: Failure of a fault subjected to constant stress rate according to the Coulomb instantaneous failure model.

1.3.2 Rate- and state-dependent friction laws

The Coulomb failure criterion is simple and elegant, but it does not capture the complex nature of friction such as the non-instantaneous nature of the earthquake nucleation process. Since the time of Coulomb, he already noticed that the static friction is not a material constant, but rather depends on the time elapsed since the first moment of contact. In his work, he never gives the value of the static friction but rather provides a few values with different elapsed time (Coulomb, 1821, Popova and Popov, 2015). Such time-dependent behaviors of friction have

motivated detailed laboratory experiments sliding two surfaces of rocks or gouge layers and led to a better understanding of the transition between static and dynamic friction (Rabinowicz, 1951, 1956) and the development of empirical rate- and state-dependent friction formulation (Dieterich, 1979, Marone, 1998a, Ruina, 1983).

In a traditional "velocity-jump" experiment, the interface is first sheared at a constant slip rate V_1. Then, the slip rate is suddenly changed to another value, V_2, which can be larger or smaller than V_1. The response of the interface to this sudden jump is depicted in Figure 1.9. If $V_2 > V_1$, the friction coefficient will suddenly jump from f_1 to $f_2 = f_1 + a \ln(V_2/V_1)$, for some constant a which is a property of the interface. This sudden jump is a direct effect and can be interpreted as locally increased shear stress at contact junctions prior to the breaking of asperities to allow for sliding at a higher slip rate. Afterwards, the larger slip rate allows less time for asperities to make contact, resulting in a smaller contact area and generally a smaller resistance leading to the weakening of the interface leading to a drop of friction coefficient of amount $b \ln(V_2/V_1)$ for some constant b which is a property of the interface. The system then evolves into a new steady state after a slip distance of approximately D_{RS}, typically in orders of a few microns for bare rock surfaces used in the laboratory. In contrast, if $V_2 < V_1$, the friction coefficient will suddenly decrease from f_1 to $f_2 = f_1 - a \ln(V_1/V_2)$. Afterward, as the system evolves to a new steady state, the interface regains its strength, and friction increases by $b \ln(V_1/V_2)$.

For a more general case with arbitrary slip evolution V(t), the friction evolution can be formulated as follows (Dieterich, 1979, Marone, 1998a, Ruina, 1983):

$$f = f^* + a \ln\left(\frac{V(t)}{V^*}\right) + b \ln\left(\frac{V^*\theta(t)}{D_{RS}}\right) \tag{1.5}$$

where $\theta(t)$ is the state parameter with a unit of time and encodes the slip history occurring on the interface and D_{RS} is the critical slip distance typically interpreted to be related to average size of contact asperities. The slip rate-dependent term (direct effect) is universally positive ($a > 0$) and can be interpreted as the breaking of asperities at stressed contact junctions from a thermally activated Arrhenius process (Rice et al., 2001). The state-dependent term (evolutionary effect) can be interpreted as the logarithmic growth of the real area of contact due to thermally activated creep (Berthoud et al., 1999, Ikari et al., 2016, Perfettini and Molinari, 2017). Such growth of contact areas has also been measured in the laboratory experiments (Dieterich and Kilgore, 1994).

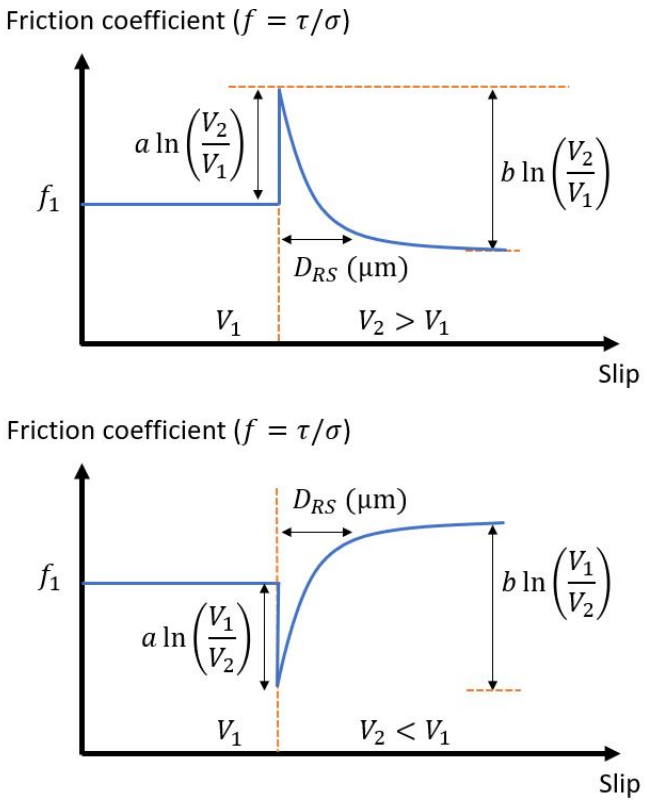

Figure 1.9: A schematic of friction evolution during velocity-jump experiments.

The law used to evolve the state variable θ is still a matter of debate. Two popular choices are the "aging law" (Dieterich, 1979) and "slip law" (Ruina, 1983), which is formulated as follows:

$$\frac{d\theta}{dt} = 1 - \frac{V(t)\theta(t)}{D_{RS}} \tag{1.6}$$

$$\frac{d\theta}{dt} = -\frac{V(t)\theta(t)}{D_{RS}} \ln\left(\frac{V(t)\theta(t)}{D_{RS}}\right). \tag{1.7}$$

In the steady state limit, i.e., $d\theta/dt = 0$, both state evolution laws converge, and $\theta = D_{RS}/V$ reflects the contact age, i.e., the amount of time since the two surfaces become in contact. Moreover, the friction coefficient becomes purely slip rate-dependent:

$$f = f^* + (a - b) \ln\left(\frac{V}{V^*}\right) \tag{1.8}$$

If $a < b$, the friction coefficient at steady state decreases with slip rate, and the interface is said to be "velocity-weakening." On the contrary, if $a > b$, friction increases with slip rate, and the interface is "velocity-strengthening." If $a = b$, friction does not change with slip rate and the interface is "velocity-neutral." Stability analysis shows that unstable slip can only occur for a velocity-weakening interface (Scholz, 2019).

Unlike the traditional Coulomb friction, the rate-and-state formulation allows for different slip rates and can be used to explain various behaviors of fault slips (Ide et al., 2007, Peng and Gomberg, 2010, (Figure 1.10)). At dynamic slip rates, there can be other additional weakening mechanisms to reduce dynamic friction further than those expected from the rate-and-state formulation, such as flash heating of contact asperities (Bowden and Thomas, 1878, Rice, 1999, Rubino et al., 2017) and thermal pressurization of pore fluids in the fault zone (Segall and Rice, 1995, Sibson, 1973, Viesca and Garagash, 2015).

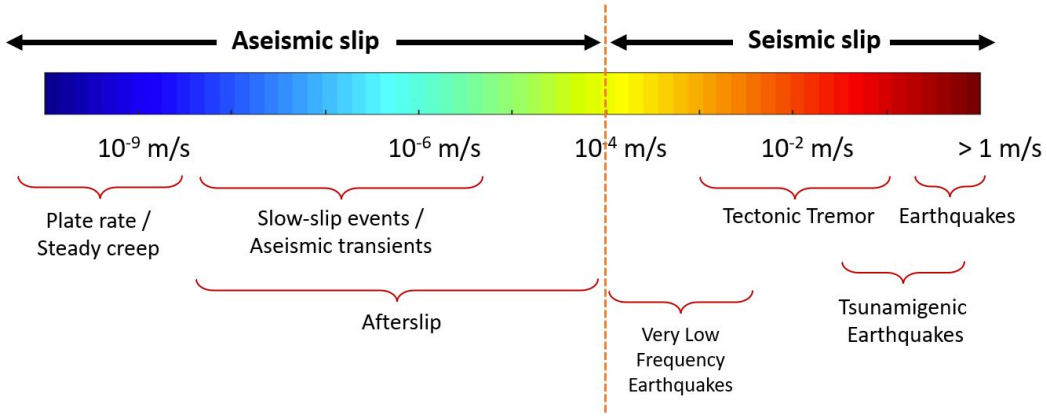

Figure 1.10: Behaviors of fault slips at different slip rates.

1.3.3 Interpreting the state variable in the rate- and state-dependent friction

One of the predictions of the rate-and-state framework is that all interfaces under non-zero shear stress are always sliding with non-zero slip rates in the form of creep, i.e., the argument in the logarithm of Equation 1.5 cannot be zero. This contradicts the Coulomb model and questions the existence of the notion of static friction (Rabinowicz, 1956). Such non-stationary has been observed in the intact bulk material (Lockner, 1998) and has been inferred from the reduction of shear stress during holds in the slide-hold-slide experiments (Beeler et al., 1998, Bhattacharya et al., 2022, Marone, 1998a).

In Chapters 2 and 3 of this thesis, we further evaluate the non-stationary nature of the interface by using a newly designed experiment mimicking a block on an inclined plane with an inclination angle that is much smaller than its critical value. We attempt to measure whether such a block is sliding. Contradicting the traditional Coulomb model but consistent with the rate-and-state formulation, we find that the interface is indeed sliding, though with decaying slip rates (Figure 1.11a). The decaying slip rate reflects the "healing" nature of the shear interface in the sense that it has become stronger with time due to the growth of the contact area, making it harder to slide. Since in our experiments, we kept the shear and normal load constant (and hence constant friction coefficient), the decaying slip rate $V(t)$ is directly related to the increasing state variable $\theta(t)$. By rearranging Equation 1.5, we can write an expression for the state variable as:

$$\left(\frac{\theta(t)}{\theta_0}\right)^{\frac{b}{a}} = \frac{V_0}{V(t)}. \tag{1.9}$$

Our measurements allow us to directly quantify the state variable evolution, which can further be used to settle the debate on the form of the state evolution laws, whether "aging law" (Equation 1.6), "slip law" (Equation 1.7), other new forms is more appropriate.

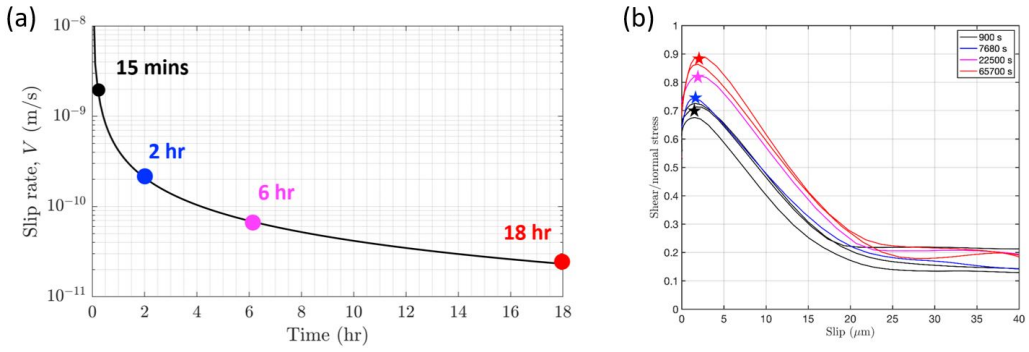

Figure 1.11: The effects of interface healing on dynamic friction evolution. (a) Slip rate evolution for an interface that is subjected to constant shear and normal loads. (b) Friction evolution upon rapidly "re-sliding" the interface in (a) after different amounts of holding times.

The "state" of the interface is expected to have a profound impact on subsequent slip events. To study such an effect, we (Attilio Lattanzi, myself, Vito Rubino, Nadia Lapusta, and Ares Rosakis) have conducted experiments in which we subjected an

interface to constant loads for different amounts of hold times (and hence different "states") and spontaneously nucleation a dynamic rupture using wire explosion following the procedures described in Rubino et al. (2019). If we approximate the slip rate increase during the arrival of dynamic rupture as an instantaneous jump from V_0 to V_{dynamic}, then the rate-and-state formulation (Equation 1.5) would predict that the peak friction f_{peak} (analogous to the static friction coefficient) according to the following expression:

$$f_{\text{peak}} = \frac{\tau_0}{\sigma_0} + a \ln \left(\frac{V_{\text{dynamic}}}{V_0} \right). \tag{1.10}$$

With longer hold time, we expect lower V_0. If the spontaneous rupture has approximately the same V_{dynamic}, then the longer the hold time, the higher the peak friction. Our experimental measurements (Figure 1.11b) show that the peak friction indeed increases with hold times, consistent with the prediction from the rate-and-state formulation. Such an increase in peak friction highlights the fact that the interface is healing and becomes "stronger" with time. During the "slide-hold-reslide" experiments, similar behavior has been observed in which the peak friction during reslide phase increases with hold times (Beeler et al., 1998, Marone, 1998b), though such "hold" is imposed as fixed displacement at loading point rather than fixed stress as done in our experiments. These results suggest that the sliding history (i.e., the "state" of the fault) matters and cannot be neglected when modeling phenomena related to frictional sliding, including earthquakes.

1.3.4 Non-instantaneous failure model based on the rate-and-state friction

A rate-and-state fault under constant stress experiences healing and has a decaying slip rate with time. If we subject this same fault to stress rate $\dot{S}$, it will accelerate toward failure (Figure 1.12a). With the following approximations, the earthquake rates can be expressed analytically (Dieterich, 1994, Heimisson and Segall, 2018): (1) faults are well-above-steady-state (critically stressed), i.e., $V\theta/D_{RS} \leq 1$, and (2) aging law is used as the state evolution law. In this case, the state variable can be written as:

$$\theta(t) = \theta_0 e^{-\frac{\delta(t)}{D_{RS}}} \tag{1.11}$$

where $\delta(t)$ is the cumulative slip.

A fault with initial slip rate V_0, subjected to constant stress rate $\dot{S}$, would then accelerate according to the following expression:

$$V(t) = \frac{V_0 K(t)}{1 - \frac{HV_0}{a} \int_0^t K(t')\, dt'} \tag{1.12}$$

where the kernel $K(t)$ can be written as follows:

$$K(t) = e^{\frac{\Delta S(t)}{a\sigma}} \tag{1.13}$$

and H is given by:

$$H = \frac{k}{\sigma_0} - \frac{b}{D_{RS}} \tag{1.14}$$

where k is the stiffness of the fault, defined as a ratio of the shear stress relaxed and the amount of slip to release that relaxation. In the original derivation of Dieterich (1994), the normal stress is assumed to be constant, and $\Delta S(t)$ is shear stress change. However, to approximately account also for normal stress change, $\Delta S(t)$ can be taken as the Coulomb stress change (Ader et al., 2014, Dieterich et al., 2000, Perfettini et al., 2003). Heimisson and Segall (2018) has shown that if the normal stress change is smaller than 10% of the effective normal stress, such an approximation is valid.

The slip rate $V(t)$ would reach singularity and produce dynamic rupture when:

$$\int_0^{t_{\text{inst}}} K(t')\, dt' = \frac{a}{HV_0}. \tag{1.15}$$

The time to failure, referred to as "the time to instability" (t_{inst}) can be written as follows:

$$t_{\text{inst}} = \frac{a\sigma_0}{\dot{S}} \ln\left(\frac{\dot{S}}{HV_0\sigma_0} + 1\right). \tag{1.16}$$

If we subject this same fault with a stress step S_{step}, there will be a sudden velocity jump from V_1 to $V_1 \exp\left(\frac{S_{\text{step}}}{a\sigma}\right)$, and therefore, reducing the time to failure (Figure 1.12b). The amount of time advance depends non-linearly on the initial slip rate and is larger for smaller V_0.

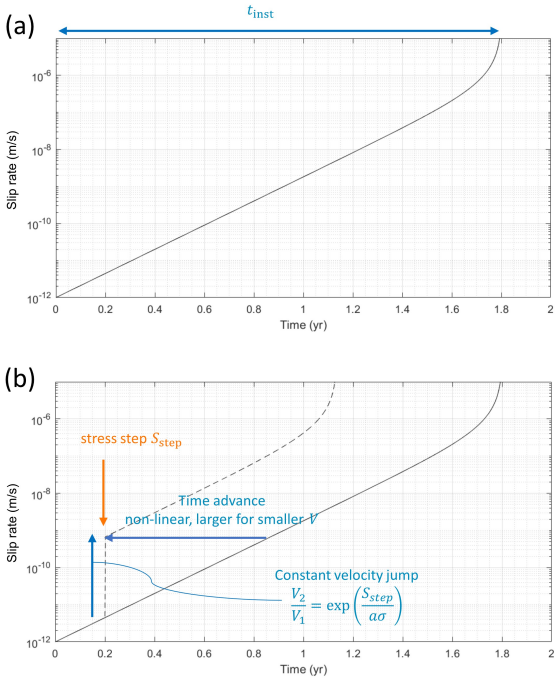

Figure 1.12: Acceleration of a rate-and-state fault under constant stress rate toward failure. (a) Time evolution of slip velocity. (b) Upon perturbation with a stress step, the time to failure decreases by a certain amount, which depends non-linearly on the initial velocity prior to experiencing the stress step.

Now, if we consider a population of fault with a range of initial velocities V_0. To get a constant seismicity rate, we need a population of fault with V_0 that is distributed logarithmically (Figure 1.13a). This is consistent with uniformly distributed healing time, which results in logarithmically distributed velocities because the slip rate decays as a power law during healing as a result of logarithmic growth of contact area (Chapter 2). Upon subjecting this population of faults to a stress step, we reproduce the Omori-Utsu law of aftershocks because of the non-linear time advance (Figure 1.13b). The response of earthquake rates $R(t)$ to an arbitrary stress perturbation $\Delta S(t)$ can be formulated analytically as follows (Dieterich, 1994, Heimisson and Segall, 2018):

$$\frac{R(t)}{r} = \frac{e^{\frac{\Delta S(t)}{a\sigma}}}{1 + \frac{1}{t_a}\int_0^t e^{\frac{\Delta S(t')}{a\sigma}}\, dt'} \tag{1.17}$$

where r is the earthquake rate occurring at background stress rate $\dot{S}$, $a\sigma$ is the frictional-stress parameter, and t_a is the characteristic time which equals to $a\sigma/\dot{S}$.

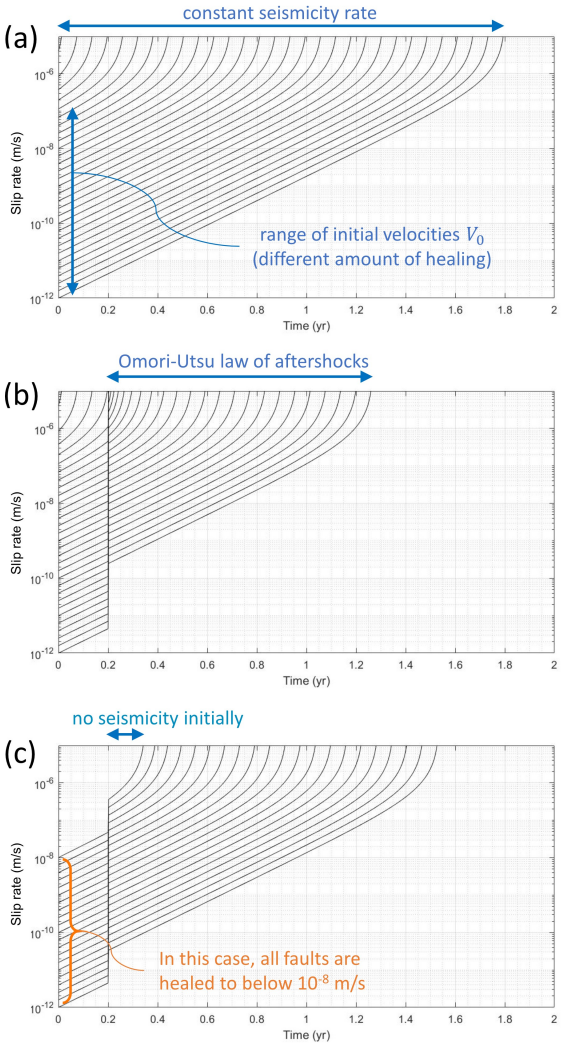

Figure 1.13: Earthquake rates for a population of rate-and-state faults. (a) Constant seismicity rate from constant stress rate. (b) Upon subjecting to a stress step, the seismicity rate is no longer constant but follows the Omori-Utsu law of aftershocks. (c) If the faults were healed below some slip rate, a stress step under a certain threshold will not immediately start seismicity.

In regions that are not tectonically active, the faults may heal down to below some slip rate. As a result, a certain amount of threshold stress ΔS_c is required to suddenly start an earthquake. If the stress is too small, there will be no seismicity initially (Figure 1.13c). This effect of healing has led to a modification of the formulation in Equation 1.17, resulting in the Coulomb threshold rate-and-state model, which can be written as follows (Heimisson et al., 2022):

$$\frac{R(t)}{r} = \begin{cases} 0 & \text{if } t < t_c \\ \dfrac{e^{\left(\frac{\Delta S(t) - a S_c}{a\sigma}\right)}}{1 + \frac{1}{t_a}\int_{t_c}^{t} e^{\left(\frac{\Delta S(x) - \Delta S_c}{a\sigma}\right)} dx} & \text{if } t \geq t_c \end{cases} \tag{1.18}$$

where t_c is the time when the threshold stress ΔS_c is first exceeded.

The models presented in this section account for the non-instantaneous nature of the earthquake nucleation and have been successfully used to describe various time-dependent behaviors of earthquakes (Acosta et al., 2023, Ader et al., 2014, Barbot et al., 2012, Dieterich, 1994, Dieterich et al., 2000, Sirorattanakul et al., 2022b), even though it is still a spring-slider zero-dimensional model without accounting for any finite fault effects. Among many others, Chapters 4 and 5 in this thesis utilize this model to explain a swarm in the Salton trough, California, driven by a spontaneous slow-slip event and the seasonal modulation of earthquake rates due to seasonal changes in hydrological loading in California, respectively.

1.3.5 Response of seismicity to harmonic perturbations

The Coulomb instantaneous failure model (CFM, Equation 1.4) and the spring-slider rate-and-state model (SRM, Equation 1.17) predict vastly different responses of earthquake rates to harmonic stress perturbations. The response of earthquake rates to harmonic stress perturbations is period-dependent. The amplitude of the response as predicted by CFM and SRM is shown in Figure 1.14. The readers can consult Ader et al. (2014) for a more thorough discussion of the topic, as it is relevant to Chapter 5 in this thesis.

In the CFM, the earthquake rate R is proportional to the stress rate $\dot{S}$. Since R cannot take a negative value, there is no earthquake when stress is decreasing (negative stress rate) until the stress grows back to its last maximum value. Given a superposition of background stress rate $\dot{S}_0$ and harmonic stress perturbation of amplitude $\Delta\tau$, the amplitude of the earthquake rate variation ΔR can be divided

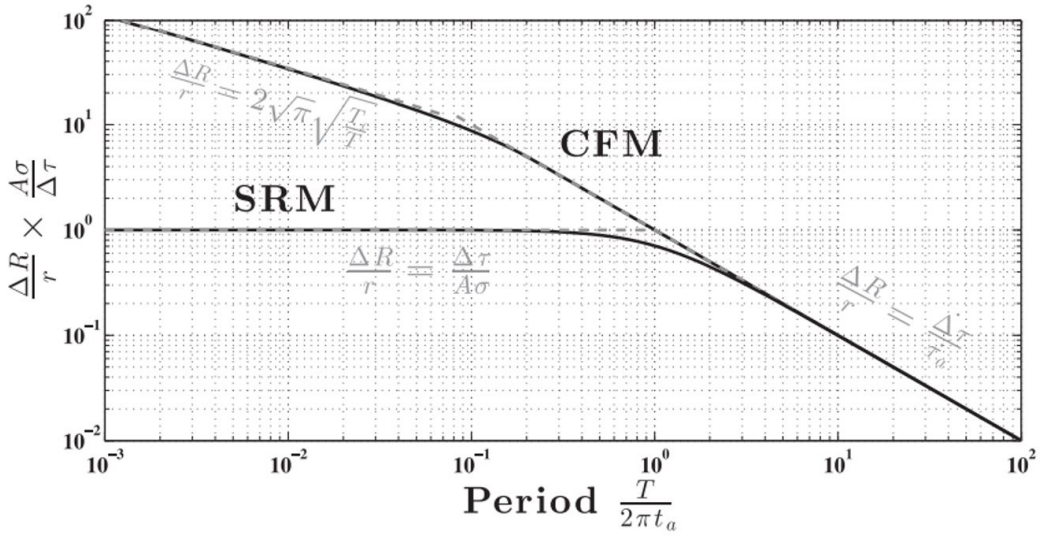

Figure 1.14: Response of seismicity to harmonic stress perturbations as predicted by the Coulomb instantaneous failure model (CFM) and the spring-slider rate-and-state model (SRM). Figure is taken from Ader et al. (2014).

into two regimes depending on the critical period $T_\tau = 2\pi\Delta\tau/\dot{S}_0$ and is given by the following (Ader et al., 2014):

$$\begin{aligned} \frac{\Delta R}{r} &= \frac{T_\tau}{T} \quad \text{when} T \geq T_\tau \\ \frac{\Delta R}{r} &= 2\sqrt{\pi}\sqrt{\frac{T_\tau}{T}} \quad \text{when} T \ll T_\tau. \end{aligned} \tag{1.19}$$

In the SRM, the earthquake nucleation is not instantaneous. For periods much larger than the characteristic period of $T_a = 2\pi a\sigma/\dot{S}_0$, the earthquake response is identical to CFM. On the other hand, for periods smaller than T_a, the amplitude of the response becomes independent of the period and is given by the following (Ader et al., 2014):

$$\frac{\Delta R}{r} = e^{\Delta\tau/a\sigma} - 1. \tag{1.20}$$

For the case of small perturbations, i.e., $\Delta\tau \ll a\sigma$, Equation 1.20 becomes $\Delta R/r = \Delta\tau/a\sigma$.

For most faults, the characteristic time t_a is approximately 1 year. Since the tidal stress (Section 1.1.6) and seasonal stress due to changes in hydrological surface

loading (Section 1.1.5) are about the same order of magnitude, the CFM predicts a much larger response to tidal stress than seasonal stress. This contradicts the general observations that seasonal modulation of earthquake rates is more prevalent than tidal modulation (Bucholc and Steacy, 2016, Cochran et al., 2004, Vidale et al., 1998). On the contrary, the SRM predicts a similar response to tidal and seasonal stress, which is closer to the observations, though it still cannot completely explain the observations. This contradiction is most likely due to the period-dependent ability to detect periodic modulation or other finite fault effects not accounted for in the SRM model. Furthermore, the CFM also cannot capture the time lag between the peak seismicity rate and the peak stress rate typically observed. The SRM predicts the time lag, which turns out to also be period-dependent.

1.4 Workflow for stress-based modeling of seismicity

Now that we have all the tools, I present a workflow that I use to model the response of earthquakes to transient stresses (Figure 1.15). The workflow consists of two independent parts.

The first part of the workflow is related to quantifying the rate of earthquakes. Typically, we start by generating a seismicity catalog or taking an existing, previously published catalog and analyzing it to determine the spatial and temporal evolution of the earthquake rates. In cases where aftershocks are prevalent and the stress changes

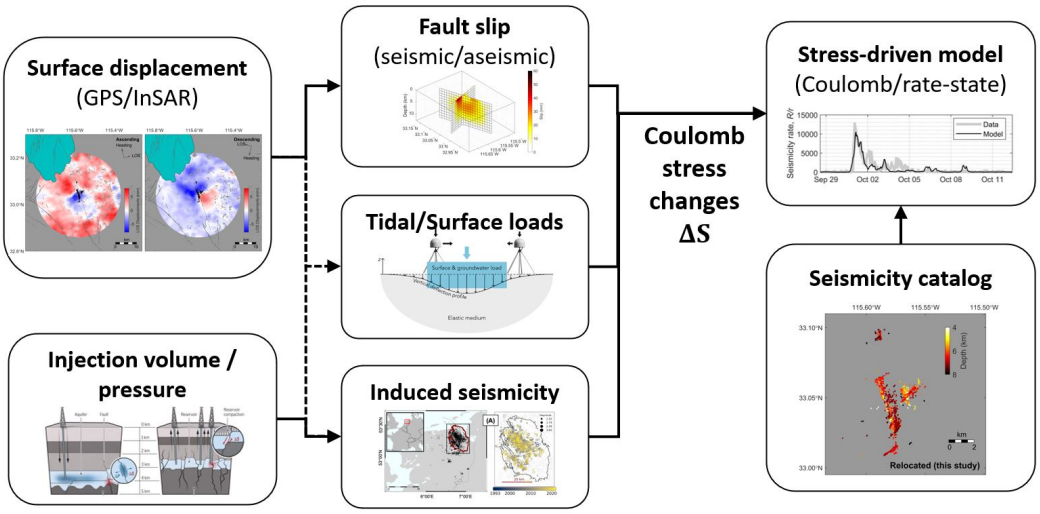

Figure 1.15: A workflow for stress-based modeling of seismicity. The illustrations are taken from the following articles: Acosta et al. (2023), Candela et al. (2018), Larochelle et al. (2022), Sirorattanakul et al. (2022b).

from the mainshocks are not the transient stresses of interest, the aftershocks will need to be removed using a process typically referred to as "declustering." For a more comprehensive review of the seismicity declustering, the readers can consult van der Elst et al. (2012). Here, we briefly describe a few popular declustering methods used:

- **Window method** is first introduced by Gardner and Knopoff (1974). For each earthquake, an interaction zone within a certain distance and time of that earthquake is defined using a functional form that depends on the earthquake magnitude (larger zone for larger magnitude). Other earthquakes that fall within this interaction zone are identified as aftershocks. This method is one of the simplest methods, but it ignores aftershocks of aftershocks.

- **Cluster method** goes beyond the window method and attempts to also identify aftershocks of aftershocks and place them together in a common cluster. The legacy method of this type was proposed by Reasenberg (1985), which also extends the Gardner and Knopoff (1974) by using a temporal interaction zone that is based on the Omori-Utsu law of aftershocks (Omori, 1894, Utsu, 1961).

- **Stochastic method** introduces a probabilistic treatment into practice. This reduces the dependency of the declustering on the chosen parameters (interaction zone sizes, etc.). A classical stochastic declustering method was proposed by Zhuang et al. (2002). The choice of space-time distance is optimized to best model the earthquakes, typically using a space-time branching process model such as the Epidemic-Type Aftershock-Sequence (ETAS) model (Ogata, 1988) or a more generalized kernel (Marsan and O., 2008).

- **Nearest-neighbor distance approach** utilizes a space-time distance metric introduced by (Baiesi and Paczuski, 2004, Zaliapin et al., 2008). For each event, we can find its nearest neighbor in space-time and calculate its distance. By exploring a space-time graphical representation of this distance, the earthquakes are typically divided into two modes – one representing a background Poissonian mode and a clustered (aftershocks) mode (Zaliapin and Ben-Zion, 2013a).

The second part of the workflow involves the quantification of the transient stresses of interest. The methods used here depend on the sources of those transient stresses. If the source of stress is a spontaneous slow-slip event, such as those in Chapter 4, a geodetic slip inversion can be performed by inverting the measured surface deformations for slip on fault planes. Then, the Coulomb stress changes can be calculated using a forward model such as the semi-analytical functions for dislocation in an elastic half-space (Okada, 1992). If the source of stress is the solid Earth tides, since it is now well-known theoretically, there exist many available software that can be used to directly compute tidal displacements or stresses, for example, the *Solid* software (Milbert, 2018). If the source of the stress is the hydrological surface loads, the seasonal water storage has to first be constrained, typically from surface displacements and gravity data (Argus et al., 2022, Larochelle et al., 2022). Then, the stresses due to surface loads or poroelastic effects can be computed using various semi-analytical functions (Boussinesq, 1878, Larochelle et al., 2022, Smith et al., 2019). If the source of stress is anthropogenic fluid injection or extraction, the flow model must first be constrained to determine the pressure changes in the subsurface reservoir (Meyer et al., 2023). The stress then can be computed using also semi-analytical functions (Acosta et al., 2023, Smith et al., 2019).

Finally, we can connect the two parts using the models described in the previous sections, such as the Coulomb instantaneous failure model (Section 1.3.1) or a stress-driven model based on rate-and-state friction formulation (Section 1.3.4). Chapters 4 and 5 utilize this workflow.

1.5 Thesis outline

This thesis attempts to further our understanding of the response of earthquakes to transient stresses and the friction laws governing the earthquake nucleation process through a collection of independent articles.

In the first two chapters, we focus on laboratory experiments conducted to enhance our understanding of the friction laws governing the shear interfaces. In Chapter 2, we investigate the state-of-the-art friction formulation used for modeling earthquakes. The traditional Coulomb friction postulates that there exists a threshold shear force, called “static friction”, below which the frictional interface remains stationary. More detailed friction measurements have revealed that friction is much more complicated and led to the development of rate- and state-dependent friction laws. Contradicting the Coulomb friction, the rate-and-state model predicts that

frictional interfaces under non-zero shear stress are always sliding. Our laboratory measurements, enabled by digital image correlation, reveal that these interfaces are actually sliding with diminishing slip rates down to 10^{-12} m/s, consistent with the prediction from the rate-and-state models. Our results support the usage of rate-and-state formulation to model earthquakes.

In Chapter 3, we discuss challenges associated with measurements performed in Chapter 2 and quantify the measurement uncertainty. The procedures developed allow us to treat displacement continuity across the interface and overcome the low signal-to-noise ratio through image averaging technique to reduce noises and conduct the measurements over a long period time enough for the interface to accumulate sufficient slip. Analysis of bulk effect and viscoelastic creep, errors due to electronic noises of the camera and micro-vibrations of the imaging apparatus, and the errors of the correlation algorithms have revealed that measurement uncertainty to be no more than 0.06 μm. This translates to a slip rate of 5 x 10^{-13} m/s.

Starting from Chapter 4, we move beyond laboratory experiments and study natural faults. In Chapter 4, we focus on a swarm sequence that occurred in 2020 near the Salton Trough, California. Using surface deformations from GPS and InSAR, we detect a shallow spontaneous slow-slip event that preceded the swarm sequence sometime between 2 – 15 hours. The time lag suggests that earthquake nucleation is not instantaneous. By using a model based on rate-and-state friction, we can explain the evolution of the swarm sequence including the time lag between the onset of slow-slip event and the swarm. We find that the early phase of the swarm is driven primarily by the slow-slip event, while the later phase is sustained by fluid diffusion as evident from the seismicity back front. We also determine that 45 – 65% of seismicity was driven by the slow-slip event, 10 – 35% by inter-earthquake interactions, and 10 – 30% by fluids.

In Chapter 5, we study the response of earthquakes to seasonal hydrological surface loading and tidal stress by using California as a case study. First, we develop a workflow to identify and quantify local regions with significant periodic modulations of earthquake rates. We find strong seasonal modulations of seismicity rate at an annual period, but no significant modulation at the tidal periods. The seasonal responses are dominated by regions that are associated with hydrothermal systems. The amplitude of seismicity rate modulation correlates with the amplitude of the seasonal stress perturbation induced by changes in surface loading. The peak seismicity rate occurred approximately 0.5 – 2.5 months after the peak stress rate,

reflecting the non-instantaneous nature of the earthquake nucleation process. The model based on rate-and-state friction can quantitatively explain the observations.

In Chapter 6, we study swarms of induced earthquakes at the Groningen gas field, Netherlands. Gas extraction from the Groningen reservoir has resulted in a pressure drop, driving compaction and induced seismicity. We create an enhanced seismicity catalog for the regions using a deep-learning-based workflow and find swarms that were not previously identified. These swarm sequences are short-lived, lasting only a few days, and often propagate at high velocities in the order of 3 – 50 km/day along directions that do not follow previously mapped faults. We suggest that these swarms are driven primarily by propagating aseismic deformation rather than fluids.

In the final chapter (Chapter 7) of the thesis, I summarize the findings from the different chapters and describe my perspectives on exciting future research directions.

Chapter 2

SLIDING AND HEALING OF FRICTIONAL INTERFACES THAT APPEAR STATIONARY

Submitted as:

K. Sirorattanakul, S. Larochelle, V. Rubino, N. Lapusta, and A. J. Rosakis. Sliding and healing of frictional interfaces that appear stationary.

Abstract

Frictional interfaces are found in many systems ranging from joints to micro-electro-mechanical devices to earthquake faults. When and how these interfaces slide is a fundamental problem in geosciences and engineering. It is commonly assumed that there exists a threshold shear force, called static friction, below which the interface is stationary for a given compressive force. Rate-and-state friction (RSF) formulations predict that interfaces are always sliding, but this feature is often considered an artifact that calls for modifications. Here, we monitor sliding rates of nominally stationary interfaces subjected to constant shear and normal loads, with a driving force that is significantly below the classically defined static friction. Our precise measurements directly at the interface enabled by Digital Image Correlation reveal that such interfaces are indeed sliding, albeit with diminishingly small rates down to 10^{-12} m/s. Such behavior contradicts classical models of friction with static friction coefficients but confirms the prediction of RSF. Our measurements of diminishing slip rates on nominally stationary interfaces enable us to quantify increasing interface healing, which would manifest itself in higher peak friction in subsequent slip events, such as earthquakes and landslides, significantly modifying their nucleation and propagation and hence their hazard.

2.1 Introduction

Sliding of frictional interfaces (Rice and Ruina, 1983, Rice et al., 2001) is a fundamental problem with numerous engineering and geosciences applications such as earthquakes (Ampuero and Rubin, 2008, Dieterich, 2007, Scholz, 2019), landslides (Handwerger et al., 2016, Helmstetter et al., 2004), glacier flow(Gräff and Walter, 2021, Thøgersen et al., 2019, Zoet and Iverson, 2018), and vibrations of automobile breaks (Kinkaid et al., 2003). The key parameter governing sliding is the ratio of

shear to normal force (or stress, defined as force per unit area) on the interface. A common assumption, dating back to Coulomb (Dowson, 1979) and before, is that a frictional interface in stationary contact remains in stationary contact until the ratio of the shear to normal force reaches a threshold value called static friction coefficient (f_s). A conventional way to measure the static friction coefficient is by placing an object on an inclined plane and slowly tilting the plane until the object starts to (visibly) slide at some critical inclination angle α_{crit} (Figure 2.1A). Consequently, $f_s = \tan \alpha_{\text{crit}}$. After sliding is initiated, the ratio of the shear to normal force is governed by the kinetic friction coefficient f_k which is often lower. In the simplest Coulomb model (Dowson, 1979), the transition from f_s to f_k is instantaneous, which is non-physical. However, it is still widely used today to model landslides (Lacroix et al., 2020) and earthquakes induced by gas extraction (Bourne et al., 2018, Dempsey and Suckale, 2017) owing to its simplicity. Alternatively, slip-weakening models (Ida, 1973, Palmer and Rice, 1973) allow the transition from f_s to f_k to occur with slip (Figure 2.1B) providing a link to fracture mechanics (Freund, 1990) and are widely used in modeling earthquake rupture (Bhattacharya and Viesca, 2019, Ohnaka, 2003, Xia et al., 2004). Although slip-weakening models are more realistic than the instantaneous Coulomb model, they still lack strengthening mechanisms and therefore cannot be used to model how interface regain strengths before future events, as occurs in earthquake sequences.

More detailed friction measurements have revealed that the friction coefficient depends on the rate of slip $V(t)$ and has memory effects encoded in an evolving state variable $\theta(t)$, which has led to the development of rate-and-state friction formulations (Dieterich, 1979, Marone, 1998a, Rice and Ruina, 1983, Rice et al., 2001, Ruina, 1983); one example is:

$$f = f^* + a \ln\left(\frac{V(t)}{V^*}\right) + b \ln\left(\frac{V^*\theta(t)}{D_{RS}}\right) \tag{2.1}$$

$$\frac{d\theta}{dt} = 1 - \frac{V(t)\theta(t)}{D_{RS}} \tag{2.2}$$

$$\frac{d\theta}{dt} = -\frac{V(t)\theta(t)}{D_{RS}} \ln\left(\frac{V(t)\theta(t)}{D_{RS}}\right) \tag{2.3}$$

where t is time, f is the evolving friction coefficient, f^* is a reference friction coefficient at reference slip rate V^*, D_{RS} is the critical slip distance, and a and

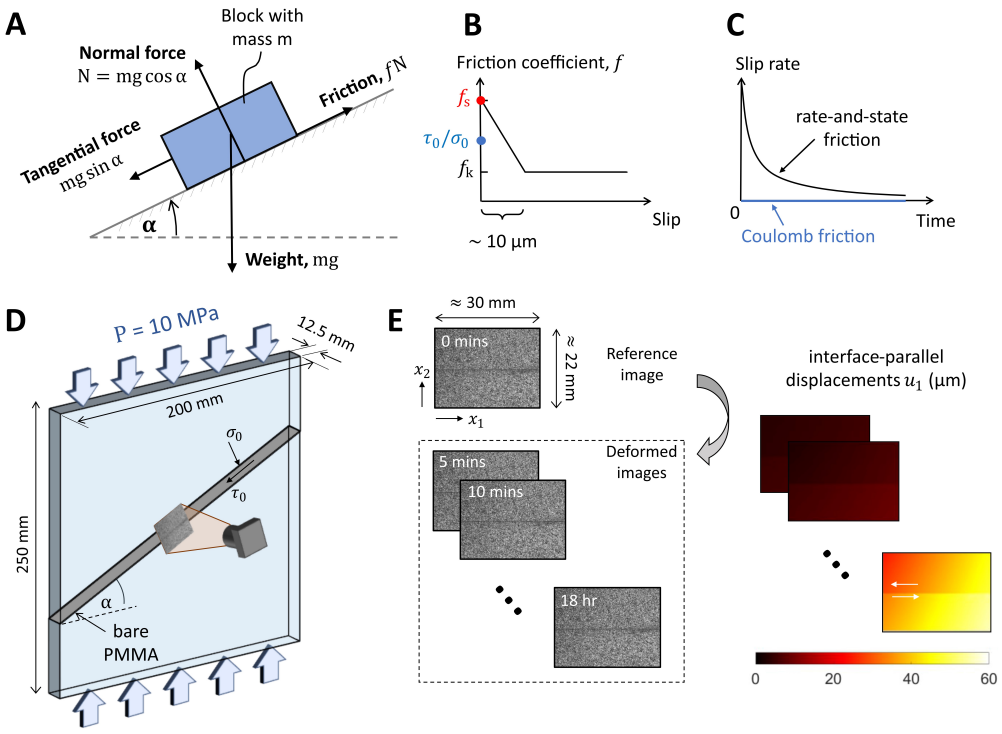

Figure 2.1: Testing the concept of static friction. (A) A block on an inclined plane. The notion of static friction posits that the block should remain motionless for inclination angles α below the critical value given by $\tan\alpha_{\text{crit}} = f_s$. (B) Slip-weakening friction law. According to this widely used classical model, the ratio of shear to normal stresses (τ_0/σ_0) needs to reach a critical value (f_s) for sliding to start. As sliding proceeds, friction coefficient transitions from the static value f_s to a lower kinetic value f_k over some slip. (C) Schematic slip-rate evolution for a nominally stationary interface governed by experimentally derived rate-and-state friction laws which predict that frictional interfaces under shear stress are always slide. (D) Experimental setup designed to study frictional PMMA interfaces with inclination angles below α_{crit} and hence $\tau_0/\sigma_0 < f_s$. A digital camera continuously monitors the displacements of a portion of the interface. The load is maintained for 18 hours in most experiments and two weeks in one experiment. Optical images are taken every 5 minutes. (E) The full-field distribution of displacements and hence slip across the interface is measured by digital image correlation (DIC).

b are nondimensional parameters quantifying the direct and evolutionary effects, respectively. Several state evolution laws have been proposed, including the aging and slip ones given in Equation 2.2 and 2.3. To make the empirical formulation (Equation 2.1) physical at zero slip rate, a widely used regularization is based on an Arrhenius activated rate process describing creep at asperity contacts, which replaces the logarithmic function of slip rate V with a function that makes the

zero slip rate only possible for zero shear stress (Lapusta et al., 2000, Nakatani, 2001, Rice et al., 2001) (see also Section A.1.5). The rate-and-state formulation has proven successful in explaining a number of time-dependent behaviors of the earthquake source, such as the evolution of postseismic slip and aftershock rates after the mainshock (Dieterich, 1994, 2007), presence of both locked and slowly creeping segments on natural faults (Bürgmann et al., 2000, Perfettini et al., 2010), nontrivial scaling of repeating earthquakes and detailed slip long-term behavior of fault segments (Barbot et al., 2012, Chen and Lapusta, 2009, Lapusta et al., 2000, Vidale et al., 1994), correlation of earthquakes with periodic loading such as solid Earth tides and hydromechanical variations (Ader et al., 2014, Beeler and Lockner, 2003), slow-slip driven earthquake swarms (Sirorattanakul et al., 2022b) and induced seismicity resulting from gas extraction (Acosta et al., 2023).

One of the predictions of the rate-and-state framework is that all interfaces under non-zero shear stress are sliding with non-zero slip rates, in contrast to the concept of static friction (Gu et al., 1984). Another prediction is that the interface heals at low enough slip rates, with the healing manifesting itself through higher peak friction during subsequent paid sliding episodes, as observed in slide-hold-slide experiments (Beeler et al., 1998, Marone, 1998a,b). The exact nature of sliding during the hold times has profound implications for healing and how it should be incorporated into the friction laws. However, sliding has never been directly measured at the interfaces during hold portions in previous experiments, but rather inferred through modeling that already assumed a rate-and-state formulation (Beeler et al., 1998, Bhattacharya et al., 2022, Marone, 1998a). That leaves open the possibility that the physics during holds is different from what is described by the rate-and-state framework (Equation 2.1, 2.2, 2.3), for example, that the slip rate vanishes at a threshold, as assumed by some formulations (Daub and Carlson, 2008, Perrin et al., 1995, Zheng and Rice, 1998). Here, for the first time, we perform local optical measurements of sliding during nominal hold that are accurate enough to address these issues.

2.2 Continuous sliding of seemingly stationary frictional interfaces

We test the concepts of static friction, continuous diminishing sliding during holds, and healing by considering seemingly stationary frictional interfaces in the laboratory (Figure 2.1). Two plates are in contact over an interface with an inclination angle lower than the critical angle needed to observe visible sliding, with the setup analogous to a block on the inclined plane (Figure 2.1). This experimental setup has been used to study key issues of frictional sliding and rupture dynamics, including

the sub-Rayleigh to supershear rupture transition, pulse-like and crack-like rupture modes, evolution of dynamic friction, and effects of fluid injection and rock gouge (Gori et al., 2021, Rubino et al., 2017, 2022, Tal et al., 2020, Xia et al., 2004). To initiate dynamic rupture in past experiments, an explosion of a thin wire was used to locally lower normal stress, underscoring the nominally stationary nature of the interfaces. In this work, we use Digital Image Correlation (DIC) (Sutton et al., 2009) to provide a direct measurement of relative displacements at the interface and to determine whether the interfaces are indeed sliding. We find that the interfaces are in fact slowly sliding, in contradiction to the static friction concept but in a manner fully consistent with predictions of rate-and-state friction formulations, as detailed below.

To create a nominally stationary frictional interface, we use two equal-sized Poly Methyl Meth Acrylate (PMMA) plates to form an interface inclined by angle α (Figure 2.1D). The specimen is compressed by a vertical load P = 10 MPa, resulting in resolved shear and normal stresses $\sigma_0 = P\cos^2\alpha$ and $\tau_0 = P\sin\alpha\cos\alpha$ with the ratio $\tau_0/\sigma_0 = \tan\alpha$. We study interfaces with values of α such that the ratio of the resolved shear to normal stresses is less than the classically defined static friction coefficient f_s, i.e., $\tan\alpha < f_s = \tan\alpha_{\text{crit}}$. To determine α_{crit}, we conduct a series of experiments incrementally increasing the inclination angle α until the surface starts to visibly slip during loading. We find this critical angle (α_{crit}) to be 30° and therefore $f_s = \tan(\alpha_{\text{crit}}) = 0.58$. Hence, we select an angle α = 26° for our study, with $\tan 26° = 0.49$ being significantly smaller than the static friction coefficient f_s = 0.58. To put the difference in friction coefficient of about 0.1 in perspective, its product with average compressive stress of 100-200 MPa over the seismogenic depths would result in shear stress changes of about 10-20 MPa, while the average shear stress change in earthquakes is 1-10 MPa (Shearer, 2019).

Once the target load P is reached, the specimen is left untouched for 18 hours in one type of experiments and two weeks in another, with the load kept constant using the automatic load-control. Six repeated 18-hour tests and one 2-week test are conducted. We measure the amount of interfacial sliding from DIC measurements (Sutton et al., 2009) using optical images taken at the center of the specimen every 5 minutes over a field of view of 30 x 22 mm^2 (Figure 2.1D and A.1). As a result, we can track the full-field distributions of displacements over the entire field of view (Figure 2.1E; see SectionA.1.3 and Tables A.1 and A.2). We have successfully used this approach to quantify the full-field behavior of dynamic ruptures (Rosakis

et al., 2020, Rubino et al., 2019, 2020) and characterize the evolution of dynamic friction (Rubino et al., 2017, 2022, Tal et al., 2020). The relative sliding (slip) at the interface is obtained locally from the difference of the displacement component in the interface-parallel direction, measured immediately above and below the interface. The ability to perform such local measurements is a key advantage compared to most frictional experiments that infer slip from far-field measurements of the load-point displacement.

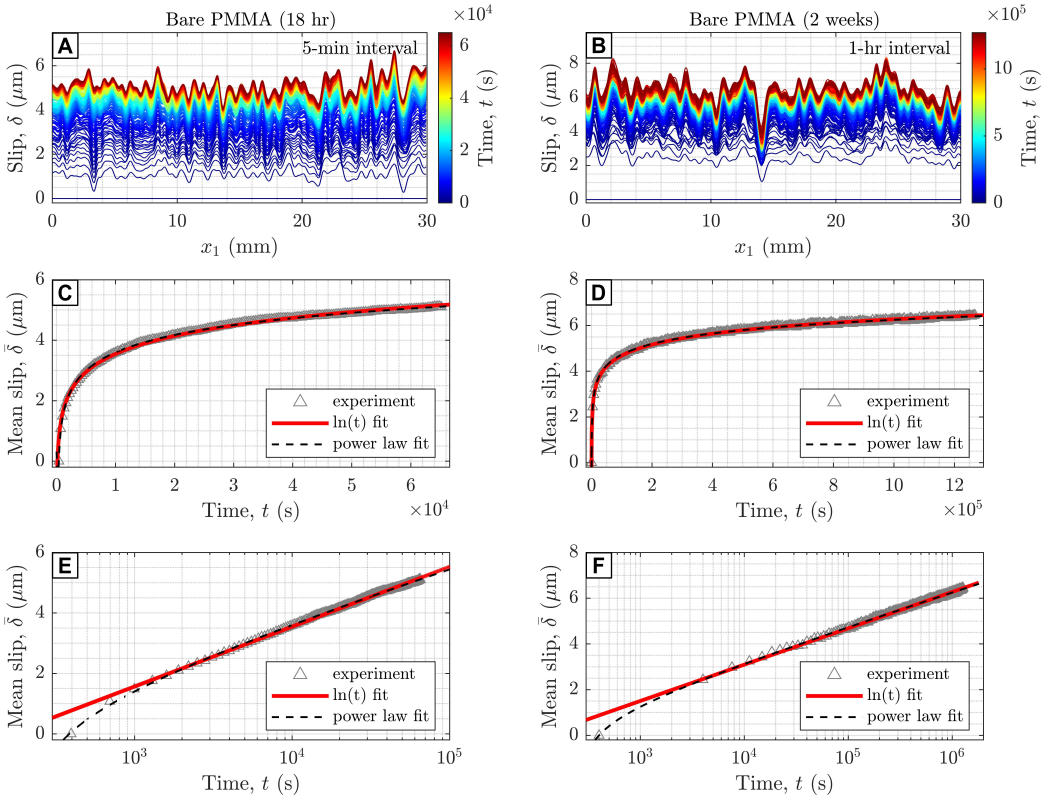

Figure 2.2: Experimental measurements showing continuous sliding of nominally stationary frictional interfaces. (A, B) Accumulating slip $\delta(x_1, t)$ along the PMMA interfaces color-coded by time, from two distinct experiments, one over 18 hr (6.48 x 10^4 s) (left) and another over 2 weeks (1.21 x 10^6 s) (right). (C–D) The corresponding evolution of the mean slip (triangle symbols). The mean slip is fitted using predicted functions from rate-and-state friction, with logarithmic functions arising from the velocity-neutral ($a = b$) assumption (red lines) and power-law functions arising from the aging state evolution law when $V\theta/D_{RS} \ll 1$ ($\theta = t$ approximation) (dashed black lines). (E-F) The same results with the time on log scale, emphasizing that power laws provide a better fit.

Our measurements reveal that the PMMA interfaces exhibit continuous sliding over the entire duration of the experiments (Figure 2.2), in contradiction to the notion

of static friction and laws that incorporate it, such as slip-weakening friction (Ida, 1973, Palmer and Rice, 1973). Tracing slip distributions over the interface at equally spaced time instants shows curves clustering with increasing time. This indicates that slip rates are decreasing with time, consistent with rate-and-state friction formulations which predict that such interfaces should be healing with time. Mathematically, this is expressed through the increasing state variable, which results in the decay of slip rates to add up to the same resolved shear stress in Equation 2.1. Falling slip rates with time are also displayed by the time histories of the mean cumulated slip $\bar{\delta}$, with $\bar{\delta} = \frac{1}{L}\int \delta(x_1, t)\, dx_1$ (Figure 2.2C-D).

After 18 hours of hold time, the mean accumulated slip δ ranges from 4 to 6 microns for bare PMMA surfaces. Only a minute part (< 0.05 microns) of the slip budget can be accommodated by viscoelastic relaxation of the specimens, as revealed by tests conducted on specimens without interface and in which no frictional sliding is present (Figure A.2 and see also Section A.1.4). Moreover, the sharp discontinuity in the displacement field across the interface indicates that shear-induced deformation of the material near the interface contributes a negligible portion of the slip budget (Figure A.3 and see also Section A.1.4). Moreover, given that the average height of the microscale roughness is typically *sim* 0.5 microns for a similar material (Homalite-100) prepared with a similar procedure (Mello, 2012), microscale inelastic deformation/bending of interfacial asperities can probably account for only a small fraction of the measured slip. The averaged slip evolution for different tests under the same conditions is also remarkably similar (Figure A.4).

2.3 Continuous sliding of interfaces with granular materials

To examine friction in granular materials and provide an analog of natural earthquake faults, we have also conducted 18-hour experiments with a rock gouge layer filling most of the interface (Figure 2.3A; see also Section A.1.1). Gouge is the fine granular material present in faults in the Earth's crust (Chester and Chester, 1998, Mitchell and Faulkner, 2009). The fault gouge layer exhibits the same qualitative behavior as the bare PMMA interface, with continuously accumulating slip which slows down with time (Figure 2.3B-C). Given the time dependence of the measured relative displacement, it cannot be due to elastic deformation of the gouge layer, which would occur at the beginning of the hold. One difference of the gouge experiments in comparison with the PMMA-interface ones is that the former visibly slip during loading as well, and then result in much larger net slip in the same

amount of monitored time. Yet they do appear nominally stationary at the end of the experiment, at 18 hours, when their slip rate reduces to nearly 10^{-10} m/s. Hence their behavior also violates the notion of static friction coefficient since the interfaces first appear to slide and then not at the same ratio of shear to normal stress.

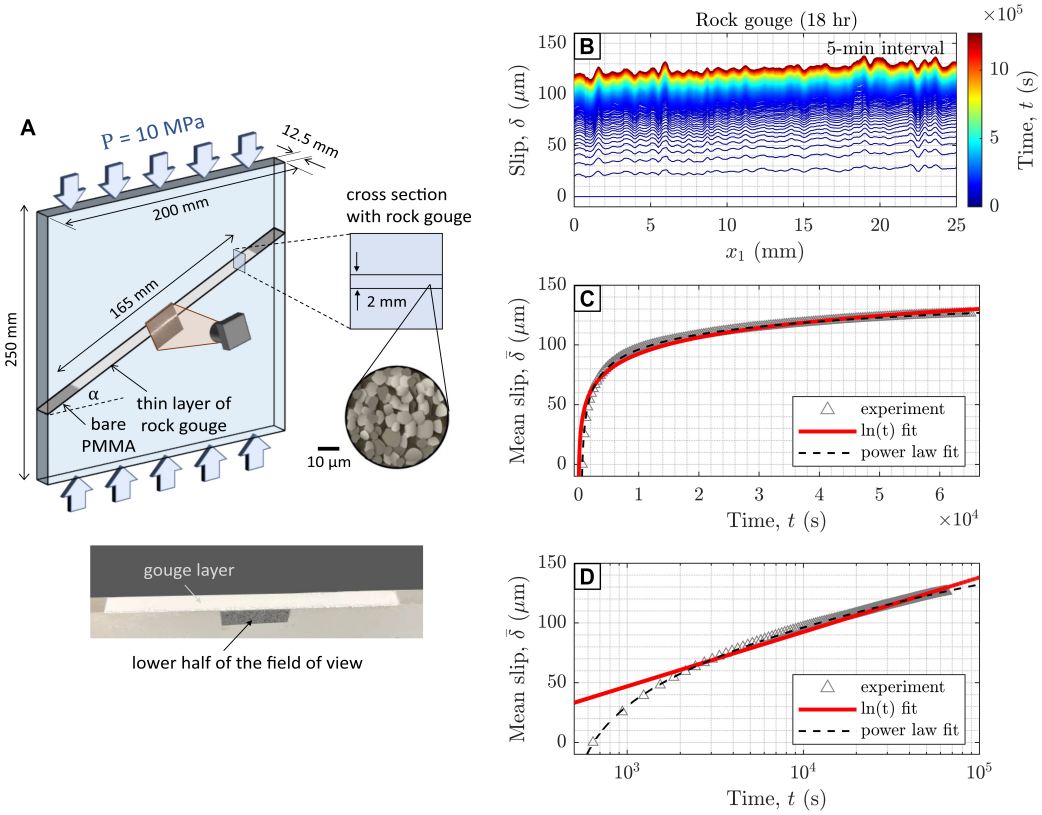

Figure 2.3: Interfaces with rock gouge sliding with decaying rates under the same loading conditions. (A) Experimental setup featuring rock gouge layer embedded within the PMMA interface. (B) Accumulating slip $\delta(x_1, t)$ along the interface color-coded with time. (C) The corresponding evolution of the mean slip across the gouge layer (triangle symbols). The fits are as in Figure 2.2C-F. (D) The same results with the time on log scale, emphasizing that power laws provide a better fit.

2.4 Explaining slip rates with rate-and-state framework

While both the observed accumulating slip and decrease in slip rate are qualitatively consistent with rate-and-state friction formulations, let us demonstrate this more quantitatively. To match the measured slip rate evolution with the rate-and-state formulation, we can change four rate-and-state parameters and one initial condition (for the history-dependent state variable). To identify all possible parameter values consistent with our observations, one could conduct a comprehensive grid search

over this parameter space by numerically iterating between Equations 2.1 and 2.2 (or Equations 2.1 and 2.3). However, here we consider two scenarios for which closed-form analytical solutions do exist, allowing us to invert for the best-fit parameters for these scenarios directly from the data.

The first scenario assumes that the frictional interface is velocity-neutral ($a = b$), i.e., friction does not depend on slip rate in steady state. In such a case, the cumulated slip is predicted to increase logarithmically with time as:

$$\delta(t) = C_1 \ln t + C_2 \tag{2.4}$$

where constant C_1 is a function of rate-and-state parameter a, critical slip distance D_{RS}, and reference friction coefficient f^* that depends on the state evolution law and constant C_2 depends on initial conditions (see also Section A.1.6). The logarithmic fit captures the qualitative features of the accumulating slip but significantly diverges from the measurements during early times for the PMMA interfaces (Figures 2.2E-F, A.4 and A.5), and even more so for rock gouge, underpredicting the slip in the middle part of the experiment and overpredicting it toward the end (Figures 2.3C-D, A.6 and A.7). The misfit suggests that, under our experimental conditions, neither interface is velocity-neutral, although this approximation fits PMMA interfaces better than rock gouge ones.

The second scenario assumes that the value of the state variable θ is equal to time t, as would be approximately correct for the aging form of the state variable evolution for small enough slip rates. If $V\theta/D_{RS} \ll 1$, the aging form reduces to $d\theta/dt = 1$ and the state variable grows with time. With this approximation, slip evolves as a power law of time:

$$\delta(t) = C_1(t - t_0)^{C_3} + C_2 \tag{2.5}$$

where C_1 is a function of a, D_{RS}, and f^*, $C_3 = 1 - b/a$, and C_2 and t_0 depend on initial conditions (see also Section A.1.7). In particular, parameter C_3 can be used to constrain the ratio b/a and determine whether the interface is velocity-weakening, velocity-neutral, or velocity-strengthening. We find a near-perfect fit for both bare PMMA interfaces (Figures 2.2E-F, A.8 and A.9) and interfaces with rock gouge (Figures 2.3C-D, A.10 and A.11). A better fit than the first scenario is expected because this scenario contains more fitting parameters. The fit is nonunique, in

that similar errors can be achieved for different combinations of the rate-and-state parameters (Figure A.12). The best fit suggests that both types of interfaces are velocity-weakening, but the PMMA interfaces are closer to velocity-neutral than those with rock gouge (Figure 2.3C-D), consistent with the first approximate approach. We note that this fit assumes that interface healing - and the state variable evolution - occurs mainly with time; recent experimental studies indicate that healing may occur predominantly with slip (Bhattacharya et al., 2022). While the fit here is done mainly to illustrate that the results are consistent with the rate-and-state framework, it would be important to develop more general fitting procedures.

Since the $\theta = t$ approximation better explains our observations, we compute the temporal evolution of slip rates using time derivatives of the best-fitting power laws (Figure 2.4A-B). We find that, after 18 hours of hold time, the interfaces are still sliding, with the slip rates decaying by more than 3 orders of magnitude, starting from 10^{-7} m/s and reaching values of 10^{-11} m/s and 10^{-10} m/s for bare PMMA and for rock gouge interfaces, respectively (Figure 2.4A). Furthermore, the (separate) two-week-long test with bare PMMA interfaces picks up right where the 18-hour test ends, with slip velocities decreasing another order of magnitude but never reaching zero (Figure 2.4B). The fact that we find very similar slip rate decay curves for the series of repeated tests confirm the repeatability of the experimental findings. The measurement of miniscule slip rates (10^{-12} m/s) and repeatability are enabled by a meticulous experimental procedure involving highly tailored DIC analysis and a strict protocol for the preparation of the frictional interfaces.

2.5 The diminishing slip rates capture interface healing

Our setup features a unique scenario in which the friction coefficient (ratio of shear to normal stress) remains constant throughout the experiments, even during the initial loading phase. This provides a unique opportunity for us to directly quantify healing, as the decaying slip rates $V(t)$ directly reflect the increasing state variable $\theta(t)$. With respect to a reference value of slip rate V_0 at state variable θ_0, the evolution of the state variable can be rewritten from Equation 2.1 as follows:

$$\left(\frac{\theta(t)}{\theta_0}\right)^{\frac{b}{a}} = \frac{V_0}{V(t)}. \tag{2.6}$$

This means that we can visualize the interface healing by interpreting the measured slip rates in terms of the evolution of the state variable that records healing (Figure 2.4C). Hence the experiments developed here provide new opportunities for direct

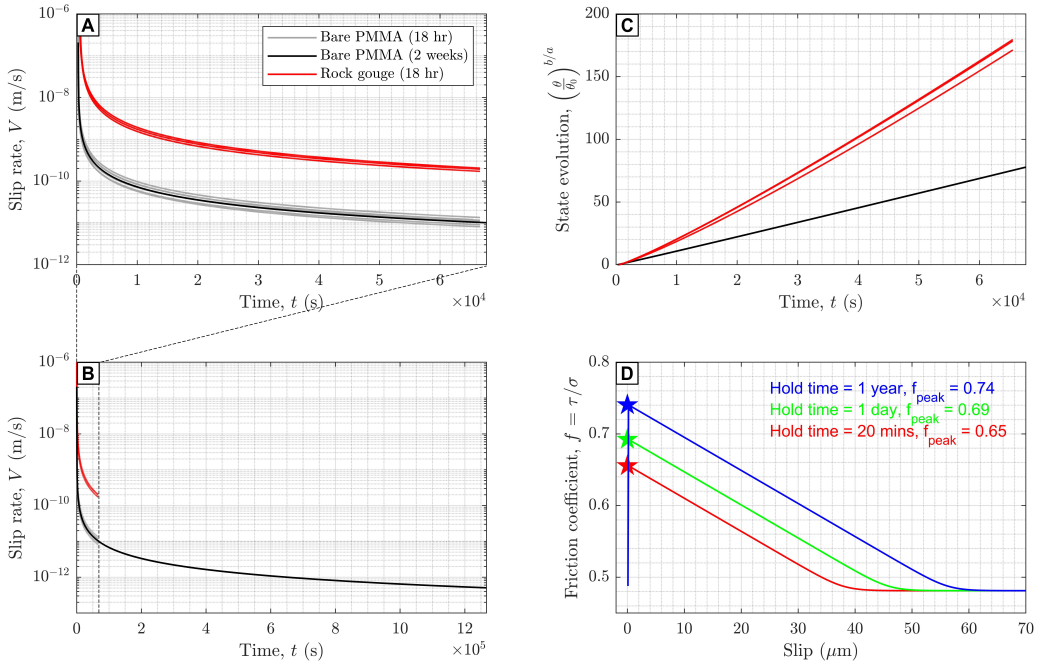

Figure 2.4: Non-zero, diminishing slip velocity of nominally stationary interfaces validates the rate-and-state formulation and captures healing. (A-B) The evolution of slip rate for all experiments (six 18-hour and one 2-week experiments for PMMA interfaces and three 18-hour experiments for rock gouge) obtained by differentiating the best power-law fit of slip. The experiments are highly repeatable and are consistent with the rate-and-state framework. (C) Healing is recorded by increases in the state variable, which can be inferred directly from our measurements without assuming any form for the state evolution law. (D) Rapid velocity jump to a slip rate of 1 m/s after longer hold times would result in significantly higher peak friction, larger critical slip distance, and larger effective fracture energy.

quantification of state variable evolution and healing without needing to infer it from modeling.

One of the consequences of healing is the higher peak friction for more healed interface (Beeler et al., 1998, Marone, 1998a,b). Assuming reasonable rate-and-state parameters for PMMA consistent with our fits (a = 0.008, $a - b$ = - 0.001, D_{RS} = 2 μm, V^* = 1 μm/s, f^* = 0.50) and aging law (Dieterich, 1979), by increasing the hold times from 20 mins to 1 year, the peak friction is expected to increase by 0.09 (Figure 2.4D). This translates to peak shear resistance increases of about 10–20 MPa at seismogenic depths, much larger than the average stress drops of 3 MPa for earthquakes (Shearer, 2019), highlighting the importance of healing in geologic faults. Furthermore, if we approximate the friction evolution with slip-

weakening laws (Ida, 1973, Palmer and Rice, 1973), the critical slip distance D_c would also increase from roughly 40 to 60 μm and the effective fracture energy $G = \frac{1}{2}\left(\tau_{peak} - \tau_d\right) D_c$ would change from 3.5 to 8 J/m^2. While slip-weakening laws can be a good approximation for modeling friction, their parameters are not constant in time but rather depend on the state of the interfaces and the sliding processes.

2.6 Discussion and conclusions

Although previous studies indicate that the concept of static friction does not capture the entire frictional behavior (Dieterich, 1979, Marone, 1998a, Rice et al., 2001, Ruina, 1983), such a concept is still widely used to model earthquakes and landslides (Bourne et al., 2018, Dempsey and Suckale, 2017, Lacroix et al., 2020). Our experiments provide the first direct measurements that nominally stationary frictional interfaces – with driving forces below static friction – are, in fact, sliding with diminishing slip rates, and hence also healing. By using local interfacial sliding measurements of unprecedented accuracy, we demonstrate that, under shear, nominally stationary bare frictional interfaces and those embedded with granular materials are sliding with decreasing slip rates, imperceivable to the eye, that can only be measured with an extremely accurate technique. This is even true when the ratio of shear to normal stress is lower than the classically defined static friction coefficient, measured for PMMA based on the critical angle concept. Our experimental observations can be fitted with rate-and-state friction formulations but cannot be explained by laws that incorporate the concept of static friction such as the widely used slip-weakening laws. The decrease of slip rates with time allows us to infer the increase in the state variable and hence quantify interface healing. Our findings suggest that the prediction of rate-and-state friction that interfaces under shear are always sliding is not an artifact – as still commonly assumed – and holds down at least to slip rates of the order of 10^{-12} m/s. While such slip rates may be negligible for some applications, they are crucial for understanding earthquake nucleation (Ampuero and Rubin, 2008, Dieterich, 2007, Gvirtzman and Fineberg, 2021) as well as for validation of the rate-and-state formulation which posits that the properties of frictional interfaces change even when they appear stationary, in terms of decreasing slip rates and increasing values of the state variable that record healing. The healing then manifests itself in terms of higher peak friction during more rapid sliding episodes (Beeler et al., 1998, Marone, 1998a,b), making earthquake and landslide hazard dependent on the amount of healing. In addition, our

experiments on nominally stationary interfaces give access to very small slip rates V down to 10^{-12} m/s that have never been reported in a frictional study. Hence our experimental procedure can serve as a complementary method to constrain frictional parameters and study different state evolution laws. By combining our experiments with classical velocity-jump experiments (Dieterich, 1979, Marone, 1998a) ($V \sim 10^{-6}$ m/s) and dynamic rupture experiments (Rubino et al., 2017, 2022, Tal et al., 2020) ($V \sim 1$ m/s), we can enhance our understanding of how friction behaves across different scales of slip rates with far-ranging implications from engineering to geoscience.

Chapter 3

EXPERIMENTAL QUANTIFICATION OF ULTRASLOW SLIP RATE OF SHEAR INTERFACES USING DIGITAL IMAGE CORRELATION

To be submitted as:

K. Sirorattanakul,V. Rubino, A. Lattanzi, and A. J. Rosakis. Experimental quantification of ultraslow slip rate of shear interfaces using digital image correlation.

Abstract

Frictional interfaces subjected to constant shear and normal loads are expected to strengthen with time through the growth of contact area at the microscale. During the healing period, the interfaces are thought to continuously slide with a decaying slip rate. In this work, we develop a novel experimental methodology designed to capture the local evolution of the slip rate of shear interfaces, enabling the quantification of interfacial healing without needing to infer it from far-field measurements at the loading point. Specimens with pre-existing interfaces are subjected to constant shear and normal load, well-below the classically defined static friction. Such load is kept constant for 18 hours. Optical images are taken to monitor the specimen and analyzed by digital image correlation (DIC) optimized to capture small displacements and enhanced to treat displacement discontinuities. The developed procedure achieves unprecedented levels of accuracy in the spatio-temporal evolution of slip rate measurements. We find that the frictional interfaces are indeed sliding with a decaying slip rate down to 10^{-12} m/s after 18 hours, which is imperceivable to the eye. Uncertainty analysis using a loaded specimen with no interface, motionless images, and numerically simulated experiments suggest that we can measure slip to the precision of sub-micron. With a carefully designed experiment enabled by DIC, we achieve a new level of precision in measuring ultraslow slip rate. While the method is developed for the frictional problems, it can also be applied to measure minute deformation in a host of other settings featuring pre-existing interfaces, including composite materials and bimaterial interfaces.

3.1 Introduction

The study of the failure of shear interfaces (Rice and Ruina, 1983, Rice et al., 2001) is relevant to a wide range of geophysics and engineering topics, including earthquakes and landslides (Ampuero and Rubin, 2008, Daub and Carlson, 2008, Dieterich, 2007, Handwerger et al., 2016, Scholz, 2019), delamination of composites (Zhou and Huang, 2020), automobile breaks (Kinkaid et al., 2003), adhesion of climbing animals (Labonte and Federle, 2016), orthopedic and dental implant (Gao et al., 2019), etc. In the classical model of Coulomb friction, the shear interfaces start to slide when the driving force overcomes the shear resistance of the interface and remains stationary otherwise (Dowson, 1979). In contradiction, measurements based on traditional slide-hold-slide experiments suggest that the shear interface is sliding even when the driving force is smaller than the shear resistance, albeit with a continuously decaying slip rate, as inferred from the reduction of shear stress during the hold phase when the displacement at the loading point is kept at constant (Bhattacharya et al., 2022, Dieterich, 1979, Marone, 1998a). The decay in slip rate reflects the strengthening and hence "healing" of the interface through the growth of the contact area with time (Dieterich and Kilgore, 1994). Such a phenomenon has led to the development of an empirical friction formulation that depends both on the slip rate and the healing state of the interface, typically referred to as "rate-and-state" friction formulation (Dieterich, 1979, Ruina, 1983). While such a small sliding rate (10^{-6} m/s or less) can be considered stationary in many applications (Daub and Carlson, 2008, Perrin et al., 1995, Zheng and Rice, 1998), its healing state plays a major role in controlling the nucleation and propagation of subsequent dynamic ruptures in earthquake faults (Beeler et al., 1998, Marone, 1998a,b).

Thus far, existing experimental studies infer slip rate evolution during healing through modeling of shear stress evolution or displacement at loading point which already assumes rate-and-state friction formulation (Bhattacharya et al., 2022, Dieterich, 1979, Marone, 1998a). In this study, we present a setup capable of locally capturing spatial and temporal evolution of ultraslow slip rate of shear interfaces during healing without needing to infer it from modeling (Figure 3.1). Our experimental measurements and analysis allow us to detect slip across the interface on the orders of 0.1 microns and slip rate levels of less than 5 x 10^{-13} m/s, over timescales of 18 hr and up to 2 weeks for a select test, something that has not been achieved before, to the best our knowledge. The metrological advance relies on the digital image correlations (DIC) method (Chu et al., 1985, Sutton et al., 1983, 2009) and enables precise measurements of the displacement fields. A version of this setup has

also been used with ultrahigh-speed photography to capture the full-field evolution of dynamic shear ruptures (Ross et al., 2020, Rubino et al., 2019) resulting in the advancement of our understanding of sub-Rayleigh and supershear ruptures (Rubino et al., 2020), evolution of dynamic friction (Rubino et al., 2017, 2022), interaction of ruptures and free surface (Tal et al., 2020, 2022), pressure shock fronts in viscoelastic materials (Gori et al., 2018) and ruptures induced by fluid injection (Gori et al., 2021).

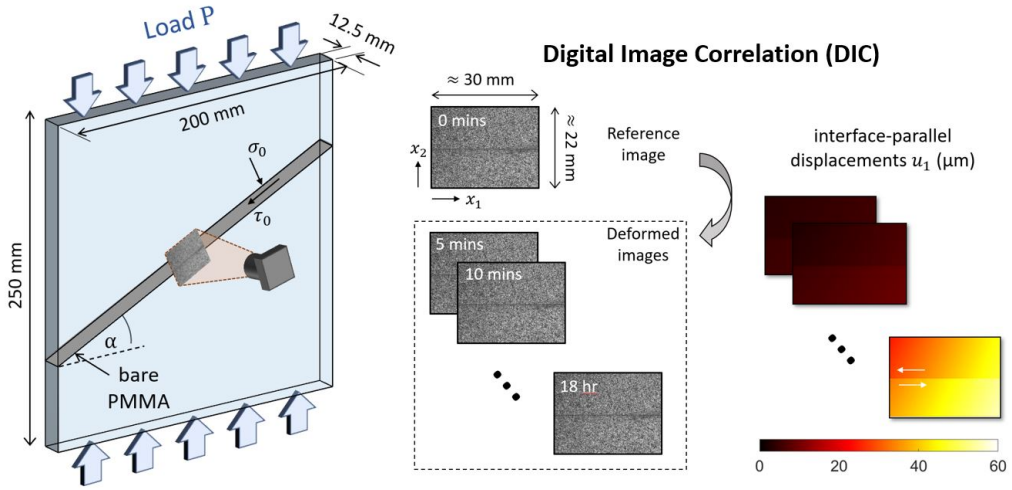

Figure 3.1: Schematic of experimental setup designed to study the ultraslow slip rate of shear interfaces during healing. The specimen is subjected to a constant load P and made up of two PMMA plates placed together at an inclination angle α. The area of 30 x 22 mm^2 at the center of the specimen assembly is patterned using spray paints to provide textures for imaging matching algorithms. The images are correlated against the first image, taken as a reference. The correlation produces displacement fields which can then be used to evaluate interfacial slip rate.

To locally measure the evolution of ultraslow slip rate of shear interfaces with DIC, we need to overcome two major obstacles. First, DIC is an optical technique that relies on matching features in small windows or "subsets" which assumes continuous displacement fields (Sutton et al., 1983, 2009) and cannot capture discontinuity related to pre-existing interfaces. There exist several techniques that can treat discontinuous displacement fields utilizing flexible finite element based meshes or additional mechanical constraints (Hassan et al., 2015, Nguyen et al., 2011, Poissant and Barthelat, 2010, Réthoré et al., 2007, 2008, Tomičevć et al., 2013, Yang et al., 2022), but their applications limit to problems with well-defined physics. Here, we overcome this unique challenge by separating the correlation domain into two

independent domains, one above the interface and one below the interface, which is first proposed in Rubino et al. (2019) and has been successfully adapted for various applications (Dong et al., 2022, 2023, 2024, Gori et al., 2018, Rubino et al., 2017, 2020, 2022, Tal et al., 2020, 2022). The second obstacle is related to the time- and length-scales of our problem. Shear interfaces are expected to slide very slowly, typically no more than a few microns per hour (Sirorattanakul et al., 2024). To tackle this challenge, we employ an image averaging technique to reduce the noise level (Gao et al., 2016) and conduct measurements over extended periods of time, typically 18 hours and 2 weeks for a select test. Such prolonged test duration is required to allow the interface to accumulate sufficient slip for DIC to measure. Our measurements are able to detect ultraslow slip rates of frictional interfaces down to 5 x 10^{-13} m/s. Since these are extremely small values, our goal in this study is to conduct a thorough analysis to quantify the measurement uncertainty and resolution.

The article is organized as follows. We start by describing the experimental setup and the developed procedure that enables us to capture the spatial and temporal evolution of the ultraslow slip rate of shear interfaces during healing. We then present some selected examples of our slip rate measurements for interfaces with both uniform and heterogeneous roughness. To further demonstrate that these measurements feature true sliding and not some artifacts from viscoelastic creep, we also conduct an experiment on a loaded specimen with no interface to measure these bulk effects. Finally, we quantify the uncertainty of the measurements and determine the best experimental and analysis parameters (e.g., field of view, subset sizes, etc.) for measuring the ultraslow slip rate of shear interfaces. The method developed here is not restricted to only measurements of slip rate during interface healing but has a wide range of applications to any experiment desired to measure relative displacements across some pre-existing discontinuity, such as bimaterial interfaces and composite materials.

3.2 Experimental procedure

3.2.1 Specimen manufacturing and interface preparation

In this study, we employ quadrilateral specimens made of Poly(Methyl Meth-Acrylate) (PMMA). Acrylic materials such as PMMA and Homalite-100 have been used as analogs to rocks to study dynamic rupture propagation in the laboratory as they are brittle like rocks but have ~25 times lower shear modulus, resulting in a smaller nucleation length scale compared to rocks, allowing to produce well-developed dynamic ruptures in centimeter-sized samples (Ben-David et al., 2010,

Dong et al., 2022, 2023, 2024, Gori et al., 2021, Gvirtzman and Fineberg, 2021, Lu et al., 2007, Mello et al., 2010, Paglialunga et al., 2023, Rubino et al., 2017, 2019, 2020, 2022, Rubinstein et al., 2004, Svetlizky and Fineberg, 2014, Tal et al., 2020) instead of meter-sized for rocks (McLaskey, 2019, McLaskey et al., 2014).

Starting from PMMA sheets of size 250 mm x 200 mm x 12.5 mm manufactured by Reynolds Polymer Technology®, we use a computer-numerical-control machine to cut them to two equal-sized quadrilateral plates at an oblique inclination angle α. The two plates are then placed into contact along the inclined frictional interface. We first determine the critical friction angle by incrementally increasing the inclination angle until the interface visibly slips during loading, which is approximately 30°. Then, we consider two different angles (α = 5° and 26°) in this study, both of which are chosen to be lower than the critical friction angle, so that the specimen will not abruptly slide when the mating interfaces are placed together. To ensure experimental reproducibility, the mating surfaces are prepared using a meticulous surface finish procedure (Mello et al., 2010, Rubino et al., 2019). First, machining marks left by milling are removed by polishing the interface using a 12-inch rotating polishing wheel at 100 r.p.m. The wheel is covered with Buehler® Microcloth soaked with a 2:1 mixture of water and Buehler® MiroMet Cerium Oxide. Polishing the surfaces produces a near-optical grade finish, giving a baseline surface condition with roughness of at most the wavelength of natural light. Typically, the surface roughness $R = \frac{1}{L}\int_0^L |z(x)|\,dx$ is 0.016 μm (Mello, 2012). A surface of controlled roughness is subsequently obtained by using a pressurized air gun to blast the mating surfaces with abrasive glass beads of different sizes. In this study, we use McMaster Carr® abrasive glass beads with 70 – 140 mesh size corresponding to diameters ranging from 104 – 211 microns and blasting it using a pressure of 75 psi for 3 minutes similar to those done in Gori et al. (2021), Rubino et al. (2017, 2019, 2020), Tal et al. (2020). After bead-blasting, the specimen typically has a roughness $R \sim 1.5\mu$m (Mello, 2012). More details, including the drawings of the setup for polishing, can be found in Gabuchian (2015), Mello (2012). In addition to an interface with single uniform roughness, we also study the long-term frictional response of an interface with regions of varying roughness. In select experiments, a 10 mm portion in the middle of the interface is polished but not bead-blasted and hence displays different roughness from its surroundings.

3.2.2 Surface patterning for imaging correlation

To perform digital image correlation, images should contain a characteristic texture (Sutton et al., 2009). Such a texture can be provided by coating the specimen's surface with a speckle pattern. Ideally, speckle patterns should have high contrast with a range of grayscale intensities, minimal repetitive or directional pattern, and adhere well to the specimen's surface so that it deforms with the specimen (Sutton et al., 2009). For length scales applicable to experimental mechanics (millimeters to meters), speckle patterns are typically fabricated from paints because of their relative compliance in comparison to most materials allowing them to deform with the surface (Dong and Pan, 2017). Speckle patterns can be created using spray paint, airbrush, or dot-on-dot technique (Lionello and Cristofolini, 2014, Rubino et al., 2019). We choose the spraying method for this study due to its simplicity and fast applications, though with a tradeoff of limited ability to control the density and distribution of speckle sizes.

Before application of paints, we first thoroughly remove any dust particles on the specimen's surface using with Kimtech Science® Kimwipes wetted with Isopropyl Alcohol. We then create a uniform thin layer of basecoat by spraying Krylon® flat white paint. The basecoat helps maximize contrast and reduce glares which may create saturated pixels and reduce correlation accuracy (Sutton et al., 2009). Finally, we create random black speckles by spraying a fine mist of Krylon® flat black paint. Typically, a basecoat of white paint followed by black speckles is preferred over the inverse because it maximizes contrast and provides a higher mean intensity gradient (LePage et al., 2017). The grayscale distribution of a typical image taken during the experiments is shown in Figure 3.2a. To optimize gray level distribution, if the initial black speckle pattern is too dense or if black paint creates too large droplets, the specimen is over-sprayed with a fine mist of white paint, which results in reducing the density of black paint and creating some features within the large droplets.

To quantify the average feature size, we utilize the normalized autocorrelation function defined as follows:

$$A(\Delta x) = \frac{\int_{-\infty}^{\infty} I(x) \cdot I(x - \Delta x)\, dx}{\int_{-\infty}^{\infty} [I(x)]^2\, dx} = \frac{\sum_{i=1}^{M} I(x_i) \cdot I(x_i - \Delta x)}{\sum_{i=1}^{M} [I(x_i)]^2} \tag{3.1}$$

where $I(x)$ is the one-dimensional normalized grayscale intensity pattern between -1 and 1 over M pixels along a direction, here chosen to be horizontal along x_1 (Figure 3.2b) and Δx is the lag for the shifting signal. The full width at half maximum

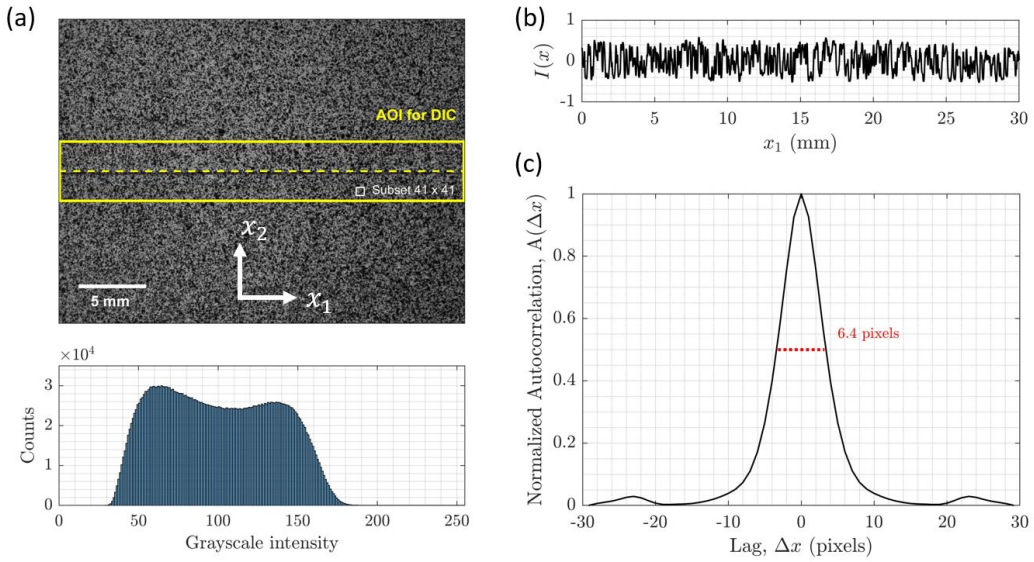

Figure 3.2: Features of the speckle images. (a) An image of size 2048 x 1536 pixels^2 taken during the experiments covering an area of approximately 30 x 22 mm^2 and the corresponding histogram of the grayscale intensity. The yellow box denotes the area of interest (AOI) of size 2048 x 300 pixels^2 where we perform image matching analysis. The yellow dashed line outlines the shear interface. (b) A representative horizontal profile of the grayscale intensity $I(x)$ normalized to be between -1 and 1. (c) Normalized autocorrelation of the profile in (b). The full width at half maximum of 7 pixels represents the average feature size.

of the autocorrelation function $A(\Delta x)$ is the feature size (Sutton et al., 2009), here taken to be representative of the mean speckle size. In our experiment, we take an image of size 2048 x 1536 pixel^2 over the field of view of approximately 30 x 22 mm^2. We find mean speckle size of 6.4 pixels (98 μm) (Figure 3.2c), which is within the recommended range of 3 – 6 pixels (Sutton et al., 2009). Since the quasi-static camera provides relatively high spatial resolution, over-sampling is less critical than reducing aliasing, and hence, larger speckle sizes are preferred over the smaller ones. Practically, if we adjust the field of view so that the speckle size is reduced, we would improve the measurement precision in pixels, but not necessarily in microns (Section 3.5.2).

3.2.3 Testing procedure

To study the evolution of slip and slip rate as the frictional interfaces heal under constant load, we follow a strict testing protocol summarized in Figure 3.3. First, the two mating halves of the specimen are aligned and assembled using a specimen

holder. The assembly is carefully inspected to make sure that the loading surfaces are parallel to prevent buckling at high loads. Then, the specimen is quasi-statically and uniformly loaded with uniaxial compression using the Instron® 300LX loading machine controlled by Instron® Partner software. Initially, the specimen is loaded with a constant loading rate of 2.5 mm per minute until the uniaxial load reaches 1 kN. During this initial soft start period, the platen of the loading machine, the specimen holder, and the specimen's interface start to come in contact. After this soft start period, the load and displacement are zeroed, and the loading rate is ramped down to 0.2 mm per minute until the target vertical load P is reached. The loading rate of 0.2 mm per minute is equivalent to a vertical strain rate of 1.3 x 10^{-5} s^{-1} on the specimen, well within the quasi-static regime. This vertical load P produces a resolved shear stress of $\tau_0 = P \sin\alpha \cos\alpha$ and a normal stress of $\sigma_0 = P \cos^2\alpha$ on the shear interface. Here, we choose to set the load P such that we have a resolved normal stress, σ_0 = 8.08 MPa. Consequently, P = 10 MPa for the inclination angle α = 26° and P = 8.14 MPa for the inclination angle α = 5°. The entire period of loading takes approximately 6 minutes to complete. The vertical load P is maintained at a constant level for 18 hours using an automatic load control system. The vertical load and displacement are recorded at a default rate of 10 samples per second. Because of the viscoelastic behavior of PMMA, the machine typically imposes 0.1 – 0.2 mm of additional displacement at the loading point to maintain constant stress. The relatively long duration of the experiments allows for the shear interfaces to accumulate sufficient slip to be measurable by the digital image correlation method.

3.2.4 Diagnostics with optical imaging

The specimen is monitored by optical images taken by the Imaging Source® monochromatic camera DMK 37BUX250 equipped with a 50 mm fixed focal length Schneider Optics® Xenoplan compact series lens (21-1001976) and 10 mm Tamron® extension ring. To ensure that the pixels in the images align with the specimen's interface, the camera is rotated about its optical axis by the inclination angle α. The 2048 x 1536 $pixels^2$ images cover a field of view of approximately 30 x 22 mm^2 at the central portion of the specimen. The lens aperture was set at f/2.8. Field of view of different sizes are obtained by changing the working distances between the camera and the specimens and selecting extension rings of appropriate lengths to allow focusing from different working distances. The specimen is illuminated using a 300W studio light source to enhance image contrast. Before we begin each experiment, the camera is turned on to warm up at least 30 minutes prior to the start

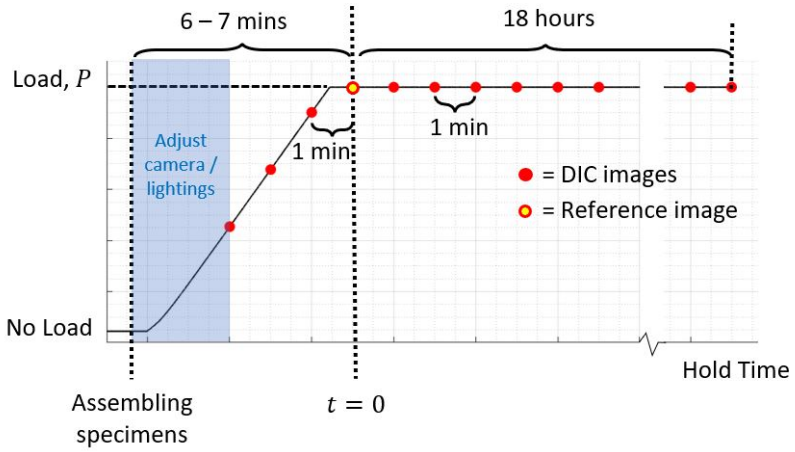

Figure 3.3: Schematic summarizing loading and image acquisition protocols. The specimen is aligned using the specimen holder before being loaded uniaxially to a preset load P using a constant loading rate of 0.2 mm per minute. Once the specimen bears some loads and stops moving, we adjust and focus the camera, optimize lighting, and start to take DIC images every 1 minute. The reference image is the first image taken after the load P is reached. Only every 5th image is analyzed to make the DIC analysis more computationally tractable.

of the experiment to reduce systematic deformation of images resulting from the self-heating of camera sensors (Ma et al., 2012).

The camera is controlled with the Imaging Source® IC Capture software Version 2.4. Once the camera is aligned and focused on the specimen, images are taken at an interval of 1 minute (Figure 3.3). To make the analysis computationally amenable, we analyze every 5th image, starting from the first image after the target load is reached. We also activate the noise reduction utility in the software, which will automatically take 32 images each time, compute the numerically averaged grayscale intensity for each pixel, and save the averaged value as a denoised image. The image averaging method is proven to greatly reduce measurement uncertainty for quasi-static measurements (Gao et al., 2016). We explore the effect of image averaging on our measurements in Section 3.5.1. The imaging parameters are summarized in Table 3.1 following the format recommended by the good practices guide of the International DIC Society (iDICs) (International Digital Image Correlation Society, 2018).

Camera	Imaging Source monochrome camera DMK 37BUX250
Image size	3 MP, 2048 x 1536 px^2
Lens	Schneider Optics Xenoplan compact series (21-1001976) with 10 mm extension ring
Focal length	50 mm
Aperture	f/2.8
Field of view	Main: 30 x 22.5 mm^2 Also explored: 15 x 11 mm^2, 60 x 45 mm^2, 90 x 67 mm^2, 120 x 90 mm^2
Image scale	68.3 px/mm
Stand-off distance	300 mm
Image acquisition rate	32 frames at 50 fps every 5 mins
Exposure time	0.02 second (without denoising) 0.64 second (with 32 frames averaging denoising)
Patterning technique	base coat of Krylon white paint with small black and white speckles on top
Pattern feature size	6.4 px

Table 3.1: Digital image correlations (DIC) hardware parameters used in this study.

3.2.5 Using digital image correlation to obtain full-field displacements

The acquired images are analyzed using the two-dimensional digital image correlation (DIC) method implemented in the commercial software VIC-2D version 6.2.0 developed by Correlated Solutions Inc®. Digital image correlation is an optical technique able to produce full-field maps of small displacements with sub-pixel accuracy (Sutton et al., 2009). Displacement field maps are obtained with DIC by correlating a deformed with a reference image. Correlation can be performed using a fixed reference image or incrementally, between image pairs in a sequence. The latter approach is appropriate for large deformations. Since we expect the total deformations to be small in our experiments, despite the long monitoring times, we choose to perform the correlation analysis using a single reference image rather than employing an incremental correlation algorithm. The reference image is chosen as the first image acquired after the target load is reached.

Two key parameters in the DIC analysis are the subset size and the step size. Subsets are sub-regions of the image over which image matching is performed. The step is the distance between adjacent subsets centers. A step of less than half a subset size means there is subset overlap, which allows for larger data density. Smaller subsets provide finer resolution but also contain less grayscale intensity information, resulting in larger errors (Sutton et al., 2009). Here, we explore 3 different subset sizes (21 x 21 pixels^2, 41 x 41 pixels^2, and 61 x 61 pixels^2). We discuss their effects on the correlation results in Section 3.3. To produce the densest displacement map possible, we employ a step size of 1 pixel. We use the zero-normalized sum of square differences (ZNSSD) criterion for pattern matching. Even though it is more computationally expensive than non-normalized sum of square differences (SSD), it can compensate for changes in lighting over time (International Digital Image Correlation Society, 2018, Sutton et al., 2009, Tong, 2005), which may occur in experiments over long duration such as the one performed in this study. This matching criterion is also Gaussian weighted such that the center pixel is more important than those further away from it, which provides best combination of spatial and displacement resolution (Correlated Solutions Inc., 2019). To model the displacement field within the subset, first-order affine functions are employed as the subset shape functions. While higher-order shape functions are more accurate, correlation results are also affected by higher noise levels. Using smaller subset size can compensate for not using higher-order affine functions (International Digital Image Correlation Society, 2018, Lava et al., 2009, Sutton et al., 2009). Sub-pixel accuracy is obtained through interpolation of the grayscale intensity. We choose the optimized 8-tap spline interpolant, which is based on B-spline interpolation with recursive pre-filter parameterized using a spline with eight coefficients (Schreier, 2000). In comparison to simple cubic interpolants, the optimized 8-tap interpolation filters could reduce the interpolation bias up to five times (Sutton et al., 2009). DIC analysis parameters are summarized and reported in Table 3.2 following the format recommended by good practices guide of the International DIC Society (iDICs) (International Digital Image Correlation Society, 2018).

Moreover, for our setup, we expect a discontinuous displacement field across the interface if the interface is sliding. Most DIC algorithms are developed based on the assumption of continuous displacement fields and cannot resolve discontinuous displacements. By applying them directly to our scenario, there would exist subsets that span across the interface and include regions with opposite directions of motion. The correlation would result in averaging displacements, which prevents

DIC software	Correlated Solutions VIC-2D (version 6.2.0)
Image filtering	32 frames numerically averaging
Reference image	single reference image (standard correlation)
Interpolant	continuous splines (8-tap)
Matching criterion	zero-normalized squared differences
Subset / Element size	Main: 41 pixels (approximately 0.6 mm) Also explored: 11 pixels (0.16 mm), 21 pixels (0.31 mm), 31 pixels (0.45 mm), 51 pixels (0.75 mm), 61 pixels (0.89 mm)
Step size	1 px (approximately 15 μm)
Subset shape function	affine
Subset weights	Gaussian

Table 3.2: Digital image correlations (DIC) analysis parameters used in this study.

the algorithm from resolving sharp jumps in displacements across the interface. Here, we choose to treat the discontinuous displacements by separating the correlation domain into two independent domains, one above the interface and one below the interface, similar to those done in Rubino et al. (2019). To make the analysis computationally amenable, only subregions of size 2048 x 150 pixels^2 on the different sides of the interface are considered. Furthermore, since DIC only provides displacement for the center of the subset, in addition, we employ the "Fill Boundary" algorithm developed by Correlation Solutions Inc.®, which uses affine transformation functions to extrapolate the displacements from half the subset size away from the interface to directly at the interface. We examine the accuracy of the "Fill Boundary" algorithm using numerically simulated experiments and find that it performs relative well, despite being purely from extrapolation (Section 3.5.3.

Since we are interested in the relative motion of the two halves of the specimen rather than their absolute displacements, we subtract the mean value $\bar{u_1}$ from the total displacement field u_1^{tot} at each frame: $u_1(x_1, x_2, t) = u_1^{\text{tot}}(x_1, x_2, t) - \bar{u_1}(t)$. Such rigid body motion is further discussed and constrained in Section 3.5.1. The high-frequency noise in the displacement field can be filtered out using a non-local-means (NL-means) filter to smooth out the noises while maintaining features with sharp discontinuities (Buades et al., 2005, 2006, Rubino et al., 2015, 2019). Here, since we are interested in the average slip across the interface, which does not require the

use of spatial derivatives like the computation of strain fields, we find this filtering to be unnecessary.

3.2.6 Post-processing to determine slip and slip rate

The evolving displacement field maps include the interface-parallel (u_1) and interface-normal (u_2) components. The accumulated slip along the interface $\delta(x_1, t)$, is computed by the difference between the interface-parallel displacement u_1 at pixels immediately above ($x_2 = 0^+$) and below ($x_2 = 0^-$) the interface:

$$\delta(x_1, t) = u_1(x_1, x_2 = 0^-, t) - u_1(x_1, x_2 = 0^+, t). \tag{3.2}$$

Based on the direction of shear, positive slip occurs when the displacements are negative (leftward) above the interface and positive (rightward) below the interface. To concentrate on the macroscopic behavior of the interface, we calculate the mean accumulated slip $\bar{\delta}$ by averaging the slip across the interface as $\bar{\delta} = \frac{1}{L}\int_0^L \delta(x_1, t)\, dx_1$ for each image which allows us to reduce the noise level even further in the measurement. The slip values from within half a subset size from the left and right boundaries of the domain are excluded to reduce biases from interpolation in the mean accumulated slip calculations.

The mean slip rate on the interface is computed by taking the time derivative of the mean accumulated slip $\bar{\delta}$. The task of taking the time derivative of such small slip measurements is not trivial as even low noise level would interfere with the signal interpretation. To regularize slip measurements, we fit the mean accumulated slip $\bar{\delta}$ by the following selected analytical functions:

$$\bar{\delta}(t) = C_1 \ln(t) + C_2 \tag{3.3}$$

$$\bar{\delta}(t) = C_3(t - C_4)^{C_5} + C_6 \tag{3.4}$$

where all C_i for $i = 1, 2, \ldots, 6$ are parameters to be fitted. After performing the fits, we can simply take a time derivative of the function to obtain the slip rate. By using analytical functions rather than a more numerical method such as linear fitting with moving window, we additionally constrain the measurement to be physical. In particular, the logarithmic function and the power law require the slip

to increase monotonically, preventing the shear interface under constant load from sliding backward.

These forms are motivated by the rate-and-state formulation developed from laboratory measurements sliding two rock surfaces or gouge layers (Dieterich, 1979, 1981, Marone, 1998a, Ruina, 1983). In this formulation, friction coefficient, defined as the ratio of shear to normal stress acting on an interface (τ/σ), evolves with slip rate $V(t)$ and the state variable $\theta(t)$ encoding the sliding history as follows:

$$f = f^* + a \ln\left(\frac{V(t)}{V^*}\right) + b \ln\left(\frac{V^*\theta(t)}{D_{RS}}\right) \tag{3.5}$$

where t is time, f^* is the steady-state friction coefficient at reference slip rate V^*, a and b are the non-dimensional friction parameters, and D_{RS} is the critical slip distance. The state variable can be evolved using different state evolution laws. Two popular choices include the "aging law" (Dieterich, 1979) and the "slip law" (Ruina, 1983), respectively:

$$\frac{d\theta}{dt} = 1 - \frac{V(t)\theta(t)}{D_{RS}} \tag{3.6}$$

$$\frac{d\theta}{dt} = -\frac{V(t)\theta(t)}{D_{RS}} \ln\left(\frac{V(t)\theta(t)}{D_{RS}}\right). \tag{3.7}$$

The evolution of slip rate can be rewritten from Equation 3.5 as follows:

$$V(t) = V^* \exp\left(\frac{f - f^*}{a}\right)\left(\frac{V^*\theta(t)}{D_{RS}}\right)^{-\frac{b}{a}}. \tag{3.8}$$

In our experiments, because we kept a constant load, the friction coefficient did not change throughout the duration of the experiments. To interpret our experimental results, we consider two limiting cases (Sirorattanakul et al., 2024). First, in the limit where the frictional interface is velocity-neutral ($a = b$) as is the case for PMMA surfaces, the slip rate decays with time as $1/t$, regardless of whether the aging or slip law is used. As a result, the slip is expected to accumulate as $\ln(t)$ (Equation 3.3). In the second case, we consider an approximation that $V\theta/D_{RS} \ll 1$. In this case, the aging law predicts that the state variable θ is proportional to time. The expression for slip and slip rate, in this case, becomes a power law (Equation 3.4).

3.3 Capturing the evolving ultraslow slip rate of shear interfaces

Our experimental setup and analysis procedure allow us to measure accumulated slip across the interface on the orders of 0.1 microns, and slip rate levels of less than 10^{-12} m/s, something that has not been achieved before, to our knowledge. In this section, we present selected examples of our measurements and examine the effects of subset sizes and post-processing method on the resulting slip rate evolution. We first discuss the method application for interfaces with spatially uniform roughness, which results in uniform slip rate, and then we discuss the case of heterogeneous interfaces with regions of varying roughness, which results in spatially varying slip rate.

3.3.1 Interface with single uniform roughness

In this section, we analyze the evolution of slip rate from experiments conducted on the inclined interface with two different inclination angles α of 5° and 26°. To apply the same level of normal stress σ_0 of 8.08 MPa for the two different angles of α = 5° and 26°, a different load P is used in each case (8.14 and 10 MPa, respectively), which results in shear stress levels of $\tau_0 = P \sin\alpha \cos\alpha$ of 0.71 and 3.94 MPa, respectively. Since the specimen with α = 26° has larger driving shear stress, we expect the interface to accumulate more slip and, hence, result in a better signal-to-noise ratio. We first present the detailed results from one experiment with α = 26° before discussing the results from α = 5° and the reproducibility of our results from repeated tests.

Snapshots of the interface-parallel displacement map $u_1(x_1, x_2)$ are presented for three selected time frames (t = 1 hr, 2 hr and 18 hr), and for three subset sizes, 21 x 21 pixels^2, 41 x 41 pixels^2 and 61 x 61 pixels^2, in Figure 3.4a and 3.4b, respectively. The panels show how most of the displacement offset is accumulated during the first few hours of the test, and incrementally, less displacement is accrued later on, as will be further discussed below. The displacement fields obtained with the two subset sizes are qualitatively similar, with the larger subset providing less noisy fields, as expected. Profiles of the interface-parallel displacement $u_1(x_1)$ just above ($x_2 = 0^+$) and below ($x_2 = 0^-$) the interface are given at selected times (every 5 mins) in Figure 3.4c. The profiles of the interface-parallel displacement u_1 increase linearly with the position x_1, indicating that the interface-parallel strains e_{11} are extensional. Further, the slope displayed by the profiles of u_1 vs. x_1 becomes steeper with time, reflecting that the extensional strains e_{11} grow with time. We interpret such strains to be a result of viscoelastic creep of the bulk material. Since

we impose the load to be constant throughout the experiments, relaxation of the bulk material requires the adjustment of the loading platen by increasing displacement at loading point with time. As a result, compressive strains e_{22} are produced in the vertical direction. Because of Poisson effect, the vertical compression results in horizontal expansion, which produces the observed positive strains e_{11}. The plot of the interface-parallel displacement $u_1(x_2)$ at $x_1 = 14.7$mm (Figure 3.4d), with curves plotted at the same time interval as in Figure 3.4c, shows a persistent discontinuity of displacements across the interface with relatively uniform amplitudes throughout the field of view, reflecting the accumulated slip. This is in contrast with cases when the material near the interface is deforming but not sliding, which would have resulted in gradual change of u_1 with the distance from the interface x_2 as an S-shaped bend rather than a sharp discontinuity. Note that positive strains e_{11} are also observed in experiments done on a loaded specimen without any interface (Section 3.4. However, no discontinuity in displacement is observed for a loaded specimen without an interface but rather an S-shaped bend. A comparison of the profiles of u_1 vs. x_1 at $x_2 = 0^{\pm}$ and u_1 vs. x_2 at $x_1 = 14.7$mm obtained with three different subset sizes after 18 hr is shown in Figure 3.4e and 3.4f, respectively. The different subset sizes show the same qualitative behavior of the displacement fields, with larger subsets more effective in reducing noise and the intermediate size of 41x41 pixels^2 offering the best compromise between noise reduction and signal accuracy, as discussed further below.

Next, we calculate the spatial distribution of slip $\delta(x_1, t)$ from the displacement field $u_1(x_1, x_2, t)$ at each time frame by using Equation 3.2 for various subset sizes (Figure 3.5). Our measurements show a monotonic increase of $\delta(x_1, t)$ over the entire duration of the experiments, indicating that the interface is continuously sliding. The slip curves become more closely spaced with increasing time, suggesting slip rates that are decaying with time, as confirmed by our further analysis. The slip is relatively uniform spatially, though some levels of fluctuation are present and are more pronounced for larger subset sizes. Further discussion in Section 3.5.6 shows that these variations are most likely artifacts resulting from the image correlation procedure rather than a real physical feature.

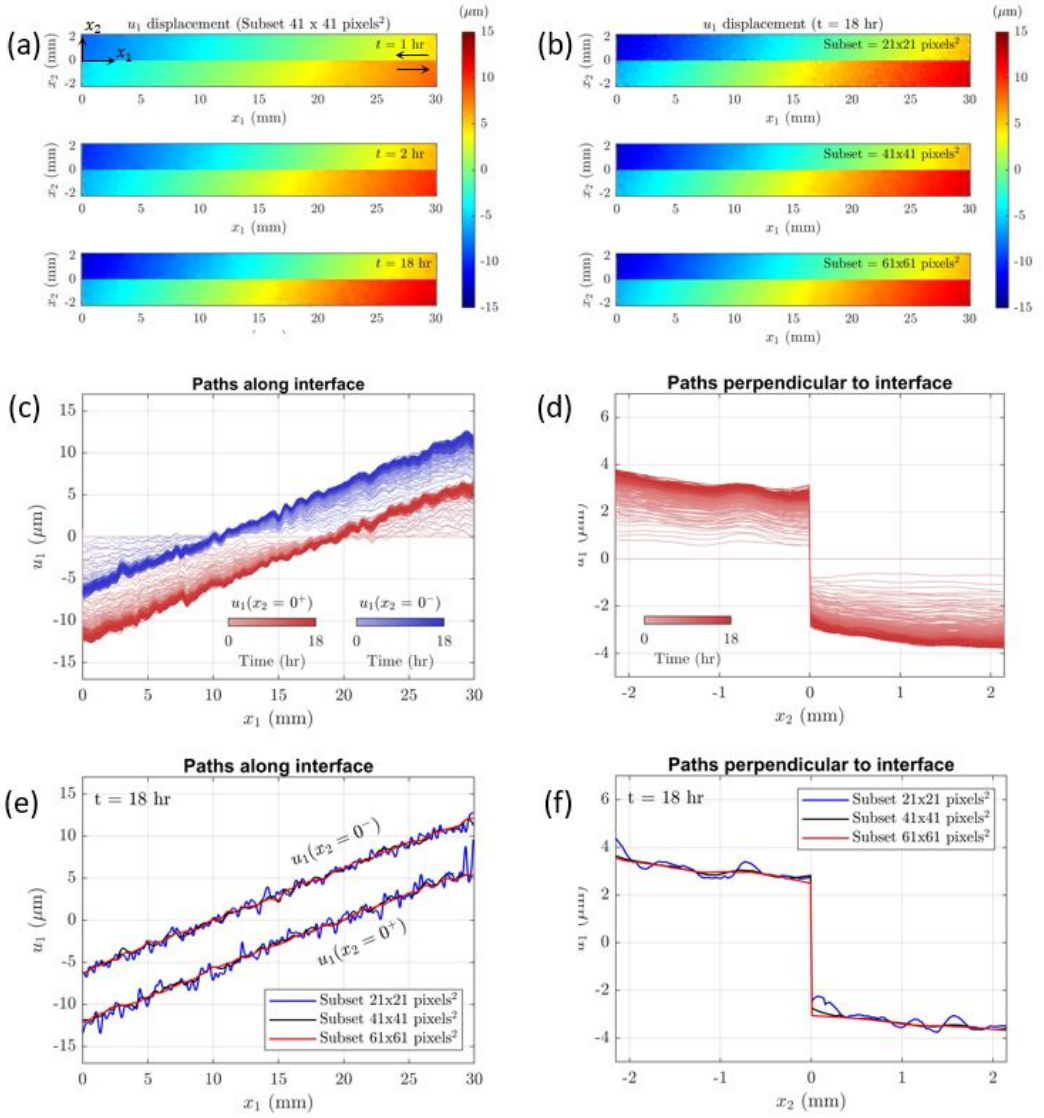

Figure 3.4: Interface-parallel displacement u_1 captured by digital image correlation (DIC) for a specimen with inclination angle $\alpha = 26°$ and a single uniform roughness, subjected to constant uniaxial compressional load of $\sigma_0 = 8.08$ MPa. (a-b) Full-field u_1 displacement for three selected time frames (t = 1 hr, 2 hr and 18 hr) and three selected DIC subset sizes (21x21 pixels^2, 41x41 pixels^2, and 61x61 pixels^2). (c) u_1 displacement from the pixel just above ($x_2 = 0^+$) and below the interface ($x_2 = 0^-$) vs. position along the interface x_1 at the different time frames. The slope reflects extensional strain along x_1 direction resulting from viscoelastic creep in the bulk. (d) u_1 displacement along paths perpendicular to the interface (x_1 = 14.7 mm) at the different time frames. (e) and (f) is similar to (c) and (d), but for different subset sizes and at t = 18 hr.

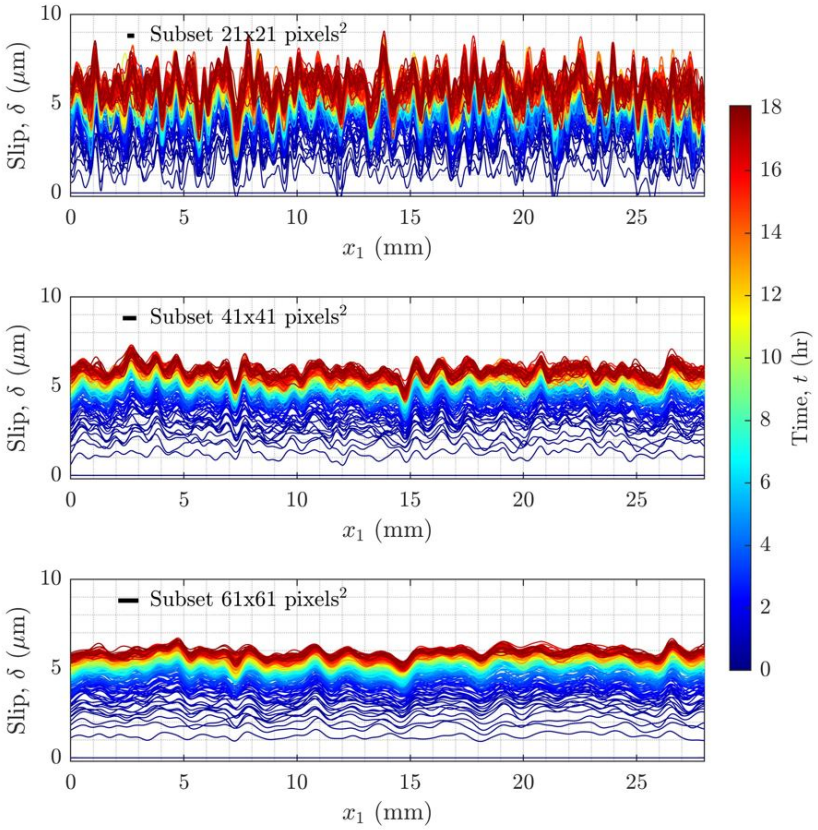

Figure 3.5: Spatial distribution of accumulated slip of an interface with a single uniform roughness with the corresponding full-field u_1 displacement map shown in Figure 3.4. Each line plot is color-coded by time. The different panels show results using different subset sizes for DIC analysis. The extent of black bars denotes the equivalent subset dimension in mm.

Since the measured slip does not contain any significant spatial variations, to further reduce the noise, we evaluate the mean accumulated slip $\bar{\delta}$ for each time frame, using three different subset sizes (Figure 3.6a). The time history of $\bar{\delta}$ shows that slip accumulates rapidly toward the beginning of the experiment with accumulation rates that decay with time, regardless of the choice of subset size. To facilitate time differentiation of slip time histories, we fit the mean slip using two different analytical forms: the logarithmic function (Equation 3.3) and the power law (Equation 3.4), concentrating on the results from DIC subset of 41 x 41 pixels^2. As it was explained in the introduction, these analytical forms are consistent with the slip evolution predicted by rate-and-state friction laws. We find that both forms fit the data quite well with the root-mean-square error (RMSE) less than 0.1 μm (Figure 3.6b), well below the mean slip signal which reaches the value of 6 μm. When comparing the two functions, the power law provides smaller errors, though not unexpectedly

because it has more fitting parameters than the logarithmic form. A zoom in to the first hour of the measurements reveals that the logarithmic fit deviates from the data, suggesting that it is not appropriate for explaining the early phase of sliding. Further, we have expanded our analysis to include more flexible analytical functions, such as the additive of two power laws, but we find that they do not significantly improve data fitting. This is because the RMSE for the power law fit is already quite small (0.036 μm), approaching the noise floor of our measurements (Section 3.5.6. Since the power law fits better the initial phase of the data, we employ this law in the subsequent analysis.

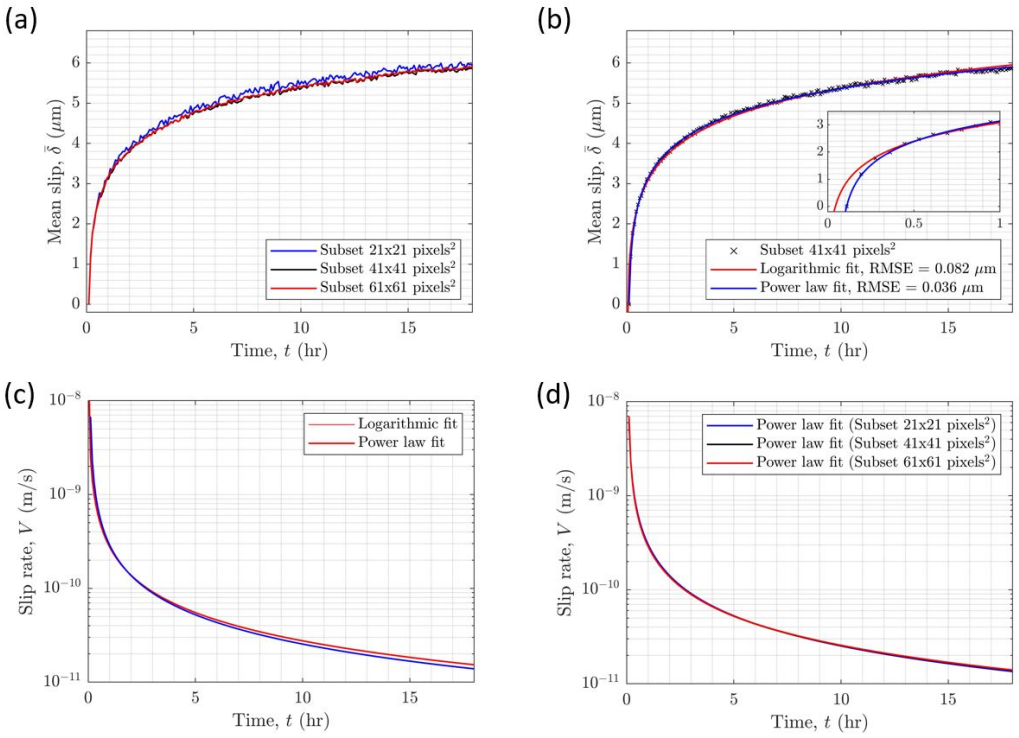

Figure 3.6: Evaluating mean slip and slip rate. (a) Mean accumulated slip δ vs. time calculated by spatially averaging the slip distribution in Figure 3.5. (b) Fitting the time evolution of mean slip using logarithmic function (Equation 3.3) and power law (Equation 3.4). The inset zooms in to the first hour. (c) Slip rate evolution obtained by differentiating the fitted slip evolution. (d) Effects of DIC subset sizes on the slip rate evolution.

To obtain slip rate evolution, we compute the time derivative of the fitted analytical functions (Figure 3.6c). Due to the exponential decay of slip rate, we employ a semi-log plot in Figure 3.6c to better visualize the results. We find that the power law and logarithmic functions yield a similar slip rate evolution with < 10% differences

of slip rate at t = 18 hr. These results are independent of the subset size (Figure 3.6d). Repeating the procedure described above with the mean slip obtained with various subset sizes reveals that all subset sizes considered produce almost identical slip rate evolution with < 4% differences of slip rate at t =18 hr.

We now analyze measurements performed for specimens with inclination angle α = 5°. Since we expect the specimens with smaller inclination angles to slide less, this configuration pushes the limit of our measurements. Even with such a small angle, our analysis procedure is still capable of clearly resolving the accumulated slip (Figure 3.7a). Qualitatively, the curves obtained for both angles α = 26° and α = 5° have similar shapes, with faster accumulation toward the beginning, and can be well-fitted using the power law (Equation 3.4). The magnitude of total accumulated slip at t = 18 hr reduces from approximately 6 μm for α = 26° to just above 0.6 µm for α = 26°, almost a ten-fold decrease. Because of these differences, the slip rate at t =18 hr reduces from 10-11 m/s for α = 26° to ~10^{-12} m/s for α = 5°, almost 10 times smaller (Figure 3.7b). To demonstrate the repeatability of our experimental results, we repeat nominally identical experiments for each of the inclination angles three times. Since there is sliding during previous experiments that may produce wear on the contact interfaces, to ensure that the starting interface contact height distribution is as reproducible as possible, the contacting surfaces are polished and bead-blasted prior to every test. The results from these repeated tests are shown in Figure 3.7b and demonstrate our ability to reproduce the results, with slip rate varying no more than a factor 2.

Furthermore, we also conduct a test for a specimen with inclination angle α = 26° over a much longer duration of up to 2 weeks (350 hr). We find that the method developed here still has enough precision to continue to measure the accumulation of slip. In the first 18 hr, the interfaces accumulate ~4.4 μm of slip. During the additional 332 hr, only ~2 μm of slip is accumulated, half of the amount of the first 18 hr (Figure 3.7c). The experimental results are still well-fitted with the power laws and suggest that the interfaces continue to slide with decaying slip rate down to 5 x 10^{-13} m/s after 2 weeks (Figure 3.7d).

3.3.2 Interface with regions of varying roughness

To further explore the ability of our method to capture the slip rate evolution of apparently stationary interfaces, we test a specimen with an interface featuring patches of varying roughness, and with an inclination angle α = 26° and applied load

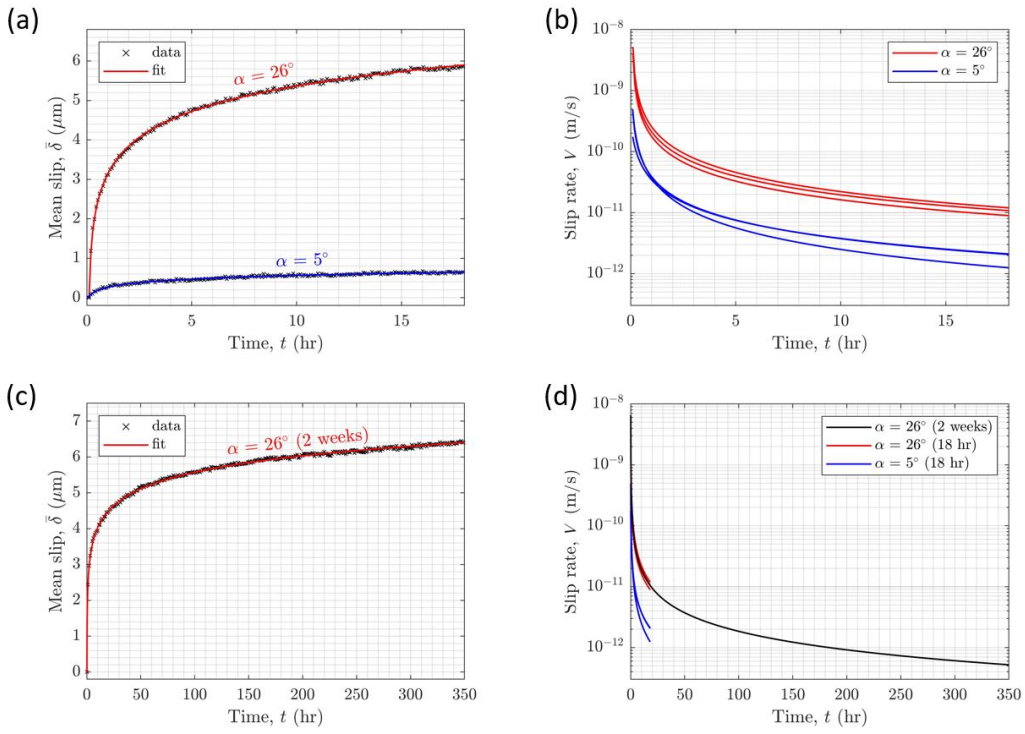

Figure 3.7: Experiments on specimens with different inclination angles α. The load P is adjusted so that the normal stress σ_0 acting on the interfaces remains constant at 8.08 MPa. (a) Mean slip and the corresponding power law fit for α of 5° and 26°. (b) Slip rate evolution from three different experiments for each inclination angle. The interface is prepared by polishing and bead-blasting again prior to each new experiment. (C) is similar to (a) but for a 2-week long test. (d) is similar to (b) but includes also the slip rate from the 2-week long test. The slip data is plotted every 5 mins in (a) and every 1 hr in (c). The analysis here uses a subset size of 41 x 41 pixels^2.

P = 10 MPa. This configuration is expected to produce spatially varying slip rates as a result of the patches of different roughness, and as a consequence, is a suitable testbed to assess the ability of our method to differentiate between such minute slip rate levels. To manufacture an interface with patches of different roughness, after polishing the interface uniformly, we cover a 10 mm portion with two layers of painter's tape and proceed to roughen the interface with the bead-blasting protocol, as described in Section 3.2.1. This procedure results in roughening the interface, except for the 10 mm patch, which preserves the polished surface finish because of the masking. Due to the substantially different surface roughness and different frictional properties, we expect the slip rate to evolve differently for the polished and bead-blasted portions.

The slip distribution $\delta(x_1, t)$ along the interface with patches of different roughness is shown in Figure 3.8a. The test is conducted using the same experimental protocol and analysis procedure as for the test on single uniform roughness, described in the preceding section. The bead-blasted portion has a similar accumulated slip as in the case of uniform roughness, reaching the value of 5 – 6 μm after 18 hr. By contrast, the central polished portion displays a much smaller accumulated slip, reaching only 1 – 2 μm. The transition of accumulated slip between these different regions is relatively abrupt and can be captured by the methodology developed here. To study the evolution of slip with time and enable comparison with the case of interface with uniform roughness, we evaluate the mean slip $\bar{\delta}$ using the same procedure described above, but we perform separate calculations for the polished and bead-blasted portions. The evolution of accumulated slip is well-described by a power law for both portions, with different coefficients required for the two cases (Figure 3.8b). The slip rate time-history obtained by analytically deriving the power law adopted in each case is shown in 3.8c. The bead-blasted portion displays a very similar behavior with the previous experiment on single uniform roughness. On the other hand, the polished portion shows much smaller slip rates. After 18 hr, the slip rate if the polished portion is roughly half of the bead-blasted portion (3.8c).

By performing an experiment on interfaces with regions of varying roughness, we have shown the ability of our method to resolve spatially varying slips and slip rates. In the next sections, we characterize the measurement uncertainty due to a variety of sources, including viscoelastic creep, camera electronic noises, micro-vibrations of the imaging apparatus, and errors in the correlation algorithm. The spatial resolution is not easy to address experimentally since the ground truth is unknown, and we cannot exclude the possibility of sharp discontinuities being smoothed out by DIC subsets or spatially varying slips due to non-linear filtering of DIC rather than a real feature. To better characterize the spatial resolution of our measurements, we conduct further analysis in Section 3.5.4.

3.4 Quantifying bulk effects and viscoelastic creep

Given the long timescales of our measurements (typically 18 hr) and the viscoelastic nature of PMMA, viscoelastic creep occurring in the bulk may result in displacements affecting our measurements of slip across the interface. While DIC measurements detect accumulating slip across the interface, they cannot distinguish slip due to actual sliding of the interface from displacements due to bulk deformations over the distance across which slip is computed, which is 1 pixel (15 μm). To quantify

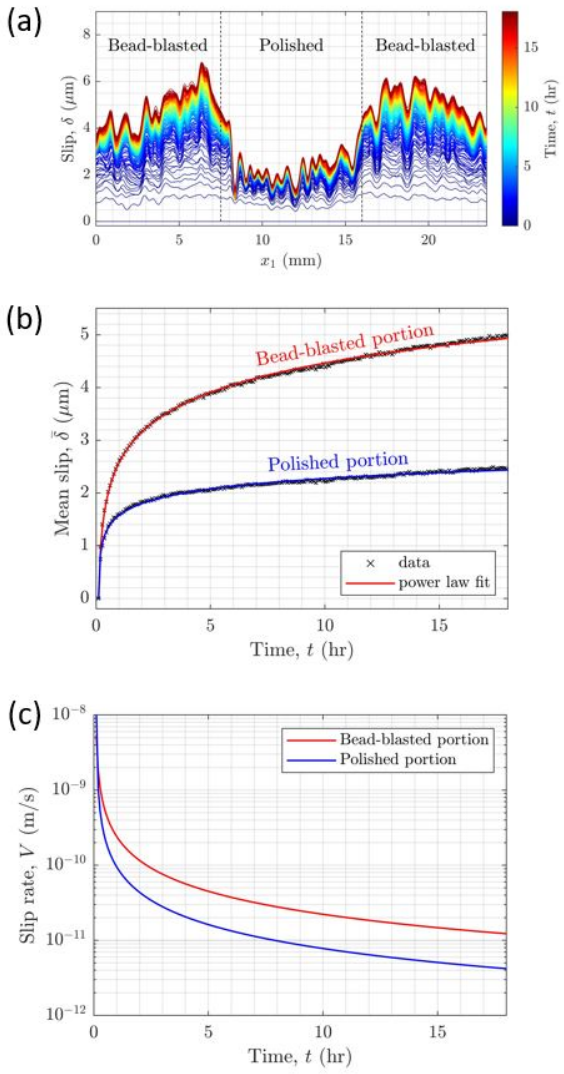

Figure 3.8: Measurements of slip and slip rate for inhomogeneous interface. Approximately 10 mm portion in the middle of the field of view is polished but not bead-blasted and hence reflect different frictional properties. The specimen used (a) Spatial distribution of slip color coded by time showing significantly lower accumulated slip in the polished portion. (b) Mean slip vs. time averaging over their respective regions. (c) Comparison of slip rate from the two different regions. The analysis here uses a subset size of 41 x 41 pixels^2.

the amount of bulk viscoelastic deformation typically occurring in our specimen, we perform an identical experiment on a loaded specimen without an interface under the same loading conditions as the regular experiments. The DIC analysis is conducted following the same procedure detailed in Sections 3.2.5 and 3.2.6, with the two domains divided by an imaginary mathematical line rather a physical interface.

Slip measured in this configuration can only be attributed to viscoelastic bulk deformation of PMMA across 1 pixel where slip is computed and measurement errors related to DIC, which will be quantified in the next section.

Our results show clear evidence of viscoelastic creep in the form of an increasing inclined slope of u_1 displacement profile along the position x_1 reflecting increasing positive extensional strain e_{11} along the direction parallel to the interface (Figure 3.9a-b). These features resemble those observed in our typical experiment (Figure 3.4), confirming our prior interpretation of these strains as viscoelastic creep of the bulk material. However, such viscoelastic displacements do not produce an offset across the interface (Figure 3.9b), as opposed to the test with an actual interface (Figure 3.4c). Computation of slip reveals no accumulation after 18 hr but rather random oscillations (Figure 3.9c-d), suggesting that the bulk viscoelastic deformation of PMMA across 1 pixel do not contribute to slip measurements. More quantitatively, we can take the maximum value of mean slip measured throughout the experimental duration as the upper limit of our measurement uncertainty. For a subset of 41 x 41 pixels^2, the mean slip error is no larger than 0.06 μm (Figure 3.9e), much smaller than a typical slip of 0.5 – 6 μm measured in our experiments. Additionally, we can also evaluate the spatial fluctuation of mean slip by evaluating the standard deviation of spatial distribution of slip from each frame and compute their means (Figure 3.9f). Spatial variation of slip that is smaller than these values should be attributed to other sources, such as measurement noise. For a subset of 41 x 41 pixels^2, the spatial fluctuation is 0.19 μm.

3.5 Characterization of the measurement uncertainty

The DIC measurements are affected by a variety of factors, including the electronic noise of the camera, micro-vibrations of the imaging apparatus, characteristics of the speckle pattern, environmental factors such as lighting changes and the DIC analysis parameters such as the subset shape functions, subset sizes, and matching criterion (Bornert et al., 2009, Gao et al., 2016, Haddadi and Belhabib, 2008, Lecompte et al., 2006, Pan et al., 2008, Reu et al., 2015, Schreier, 2000, Sun et al., 1997, Wang et al., 2009, 2007). There exist two popular approaches for assessing DIC measurements uncertainty. The first is based on correlating motionless images subjected to electronic noise of the imaging apparatus but with no deformation (Gao et al., 2016, Rubino et al., 2015, 2019, Wang et al., 2007). The measured displacements reflect uncertainties due to the imaging environment (i.e., camera noise, lighting, speckle pattern). The second approach assesses the goodness of

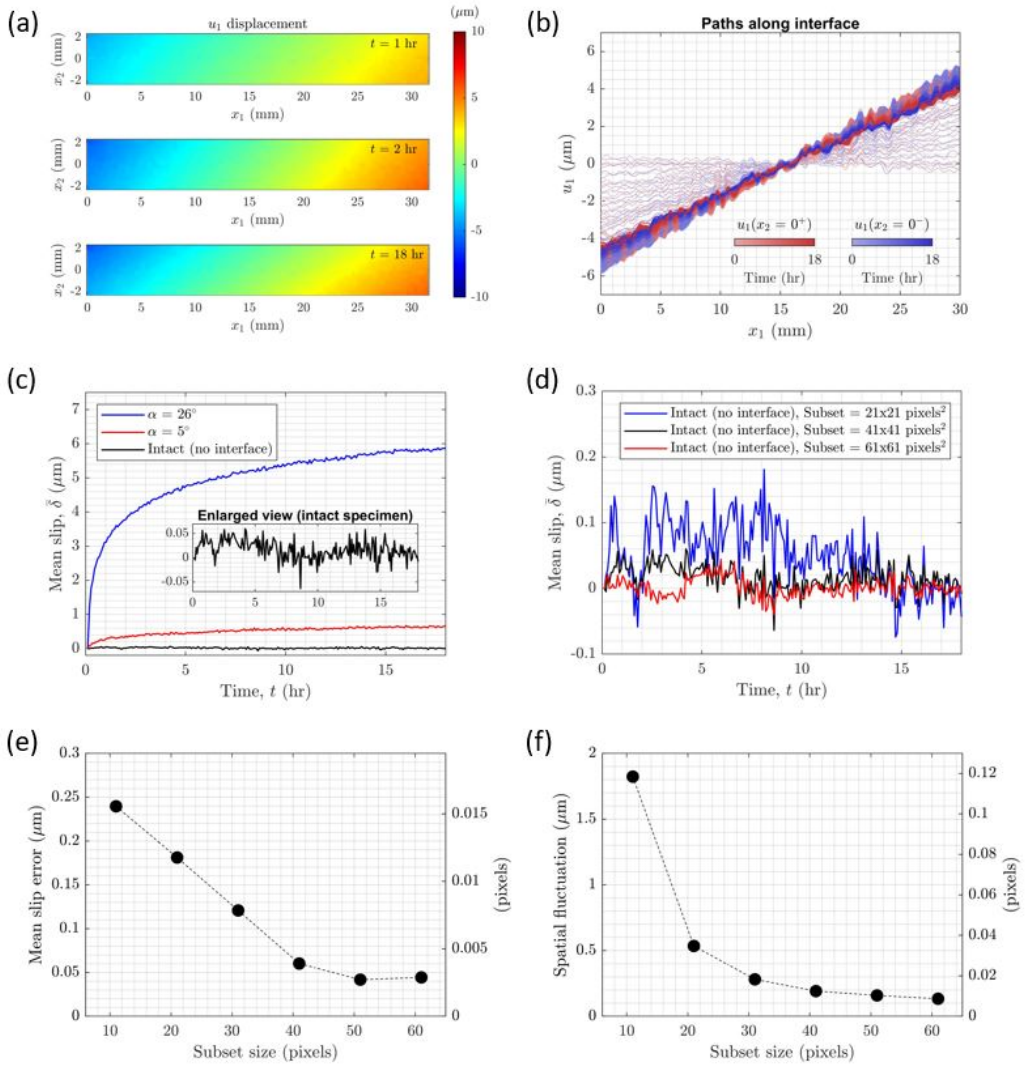

Figure 3.9: Measurements conducted on a loaded specimen with no interface using identical testing and analysis procedure as our typical experiment. (a) Full-field distribution of interface-parallel u_1 displacement. (b) u_1 displacement from the pixel just above ($x_2 = 0^+$) and below the interface ($x_2 = 0^-$) vs. position along the interface x_1. The slope reflects extensional strain along x_1 direction resulting from viscoelastic creep in the bulk and has similar magnitudes as experiments on specimen with an interface (Figure 3.4). (c) Comparison of the mean slip measured on the intact specimen with specimens with interfaces. (d) Effects of DIC subset sizes on the mean slip evolution. (e) Mean slip error vs. subset sizes. Here, the errors are bounded by the maximum measured mean slip of the intact specimen, which includes also the viscoelastic creep across the distance of 1 pixel used to calculate slip. (f) Spatial fluctuation evaluated as the means of standard deviations of spatial distribution of slip computed for each frame vs. subset sizes.

the correlation algorithm by numerically or experimentally deforming a reference image using a known displacement field and quantifying the differences between the correlation results and the known field (Bornert et al., 2009, Haddadi and Belhabib, 2008, Lattanzi et al., 2023, Lecompte et al., 2006, Reu et al., 2015, 2018, 2022). This approach can also be employed to assess the spatial resolution of DIC and to determine the optimal DIC analysis parameters (Bornert et al., 2012, Lattanzi et al., 2023, Reu, 2011, Rossi et al., 2015).

In this section, we assess the uncertainty of DIC measurements using both correlation of motionless images and numerically simulated experiments. Additionally, we discuss the impact of the field of view (FOV) size on the misidentification of the interface location in our measurements. The discussion is first focused on the uncertainty of slip measurement and then expanded to the uncertainty of slip rate measurements.

3.5.1 Correlation of motionless images

To assess uncertainty due to the imaging system, we take a sequence of 100 images of the motionless speckle pattern on an unloaded specimen with no interface at a rate of 1 frame per second. The optics and lighting settings are the same as in our typical experiment. All images are correlated using the first frame as a reference. An imaginary interface is introduced in the images and we employ the same analysis procedure as that used in our experiments (Sections 3.2.5 and 3.2.6) to assess its robustness. Given that specimens do not undergo any deformation, perceived deviation from zero displacements and slip derived from DIC measurements reflects the noise floor of our imaging system.

We start by using a subset size of 41 x 41 pixels^2. The correlation analysis produces displacement fields for each image frame. To better understand their statistics, we calculate the bias (mean) and standard deviation of the interface-parallel u_1 displacement for each frame (Figure 3.10a), as this component is relevant to the measurements discussed here. The standard deviation of a typical frame is 0.046 μm (0.0031 pixel), while the bias is considerably larger reaching a value of 1.5 μm (0.1 pixel). The distribution of u_1 from each frame is shown to be Gaussian and hence can be fully described with only the means and standard deviations (3.10b). Next, we perform similar analysis for slip and find a similarly small standard deviation of 0.039 μm (0.0026 pixel) and even smaller bias of 0.0036 μm (0.0002 pixel) (3.10c). The probability distribution of slip is very similar across all frames (3.10d).

The dominant source of noise in our setup comes from the micro-vibrations of the imaging apparatus which could result in the rigid body translation of up to 1.5 μm or 0.1 pixel over the duration that we used to take a sequence of motionless images (100 seconds) and hence affecting the biases of u_1. In our typical experiment which lasts for 18 hr, this rigid body translation could be much larger. Fortunately, these micro-vibrations only affect absolute motion and not relative motion. As a result, small slip changes, which are based on relative motion, are much easier to capture than small displacement changes.

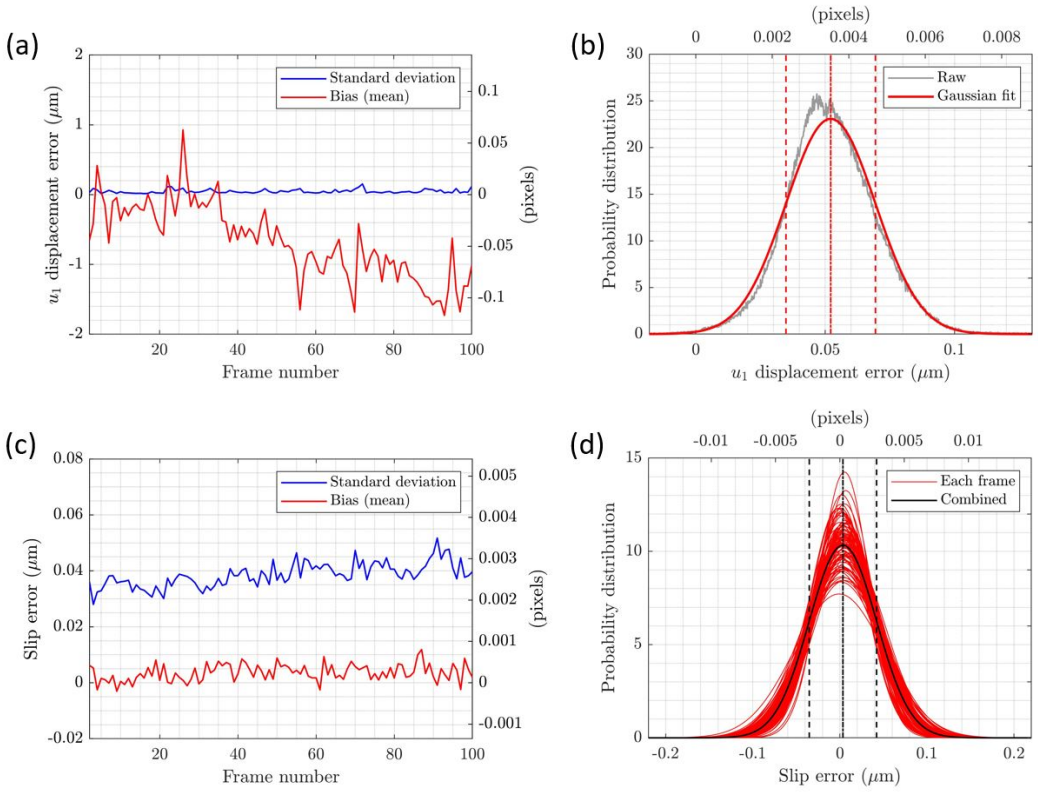

Figure 3.10: Displacement and slip error analysis conducted on a sequence of 100 motionless images. Each image is correlated with the first image in the sequence using an identical procedure as our regular experiments. The discrepancy from zero reflects the noise floor of the imaging system. (a) Standard deviation and bias of u_1 displacement error from each frame. (b) Probability distribution of the u_1 displacement error from a selected frame (gray) and a corresponding fit with Gaussian distribution (red). The vertical lines mark the mean and one standard deviation. (c) is the same as (b) for slip error. (d) Gaussian fitted probability distribution of the slip error from each frame (red) and a combined fitted distribution (black). The analysis here uses a subset size of 41 x 41 pixels^2.

Next, we extend our analysis to study the effects of DIC subset sizes on the measurement uncertainty and the effectiveness of denoising procedures. In this regard, we take another sequence of motion images, without activating the 32 frames averaging denoising procedure. We find that larger subsets result in smaller noise amplitudes and that denoising effectively reduces slip error by at least three times (3.11a). The spatial fluctuation of slip can be quantified using the means of the standard deviations of spatial distribution of slip computed from each frame, which decay exponentially with subset sizes (3.11b). Although a larger subset might be preferable because of lower error, it will also result in a longer computation time and lower spatial resolution when the slip is non-uniform (Section 3.5.4). For a homogeneous interface, we can further reduce the measurement noise by almost one order of magnitude by considering only the mean value of slip along the interface length (3.11c). For the case of denoised images and a subset of 41 x 41 pixels^2, mean slip error is only 0.0031 μm (0.0002 pixel) in comparison to 0.038 μm (0.0026 pixel) for slip (3.11d). Our analysis suggests a subset of 41 x 41 pixels^2 as an optimal choice as further increasing the subset size does not significantly improve the reduce the error.

3.5.2 Choosing the field of view

The analysis presented so far uses the field of view (FOV) of 30 x 22 mm^2. This FOV was chosen because it results in the smallest measurement uncertainty. In this section, we discuss DIC analysis correlating 100 motionless images with the different fields of view (Figure 3.12a). The images are taken using the same speckle pattern for all FOVs and different magnification for each FOV. The magnification is adjusted by changing the length of the extension ring and the standoff distance between camera and target. We perform identical analysis as described in Section 3.5.1 using a subset size of 41 x 41 pixels^2. The smallest absolute errors in microns observed for the FOV of 30 x 22 mm^2 (Figure 3.12b-c). For the same speckle pattern, smaller FOV generally produces smaller errors. However, if the FOV is too small such that the average feature size is much larger than the optimal values of 3 – 6 pixels and if the subset size is not adjusted accordingly, the overall errors can decrease as shown here for FOV of 15 x 11 mm^2. Instead, if we express the errors in pixels instead of microns, the errors show different distributions. FOV of 30 x 22 mm^2 is no longer the most optimal choice, but rather the 60 x 45 mm^2 (Figure 3.12d-e). For the pattern generated in this study, the average feature size is 6.4 pixels for FOV of 30 x 22 mm^2 (Section 3.2.2) and 3.2 pixels for FOV of 60 x 45

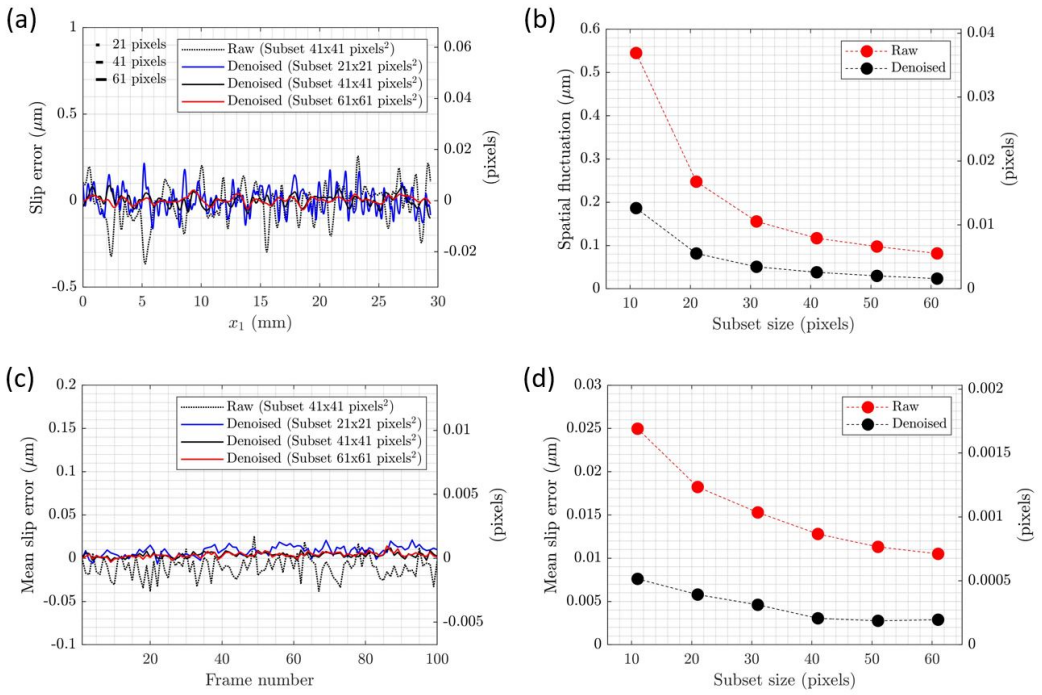

Figure 3.11: Statistics of slip error estimated from 100 motionless images. The analysis is done for both the raw images and denoised images with 32 frames averaging. (a) Slip error vs. interface location x_1 from a selected frame. (b) Spatial fluctuation evaluated as the means of standard deviations of spatial distribution of slip computed for each frame vs. subset sizes. (c) Mean slip error vs. frame number. (d) The combined mean slip error evaluated as the standard deviation of mean slip error from each frame vs. subset sizes.

mm^2. The smaller feature size for the largest FOV, at the lower end of the optimal size, explains why it results in lower errors in pixels. If the goals of the experiment were to capture as much information as possible and to both maximize the FOV to see more features and to minimize the uncertainty, the FOV 60 x 45 mm^2 would be the most appropriate. However, since in this study we are interested in measuring very small deformation, we are seeking the configurations resulting in the lowest uncertainty even with a slightly smaller imaging window, the FOV choice of 30 x 22 mm^2 is the most appropriate.

3.5.3 Evaluating errors from the correlation algorithm using numerically simulated experiments

To assess the goodness of the correlation algorithms in resolving small displacements, we numerically deform the reference image with a known displacement field and compare the field obtained with DIC to the known input. While it would be

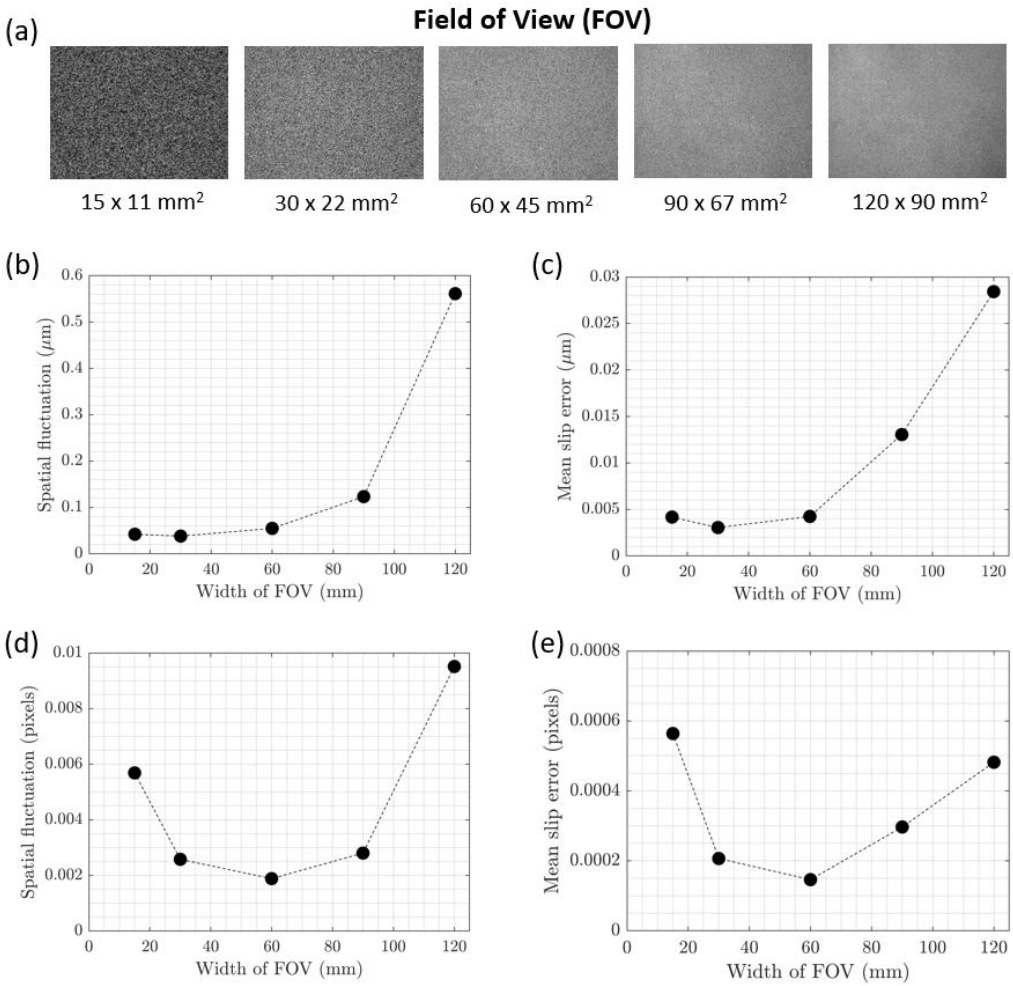

Figure 3.12: Slip error for the different fields of view (FOV) evaluated using 100 motionless images. (a) Representative images of the speckle pattern acquired for the different FOV. (b) Spatial fluctuation evaluated as the means of the standard deviations of spatial distribution of slip from each frame vs. FOV width. (c) Mean slip error evaluated as the standard deviation of mean slip from each frame. (d) is the same as (b) in pixels. (e) is the same as (c) in pixels. The analysis here uses a subset size of 41 x 41 pixels^2.

ideal to deform the image experimentally, this would result in introducing other experimental uncertainties such as stage error, motion error, drift error, and other electronic noises from the camera that would dominate the signal at the small levels of displacements relevant to our experiments. In principle, noise can be added to make the simulated images more realistic (Wang et al., 2007). However, we choose not to add any noise here so that we can single out the uncertainty contribution associated with the correlation algorithms.

There exist four different approaches to numerically deform an image. The first approach starts from an image with a speckle pattern that is numerically generated from some analytical texture functions, such as a superposition of individual Gaussian speckles (Wattrisse et al., 2001, Zhou and Goodson, 2001) or with the Perlin noise function (Orteu et al., 2006). Since the texture function is known, the image can be deformed by translating or scaling the texture functions. While this process itself does not introduce any bias, it relies on the ability of the texture function to mimic the experimental speckle pattern. The second approach relies on the Fourier shift theorem. The image is first transformed into its counterpart in the frequency domain using Fast Fourier Transform (FFT). Then, a phase shift is applied to the signal before transforming back into the spatial domain using inverse FFT (Roux and Hild, 2006, Schreier, 2000). Shifting with FFT generally produces lower errors than shifting directly in the spatial domain (Reu, 2011), but it is difficult to deal with spatially varying deformation. The third approach utilizes ultra-high resolution image and generates a lower resolution image through numerical binning by averaging grayscale intensity over a region in the ultra-high resolution image that corresponds to a pixel in the lower resolution image. With this approach, a translated image with displacement equals to integer factors of the ultra-high resolution image pixel size can be created without requiring any interpolation (Reu, 2011). Finally, the fourth approach generates the deformed image by first displacing the pixel position by the desired displacement field to new non-integer ones and performing numerical interpolation to determine the grayscale intensity values back at the integer pixel location (Cofaru et al., 2010, Koljonen and Alander, 2008, Lattanzi et al., 2023, Lava et al., 2009, Rossi et al., 2015). It should be cautioned that a priori choices of the interpolation scheme may bias DIC error assessment (Bornert et al., 2012).

In this study, we choose to use numerical interpolation because it is simple to implement and can easily be generalized to spatially varying deformation. Here, we use one of the 100 motionless images taken over an FOV of 30 x 22 mm^2 with 32 frames averaging denoising as a reference image. The image is separated into two domains using a horizontal cut representing an imaginary shear interface. The top domain is then shifted toward the left by a given amount u_1, while the bottom domain is shifted toward the right with the same amount. This creates a total slip $\delta = 2u_1$ across the imaginary shear interface. We use "*scatteredInterpolant*" Matlab® function for interpolation, which is a linear scheme based on Delaunay triangulation.

In the first numerical experiment, we deform the image using a uniform slip of increasing increments of 0.1 pixels until 2 pixels are reached. The simulated images are correlated with the original image using a subset of 41 x 41 pixels^2. The mean differences between slip derived from DIC and the input slip reflects the error from both the interpolation scheme used in generating the deformed image and the DIC correlation algorithm and it exhibits a sinusoidal pattern, as expected (Bornert et al., 2012, Rossi et al., 2015). The pattern is anti-symmetric because shifting an image to the right by u_1 pixels is equivalent to shifting it to the left at $1 - u_1$ pixels. The smallest errors typically occur at integer and half-integer of pixel shift. In our case, this would correspond to integer pixels of slip. Our results follow this well-known pattern with the largest error approaching 0.04 pixels for a slip of 0.5 and 1.5 pixels (Figure 3.13a). Unlike the analysis of motionless images, these errors are in the form of a fixed bias value rather than being Gaussian distributed.

The comparatively large error obtained from numerically deforming images with uniform slip may be due to the numerical process itself rather than DIC uncertainties. To reduce errors associated with the numerical deformation of the images, we implement a pixel subsampling scheme (Rossi et al., 2015). Starting from an image of size $n_H \times n_V$ pixels^2, a n_k times higher resolution image of size $(n_k \times n_H) \times (n_k \times n_V)$ pixels^2 is created using bi-linear interpolation. The higher resolution image is then numerically deformed following the procedure previously described. Then, the final lower resolution deformed image of size $n_H \times n_V$ pixels^2 is recovered through pixel subsampling by averaging the grayscale intensity of the corresponding $n_k \times n_k$ sub-pixel matrix. In this case, instead of correlating with the original image, we create a new reference image using zero slip. This new reference image is not exactly the same as the original image because interpolation to create a higher resolution image and image subsampling includes different mathematical operations that are not the inverse of one another. We find that by using the subsampling scheme, the slip error is reduced by a factor of two, confirming our initial estimate that large slip errors were due to the process used to numerically deform images. In principle, the interpolation error decreases as we increase n_k. However, increasing n_k beyond 5 does not further improve the results, suggesting that the slip error observed here becomes dominated by DIC algorithm and not the interpolation error during the process of image generation (Figure 3.13a).

To validate the robustness of our numerical deformation scheme, we also perform the numerical experiments using the binning approach, which does not require

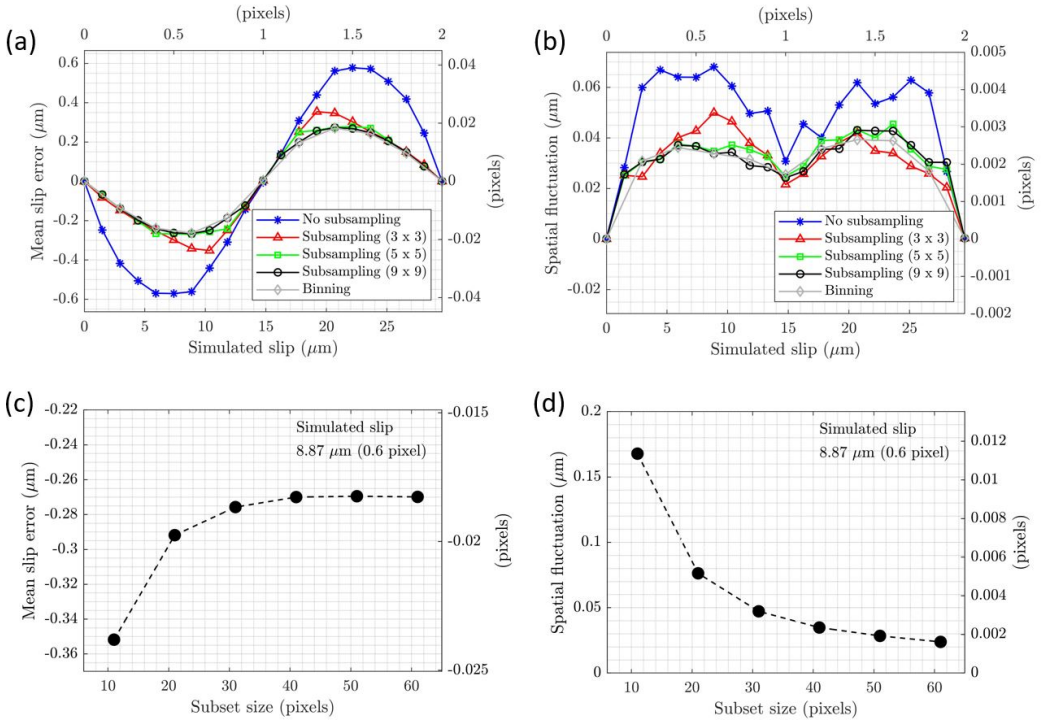

Figure 3.13: Errors of DIC correlation algorithm evaluated using numerically simulated experiments with spatially uniform slip. A variety of numerical algorithms are used to deform the image. (a) Mean slip error evaluated by subtracting the simulated slip from slip calculated with DIC. (b) Spatial fluctuation evaluated as the standard deviations of the spatial distribution of slip. Because the simulated slip is uniform, any spatial fluctuation is an artifact from the correlation algorithm. The analysis in (a) and (b) uses a subset size of 41 x 41 pixels^2. (c) Mean slip error vs. subset sizes for a simulated slip of 8.87 μm (0.6 pixel). (d) The spatial fluctuation of slip vs. subset sizes.

any interpolation. First, we create an ultra-high resolution image with 10 times higher resolution using bi-linear interpolation. Then, we shift the image in integer increments of pixels and recover the original resolution by averaging over the corresponding 10 x 10 sub-pixel matrix. To maintain a symmetrical shift, we can only simulate a slip increment of 0.2 pixels. The results using binning method is almost identical to those generated from numerical subsampling interpolation with $n_k \geq 5$ (Figure 3.13a). Therefore, for computational efficiency, we will use $n_k = 5$ for the rest of the study.

Next, using the spatial uniform slip as input, we assess the noise in the spatial distribution of slip. Since the input slip is uniform, any non-uniformity is related to errors associated with the DIC correlation algorithm. To evaluate the spatial

fluctuation of slip, we utilize the standard deviation of the spatial distribution of slip (Figure 3.13b). The spatial fluctuation correlates well with mean slip error. It is largest for simulated slips of 0.5 and 1.5 pixels and smallest for simulated slips of 0, 1, and 2 pixels.

We now evaluate the impact of DIC subset size on the analysis. We choose the interpolation method with 5 x 5 subsampling as further increasing the sampling points does not result in smaller errors. The simulated slip is chosen to be 0.6 pixel (8.87 μm), as it produces the largest mean slip error (Figure 3.13a). We find that the larger the subsets, the smaller than bias. However, increasing the subset size beyond 41 x 41 pixels^2 does not seem to improve the results (Figure 3.13c). This supports our choice of 41 x 41 pixels^2 as an optimal one (Section 3.5.1). In terms of spatial fluctuations, we observe similar trend with smaller fluctuations for larger subsets (Figure 3.13d). While fluctuations continue to decrease beyond a subset size of 41 x 41 pixels^2, further reductions become marginal.

3.5.4 Evaluating the spatial resolution of DIC using numerically simulated experiments

Because of the flexibility of the simulated experiment to impose any displacement fields, it is possible to use the simulated experiment to study also the spatial resolution of DIC. Here, we use a similar approach proposed in the global DIC challenge administered by the International DIC Society (iDICs) (Reu et al., 2018, 2022). The input slip is chosen to be a sinusoidal function with varying wavelengths of the following form:

$$\delta(x_1) = A \sin\left(2\pi \int_0^{x_1} f(x)\, dx\right) \tag{3.9}$$

where the amplitude A is chosen to be 4.43 μm (0.3 pixel) and $f(x)$ is the varying frequency (reciprocal of wavelength) chosen to be $0.0015 \cdot 10^{0.045 \cdot x\,[\mathrm{mm}]}$. The simulation assumes an anti-symmetric slip, and it displaces the domain above the interface to the left by half the amount of total slip and displaces the domain below the interface by the same amount to the right.

We correlate the numerically deformed image with the reference one using different subset sizes. The calculated slip is then compared against the input slip (Figure 3.14a). When the wavelength of the simulated slip is much larger than the subset sizes, the DIC algorithm can accurately recover the simulated slip. However, as

we the wavelength of the simulated slip decreases, slip evaluated by DIC starts to underestimate the peaks (Figure 3.14b). The underestimation increases with subset sizes. The errors exceed a threshold of 30% for the wavelengths of 32, 54 and 77 pixels for subsets of 21 x 21 pixels^2, 41 x 41 pixels^2, and 61x 61 pixels^2, respectively. As a result, any feature that is smaller than the subset sizes are generally smoothed out and cannot be accurately captured with our DIC workflow. This finding has implications for interpretation of our prior results in Section "Interface with Regions of Varying Roughness." For that experiment, the transition of slip between the polished and bead-blasted section occurs over a distance of ~1 mm, which would equate to ~70 pixels (Figure 3.8a). One could interpret that this ~1 mm zone may be related to the regions of stress concentrations. However, it is possible that the transition of slip appears to be smoother than a real feature due to the filtering of DIC subsets, and hence, the actual regions of stress concentrations may be much smaller.

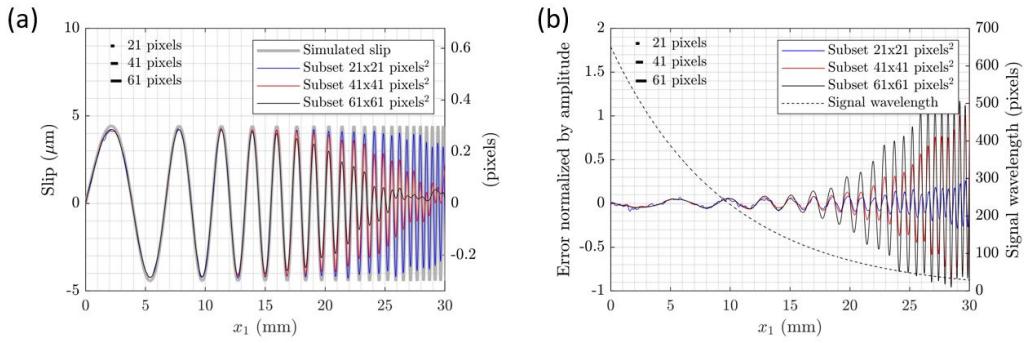

Figure 3.14: Errors of DIC correlation algorithm evaluated using numerically simulated experiments with spatially varying slip. The input slip is a sinusoidal function with spatially decreasing wavelengths. The simulation uses the interpolation method with 5 x 5 subsampling. (a) Comparison between the simulated slip and the recovered slip by DIC using different subset sizes. (b) Error calculated by subtracting the slip from DIC from the simulated slip and normalized by the amplitude of the sinusoidal slip. The errors increase exponentially as the signal wavelength approaches two times the subset size.

3.5.5 Misidentification of interface location during DIC analysis

Since it is often not obvious where the interface is located (Figure 3.15a), another uncertainty unique to our experiments arise from user errors in interpreting the interface location. Because each pixel spans a finite amount of area on the specimen, the interface generally falls within a pixel rather than being on the boundary between two adjacent pixels. In this section, we aim to quantify the uncertainty in slip measurements resulting from misinterpretation of interface location.

We utilize numerically simulated images with uniform slip of 0.6 pixel (8.87 μm). In the numerical images the interface location is placed exactly at the boundary between two pixels. We then perform DIC analyses where we purposely misidentify the interface location by offsetting it vertically (downwards) by varying amounts. Recall that the DIC analysis is performed over two independent domains juxtaposed at the interface. Misidentifying the interface location during the DIC analysis, e.g., placing the boundary between the two domains downwards from the location of the actual interface, results in one of the two domains (the top one in this case), including image rows displacing both leftward and rightward. In this configuration, the DIC analysis, which calculates average displacements over the subsets, underestimates the leftward displacement in the top domain close to the interface, while the rightward displacement in the bottom domain is unaffected (Figure 3.15b). The underestimation at the center of the subset closest to the interface is noticeable (0.007 pixel or 0.1 μm) even with only 1 pixel of offset and increases rapidly with larger offsets. With the "Fill Boundary" algorithm implemented in VIC-2D to interpolate the displacement field from the center of the subsets to domain boundaries, the bias of displacement at the pixel just above the interface becomes larger (0.2 pixel or 0.6 μm for 1 pixel of interface offset).

Further, we evaluate the mean slip averaging over the entire interface. We find the bias increases rapidly reaching a value of 2.6 μm (0.17 pixel) or a 30% underestimation for a vertical offset of 5 pixels (Figure 3.15c). The spatial fluctuation of slip also increases with interface offsets approaching the maximum value of 0.48 μm (0.033 pixel) for an offset of 9 pixels (Figure 3.15d). With a posteriori quality control of the analysis by evaluating the profile perpendicular to the interface, we are able to reduce the misidentification of interface location to no more than 2 pixels. In such a case, the upper bound of underestimation is 12%.

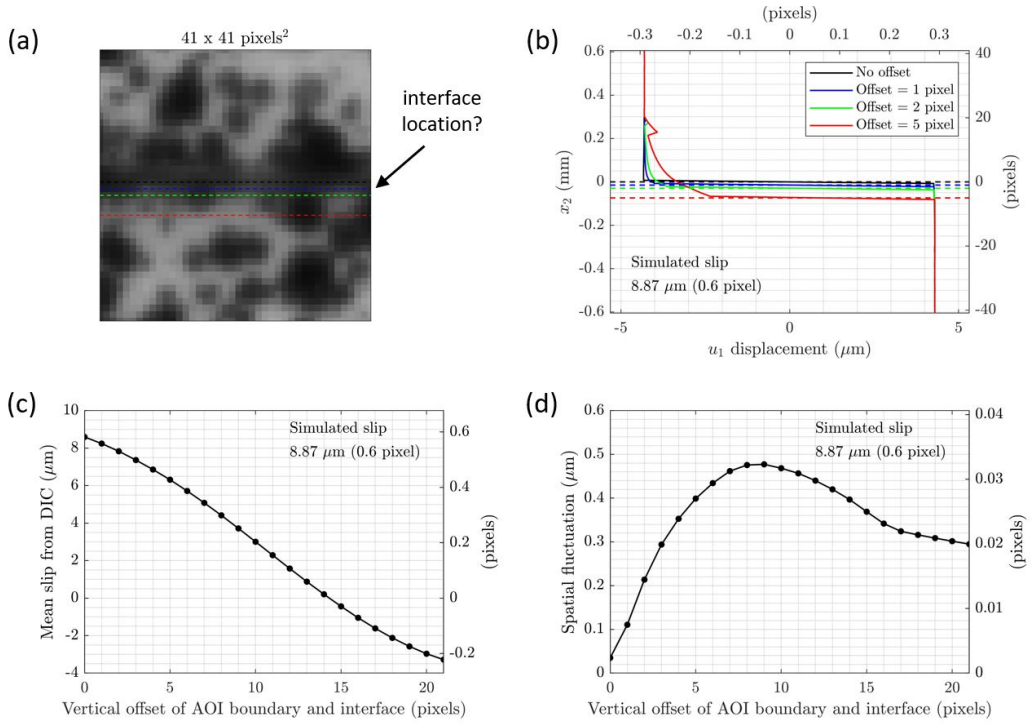

Figure 3.15: Impacts of misidentification of interface location on DIC results. The reference image is numerically deformed using numerical interpolation with 5 x 5 subsampling for a uniform slip of 0.6 pixel. (a) A 41 x 41 pixel^2 region of a representative speckle pattern. The interface is generally blurred out and cannot always be accurately located. (b) A vertical profile of u_1 displacement calculated from DIC assuming the interface location offsetting from the ground truth used to perform simulated experiment. (c) Mean slip evaluated from DIC and (d) spatial fluctuation for the different amount of interface location offsets. The analysis here uses a subset size of 41 x 41 pixels^2.

3.5.6 Summarizing the uncertainty quantification of slip

We have conducted uncertainty analysis of slip along the shear interface using various methods, aiming to separate contributions from different sources. Here, we summarize and compare those results using the DIC subset sizes of 41 x 41 pixels^2 as a baseline (Table 3.3).

The analysis of the loaded specimen with no interface provides the most realistic estimate of uncertainty due to experimental noises, which is Gaussian distributed. However, because the deformation is small (< 0.06 μm or 0.004 pixel), it does not assess the bias of DIC correlation algorithm in recovering larger deformations, which we typically observe in our experiments. The analysis of motionless images is similar to the case of loaded specimens with no interface, but it removes the

impacts from viscoelastic creep across the 1 pixel that slip is computed. As a result, the motionless images provide significantly lower error than the test with loaded specimen at 0.003 μm (0.0002 pixel) and can be taken as a true measurement error in absence of viscoelastic deformation. To assess the bias of DIC correlation algorithm in recovering larger deformation, we make use of numerically simulated experiments. Between the slip of 0 and 2 pixels, the largest bias occurs for a slip of 8.86 μm (0.6 pixel) and 20.68 μm (1.4 pixels), reaching a value of 0.28 μm (0.02 pixel). For larger slips, as long as the algorithm is able to correlate the images, the uncertainty will not be much larger than 0.28 μm because any additional integer shift does not contribute to correlation errors. Unlike the analysis of a loaded specimen with no interface and motionless images, these uncertainties are fixed for a particular speckle pattern rather than being Gaussian distributed. Another source of uncertainty that we assessed in this work is the user errors in identifying the interface location. In case the interface is slightly tilted in comparison to the horizontal axis of the image, the horizontal line used to separate the two regions for DIC analysis can become offset with the actual interface location, resulting in a similar effect. With careful alignment and a posteriori analysis of the results, we are able to minimize the interface offset to no more than 2 pixels. In such case, we introduce an error in mean slip that is no greater than 1.03 μm (0.07 pixel) for a simulated slip of 8.87 μm (0.6 pixel), which is approximately 12%. This error is expected to change proportionally with the ground truth amount of slip rather than being a fixed bias. By combining all these results, we find that the uncertainty of slip measurement has a bias of up to 0.28 μm or 12% of slip, whichever is larger, and a standard deviation of 0.06 μm.

As for the spatial distribution of slip, our noise floor is approximately 0.2 μm for a loaded specimen with no interface case, which includes the viscoelastic response of the bulk material. Features from our experiments that are below this noise floor may not necessarily be physical. In Figure 3.16, we visually compare the spatial distribution of slip typically observed in our experiments with the loaded specimen with no interface, motionless images, numerically simulated experiments, and in cases where the interface is offset from the domain boundary by 2 pixels. We find that the spatial distribution of slip from our experiments is not significantly larger than the others. Therefore, it is unlikely that these spatial variations are a real feature, but rather related to noise from the DIC analysis. On the other hand, the sharp transitions between the polished and bead-blasted regions (Figure 3.8a) discussed in Section “Interface with Regions of Varying Roughness” is a real feature

because the amplitudes are much larger than the noise floor of 0.2 μm. The analysis conducted here allows for a better interpretation of the physical features presented in our measurements.

Method	Source of uncertainty	Mean slip error	Spatial fluctuation of slip
Loaded specimen with no interface	Viscoelastic Creep, DIC Correlation Algorithms, Noises from Imaging Setup	0.06 μm (0.004 pixel)	0.16 μm (0.012 pixel)
Motionless images	DIC Correlation Algorithms, Noises from Imaging Setup	0.003 μm (0.0002 pixel)	0.04 μm (0.003 pixel)
Numerically simulated experiments	DIC Correlation Algorithms, Synthetic Images Generation	0.28 μm (0.02 pixel)	0.05 μm (0.003 pixel)
Mislocating the interface by 2 pixels (simulated uniform slip of 8.87 µm or 0.6 pixel)	DIC Correlation Algorithms, Noises from Imaging Setup, Errors from Users	1.03 μm (0.07 pixel)	0.21 μm (0.015 pixel)

Table 3.3: A compilation of different uncertainty analyses conducted in this study and their results.

3.5.7 Relating uncertainty in slip to uncertainty in slip rate

Thus far, we have discussed the uncertainty in slip measurements. In this section, we extend the analysis to discuss the implications of the uncertainty of slip rate using simulations.

We consider interfaces with single uniform roughness with inclination angles α of 5° and 26°. Assuming that the best-fitting power law (Figure 3.7a) is the ground truth for the slip evolution, we generate synthetic slip evolution that would have been measured with DIC using our standard subset size of 41 x 41 pixels^2 (Figure 3.17a). First, we introduce the error of the DIC correlation algorithm in terms of bias. These errors are additive and depend on the amount of slip, as we have shown using the simulated experiments with uniform slip (Figure 3.13a, see Section 3.5.3). Next, we add random Gaussian noises to each data point to mimic the standard deviations of the measurements. We use the largest value of 0.06 μm (Table 3.3), which includes

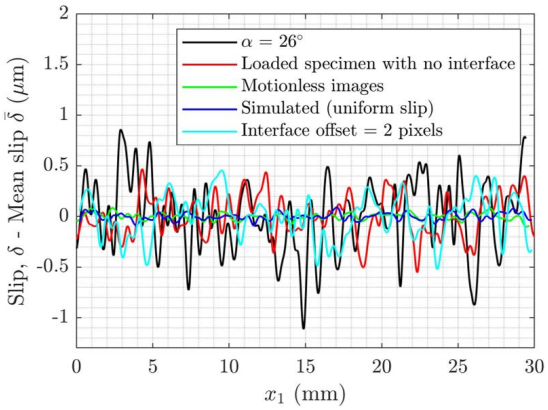

Figure 3.16: Comparison of spatial variation of slip from our typical experiment (taken here at t = 18 hr for interface with inclination angle α = 26°) with those from intact specimen, motionless images, simulated experiments with uniform slip of 8.87 μm (0.6 pixel), and simulated experiments with uniform slip of 8.87 μm (0.6 pixel) and misidentification of interface location by 2 pixels. The analysis here uses a subset size of 41 x 41 pixels^2.

errors due to viscoelastic deformation, camera noises, and micro-vibrations of the imaging systems (Figure 3.9e, see Section 3.4). To keep the analysis simple, we assume that the interface location is properly identified. Because the Gaussian noises are random, we can simulate 100 realizations of slip evolution expected to be observed with DIC for each inclination angle. Then, we can fit each realization with a power law and determine the respective slip rate evolution. The 1σ-confidence interval can then be calculated to represent the variations of slip rate evolution due to measurement noises (Figure 3.17b). Overall, since we expect the bias to increase with slip (but peaking at the slip of approximately 7.3 μm or 0.5 pixel, Figure 3.13a), the interface with inclination angle α = 26° has a larger bias on slip rate than the interface with α = 5°. At t = 18 hr, the bias of slip rate is approximately 5 x 10^{-13} m/s for α = 26°. On the other hand, the standard deviation of slip rate at t = 18 hr due to Gaussian noises for both angles is approximately the same at a value of 5 x 10^{-13} m/s. The uncertainty estimated here is much smaller than the scatter between the repeated experiments (Figure 3.7b), implying that the uncertainty due to slight differences in interface preparation and specimen alignment dominate the scatter of the curves rather than noise from DIC measurements.

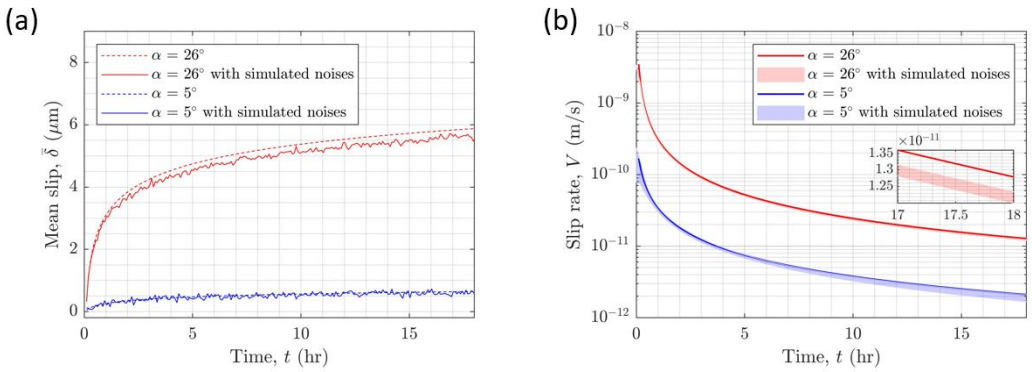

Figure 3.17: Relating uncertainty of slip to uncertainty of slip rate using simulations. (a) Models of mean slip evolution taken from the best-fitting power law (solid lines) and one realization of simulated DIC results for each angle α accounting for bias and standard deviations of the DIC measurements (dashed lines) assuming a subset size of 41 x 41 pixels^2. (b) Slip rate evolution for the input models (solid lines) and 1σ interval of 100 simulated DIC results for both angles. The inset zooms in to the curves for α = 26°.

3.6 Conclusions

The novel experimental methodology designed in this study allows us to capture the local evolution of extremely small slips along a frictional interface over very long timescales from several hours to weeks. An important product of this analysis, particularly in the context of frictional studies (Sirorattanakul et al., 2024), is the ability to detect ultraslow slip rate of shear interfaces down to 5 x 10^{-13} m/s. This is a key metrological advance over classical frictional studies inferring slip rate evolution through modeling (Beeler et al., 2022, Bhattacharya et al., 2022, Marone, 1998a). Our experimental procedures overcome two major challenges for such measurements. First, we successfully treat the displacement discontinuity across the interface following the method proposed in Rubino et al. (2019). In particular, we divide the images into two analysis domains, above and below the interface, and perform image correlation separately for the two domains. The "Fill-Boundary" algorithm allows for extrapolation of the displacement from half a subset size away from the interface to directly at the interface. Second, to overcome a low signal-to-noise ratio, we conduct measurements over a long period of time enough for the interface to accumulate sufficient slip. Additionally, we employ the usage of image averaging (Gao et al., 2016), which further reduces the measurement noise by over three times allowing for measuring even smaller displacement down to approximately 0.05 μm or 0.3% of the pixel size. An important feature of this

problem is that slip is a relative motion and can be done at a much higher precision than displacement, which is the absolute motion because they are less affected by micro-vibrations of the imaging system. A wealth of uncertainty analyses, including the quantification of bulk effect and viscoelastic creep, errors due to electronic noises of the camera and micro-vibrations of the imaging apparatus, the effects of choosing different fields of view, and evaluation of the errors from the correlation algorithms, were also conducted to quantify the noise levels of the measurements due to the imaging systems and the accuracy of the DIC correlation algorithms for capturing small displacements. Our experimental capability to measure the ultraslow slip rate of shear interfaces provides a leap in metrological advances. While the method was developed for a frictional problem, it can be applied to a wide range of scenarios, such as the slow quasi-static failure and fatigue of composites and other bimaterial interfaces.

Chapter 4

THE 2020 WESTMORLAND, CALIFORNIA EARTHQUAKE SWARM AS AFTERSHOCKS OF A SLOW SLIP EVENT SUSTAINED BY FLUID FLOW

Published as:

K. Sirorattanakul, Z. E. Ross, M. Khoshmanesh, E. S. Cochran, M. Acosta, and J.-P. Avouac. The 2020 Westmorland, California earthquake swarm as aftershocks of a slow slip event sustained by fluid flow. *Journal of Geophysical Research: Solid Earth*, 127(11):e2022JB024693, 2022. doi: 10.1029/2022JB024693.

Abstract

Swarms are bursts of earthquakes without an obvious mainshock. Some have been observed to be associated with transient aseismic fault slip, while others are thought to be related to fluids. However, the association is rarely quantitative due to insufficient data quality. We use high-quality GPS/GNSS, InSAR, and relocated seismicity to study a swarm of > 2,000 earthquakes which occurred between September 30 and October 6, 2020, near Westmorland, California. Using 5-min sampled GPS supplemented with InSAR, we document a spontaneous shallow M_w 5.2 slow slip event that preceded the swarm by 2 – 15 hours. The earthquakes in the early phase were predominantly non-interacting and driven primarily by the slow slip event resulting in a non-linear expansion. A stress-driven model based on the rate-and-state friction successfully explains the overall spatial and temporal evolution of earthquakes, including the time lag between the onset of the slow slip event and the swarm. Later, a distinct back front and a square root of time expansion of clustered seismicity on en-echelon fault structures suggest that fluids helped sustain the swarm. Static stress triggering analysis using Coulomb stress and statistics of interevent times suggest that 45 – 65% of seismicity was driven by the slow slip event, 10 – 35% by inter-earthquake interactions, and 10 – 30% by fluids. Our model also provides constraints on the friction parameter and the pore pressure and suggests that this swarm behaved like an aftershock sequence but with the mainshock replaced by the slow slip event.

4.1 Introduction

Earthquakes are often seen to cluster in time and space. Many clusters have a clearly identifiable mainshock followed by numerous smaller aftershocks. Others occur as a sustained burst of small magnitude earthquakes lasting from hours to several years without an obvious mainshock, referred to as a swarm (Mogi, 1963). The peak seismicity rate during swarms can reach > 10,000 times the background level with complex temporal evolution that cannot be explained by the simple Omori-Utsu type power-law decay (Omori, 1894, Utsu, 1961) typical of mainshock-aftershock sequences (Holtkamp and Brudzinski, 2011, Vidale and Shearer, 2006). Swarms also often expand spatially (Chen et al., 2012) with a velocity ranging from m/day (e.g., Ross et al., 2020) to km/hr (e.g., Roland and McGuire, 2009). Swarms can occur in a wide range of geological settings, such as volcanoes (e.g., Shelly and Hardebeck, 2019, Wicks et al., 2011, Yukutake et al., 2011), subduction zones (e.g., Holtkamp and Brudzinski, 2011, Hoskins et al., 2021, Nishikawa and Ide, 2018), transform faults (e.g., Roland and McGuire, 2009), hydrothermal systems (e.g., Heinicke et al., 2009), stable continental regions (Sharma et al., 2020), and reservoirs with anthropogenic hydraulic stimulations (e.g., Im and Avouac, 2021, Wei et al., 2015). In some cases, swarms can include larger destructive earthquakes (Chiaraluce et al., 2011, Nishikawa and Ide, 2018). The epidemic-type aftershock sequence (ETAS) model (Ogata, 1988, 1992), based on empirical laws, can reproduce different regimes of seismicity evolution, including standard Omori-type aftershocks and swarm sequences (Helmstetter and Sornette, 2002b). However, in terms of their mechanics, why spatiotemporal evolutions of swarms are fundamentally different from mainshock-aftershock sequences remains poorly understood.

The seismicity evolution during a swarm is often thought to be governed by external aseismic processes such as a slow slip event, fluid flow, magma intrusion, or a combination. Transient aseismic fault slip in the form of a slow slip event can increase shear stress on neighboring fault patches and has in particular been associated with swarms along oceanic transform faults (e.g., Roland and McGuire, 2009) and extensional or transtensional continental fault systems (e.g., Gualandi et al., 2017b, Jiang et al., 2022, Lohman and McGuire, 2007, Martínez-Garzón et al., 2021, Passarelli et al., 2015). Alternatively, elevated pore pressure from fluid flow or magmatic intrusion can decrease effective normal stress, thus reducing fault strength and bringing the faults closer to failure (e.g., Dieterich et al., 2000, Hubbert and Rubey, 1959, Nur and Booker, 1972). This mechanism has been associated with swarms in volcanic (e.g., Cappa et al., 2009, Fischer et al., 2014, Hainzl et al., 2016,

Roman and Cashman, 2006, Shelly et al., 2013, 2016) and hydrothermal settings (e.g., Audin et al., 2002, Got et al., 2011). Fluid-driven swarms are expected to expand as a square root of time, as observed in seismicity induced by anthropogenic fluid injections (e.g., Shapiro et al., 1997, 2002). In many examples, such as in the Corinth rift (De Barros et al., 2020, Dublanchet and De Barros, 2021), in Nevada (Hatch et al., 2020), and in situ fault slip reactivation experiments (Guglielmi et al., 2015), pore-pressure changes can induce propagating slow slip fronts leading to a coupled process (e.g., Bhattacharya and Viesca, 2019, Dublanchet, 2019, Larochelle et al., 2021, Sáez et al., 2022, Yukutake et al., 2022). A few studies, such as those for the 2000 Izu volcanic swarm (Toda et al., 2002) and earthquakes on Kilauea volcano, Hawaii (Segall et al., 2006), have demonstrated that nucleation models based on rate-and-state friction (Dieterich, 1994, Heimisson and Segall, 2018) can explain how seismicity responds to these external forcings.

In this study, we focus on the Westmorland swarm, which occurred between September 30 and October 6, 2020, near Westmorland, California (Figure 4.1), in a setting (Section 4.2) where swarms are common and where some have been associated with slow slip events (Chen and Shearer, 2011, Lohman and McGuire, 2007, Materna et al., 2022, Wei et al., 2015). We utilize a newly available dataset, including seismic data, daily and 5-min sampled GPS position time series, and interferometric synthetic aperture radar (InSAR), to image the time evolution of ground deformations as the swarm unfolds (Section 4.3). This unique dataset and the advanced data processing techniques allow us to extract the complete time evolution of ground deformation during the swarm and explore the spatio-temporal relationship between seismicity and the slow slip event in detail (Sections 4.4 and 4.5). Our observations and modeling results demonstrate that the 2020 Westmorland swarm was driven predominantly in the early stage by the slow slip event with limited inter-earthquake interactions and later by pore-pressure diffusion (Section 4.6).

4.2 Seismotectonic setting

The 2020 Westmorland swarm sequence began around 22:00 UTC on September 30, 2020, and lasted for approximately 140 hours until 18:00 UTC on October 6, 2020. The sequence was located in the Brawley Seismic Zone of the Salton Trough (Figure 4.1) along the North American-Pacific plate boundary at the transition between the right-lateral strike-slip San Andreas Fault (SAF) and the ridge transform system in the Gulf of California (Brothers et al., 2009). The region hosts a mixture of left-lateral strike-slip step-over faults that connect shorter segments of the main

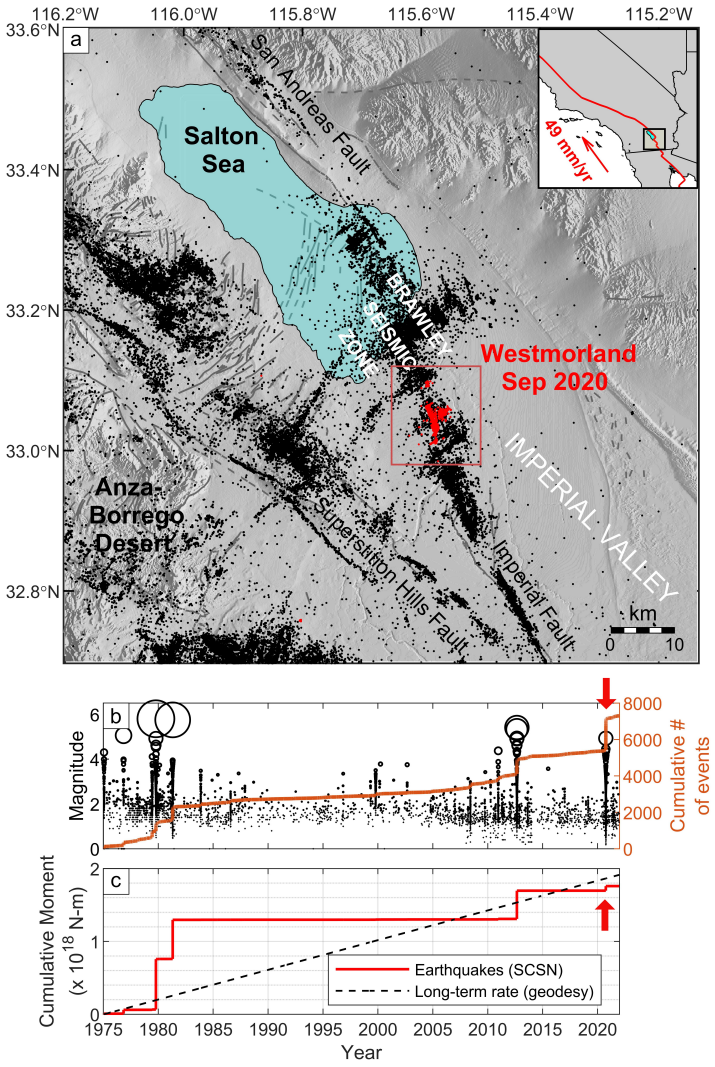

Figure 4.1: Seismicity in the Westmorland area. (a) Regional map of 1981-2019 relocated seismicity from the Hauksson-Yang-Shearer (HYS) catalog (Hauksson et al., 2012) shown as black dots. This study's high-resolution relocated seismicity catalog of the 2020 Westmorland swarm is shown as red dots. The mapped Quaternary faults are from the United States Geological Survey (USGS) QFaults database (Survey). The North American-Pacific plate boundary location (red line in inset) is from Bird (2003). Shorelines are from (Wessel and Smith, 1996). Salton Sea outline is from Google Earth images (Google). (b) Seismicity records from the Southern California Seismic Network (SCSN) catalog (Hutton et al., 2010) from 1975-2021 over the Westmorland area (red box in panel a) with a consistent completeness magnitude of 1.4 over the entire duration (Supporting Figure S1). (c) Comparison between the cumulative moment release of seismicity (SCSN catalog) and long-term geodetic strains near the Westmorland area (red box in panel a). Only geodetic strains across the seismogenic depths, constrained from our relocated seismicity catalog (Figure 4.2) to be between 4.5 – 8.5 km, are considered. Geodetic moment release is estimated using the mean slip rate of 17 mm/yr (Crowell et al., 2013) and a shear modulus of 30 GPa. During the 2020 Westmorland swarm (annotated by red arrows in panels b and c), there was a relatively large jump in the cumulative number of events but only a modest increase in seismic moment release.

right-lateral strike-slip fault (Johnson and Hill, 1982), primarily accommodating the extensional crustal stress field (Yang and Hauksson, 2013). The fault zone accounts for 17 mm/yr of right-lateral shear parallel to the SAF (Crowell et al., 2013), roughly one-third of the long-term plate rate (Argus et al., 2011, Bird, 2003). The Coachella segment of the SAF just north of the Salton Trough has a very low seismicity rate and is generally regarded to be mostly locked (e.g., Lindsey and Fialko, 2013), with the last major earthquake occurring about 320 years ago (Rockwell et al., 2016). The frequent seismic swarms in the Salton Trough (Lohman and McGuire, 2007) pose concerns about the possibility of the swarms triggering a large earthquake on the SAF (Hauksson et al., 2017).

In this region, the sedimentary cover is 5 km thick (Fuis et al., 1984) and composed mostly of quartz and calcite (Younker et al., 1982). The basement comprises primarily metasedimentary units (Fuis et al., 1984) that have undergone significant metamorphism due to a high temperature gradient of 50 – 60 °C/km (Lachenbruch et al., 1985). Deeper than 10 – 16 km, the crust mainly consists of diabase and gabbro (Fuis et al., 1984). Since mud pots and hydro-volcanic events are common in the Salton Trough (Robinson and Elders, 1976), abundant fluids and high geothermal gradients could play a significant role in swarm initiation (Ben-Zion and Lyakhovsky, 2006).

4.3 Data processing

4.3.1 Seismicity

We use a machine learning workflow for earthquake monitoring (Ross and Cochran, 2021) to build a high-resolution relocated seismicity catalog. We summarize the key steps and point to references in which the methods are described in detail.

First, we aim to detect earthquakes on individual 3-component traces. We start from the raw continuous waveform data from 47 regional seismic stations (Figure B.2) processed by the Southern California Earthquake Data Center (SCEDC, 2013) and apply a deep learning phase detector/picker model originally trained by Ross et al. (2020). This network takes in 16-sec windows of 3-component data and outputs the likelihood of P-waves and S-waves at each time step. We set a threshold of the peak sigmoid probability of 0.5 to trigger a detection and record the time at which the threshold is first exceeded. This is repeated for all stations and all days of data. Next, we associate the detected phases at individual stations to particular earthquakes using the PhaseLink deep learning-based association algorithm (Ross

et al., 2019b). Because the station distribution and local seismic velocity structure differ, we re-train the neural network following Ross et al. (2019b) and use the exact settings for the associator described in Ross and Cochran (2021). Once the association process is completed, we locate the events using HypoSVI (Smith et al., 2021), a variational Bayesian method. We use the Southern California Earthquake Center (SCEC) Community Velocity Model CVM-H (Shaw et al., 2015) and keep all tunable parameters the same as in Smith et al. (2021).

Finally, we relocate the seismicity with waveform cross-correlation. We correlate all possible pairs of events using 1.0 sec windows starting 0.1 sec before each pick using 1 – 20 Hz filtered waveforms. We retain differential times with a peak correlation coefficient of at least 0.6 and have a correlation difference between the positive and negative maxima of at least 0.2. Then, we use these differential times as the input to GrowClust (Trugman and Shearer, 2017), a cluster-based double-difference relocation algorithm. Since GrowClust works only with 1D velocity models, we use a model for the Imperial Valley from Fuis et al. (1984). In calculating the event-pair similarity, we required the cross-correlation coefficient to be at least 0.7 and the number of differential times to be at least 8.

Our method yields 2,282 detected events between September 30 – October 11, 2020, in comparison to only 1,711 events in the Southern California Seismic Network (SCSN) catalog (Hutton et al., 2010) during the same time interval (Figure B.3). Among the detected events, 1,373 of these could be relocated precisely. The spatial distribution of relocated seismicity reveals a complex fault structure with a 162°-trending main fault and several en-echelon structures striking roughly perpendicular to the main fault (Figure 4.2). At depth > 6.5 km (in the basement), the 162°-trending main fault shifts toward the North-South direction. These structures are consistent with the focal mechanisms from the Southern California Seismic Network (SCSN) catalog (Hutton et al., 2010). Our catalog does not include magnitudes since many of these events are small, and we cannot confidently estimate their magnitudes.

4.3.2 GPS

This study utilizes daily and 5-min sampled Global Positioning System (GPS) position time series in the International Terrestrial Reference Frame (ITRF) 2014 reference frame (Altamimi et al., 2016) preprocessed by Nevada Geodetic Laboratory using final orbit solutions (Blewitt et al., 2018). The original time series contains a transient geodetic signal at the time of the swarm and various other sig-

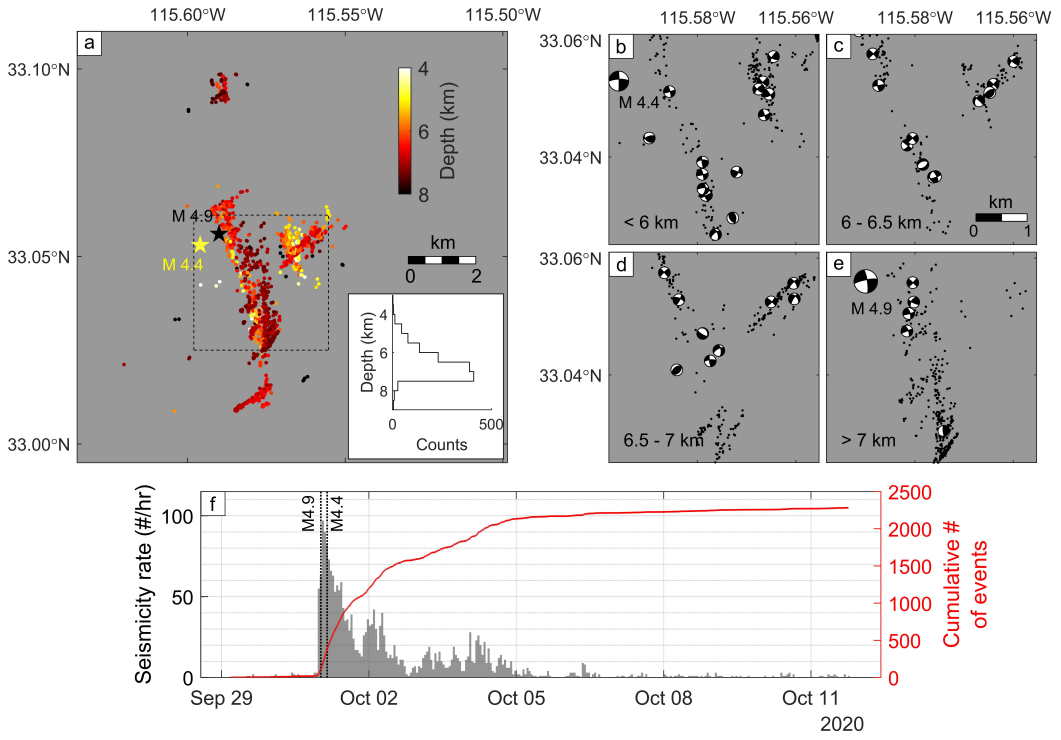

Figure 4.2: Seismicity catalog of the 2020 Westmorland swarm generated from this study (Sirorattanakul et al., 2022a). (a) Map view of 1,373 high-resolution relocated events color-coded by depth with a depth histogram as inset. The focal mechanisms are taken from the matching events in the SCSN catalog. We plot only those larger than M2.7 using relocated locations for the different depth ranges: (b) shallower than 6 km, (c) between 6 and 6.5 km, (d) between 6.5 and 7 km, and (e) deeper than 7 km. Since the relocation technique used in this study relies on waveform similarity, which can be inaccurate for large events, we use locations from the SCSN catalog for events larger than M4. (f) Seismicity rate evolution of the entire catalog of 2,282 events generated from this study, including those detected but not relocated. Our catalog does not contain magnitudes

nals (seasonal variations, co-seismic steps, common mode jitter). To make use of these GPS data in studying the swarm, we need to separate the surface displacements related to the swarm from those resulting from other sources. The key steps are summarized here. Further details can be found in Section B.1.

We first work with daily position time series between January 1, 2016, and November 25, 2020, from 113 regional GPS stations (Figure B.2). Using a trajectory model (Bevis and Brown, 2014), we remove the long-term linear trend and the co-seismic and instrumental steps (Table B.1). Then, we extract the remaining non-linear signals unrelated to the swarm, such as the seasonal signals and the common mode motion,

using the modified variational Bayesian Independent Component Analysis (vbICA) decomposition (Gualandi et al., 2016), a blind source separation technique based on the original vbICA method (Choudrey and Roberts, 2003) but also takes into account data uncertainties and missing data (Chan et al., 2003) and has recently been successfully applied to daily sampled GPS position time series (e.g., Gualandi et al., 2017b, 2020, Larochelle et al., 2018, Michel et al., 2019, Serpelloni et al., 2018). Each isolated signal ($i = 1, 2, \ldots, R$) is an independent component (IC) which includes a stationary spatial function ($U_{M\times R}$) explaining the relative amplitudes of the signals for the M different position time series ($m = 1, 2, \ldots, M$), the relative strength of the IC comparing to other ICs ($S_{R\times R}$), and a time function ($V_{T\times R}$) describing signals variation with time ($t = 1, 2, \ldots, T$). Since we first want to extract only the signals unrelated to the swarm, data points during the time of swarm (after 2020.732; September 25, 2020) from 34 stations within 45 km from the center of the Westmorland swarm are not used in the vbICA decomposition. We choose to decompose the signals unrelated to the swarm into 8 ICs (Figure B.7) and they are all removed from the detrended position time series. We run the vbICA decomposition again, this time for the purpose of extracting deformations related to the swarm on a local-scale. Only the position time series near the time of the swarm between 2020.65 and 2020.81 (August 27 – October 24, 2020) from 17 stations within 35 km from the center of the Westmorland swarm are used. We find that the first IC dominates and by itself explains over 77.2% of data variance (Figure B.9). Therefore, we only keep this first IC and associate it with the swarm.

Since the extracted transient geodetic deformation started within one day from the onset of the swarm, it is not sufficient to use daily position time series to determine whether the geodetic deformation preceded the swarm or was coeval. We further improve the temporal resolution of our results by using the 5-min sampled position time series, also processed by the Nevada Geodetic Laboratory (Blewitt et al., 2018). Given larger uncertainties of the 5-min sampled position time series, directly performing vbICA decomposition does not provide the best possible result. Instead, we assert that the spatial function derived from the daily sampled position time series is generalizable to the 5-min sampled position time series and perform a projection to determine the associated time function with the 5-min temporal resolution. We further apply a low-pass Savitzky-Golay filter (Savitzky and Golay, 1964) based on a moving polynomial fit to mitigate high-frequency noises (Figure 4.3) and find a time lag of at least a few hours between the onset of geodetic deformation and seismicity. This filtering technique is non-causal and, therefore, does not temporally shift the

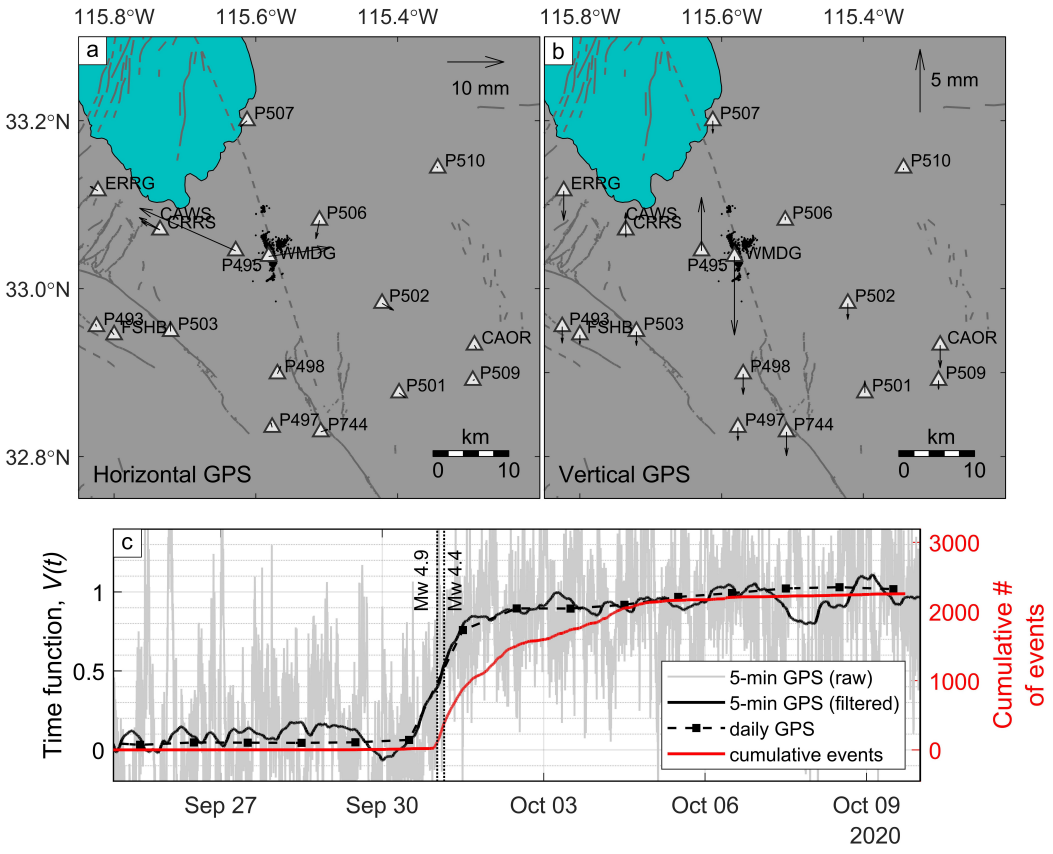

Figure 4.3: Extracted independent component (IC) related to the 2020 Westmorland swarm, which includes the spatial distribution (horizontal motion in a and vertical motion in b) and the associated time function (c). Unfiltered (gray) and filtered (black solid) time functions derived from 5-min GPS position time series are compared with those derived from daily GPS position time series (black dashed) and the cumulative number of events (red). The filter used is a Savitzky-Golay 3rd order moving polynomial fit with a window of 50 hours (Savitzky and Golay, 1964). The hypocentral times of the two most significant earthquakes are shown as vertical dashed lines. The geodetic deformations due to these M4 earthquakes are not removed. Compared to the noise levels of the 5-min GPS, these deformations are too small to be visible. Relocated seismicity from this study are shown as black dots in panels a and b. Fault traces from the QFaults database (Survey) are shown as gray lines. The outline of the Salton Sea (cyan) is from Google Earth images (Google).

onset of geodetic deformation. We further justify the choice of filter later in Section 4.5.4. We find the iterative GPS processing procedures presented here best suited for extracting the faint deformation related to the swarm. Raw and processed GPS time series at different processing steps from selected stations and vbICA components can be found in Figures B.4 – B.11.

4.3.3 InSAR

To supplement the GPS measurements, we use the C-band Synthetic Aperture Radar (SAR) images acquired over the region by the Sentinel-1A satellite during September and October 2020. A total of 5 images between September 9 and October 27, 2020, from ascending track 166, frame 105, and 9 images between September 3 and October 27, 2020, from descending track 173, frame 480 were used. The original pixel size of the Sentinel-1 Single Look Complex (SLC) images generally ranges between 2 – 5 meters, depending on the look angle of that pixel (see European Space Agency, 2014, for details). To reduce the spatial noise and estimate the coherence, all the Single Look Complex (SLC) images are averaged by a factor of 30 and 6 along range and azimuth, respectively, resulting in multi-look imagery with a pixel size of 70 m by 84 m. Next, the multi-look images in each track are separately coregistered (Werner et al., 2000) to a single reference image, which is chosen to minimize the total spatiotemporal baseline. 6 ascending and 20 descending interferograms are generated between all the possible pairs of SAR imagery acquired before and after the significant part of the swarm event (Table B.3). The interferograms are then flattened using satellite ephemeris data and a Digital Elevation Model (DEM) with 90 m resolution provided by the Shuttle Radar Topography Mission (SRTM) (Farr et al., 2007) to remove the effects of a flat earth and surface topography (Franceschetti and Lanari, 1999). A 2-D phase unwrapping algorithm proposed by Chen and Zebker (2001) is used to recover the absolute values from ambiguous phase observations at the location of pixels with coherence above 0.80.

A set of wavelet-based filters are then used to remove the nuisance signal associated with various sources of error in the unwrapped interferograms. The effect of residual DEM error, which appears as a high-spatial-frequency noise, is reduced using a low-pass filter generated based on the Legendre polynomial wavelets (Shirzaei, 2013). This filter applies a hard thresholding operation to the high-pass sub-band (i.e., details components) of each decomposed unwrapped interferogram. The spatially correlated nuisance terms are mainly caused by the atmospheric delay and the orbital and satellite clock errors. To remove these errors, each unwrapped interferogram is decomposed into its high-pass and low-pass sub-bands using a two-dimensional multiresolution wavelet transformation (Mallat, 1989). The effect of orbital errors is removed by fitting a ramp to the average component (i.e., the high-pass sub-band) through a robust regression method (Shirzaei and Walter, 2011). The detail coefficients, on the other hand, are used to correct the interferogram for the phase contributions from the topography-correlated component of atmospheric delay. To

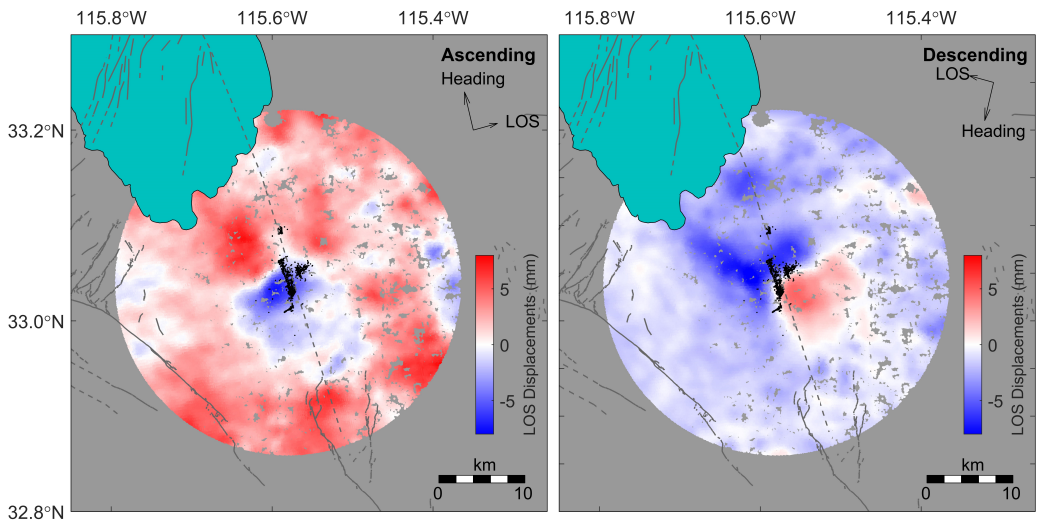

Figure 4.4: Interferometric Synthetic Aperture Radar (InSAR) Line-Of-Sight (LOS) displacements from Sentinel-1A. The ascending LOS displacements (track 166, frame 105) include 5 images and 6 interferograms, while the descending LOS displacements (track 173, frame 480) include 9 images and 20 interferograms. Relocated seismicity from this study is shown as black dots. Fault traces from the QFaults database (Survey) are shown as gray lines. The outline of the Salton Sea (cyan) is from Google Earth images (Google).

this end, a multiresolution wavelet analysis is also applied to the DEM of the study area, and the correlation between the resulting detail coefficients and that of the interferogram is estimated. Next, the correlated coefficients are down-weighted and fed into an inverse wavelet transformation to reconstruct the corrected unwrapped interferogram (Shirzaei and Bürgmann, 2012). We further apply a Gaussian filter with a width of 7 km to each interferogram to isolate the remaining spatially correlated errors in the unwrapped interferograms (Hooper et al., 2007), which are mainly caused by the turbulent atmospheric delay.

The deformation at the location of each pixel in each of the flight directions is then estimated as the weighted average of the displacements measured by individual interferograms (i.e., stacking), where weight is determined by the calculated spatial coherence. To enable this, all the interferograms are first interpolated at the location of all the pixels that had a coherence of 0.80 in at least one of the interferograms (i.e., the union of pixels). The resulting Line-Of-Sight (LOS) displacements for ascending and descending tracks are shown in Figure 4.4.

To make the inversion more computationally amenable, we apply an equation-based quadtree downsampling procedure (Wang et al., 2014) to reduce the number of

surface deformation observations while maintaining the essential features. This procedure is similar to the quadtree downsampling (e.g., Jónsson et al., 2002) in that it starts with a regular grid and iteratively subdivides the grid cells. However, the criteria for the subdivision of cells are based on fault geometry and gradients of the observed displacements. We start by generating a coarse grid with 1 km spacing and calculating the Green's function using the semi-analytical solutions for a dislocation embedded in an elastic homogeneous half-space (Okada, 1985) at the four corner points of each grid cell. We then compute the largest Green's function differences (g_i) and largest displacement gradients (d_i) for all the grid cells. Next, we select the grids above the 50th percentile of g_i and above the 10th percentile of d_i and divide them into four quadrants. We repeat this procedure until we have at least 2000 quadrants. Using this procedure on data points that are within 15 km from the center of the swarm, we end up with 2590 cells. The location and displacement rate of the sample point associated with each quadrant is estimated as the average coordinates and Line-of-Sight (LOS) rates of the enclosed points, respectively.

4.3.4 Geodetic slip inversion

We use the observed cumulative surface displacements over the entire period of the swarm from both GPS and InSAR to invert for corresponding slip distribution at depth. Seismicity patterns and focal mechanisms (Figure 4.2a-e, 4.5a-c) suggest that the swarm occurred on a system of conjugate strike-slip faults dipping closely to vertical. We simplify this fault system with a fault model consisting of two orthogonal vertical faults. The fault model is meshed as 1 km x 1 km rectangular patches. The first fault (F1) is 22 patches long, 14 patches deep, and has a strike of 162°. The second fault (F2) is 16 patches long, 14 patches deep, and has a strike of 72° (Figure 4.6a-c). The location and the strike of the two faults were chosen based on the discontinuity observed in the InSAR data. The faults extend beyond the significant features visible in the InSAR data and encompass the zone of seismicity.

Assuming an elastic homogenous medium, we can relate slip on the fault with ground deformations using the linear equation:

$$\vec{d} = \boldsymbol{G} \cdot \vec{m} \tag{4.1}$$

where $\vec{d}$ is the data vector representing surface displacements at different spatial locations, G is the Green's functions matrix computed from the semi-analytical solutions for a dislocation embedded in an elastic homogeneous half-space (Okada,

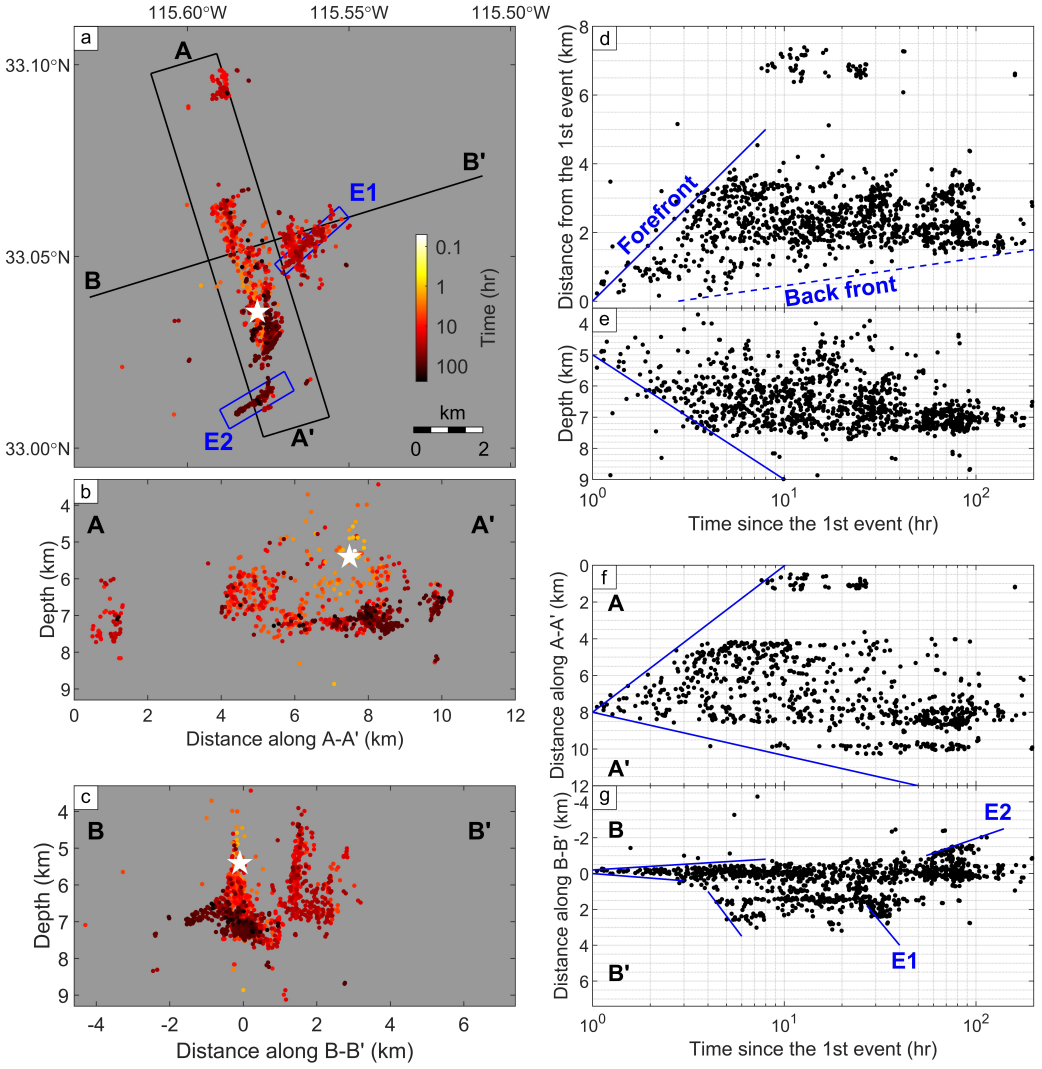

Figure 4.5: Spatio-temporal evolution of relocated seismicity generated from this study in (a) map view, (b) A-A', and (c) B-B' cross-sections color-coded by the logarithm of time since the first relocated event (white star). The complex behaviors of seismicity expansion are shown using (d) three-dimensional distance from the first relocated event, (e) depth distribution, (f) distance along A-A', and (g) distance along B-B'. Blue solid lines denote the various seismicity expansion fronts. In particular, the expansions of seismicity on the en-echelon structures E1 and E2 (blue boxes in panel a) are annotated in panel g. The blue dashed line indicates seismicity back front marking the expansion of the zone of seismicity quiescence. For panels b and f, only events within 1 km from the main fault (black box in panel a) are shown. Because the relocation technique used in this study relies on waveform similarity, a few larger events are excluded.

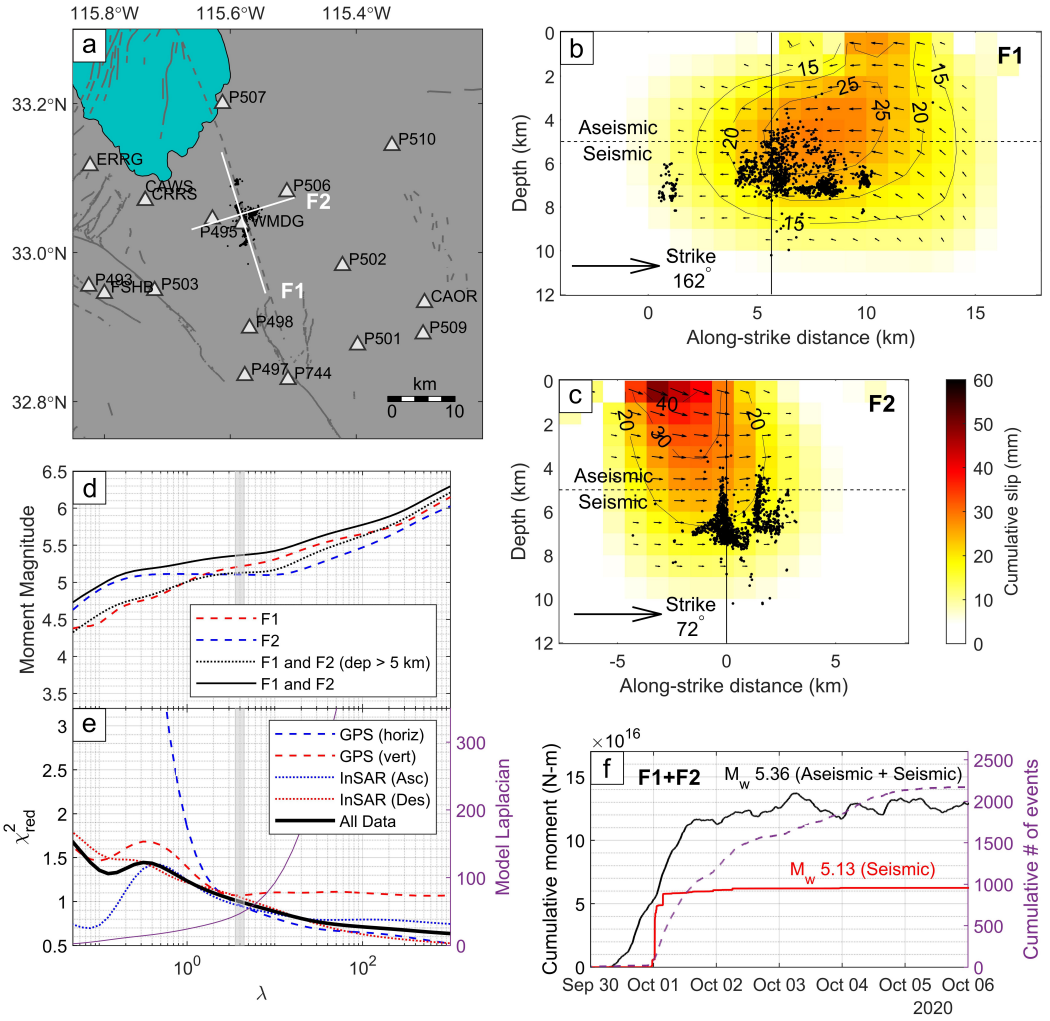

Figure 4.6: Geodetic slip inversion. (a) Location of the fault planes (white lines) and the GPS stations (black triangles) used in the inversion. Cumulative slip over the swarm duration along (b) F1 and (c) F2 from the preferred slip model. The intersection of F1 and F2 (black vertical lines), the inferred aseismic-seismic depth boundary (black horizontal dashed lines), and the relocated seismicity from this study (black dots) are shown in panels b and c. (d) Moment and (e) reduced chi-squared as a function of smoothing parameter λ. The preferred model uses $\lambda = 10^{0.6}$ (gray bar). (f) The time evolution of cumulative moment release from the geodetic inversion (black, filtered with the Savitzky-Golay filter (Savitzky and Golay, 1964) similar to Figure 4.3c), which reflects both the aseismic and seismic processes, and the cumulative seismic moment (red) calculated using magnitudes from the Southern California Seismic Network (SCSN) catalog (Hutton et al., 2010). The slip model is stationary but evolves according to the cumulative geodetic moment.

1985), and $\vec{\boldsymbol{m}}$ is the model input vector representing the amount of strike-slip and dip-slip on each fault patch. For InSAR data, the Green's functions are projected directly to the LOS displacements using the LOS unit vector at each pixel.

To include multiple data sets simultaneously, each data type i (horizontal GPS, vertical GPS, InSAR ascending, InSAR descending) is weighted by its variance (instrumental uncertainty squared, σ_i^2). We further impose the Laplacian smoothing to prevent unreasonably large spatial variations in slips resulting from the tradeoffs between slips at the neighboring cells and zero-slip along all fault boundaries that are not the free surface. The Laplacian is calculated using a formulation from Huiskamp (1991) with 16 nearest neighbors. With these additional constraints, we now seek to minimize the following cost function $\Phi(\vec{\boldsymbol{m}})$ for a slip model $\vec{\boldsymbol{m}}$:

$$\Phi(\vec{\boldsymbol{m}}) = \left(\sum_{\text{all data types}} \frac{1}{\sigma_i^2} \|\mathbf{G}_i \cdot \vec{\boldsymbol{m}} - \vec{\boldsymbol{d}}_i\|_2^2 \right) + \frac{1}{\lambda} \|\Delta \vec{\boldsymbol{m}}\|_2^2 \tag{4.2}$$

where $\|\cdot\|_2$ is the L2-norm, Δ is the Laplacian matrix, and λ is the weight attributed to the Laplacian smoothing constraint. Zero-slip constraints can be imposed by forcing non-diagonal values in the Laplacian matrix corresponding to the boundary patches to zero. This minimization problem can be written as a system of linear equations and can be solved with a matrix inversion.

We explore the range of possible slip models by varying the Laplacian weight λ and compare the tradeoff between the smoothness of the slip model and the misfit between the forward model and the data using the L-curve criterion (Hansen, 1992). Additionally, we further evaluate the reduced chi-squared for each data type i, defined as follow:

$$\chi^2_{\text{red},i}(\vec{\boldsymbol{m}}) = \frac{1}{n\sigma_i^2} \|\mathbf{G}_i \cdot \vec{\boldsymbol{m}} - \vec{\boldsymbol{d}}_i\|_2^2 \tag{4.3}$$

where n is the number of data points for data type i. The most appropriate model that does not overfit or underfit would have a reduced chi-squared of one for every individual data type. To properly account for errors in the a priori estimates of data uncertainties, the geodetic inversion is performed iteratively, similar to the scheme adopted by Thomas et al. (2014). In the first inversion, data uncertainty for all data types is assumed to be one. Afterward, the data uncertainty for each data type is renormalized so that the corresponding reduced chi-squared for that data type is

equal to one. The subsequent inversion is then performed using the updated data uncertainties. After a few iterations, the slip inversion should produce a reduced chi-squared that converges to one.

4.4 Kinematics of the 2020 Westmorland swarm

4.4.1 Spatio-temporal evolution of seismicity

Our high-resolution seismicity catalog reveals the swarm's complex migratory behaviors (Figure 4.5). A cluster of ~10 seismic events at 4.5 – 5.5 km depth (Figure B.12) were detected ~10 hr before the main swarm activity, which started on September 30, 2020, at 21:57 UTC. The overall pattern can be described by an expansion of seismicity forefront and back front, with sustained seismic activity in between lasting ~140 hr (Figure 4.5d). Both fronts expanded non-linearly with a rapid onset followed by decaying expansion rates, which we discuss more in Sections 4.5.3 and 4.5.7.

Figure 4.5 shows the detailed spatio-temporal evolution of the swarm. During the first 20 hr, the swarm expanded logarithmically along the main 162°-trending vertical fault zone, roughly 500-m wide. The expansion was asymmetric, with a dominant northward along-strike propagation. The along-dip expansion terminated at ~8 km. Coincident with the expansion along the main fault, two adjacent 500-m wide steeply dipping structures parallel to the main fault forming a flower structure were reactivated ~4 hr after the swarm activity started. Later at 25 and 55 hr, en-echelon structures perpendicular to the main fault (structures E1 and E2 in blue boxes of Figure 4.5a, respectively) were reactivated. Seismicity on these en-echelon structures was localized along narrow zones no more than 200-m wide at a depth of ~6.5 km or deeper, coinciding with the basement. Compared to the swarm duration, the reactivations were short-lived and exhibited a non-linear migration front (blue lines annotated with E1 and E2 in Figure 4.5g). We also observed a seismicity gap between latitude 33.07 – 33.09°N that could be related to the heterogeneity of stresses on the fault. All large earthquakes with $M > 4$, including the largest M_w 4.93 event, were within the first 6 hr of the swarm, and they did not appear to cause any significant changes in the seismicity rate (Figure B.12). This could be partly due to catalog incompleteness in the early period after large events (e.g., Hainzl, 2016).

4.4.2 Time-dependent geodetic slip model

The linear decomposition of the signal into a limited number of components, whether using a PCA or an ICA, makes it very effective for carrying out an inversion of the time evolution of slip (Kositsky and Avouac, 2010). Instead of epoch-by-epoch inversions, we can perform inversions for only the spatial functions associated with each component ($U_{M\times r}$), where r refers to a set of all components representing the geodetic transient of interest. The time evolution of slip is obtained by multiplying the slip models resulting from these inversions by $S_{r\times r}V^T_{r\times T}$ (see Kositsky and Avouac, 2010, for details). Since only one component related to the swarm sequence was extracted, our resulting model is stationary in space with cumulative moment varying according to the time function $V(t)$ retrieved from the vbICA decomposition (Figure 4.3). Our preferred model (Figure 4.6) uses a Laplacian weight of 100.6, which yields the best trade-off between data fitting and the smoothness of the solution (Figures 4.6e Figure B.13). Although the details of slip distribution would vary if we were to choose a different Laplacian weight, the total moment release is relatively well-constrained at M_w 5.3-5.4 (Figure 4.6d). The uncertainties assigned to each dataset following our iterative inversion (Section 4.3.4) are reported in Table 4.1. After only one iteration, the reduced chi-squared for each data type gets close to unity within 7% (Table 4.1). Therefore, no further iteration was deemed necessary. Further analysis on the sensitivity of the results to the assumed fault geometries, checkerboard resolution test (Lévěque et al., 1993), and variances estimation with jackknife test (Efron and Stein, 1981) are provided in Section B.2 and Figures B.14 – B.17.

Our slip model reveals conjugate faulting with right-lateral strike-slip motion along the 162°-striking main fault F1 and left-lateral strike-slip motion along 72°-strike orthogonal fault F2 with peak slip occurring along F2 near the surface (Figure 4.6). To determine the slip modes observed, we compare the geodetically resolved moment with the seismic moment. Since we do not calculate magnitudes for our seismicity catalog, we use magnitudes from the SCSN catalog. The additional events in our enhanced catalog are small and contribute only a small fraction to the total seismic moment. We find that the relative contribution of the seismic and aseismic moment vary systematically with depth. For the depth range of seismicity (5 – 10 km), the geodetically resolved slip is equivalent to M_w 5.13, roughly equal to the total moment release estimated from the seismicity itself. This suggests that the slip mode for this depth range is predominantly seismic. On the contrary, since there is only little seismicity above a depth of 5 km, the shallow slipping region on F2

must be mostly aseismic. Cumulatively over the entire swarm period, the aseismic moment release (M_w 5.19) is ~20% larger than the seismic moment release (M_w 5.13).

The predicted displacements from our preferred slip model show large misfits to the InSAR data close to the faults suggesting that the fault zone is complex and cannot be modeled perfectly with simple planar shear faults (Figure 4.7). The en-echelon step-over fault structures, prominent dilatational motion in this region (Crowell et al., 2013), plastic deformation, and inhomogeneity of elastic moduli could contribute to these misfits. However, we did not try to refine the model further because we are chiefly interested in the effect of the aseismic processes on the evolution of the swarm. Furthermore, the seismicity occurred in the basement, at ~5 km distance from the peak aseismic slip, and stress changes there are not very sensitive to the detail of the source near the surface.

GPS position time series with sub-daily resolution resolves that the onset of geodetic deformation preceded the onset of seismicity by at least a few hours (Figures 4.3 and 4.6f). This suggests that fault slip in the early period was aseismic. Moreover, since the moment release at depth > 5 km is related predominantly to seismicity, the slow slip event was probably initiated in the shallow portion of F2, where aseismic slip was the highest. Although it seems reasonable at this point to conclude that the slow slip event triggered the swarm sequence, proximity in space and time does not require a causal relationship. We explore further the relationship between the slow slip event and the swarm sequence using triggering analysis and a stress-driven model in Section 5. We also note that most geodetic moment releases terminated ~1 day after the swarm began (Figure 4.6f). However, seismicity continued for ~5 more days, suggesting a secondary mechanism other than the slow slip event that drove the latter part of the swarm.

4.5 Modeling the 2020 Westmorland swarm

The seismic and geodetic observations of the 2020 Westmorland swarm provide a unique opportunity to study the mechanics of the swarm in detail. This section discusses the interplays of the processes driving the swarm (the slow slip event, inter-earthquake static stress triggering, and pore pressure diffusion) and quantifies their relative contributions in driving the seismicity. We first show that the swarm was driven by the slow slip event rather than a result of cascade triggering using static stress transfer (Sections 4.5.1 – 4.5.3). Next, we model the temporal evolution of

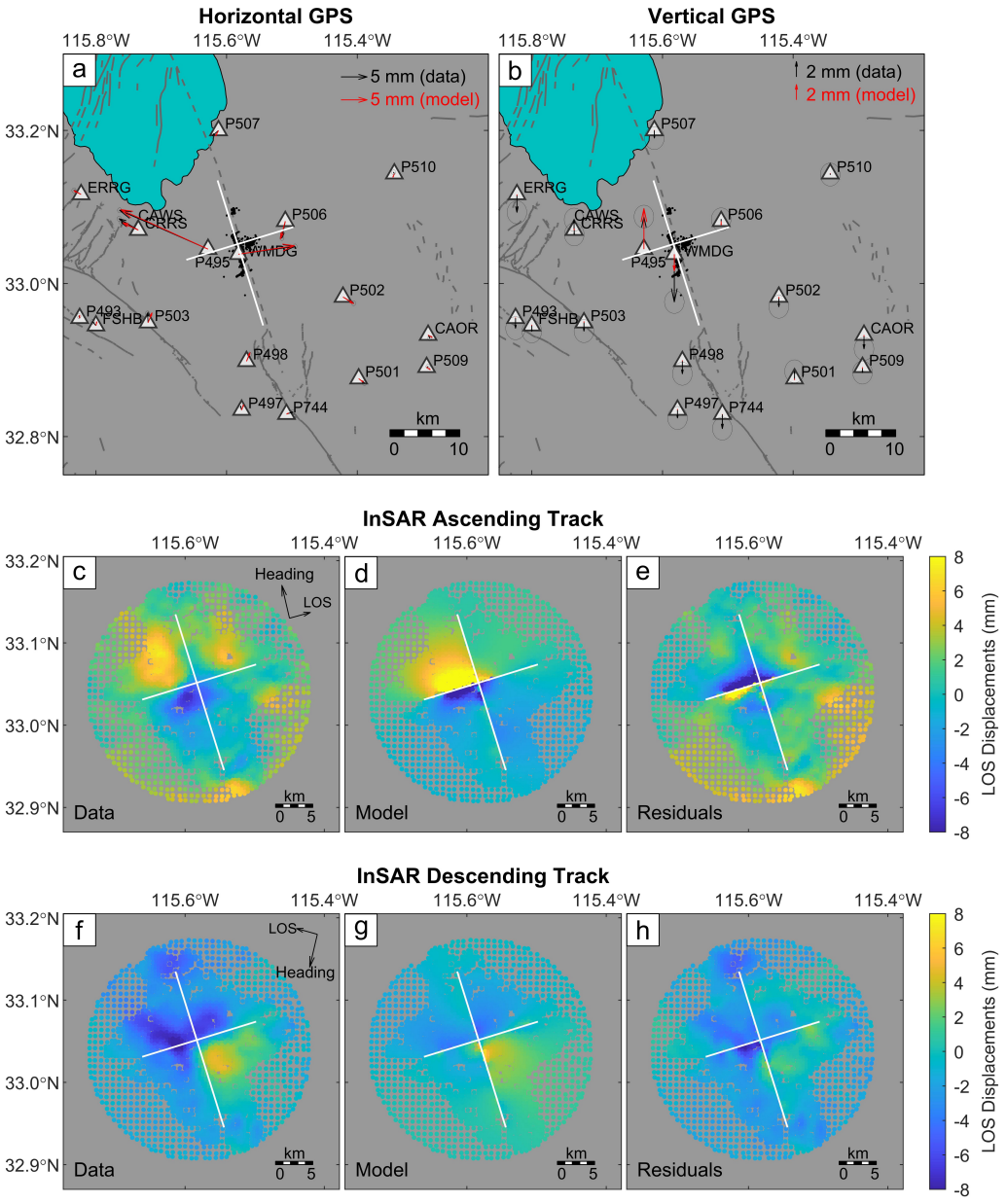

Figure 4.7: Comparison of the observed and predicted values from our preferred slip model for (a) horizontal and (b) vertical GPS displacements. (c) Observed values, (d) predicted values, and (e) the residuals for InSAR ascending track. (f) Observed values, (g) predicted values, and (h) the residuals for InSAR descending track. The location of the fault planes is shown as white lines.

Data Type	Uncertainty, σ_i	Reduced chi-squared, χ^2_{red}
GPS (horizontal)	0.4 mm	0.96
GPS (vertical)	1.5 mm	1.07
InSAR (Ascending)	2.9 mm	0.95
InSAR (Descending)	2.1 mm	1.05
Combined	N/A	1.00

Table 4.1: Data uncertainty (σ_i) and reduced chi-squared statistics of the misfit between observations and the forward prediction of ground deformations (χ^2_{red}) calculated using the preferred slip model after normalization of the data uncertainties (Figure 4.6b-c).

seismicity during the swarm sequence using stress changes from the slow slip event and a stress-driven model based on rate-and-state friction (Sections 4.5.4 – 4.5.6). Then, we associate the unexplained seismicity with pore pressure diffusion, which helps sustain the swarm sequence (Section 4.5.7). Finally, our models provide constraints on the friction parameter and pore pressure, which we compare with values independently derived from the responses of seismicity to hydrological cycles and solid Earth tides (Section 4.5.8).

4.5.1 Aseismic slip driven vs. cascading failures

Two end-member scenarios explaining the spatial and temporal evolution of the swarm can be envisioned. The first scenario postulates that the earthquakes are driven only by external forcings, such as the slow slip event, through Coulomb Failure Stress changes (dCFS) with minimal interactions between the earthquakes themselves. This scenario is similar to Dieterich's model of aftershocks (Dieterich, 1994), which assumes that all aftershocks are directly triggered by a single mainshock. The second scenario postulates that an earthquake produces earthquakes resulting in a series of cascading events (Ellsworth and Beroza, 1995). To distinguish which of these mechanisms is dominant, we compute and compare dCFS induced on each seismic event by the slow slip event and by all earthquakes preceding it to investigate which of these two end-member scenarios is more likely. The hydrothermal setting of Westmorland, California, suggests that the presence of fluids must be accounted for. All dCFS calculations in this study assume a friction coefficient of 0.4, chosen to account approximately for the effect of a hydrostatic pore pressure as is customary in such studies (King et al., 1994).

The computation of dCFS requires knowledge of the receiver's fault plane. Since we did not specifically determine focal mechanisms for this study, we restrict the analysis to 562 events with reported SCSN focal mechanisms. This is valid because large events, which dominate the stress transfer, are those with focal mechanisms. For each event, the fault plane is chosen to be the nodal plane from the focal mechanism that maximizes dCFS induced by each end-member scenario. For scenario 2 of cascade triggering, since the fault plane of the current event depends on dCFS from previous events and hence their fault planes which depend on all events before it, errors from previous calculations would stack up rapidly. To prevent erroneous results from staggering uncertainties, given that geodetically resolved slips at seismogenic depths are mostly constrained on F1, we further assert that the fault planes of the first event and largest M4.9 event are the nodal planes closer to right-lateral strike-slip motion along F1. Concerning locations, we use the relocated locations from this study except for those with M > 4 in which we use the locations from the SCSN catalog because we find their relocated locations inaccurate due to the dissimilarity of the waveforms with other small events in the catalog.

Besides the receiver's fault planes, we also need to know the properties of the sources. For scenario 1 of slow slip driven, since aseismic slip dominates the shallower parts of the faults (depth < 5 km) while seismicity dominates the deeper parts (depth > 5 km), the slow-slip source is taken to be the top 5 km of the geodetic slip model. However, instead of temporally evolving the slips according to the cumulative geodetic moment, we use the cumulative aseismic moment, calculated by subtracting the cumulative seismic moment (magnitudes from SCSN catalog) from the unfiltered cumulative geodetic moment and then filtered with the 3rd order Savitzky-Golay filter with 50-hr window. For scenario 2 of cascade triggering, since we need focal mechanisms to determine the source properties, we restrict the dCFS sources to only events with SCSN focal mechanisms. We approximate the earthquake source as a circular crack with a uniform stress drop assumed to be 0.1 MPa, consistent with other regional earthquakes in the Brawley Seismic Zone (Chen and Shearer, 2011, Hauksson, 2015), and the mean Coulomb stress drop of our geodetic model (Figure B.18) estimated using a formulation based on energy considerations (Noda et al., 2013). Using stress drop and SCSN magnitudes, we estimate the slipping area A and the amount of slip D using the scaling relation $M_0 \sim \Delta\sigma A^{3/2}$ (Kanamori and Anderson, 1975) and the definition of seismic moment $M_0 = \mu AD$ along with the assumed crustal shear modulus $\mu \sim 30GPa$. For simplicity in calculation, we further approximate the circular rupture as a square

of equal area and use semi-analytical solutions in an elastic half-space to calculate dCFS (Okada, 1992). For a given event, the dCFS are calculated using all events before it as sources, not just from the most recent event.

Using the outlined procedures, we find that dCFS induced on each seismic event by the slow slip event is generally larger than those induced by all preceding earthquakes (Figure 4.8). This holds even for scenario 2, where the fault planes were chosen to be more favorable for cascade triggering. We find that up to 68% of events could be driven by the slow slip event, with the median dCFS of 22 kPa (Figure 4.8a). About 22 – 35% of events can be attributed to inter-earthquake static stress triggering. The remaining 9 – 14% of events have negative dCFS and are neither encouraged by the slow slip event nor cascade triggering, requiring a third mechanism.

Since stress drops for each event can vary over a few orders of magnitude, we further investigate the sensitivity of our analysis to the assumed stress drop of 0.1 MPa. We find a systematic trend with more events likely triggered by the slow slip event for lower stress drop. For the stress drop $\Delta\sigma$ ranging from 0.1 – 3 MPa, at least 44% of events are encouraged by the slow slip event when choosing the fault planes based on scenario 1 of slow slip driven and 35% of events for scenario 2 of cascade triggering (Figure B.19). We acknowledge that the uncertainty in the estimate of dCFS due to errors in hypocentral locations and focal mechanisms could bias the analysis toward underestimating the performance of the cascade model (Hainzl et al., 2012).

4.5.2 Faulting type of seismic events

Our high-resolution seismicity catalog reveals the fault zone structure but not the faulting type of each structure. Since dCFS induced at each event by the slow slip event is generally larger than dCFS induced by all earthquakes preceding it (Section 4.5.1), we assert that the nodal planes with larger dCFS induced by the slow slip event are the true fault planes (Scenario 1) and their associated rakes describe the faulting type. From the 437 relocated events from this study with matching SCSN focal mechanisms that are in the region with positive dCFS induced by the slow slip event (Figure 4.9c), we classify 269 events as right-lateral strike-slip, 85 events as left-lateral strike-slip, 55 events as normal faulting, and 28 events as reverse faulting (Figure 4.9). Even though only 19% of events have right-lateral strike-slip motion, they include most large events on the 162°-striking main fault F1 and makeup 94% of the total seismic moment release. The remaining seismic moment release is accommodated by primarily left-lateral strike-slip events on the

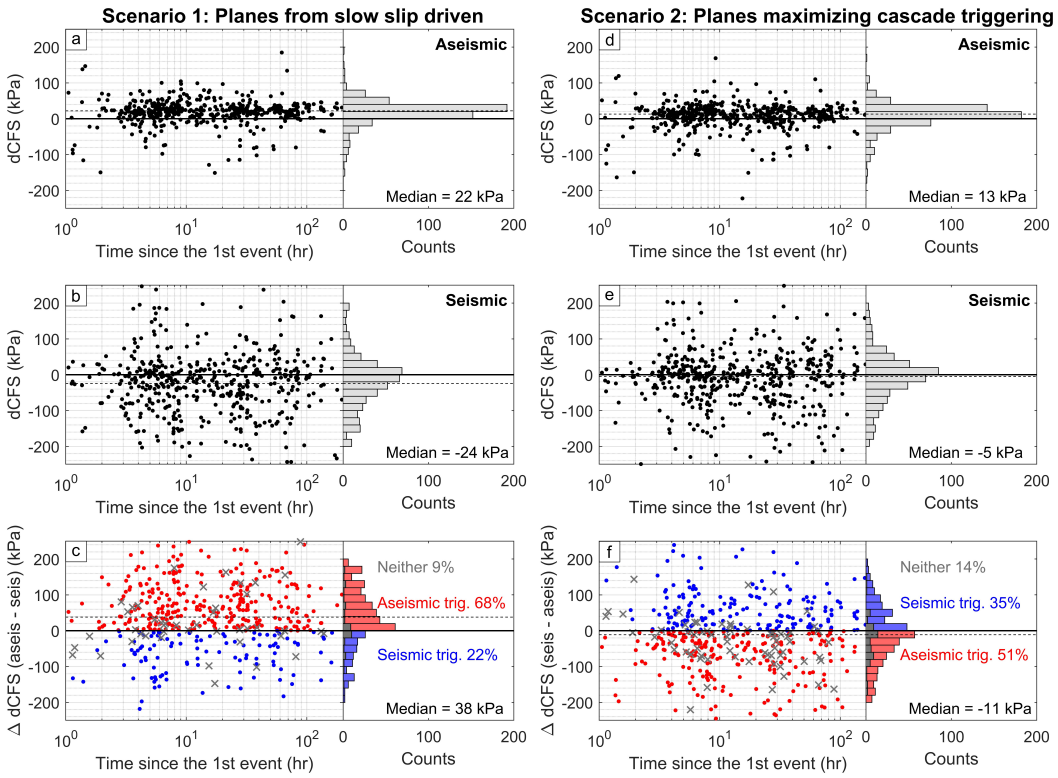

Figure 4.8: Coulomb Failure Stress changes (dCFS) at relocated events from this study with matching SCSN focal mechanisms. In scenario 1, failure planes are the nodal planes with larger dCFS induced by the slow slip event. With such nodal planes, the distribution of dCFS induced by (a) the slow slip event, (b) all preceding earthquakes, and (c) their differences are shown. In scenario 2, failure planes are the nodal planes with larger dCFS induced by all preceding earthquakes. With such nodal planes, the distribution of dCFS induced by (d) the slow slip event, (e) all preceding earthquakes, and (f) their differences are shown. The median value for each distribution is plotted as a horizontal dashed line. Based on the larger dCFS values, we can classify the events into different categories, whether they are likely triggered by the slow slip event, other seismic events, or encouraged by neither, because dCFS values are negative (gray crosses in panels c and f).

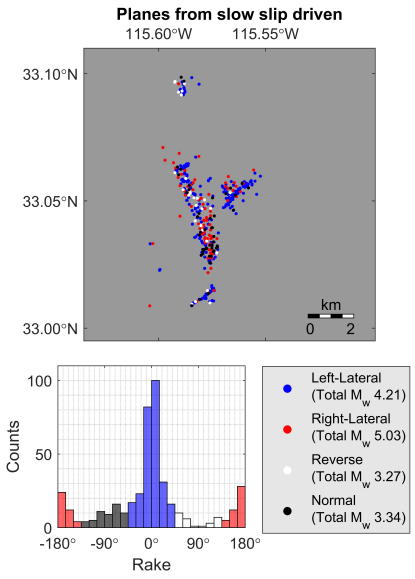

Figure 4.9: Map of relocated events from this study with matching SCSN focal mechanisms color-coded by faulting type and a histogram of the corresponding rake. The faulting types are chosen from the nodal planes with larger dCFS induced by the slow slip event (scenario 1 in Figure 4.8). Only those with positive dCFS are considered.

en-echelon structures orthogonal to the main fault F1. Normal and reverse faulting accounts for < 1% of the total seismic moment release. The relative ratio between the different faulting types does not significantly change with time (Figure B.20). The distribution of fault planes selected to favor cascade triggering (scenario 2) is shown in Figures B.21 – B.22.

4.5.3 Logarithmic expansion of seismicity controlled by the slow slip event

Our high-resolution relocated seismicity catalog reveals that seismicity during the swarm expanded non-linearly with a rapid onset followed by decaying expansion rates (Figure 4.6d). The insufficient spatial resolution of the non-relocated catalog could make these fronts appear to expand linearly. To further distinguish whether the expansion is $\sqrt{t}$ or $\log(t)$ from the observed seismicity is extremely difficult since envelopes of seismicity are not precisely defined (Figure B.23), though we think that $\log(t)$ expansion is more likely due to different reasons. First, describing seismicity front as $\sqrt{t}$ expansion would require hydraulic diffusivity of 100 m^2/s, which is outside of a commonly accepted range for fluid-driven swarms (e.g., Amezawa et al., 2021). Cascading earthquakes can also lead to an apparent diffusive expansion of the seismicity (Helmstetter and Sornette, 2002a), but this is unlikely because static

stress triggering (Section 4.5.1) and statistics of times between earthquakes (Section 4.5.5) suggest that earthquakes are predominantly non-interacting. Second, the slow slip event began abruptly, followed by a decaying slip rate, which can be reasonably modeled using an exponential decay or a logarithmic function typically used for afterslip (Ingleby and Wright, 2017). Earthquakes driven by afterslip are expected to expand as $\log(t)$ (Perfettini et al., 2018), as observed in selected case studies (e.g., Frank et al., 2017, Kato and Obara, 2014, Peng and Zhao, 2009, Tang et al., 2014).

To further investigate the possibility of the slow slip event controlling the expansion of the seismicity front, we evaluate the time evolution of dCFS induced by the slow slip event (top 5 km of the geodetic slip model) along the main fault plane F1. The time evolution of the slow slip event is assumed to be proportional to the time evolution of the aseismic moment calculated by subtracting cumulative seismic moment (magnitudes from SCSN catalog) from the unfiltered total geodetic moment and then filtered with the 3rd order Savitzky-Golay filter with 50-hr window, similar to what we used previously in Section 4.5.1. We calculate dCFS for both the right-lateral strike-slip plane F1 and the left-lateral strike-slip plane F2 to include events on en-echelon structures and retain the maximum value at each gridded point (Figure 4.10a-b). We assert that a certain threshold of dCFS is needed to nucleate a seismic event and track the expansion of the different dCFS contours along F1. The results reveal that the contours expanded non-linearly, roughly parallel to the observed seismicity front (relocated catalog from this study), with rapid onset followed by a decaying expansion rate (Figure 4.10c-d). The average dCFS required to trigger seismicity is estimated to be ~30 kPa, similar to the median dCFS value of 22 kPa required to trigger seismicity estimated in Section 4.5.1. Regardless of which dCFS contour we pick, there is a time lag between the stress changes and the observed seismicity, highlighting a finite nucleation time consistent with earthquake nucleation models based on laboratory friction laws (e.g., Dieterich, 1994).

4.5.4 Seismicity rate evolution from a stress-driven model

We have shown in Section 4.5.3 that stress changes due to the slow slip event can explain the rapid expansion of the seismicity front. Here, we further investigate the possibility of quantitatively explaining the time evolution of seismicity rate using a stress-driven model based on one degree of freedom spring-slider system close to failure (Dieterich, 1994, Heimisson and Segall, 2018), hereafter referred to as "Dieterich's model." The friction coefficient μ in this model evolves with slip velocity V and a state variable θ according to the rate-and-state formulation derived from

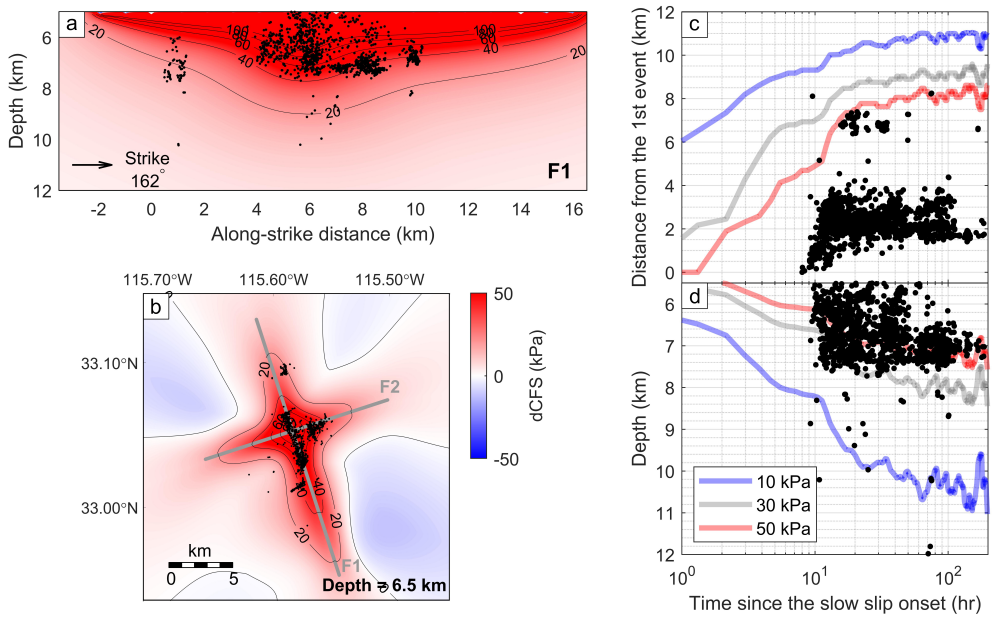

Figure 4.10: dCFS induced by the slow slip event calculated (a) on F1 and (b) at a depth layer of 6.5 km. The values displayed are the maximum assuming either the right-lateral strike-slip plane F1 or left-lateral strike-slip plane F2 as the failure plane. Time evolution of (c) the maximum distance between the contours of different dCFS values on F1 (panel a) and the first relocated event and (d) the depth extent of the same contours. Relocated seismicity from this study is shown as black dots. The onset of the slow slip event is picked to be ~8 hr before the start of the swarm.

laboratory experiments sliding two rock surfaces or gouge layer (Dieterich, 1979, 1981, Marone, 1998a, Ruina, 1983). Dieterich's model further uses an approximation that the product of slip velocity V and the state variable θ is large compared to the critical slip distance D_{RS}, i.e., $V\theta/D_{RS} \gg 1$, and assumes that the friction parameter a describing material resistance to an increase in slip velocity ($\partial\mu/\partial(\ln V)$) and initial effective normal stress σ are uniform. The seismicity rate $R(t)$ on a fault would then respond to an evolving shear stress perturbation $\Delta\tau(t)$ according to the following equation (Dieterich, 1994, Heimisson and Segall, 2018):

$$\frac{R(t)}{r} = \frac{e^{\Delta\tau(t)/a\sigma}}{1 + \frac{1}{t_a}\int_0^t e^{\Delta\tau(x)/a\sigma}\,dx} \tag{4.4}$$

where $t_a = a\sigma/\dot{\tau}_a$ is the characteristic aftershock decay time for returning to steady-state, and r is the background seismicity rate corresponding to a constant background stressing rate (τ_a) prior to the perturbation. When normal stress changes are small

relative to the effective normal stress σ, we can substitute shear stress changes $\Delta\tau(t)$ with the cumulative Coulomb Failure Stress changes dCFS(t), which we use throughout our study (Dieterich et al., 2000, Heimisson and Segall, 2018). Because the slip rate during the slow slip event is of a few mm/day, value orders of magnitude larger than the mm/year geological slip rate associated with tectonic loading, we do not consider background tectonic stressing in the stress changes term.

We further simplify the analysis by treating the observed seismicity as a point process and do not consider spatial information. All detected events in our catalog, including those not relocated, are used. The background seismicity rate r prior to the swarm is estimated from the SCSN catalog (Figure B.24) and then rescaled to our catalog using the total number of detected events N during the swarm, i.e., $r_{ourcatalog} = r_{SCSN} \cdot N_{ourcatalog}/N_{SCSN}$. Since our slip model is stationary, if the medium is assumed to be homogeneous, $\Delta\tau(t)$ is proportional to the cumulative moment release. We are left with only two fitting constants, the decay time t_a and the proportionality constant $\Delta\tau_0/a\sigma$ between $\Delta\tau(t)/a\sigma$ and the normalized cumulative moment release, where $\Delta\tau_0 = \Delta\tau(t = \infty)$ is the cumulative dCFS over the swarm duration. A set of sensitivity tests (Figure B.25) show that $\Delta\tau_0/a\sigma$ controls the amount of time lag between the slow slip event and seismicity while t_a controls the maximum seismicity rate.

Even though Dieterich's model assumes no interactions between sources, we can approximately account for it by including dCFS induced by the earthquakes themselves in the driving shear stress, such as those done in the numerical models of Ziv and Rubin (2003). Theoretically, this is valid if magnitude statistics are not altered by stress perturbations (Heimisson, 2019). To assess whether the inter-earthquake static stress transfer plays a vital role in driving the swarm, we model the seismicity rate using both the stress changes from only the slow slip event (left panels in Figures 4.11 and 4.12) and the stress changes from the total geodetically resolved slip which includes also slips due to earthquakes (right panels in Figures 4.11 and 4.12). Similar to Sections 4.5.1 and 4.5.3, the cumulative aseismic moment used here is derived by subtracting the cumulative seismic moment (magnitudes from the SCSN catalog) from the unfiltered cumulative geodetic moment. Since Dieterich's model is highly non-linear and hence affected by the high-frequency noises, we compare 3 different methods to denoise the cumulative moment:

1. fitting with a Heaviside step function $H(t - t_0)$, representing an instantaneous deformation end-member (Figure B.26),

2. fitting with an exponential function $H(t - t_0) \cdot A_{exp}(1 - e^{-(t-t_0)/\tau_{exp}})$, representing a continuous deformation (Figure 4.11), and

3. applying a Savitzky-Golay filter based on moving polynomial to remove high-frequency noises (Figure 4.12).

Model fitting is done using a standard grid search to minimize the root-mean-squared error (RMSE). Given that most of the geodetic moment release already terminated ~1 day after the start of the swarm, attempting to fit the model with the seismicity rate from the entire swarm duration leads to a significant underestimation of peak seismicity. The latter part of the swarm requires a secondary driving mechanism without significant geodetic deformation, such as pore-pressure diffusion (Section

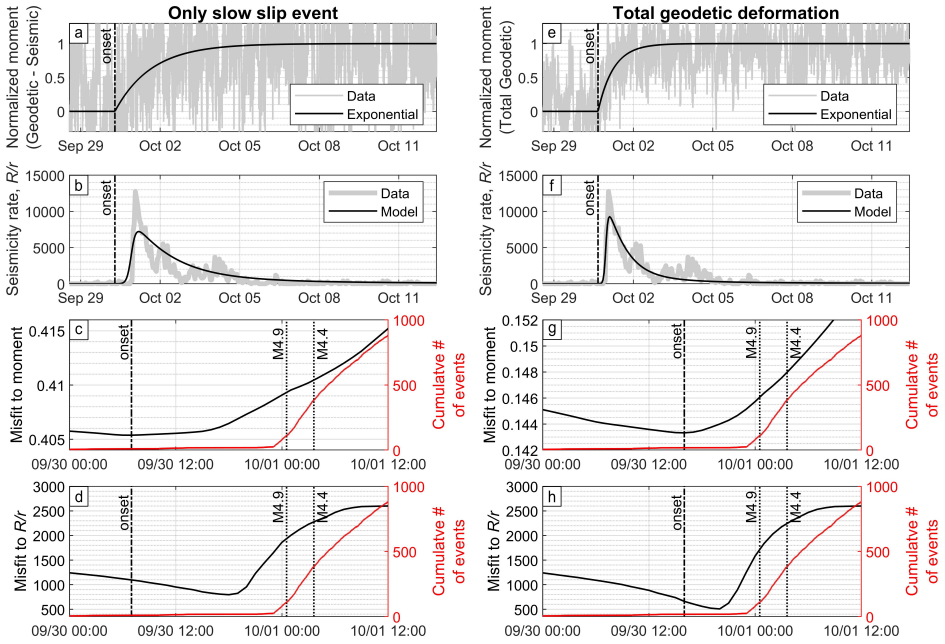

Figure 4.11: Exponential model fitting. Comparison of seismicity rate models driven by stress changes induced (a – d) by the slow slip event and (e – h) by the total geodetic deformation. For a homogeneous medium and stationary slip model, stress changes are proportional to the (a, e) moment release (unfiltered, normalized using the 5th and 95th percentiles), which can be approximated with an exponential function. (b, f) Best fit seismicity rate driven by the best fitted exponential stress changes. (c, g) Root-mean-squared-error (RMSE) misfit to the normalized moment and (d, h) and seismicity rate when varying the onset of the deformation. The seismicity rate used for modeling is derived from all detected events in our catalog, including those not relocated. The spatial distribution of seismicity is not considered.

4.5.7). We, therefore, choose to minimize RMSEs over only the first day of swarm activity. We summarize the RMSE and best fit parameters ($\Delta\tau_0/a\sigma$ and t_a) for various models in Table 4.2.

Our results suggest that the Heaviside step function (Figure B.26) ignores the finite duration of the slow slip event, gives large misfits to moment and seismicity rates, and yields erroneous estimates of parameters. The models with exponential approximation (Figure 4.11) capture the main features and could be used to provide reliable estimates of $\Delta\tau_0/a\sigma$ and t_a, though the peak seismicity rate is underestimated due to the smoothing effects. The exponential approximation can be useful when the

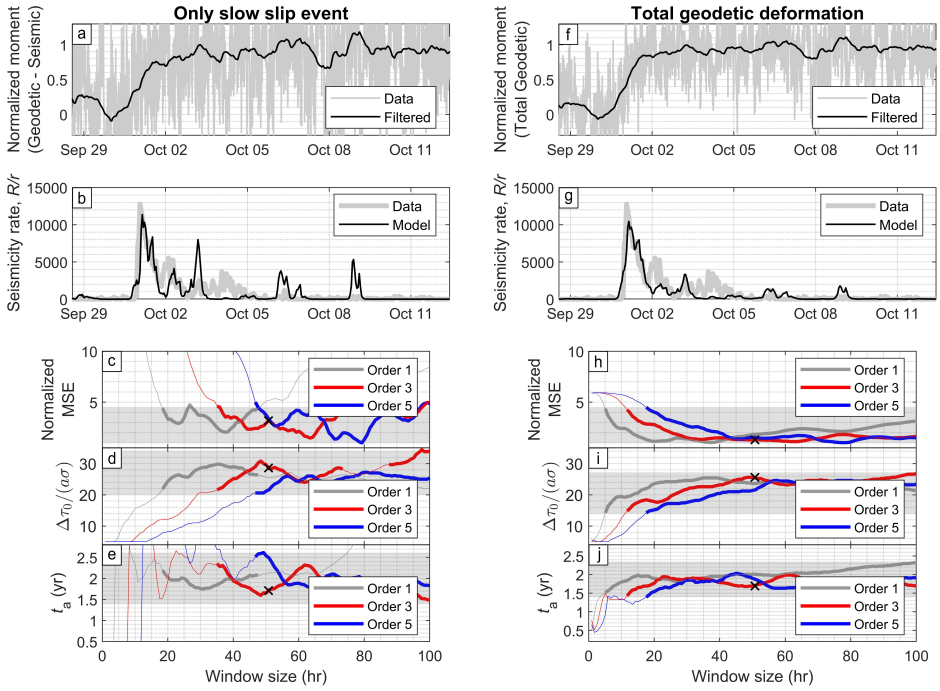

Figure 4.12: Savitzky-Golay filtered model fitting. Comparison of seismicity rate models driven by stress changes induced (a–e) by the slow slip event and (f–j) by the total geodetically resolved slip. For a homogeneous medium and stationary slip model, stress changes are proportional to the (a, f) moment release (unfiltered, normalized using the 5th and 95th percentiles), which can be filtered with a Savitzky-Golay filter based on moving 3rd order polynomial fit with 50-hr window. (b, g) Best fit seismicity rate. (c, h) Normalized mean squared error (MSE) from fitting the seismicity rate, (d, i) best fit $\Delta\tau_0/a\sigma$ and (e, j) best fit t_a for the different window sizes and polynomial orders. The gray areas and thicker lines in (c–e, h–j) correspond to 1σ confidence interval based on the chi-squared criterion. The seismicity rate used for modeling is derived from all detected events in our catalog, including those not relocated. The spatial distribution of seismicity is not considered.

Driving stress	Denoising method	RMSE	$\tau_0/a\sigma$	t_a (yr)
Slow slip event only	Heaviside step function	1387	10.0	8.6
	Exponential function	1097	24.6	2.6
	Savitzky-Golay filter (3rd order, 50 hr)	1159	28.6	2.4
Total geodetically resolved slip	Heaviside step function	890	10.3	7.8
	Exponential function	661	23.0	2.0
	Savitzky-Golay filter (3rd order, 50 hr)	834	26.2	1.7
Total geodetically resolved slip (with threshold, Section 4.5.6)	Savitzky-Golay filter (3rd order, 50 hr)	702	74.0 ($\tau_c/a\sigma$ = 18)	1.1

Table 4.2: Root-mean-squared error (RMSE) of seismicity rate modeling and the best fit parameters for the different models tested in this study.

details of the slip evolution are unavailable, as done in Lohman and McGuire (2007). However, further studies could assess the generalizability of this assumption as the model is an ad hoc analytical choice and is thus not based on any physical mechanism. Models using directly the Savitzky-Golay filtered cumulative moment release (Figure 4.12) best capture the detailed evolution of the seismicity rate. However, their misfit is larger than the exponential approximation due to noises that still persist even after the filter is applied. Furthermore, when comparing models driven by only slow slip event (left panels of Figures 4.11, 4.12, B.26) with models driven by total geodetically resolved slip (right panels of Figures 4.11, 4.12, B.26), we find that the latter performs better for all denoising methods tested. This means that even though the slow slip event plays a significant role in driving the swarm, the inter-earthquake static stress transfer is not negligible. We further quantify their relative contribution using point process statistics in Section 4.5.5.

With our preferred denoising method being the Savitzky-Golay filter, we further assess the effects of filtering parameters on the estimated parameters (Figure 4.12c–e and 4.12h–j). We vary the window size from 1 – 100 hr, use polynomial orders 1, 3, and 5, and find the window size of 50 hr and 3rd order polynomial preferable. While there are other options with smaller mean squared error (MSE), we find that

they start to overfit the noises (Figures B.27 and B.28). If we were to choose such an overfitting model, it would not change the key conclusions of the study. Using chi-squared criterion with 1σ confidence interval ($\Delta\chi^2 = \Delta MSE = 3.53$ for 3 degrees of freedom: $\Delta\tau_0/a\sigma$, t_a, and filtering window size) to estimate the uncertainties of the parameters, we find $\Delta\tau_0/a\sigma = 29^{+5}_{-9}$ and $t_a = 1.7^{+0.9}_{-0.3}$ yr, when using a model driven by the slow slip event and $\Delta\tau_0/a\sigma = 26^{+1}_{-10}$ and $t_a = 1.7^{+0.6}_{-0.3}$ yr, when using a model driven by the total geodetically resolved slip. It is not unexpected that the estimated t_a is large compared to the swarm duration as the area still has an elevated seismicity rate several months after the swarm (Figure B.29), though t_a may still be overestimated as the stress releases from events driven by pore-pressure diffusion are not accounted for in the model (Section 4.5.7). We discuss more how these values compare with other studies in Section 4.5.8.

Furthermore, given that the 5-min sampled position time series are considerably noisy (Figure 4.3c), the amount of time lag may be affected by the choice of filter used. We further quantify the uncertainty range of the time lag using Dieterich's model driven by an exponential stress change with different onset times. By fitting the moment release with the exponential function, we find that the best fit model has an onset with a time delay of 15 hours for those driven by only the slow slip event (Figure 4.11c) and 6 hours for those driven by total geodetically resolved slip (Figure 4.11g). Instead of selecting the best fit for the moment release, if we select the best fit based on the observed seismicity rate, the time delay of the onset shrinks considerably for both driving scenarios to 4 hours (Figure 4.11d) and 2 hours (Figure 4.11h), respectively. While misfits to the moment release and the seismicity rate increase only gradually as the time lag becomes longer, the misfits increase rapidly as the time lag becomes shorter than 2 hours. Therefore, the analysis supports that the time lag between the slow slip event and seismicity exists and cannot be an artifact of filtering. The best estimates yield a time lag between 2 – 15 hours, consistent with the onset derived from filtering the geodetic deformation with a Savitzky-Golay filter.

4.5.5 Seismicity as an inhomogeneous Poisson process

With Dieterich's model (Section 4.5.4), the earthquakes are assumed to be fully characterized by the Coulomb stress transfer. That is, seismicity follows an inhomogeneous Poisson process with varying seismicity rates $R(t)/r$ governed by Equation 4.4. To test a posteriori if the observed seismicity follows an inhomogeneous Poisson process, we examine the distribution of times between consecutive seismic events Δt, hereafter referred to as the "interevent times." In this section, we continue to treat the observed seismicity as a point process and do not consider spatial information. All detected events in our catalog, including those not relocated, are used.

For a homogeneous Poisson process with a constant seismicity rate λ, the interevent times Δt are expected to distribute exponentially, i.e., $P(\Delta t) \sim \lambda e^{-\lambda \Delta t}$. For an inhomogeneous Poisson process with varying seismicity rates $\lambda(t)$, interevent times would appear on average to be shorter than the exponential distribution due to apparent clustering, as seen in the observed seismicity (Figure 4.13a). Any given inhomogeneous Poisson process can be converted to a homogeneous one if the evolving Poisson rates can be estimated. In our case, we can use the modeled seismicity rate $R(t)/r$ from Section 4.5.4 that uses Savitzky-Golay filter as a denoising method (Figure 4.12b,d). The interevent times of the converted homogeneous Poisson process, referred to as the "modified interevent times," can be calculated as follows: $\Delta t_{\text{modified}} = \Delta t_{\text{observed}} \cdot R(t)/r$, where $R(t)/r$ is the modeled seismicity rate. Using the modeled seismicity rate from Dieterich's model driven by the slow slip event (Figure 4.12b), the $\Delta t_{\text{modified}}$ follows better the exponential distribution (Figure 4.13b) than the $\Delta t_{\text{observed}}$ (Figure 4.13a). $\Delta t_{\text{modified}}$ follows even better the exponential distribution (Figure 4.13c) if the modeled seismicity rate from Dieterich's model driven by the total geodetic deformation (Figure 4.12d) is used. Regardless of the modeled seismicity rate used, $\Delta t_{\text{modified}}$ is still shorter than expected by the exponential distribution suggesting that some level of clustered seismicity exists and is not captured by the inhomogeneity of seismicity rates.

The amount of clustering beyond those expected from the Poisson process can be quantified by fitting the interevent times distribution with a Gamma distribution, $P(\Delta t) \sim C \cdot \Delta t^{\gamma-1} \cdot e^{-\Delta t/\beta}$, where $\mathrm{C} = (\beta^{\gamma}\Gamma(\gamma))^{-1}$ and $\Gamma(x)$ is a Gamma function. If the interevent times Δt are normalized so that $\bar{\Delta t} = 1$, the fraction of clustered events is simply $1 - \gamma$, where $\gamma = 1/\beta$ and β is the variance of the interevent times $\sigma^2_{\Delta t}$ (Hainzl et al., 2006, Molchan, 2005). The Gamma distribution can explain clustering typically expected for aftershocks, but it fails to capture clustering due to

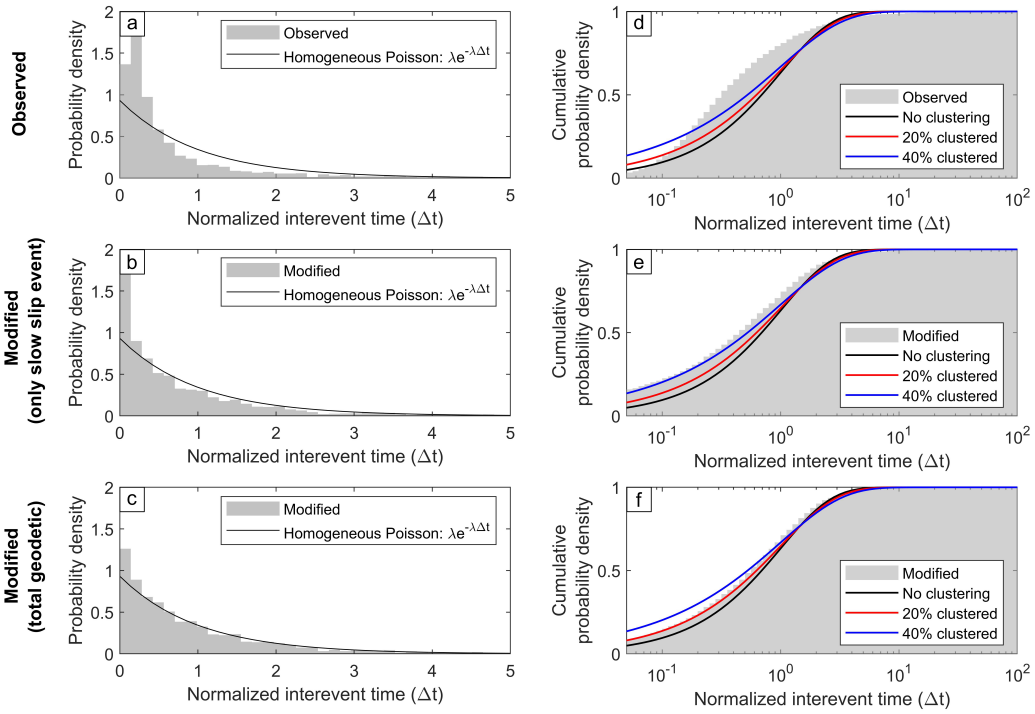

Figure 4.13: Statistics of times between seismic events. Comparison of the probability density of (a, d) the observed and the modified interevent times calculated by removing the inhomogeneity of seismicity rates using Dieterich's model driven by (b, e) the slow slip event and (c, f) total geodetic deformation which also includes the stress transfer from seismicity. The percentage of clustering is estimated using the Gamma distribution. This analysis does not consider spatial information and uses all detected events from this study, including those that are not relocated.

the inhomogeneity of Poisson rates (Figure 4.13d). After removal of inhomogeneous Poisson rates using the modeled seismicity rate from Dieterich's model driven by the slow slip event (Figure 4.12b), we find that $\Delta t_{\text{modified}}$ can be described by a Gamma distribution with $\gamma = 0.6$, meaning that the slow slip event can explain 60% of all events, leaving 40% of unexplained clustered events (Figure 4.13e). On the other hand, if the rates are taken from Dieterich's model driven by the total geodetic deformation (Figure 4.12d), $\Delta t_{\text{modified}}$ can be described by a Gamma distribution with $\gamma = 0.8$, meaning that the geodetic deformations (including both aseismic and seismic components) can explain 80% of all events, leaving only 20% unexplained clustered events (Figure 4.13f). The additional 20% of events explained by the total geodetic deformation but not by the slow slip event must then be explained by stress transfer from the seismic events, i.e., inter-earthquake static stress triggering.

To further assess the reliability of the amount of clustering, we assume that Dieterich's model perfectly fits the data and examine $\Delta t_{\text{modified}}$. If the seismicity perfectly follows an inhomogeneous Poisson process, $\Delta t_{\text{modified}}$ would be exactly exponentially distributed. Our analysis finds that this is not the case. Approximately 10% of $\Delta t_{\text{modified}}$ with shortest durations are missing (Figure B.30). Given that $\Delta t_{\text{observed}} < 15$ seconds near the peak seismicity, this is likely due to under detection. Further analysis using a temporal variation of coefficient of variations (Kagan and Jackson, 1991) supports this interpretation (Section B.3 and Figure B.31). Accounting for this 10% of missed events, stress transfer from the slow slip event can explain at least 55% and potentially up to 64% of all events. The total geodetic deformation can explain at least 73% and potentially up to 82% of all events, meaning that ~10 – 25% can be explained with inter-earthquake static stress transfer. The remaining ~20 – 30% unexplained clustered events must then be accounted for by a secondary driver (Section 4.5.7).

4.5.6 Improving the model with stress threshold

Even though Dieterich's model used in Section 4.5.4 can explain the overall evolution of the seismicity rate, it did not explain the sharp onset well. Previous studies have also encountered difficulty explaining the delayed onset and attributed it to the violation of the model assumptions that the system is well above the steady-state limit and is accelerating toward instability (Candela et al., 2019, Zhai et al., 2019). An introduction of thresholds in the form of critical stress (Bourne and Oates, 2017, Dempsey and Riffault, 2019, Dempsey and Suckale, 2017, Heimisson et al., 2022) or critical time (Zhai et al., 2019) can be implemented to improve the model. Introducing a critical time is a proxy for reducing a stress threshold that is valid if the stress changes are uniform in space. Here, we improve the model by adding a critical stress threshold τ_c to Equation 4.4 following the formulation by Heimisson et al. (2022):

$$\frac{R(t)}{r} = \begin{cases} 0 & \text{if } t < t_c \\ \dfrac{e^{\left(\frac{\Delta\tau(t)-\Delta\tau_c}{a\sigma}\right)}}{1+\frac{1}{t_a}\int_{t_c}^{t} e^{\left(\frac{\Delta\tau(x)-\Delta\tau_c}{a\sigma}\right)} dx} & \text{if } t \geq t_c \end{cases} \tag{4.5}$$

where t_c is the time when the stress threshold is first exceeded, i.e., $\Delta\tau(t = t_c) = \Delta\tau_c$. With this modification, the longer time lag between the slow slip event and seismicity can be accounted for by increasing the stress threshold (Figure B.32). By minimizing

the root-mean-squared error (RMSE) over the swarm duration using a grid search, the best model yields a negligible threshold (< 1 kPa). If we minimize the RMSE over only the first seismicity peak (up to the first day of the swarm), we find $\Delta\tau_0/a\sigma = \Delta\tau(t = \infty)/a\sigma = 74$, $\Delta\tau_c/a\sigma = 18$ and $t_a = 1.1$ yr (Figure B.33), and the model better captures the seismicity's sharp onset (Figure 4.14a). Using the average dCFS of 30 kPa (Figures 4.8a and 4.10c-d) induced by the slow slip event at locations where we have earthquakes as $\Delta\tau_0$, we find $a\sigma$ ~0.4 kPa and hence $\Delta\tau_c$ ~7.3 kPa, a factor of 4 smaller than $\Delta\tau_0$.

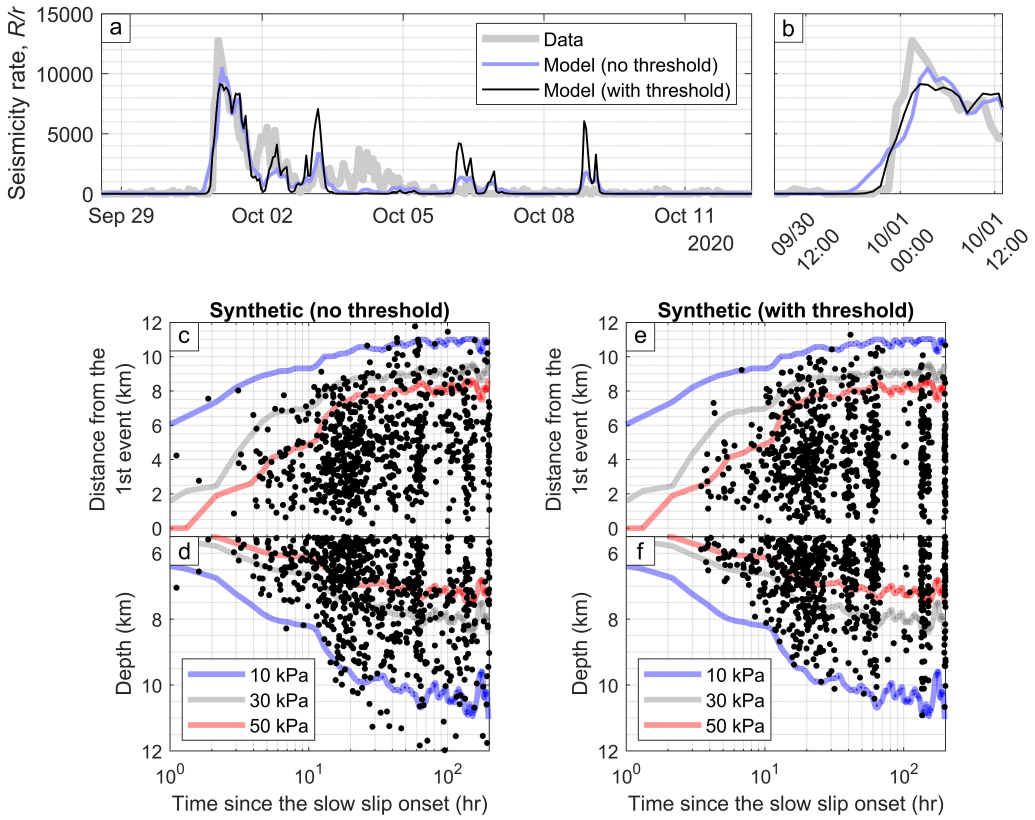

Figure 4.14: Effects of a stress threshold. (a) Modeled seismicity rate driven by total geodetically resolved deformation using stress-driven models based on Dieterich's nucleation (Dieterich, 1994) with and without stress threshold (Heimisson et al., 2022). (b) is a zoomed-in version of (a). Two-dimensional synthetic seismicity catalogs are generated using the best fit parameters for the (c-d) model without a threshold and (e-f) the model with a threshold. The spatial distribution of dCFS on fault plane F1 (Figure 4.10a) is plotted in panels c-f in the same way as Figures 4.10c-d. The onset of the slow slip event is picked to be ~8 hr before the start of the swarm.

To further assess the models, we generate two-dimensional synthetic catalogs of earthquakes along the fault plane F1. The driving dCFS is allowed to vary spatially along plane F1 (Figure 4.10a) and temporally according to the filtered aseismic moment release (Figure 4.12a). For each gridded cell, we calculate the expected seismicity rate using the best fit parameters from our models (Figure 4.14a), and seismicity is generated using the inverse transform sampling method (e.g., Zhuang and Touati, 2015). We refrain from using the total geodetically resolved slip in this analysis because our model does not capture the non-stationary nature of fault slip. We can better reproduce the spatial expansion of seismicity by enforcing the early part of fault slip to be a shallow slow slip event, as evident from comparing the spatial distribution of seismic and geodetic cumulative moment release (Section 4.4.2). Since Dieterich's model is highly non-linear, the response to the time evolution of the integrated slip in space is not equal to the integrated response to the time evolution of slip at different spatial locations. Therefore, we cannot expect the number of events in the synthetic catalogs to match the observed catalogs. However, the synthetic catalogs can still capture first-order behaviors, such as the rapid expansion of seismicity and the time lag between the onset of the slow slip event and the swarm (Figure 4.14b-e). We find the time lag from the model that includes a stress threshold more consistent with observations. Furthermore, we notice that the synthetic models cannot capture sharp boundaries that mark the extent of seismicity because of the smoothing imposed on the geodetic slip model used to calculate dCFS and the assumption that the seismicity productivity (the density of triggered earthquakes per unit of Coulomb stress increase) is homogeneous.

4.5.7 Pore-pressure diffusion as a secondary driver

Even though the swarm lasted for about 6 days, our geodetic observations find no significant surface deformation after the first day of the swarm. This, along with the poorer fit of the stress-driven model (Section 4.5.4 and Figure 4.12g) and the clustering behaviors (Section 4.5.5 and Figure B.31), suggests that the latter phase of the swarm was driven by a secondary mechanism unrelated to the observed slow slip event. Abundant fluids in this hydrothermal area (Deane and Lynch, 2020) and the observation of a propagating back front marking an expansion of a zone of seismicity quiescence (Figures 4.5d and 4.15a), which is commonly observed in borehole fluid injection scenarios after the injection has terminated (e.g., Dahm et al., 2010, Parotidis et al., 2004, 2005, Shapiro and Dinske, 2009), leads us to propose pore-pressure diffusion as a possible secondary driver of the swarm.

With a point source fluid injection, we expect a leading seismicity front following the pore-pressure diffusion front with a square root of time expansion after the injection has started and a trailing propagating back front after the injection has terminated. A simple two-dimensional diffusive model (Parotidis et al., 2004) predicts that the back front $r_{\text{back}}(t)$ would expand as a function of time t according to the following equation:

$$r_{\text{back}}(t) = \sqrt{4 \cdot D \cdot t \cdot \left(\frac{t}{t_0} - 1\right) \cdot \ln\left(\frac{t}{t - t_0}\right)} \tag{4.6}$$

where D is the hydraulic diffusivity and t_0 is the injection duration.

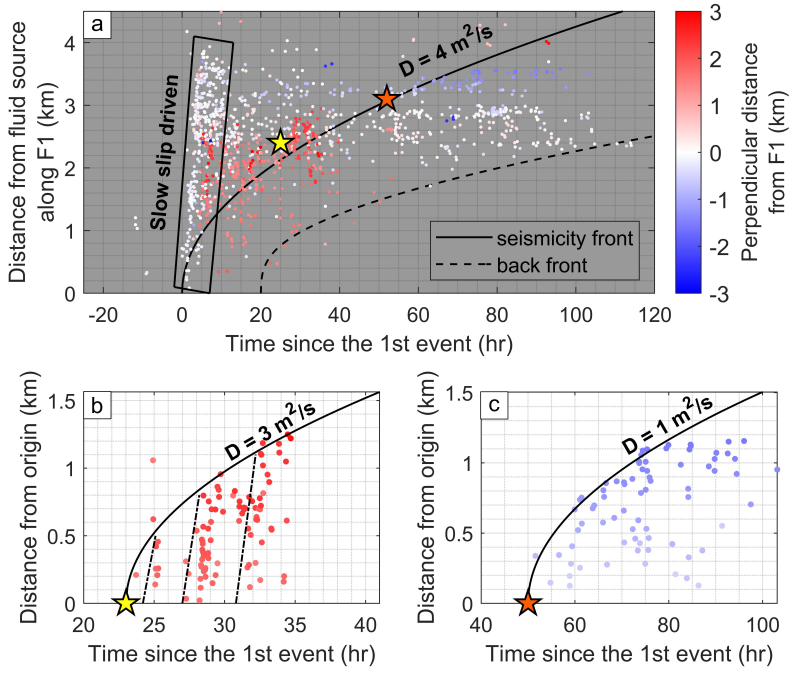

Figure 4.15: Pore-pressure diffusion as a secondary driver. (a) Expansion of seismicity along the 162°-striking main fault F1 (see geometry in Figure 4.5a) and along the en-echelon structures (b) E1 and (c) E2 (blue boxes in Figure 4.5a). The yellow and red stars are the inferred origin of expansion along the en-echelon structures. Seismic events here are from our relocated catalog, and they are all color-coded by the perpendicular distance from F1. For structure E1, the rapid expansion of seismicity at 25, 28, and 32 hr within the diffusive front are observed (dashed lines, panel b).

The back front is visible in our observations, but the leading front is not clear (Figure 4.15a). We attempt to fit the back front, assuming that the pore-pressure diffusion is mainly constrained along the 162°-striking main fault F1. A possible set of parameters that would fit well the back front include an injection location that is < 1 km from the first relocated seismic event, a diffusivity of 4 m^2/s, and an injection duration of 20 hr. The inferred leading seismicity front, $r_{\text{front}}(t) = \sqrt{4\pi Dt}$, passes through the inferred origins (yellow and red stars in Figure 4.15) of seismicity expansion observed along the en-echelon fractures (structures E1 and E2 in blue boxes of Figure 5a with associated seismicity expansion annotated in Figure 4.5g). Given the proximity between the inferred injection location and the first seismic event, pore-pressure diffusion could be initiated by a seal that was broken because of the same stress changes that triggered the seismicity, similar to the scenario proposed for the Cahuilla swarm (Ross et al., 2020). Then, the en-echelon fractures were reactivated as the pore-pressure diffusion front arrived. However, given the obscured leading seismicity front, it is also plausible that fluids may have pre-existed in the main fault zone. The seals to the en-echelon fractures could then have broken arbitrarily in time, draining the fluids from the main fault zone and leading to the seismicity back front. The over-pressurized fault could also explain the poorer fit to Dieterich's model because normal stress changes may be larger relative to the effective normal stress, violating one of the model assumptions.

Upon reactivation of the en-echelon fractures, seismicity on these structures appears to expand as $\sqrt{t}$ with inferred hydraulic diffusivities ranging from $1-3$ m^2/s (Figure 4.15b-c), slightly different from the 4 m^2/s inferred for the main fault. The different diffusivities and hence the different permeabilities between the main fault and the en-echelon structures suggest that this fault zone is anisotropic, which could be caused by stress levels on the faults (e.g., Acosta et al., 2020), or geometry and maturity of the structures (e.g., Acosta and Violay, 2020, Caine et al., 1996, Jeanne et al., 2013).

The diffusivity values over the entire fault zone range from $1-4$ m^2/s, consistent with other swarms with a duration of a few days (Amezawa et al., 2021). This corresponds to permeabilities $\sim 10^{-12} - 10^{-14}$ m^2 and porosity $\sim 0.01 - 0.2$ (Figure B.34), similar to the values inferred from fluid-driven seismicity in other regions (e.g., Amezawa et al., 2021, Audin et al., 2002). These inferred permeabilities are quite large for intact rocks, but they are not unexpected for fractured metasedimentary rocks (e.g., Wong et al., 2013, Younker et al., 1982), particularly at low effective normal stresses

(e.g., when pressurized fluids have permeated the fracture). In fractures subjected to low effective normal stress, fault slip can increase permeability by more than one order of magnitude (e.g., Guglielmi et al., 2015, Im et al., 2018, Lee and Cho, 2002, Yeo et al., 1998) due to low mechanical closure and low wear production rates, though this is not the case for fractures subjected to high effective normal stress (e.g., Acosta et al., 2020, Rutter and Mecklenburgh, 2018). The rapid migration of seismicity streaks (at times 25, 28, and 32 hr in Figure 4.15b) resembles features observed in other swarms, and that could be evidence of coupling between pore-pressure diffusion and the slow slip events (e.g., De Barros et al., 2020, Dublanchet and De Barros, 2021) that were too insignificant to detect with current geodetic instrumentations. The velocities of these rapid migrations are between 0.6 – 0.8 km/hr, which is the same order-of-magnitude as the slow slip driven seismicity front observed along the main fault F1.

Because there is only minor inter-earthquake triggering (Sections 4.5.1 and 4.5.4), we can exclude the cascade model of earthquakes (Helmstetter and Sornette, 2002a) as a cause of the observed migration of the seismicity. Additionally, such a model would not produce a back front. Another possible interpretation of this zone of seismicity quiescence is stress shadow resulting from negative dCFS (Harris and Simpson, 1996, 1998, 2002). However, since most of the total dCFS was due to the slow slip event and large earthquakes that occurred within the first day of the swarm, this mechanism cannot explain how this zone continued to grow at a much later time. Therefore, we interpret that the slow slip event drove the early part of the sequence and fluid drove the latter, similar to the aftershocks of the 2010 M_w 7.2 El Mayor-Cucapah earthquake (Ross et al., 2017).

4.5.8 Estimating the friction parameter and stress conditions

Some fault properties, such as the frictional rate-and-state parameter a responsible for the nucleation process, cannot typically be measured in situ and require extrapolation from laboratory measurements (Marone, 1998a). Other properties, such as the effective normal stress σ, in-situ measurements are possible at shallow crustal depth but are very costly (e.g., Guglielmi et al., 2015). Studying the seismicity response to a known stress perturbation offers the possibility of estimating the product of the fault frictional rate-and-state parameter a and the in-situ effective normal stress σ, providing constraints on fault properties. Some studies have estimated these parameters using seismicity responses to magmatic intrusions (Toda et al., 2002), solid Earth tidal or seasonal oscillations (Ader and Avouac, 2013, Bettinelli

et al., 2008), reservoir loading (Rinaldi et al., 2020), slow slip events (Lohman and McGuire, 2007, Segall et al., 2006), or afterslip (Cattania et al., 2015). In this study, fitting seismicity rates with Dieterich's models with and without stress threshold gives us the parameter $\Delta\tau_0/a\sigma$ (Table 4.2). Using the average dCFS induced by the slow slip event at locations where we have earthquakes (~30 kPa, see Figures 4.8a and 4.10c-d) as $\Delta\tau_0$, we can calculate the corresponding product $a\sigma$ (Table 4.3).

Methods	$a\sigma$
Dieterich's model of the 2020 Westmorland swarm (Section 4.5.4)	1.2 kPa
Dieterich's model with stress threshold of the 2020 Westmorland swarm (Section 4.5.6)	0.4 kPa
Annual hydrological loads, using dCFS from Kreemer and Zaliapin (2018)	0.1 kPa
Annual hydrological loads, using dCFS from this study	< 10 kPa
Semi-diurnal 12-hr tidal cycles, using dCFS from *Solid* software	> 2.5 kPa

Table 4.3: Estimated values of the parameter $a\sigma$ using independent methods based on seismicity responses to different types of transient driving stresses.

The estimates of parameter $a\sigma$ from this study are between 0.4 – 1.2 kPa (Table 4.3), which is relatively small. For example, if we assume $a \sim 0.001$, a lower bound value typical of laboratory measurements (Marone, 1998a), and use the overburden normal stress at 5 km of ~150 MPa, we expect $a\sigma$ ~150 kPa. This suggests that either pore pressure is very large (99% of overburden stress), or the faults in the basement would have very small a (~0.00001), or a combination of both factors. Smaller a means that the earthquakes can nucleate with smaller driving stress.

To further validate our estimates of a, we compare them with independent order-of-magnitude inferences using responses of seismicity to semi-diurnal (12-hr) tidal and annual hydrological stressing, which have been observed in natural faults (e.g., Ader and Avouac, 2013, Cochran et al., 2004, Tanaka et al., 2002, Wang et al., 2022, Wilcock, 2001) and in the laboratory (e.g., Bartlow et al., 2012, Beeler and Lockner, 2003, Chanard et al., 2019, Noël et al., 2019). We expect a larger response for smaller $a\sigma$ (e.g., Ader et al., 2014, Beeler and Lockner, 2003, Heimisson and Avouac, 2020). To estimate the periodic variations of seismicity rate in the Westmorland area (latitude 32.98 – 33.12°N, longitude 115.50 – 115.65°W), we use the Quake Template Matching (QTM) seismicity catalog (Ross et al., 2019a). Since aftershocks are seismicity responses to the stress changes from the mainshocks, which

are non-periodic, we first remove them by using the nearest-neighbor declustering approach (Zaliapin and Ben-Zion, 2013a, Zaliapin and Ben-Zion, 2020) based on a space-time-magnitude metric (Baiesi and Paczuski, 2004, Zaliapin et al., 2008) with a Gutenberg-Richter b-value estimated using maximum likelihood (Aki, 1965), as detailed in Section B.4 and Figure B.35. Then, we determine the amount of seismicity rate variation for a given periodicity using the Schuster p-value (Ader and Avouac, 2013, Schuster, 1897) and estimate the parameter $a\sigma$ (Table 4.3) that best relates the periodic stressing to the observed seismicity rate variation (Ader et al., 2014), as detailed in Section B.5 and Figures B.36 - B.37. For annual period, seismicity rate variation is ~24%. Using the seasonal geodetic strains in Southern California of ~0.02 kPa (Kreemer and Zaliapin, 2018), we find $a\sigma$ ~0.1 kPa. These seasonal strains are relatively small when comparing to similar studies (e.g., Amos et al., 2014, Johnson et al., 2017b), likely due to over smoothing. Alternatively, we can also use seasonal geodetic strains estimated from this study (IC7 in Figure B.7). Without smoothing, displacements vary ~1 mm over 10 km of distances, resulting in an upper bound of geodetic strains of 10^{-7}, which translates to $a\sigma < 10$ kPa. For semi-diurnal (12-hr) period, seismicity shows insignificant periodicity with variations < 26%. Using the semi-diurnal tidal strains of ~0.6 kPa estimated from surface displacements computed with Solid software (Milbert, 2018), as detailed in Section B.6 and Figures B.38 - B.39, we find $a\sigma > 2.5$ kPa.

To conclude, the analysis of the 2020 Westmorland swarm provides local estimates of $a\sigma$ ~0.4 – 1.2 kPa along with the patches of observed seismicity, while the hydrological and tidal analysis provides regional estimates of $a\sigma$ ~2.5 – 10 kPa. While they are within one order-of-magnitude from one another, one way to interpret the differences is to attribute parts of the faults that ruptured during the 2020 Westmorland swarm to be weaker (smaller $a\sigma$) than the surrounding areas, making them closer to failure and requiring less amount of driving stress to rupture. This weak zone might be related to the extent of the reservoir with pressurized fluid (and hence with lower effective normal stress σ) bounded by impermeable rock layers.

Many studies utilizing Dieterich's model find a similar range of $a\sigma$ between 1 – 40 kPa for various tectonic settings (Table 4.4), which is unexpectedly small. Recent dynamic simulations of two-dimensional finite faults found that the assumption of Dieterich's model that the product of slip velocity V and the state variable θ is large compared to the critical slip distance D_{RS}, i.e., $V\theta/D_{RS} \gg 1$, is often violated (e.g., Rubin and Ampuero, 2005), and as a result, the one-dimensional spring-slider

system approximation leads to underestimation of $a\sigma$ by 1 – 2 orders of magnitude (Ader et al., 2014, Kaneko and Lapusta, 2008). Using a more realistic estimate of $a\sigma$ ~50 kPa (~100 times our low bound of 0.4 kPa and ~5 times our upper bound of 10 kPa) and best fitted t_a ~1.7 yr (Table 4.2), we estimate the background stressing rate $\dot{\tau}_a = a\sigma/t_a$ ~30 kPa/yr. This is consistent with the estimates using maximum total shear strain rate of ~1 μstrain/yr from GPS observations (Crowell et al., 2013), and an assumed shear modulus of 30 GPa resulted in a long-term stressing rate $\dot{\tau}$ ~30 kPa/yr.

Methods	Estimated $a\sigma$
Aftershocks of the 1992 M_w 7.3 Landers, California earthquake (Gross and Kisslinger, 1997)	20 - 40 kPa
Aftershocks of the 1989 M_w 7.0 Loma Prieta, California earthquake (Gross and Bürgmann, 1998)	10 kPa
Aftershocks of the 2004 M_w 6.0 Parkfield, California earthquake (Cattania et al., 2015)	3 - 8 kPa
Aftershocks of the 2011 M_w 9.0 Tohoku, Japan earthquake (Cattania et al., 2015)	20 - 40 kPa
Izu volcanic island earthquake swarm, Japan (Toda et al., 2002)	30 kPa
Seasonal strains in the Himalayas (Bettinelli et al., 2008)	30 kPa
Reservoir-induced seismicity, Val d'Agri area, Italy (Rinaldi et al., 2020)	0.8 kPa
The 2020 Westmorland, California earthquake swarm (this study)	0.4 - 1.2 kPa
Seasonal strains and solid Earth tides, Westmorland, California (this study)	2.5 - 10 kPa

Table 4.4: Estimated parameter $a\sigma$ for different studies of various tectonic settings based on the seismicity response to transient stresses.

4.6 Discussion

4.6.1 Summarizing the 2020 Westmorland swarm and the mechanisms involved

We conclude that the 2020 Westmorland swarm resulted from the interplay between a slow slip event, fluid diffusion, and seismic slip, as summarized in Figure 4.16. The event began with an episode of shallow slow slip event (Section 4.4.2) occurring in the sedimentary cover, which induced a static stress change front that propagated as a logarithm of time (Section 4.5.3). Such stress change then drove the most critically stressed fault patches in the basement to rupture, forming a swarm of primarily non-interacting seismic events (Sections 4.5.4 – 4.5.6) that also expanded logarithmically with time (Section 4.5.3). A pore-pressure diffusion front could have started to expand as the square root of time after the stress change front broke the seal containing a pressurized fluid pocket. Upon reaching pre-existing en-echelon fractures orthogonal to the main fault, pressurized fluid continued to migrate along these fractures causing seismicity on these structures that expanded diffusively as a square root of time with different apparent hydraulic diffusivities (Section 4.5.7). After the fluid pressure stabilized, seismicity terminated. As this zone of stability expanded as the square root of time, we observed a propagating back front marking the zone of seismicity quiescence (Section 4.5.7). The swarm terminated within ~5 days, but the fits to seismicity using the stress-driven model with Dieterich's nucleation (Section 4.5.4) suggest that aftershocks should continue for ~1.7 yr because of the time-dependent frictional response of faults. Using results from two independent analyses, static stress triggering (Section 4.5.1) and seismicity rate modeling with stress-driven models (Section 4.5.4 – 4.5.5), suggest that 45 – 65% of seismicity was driven by the slow slip event, 10 – 35% by inter-earthquake static stress transfer, and 10 – 30% by fluid pressure changes.

We also find that lithology plays a significant role in determining the slip modes. The sedimentary cover (the top 5 km) primarily slips during aseismic slip events, while the shallow portion of the basement (between 5 – 8 km depth) primarily slips during earthquakes. Below this seismogenic zone (depth > 8 km), the faults are probably mostly creeping from ductile deformation. For continental crust with strain rates of $\sim 10^{-14}$ s, we expect the brittle-ductile transition (BDT) to occur at a temperature of ~400 ± 100°C (Violay et al., 2017). With a geothermal gradient of ~50 - 60 ºC in the Westmorland area (Lachenbruch et al., 1985), the BDT is expected at 7 – 8 km depth, consistent with the observations. Furthermore, the observed deformation modes are consistent with the interseismic model based on geodetic data, which has

a surface aseismic creep of 2.7 mm/yr and a locking depth of ~10 km (Lindsey and Fialko, 2013). Earthquakes from the decades-long catalogs (e.g., Lin et al., 2007) are primarily within the 5 – 8 km depth range.

Finally, we try to estimate the contribution of swarms to long-term deformation. For example, if we compare the long-term slip rate of 17 mm/yr (Crowell et al., 2013) across the fault system with the average slip of ~20 mm during the swarm, a return period of ~1 year would be needed if slip was only releasing as a result of repeated swarms similar to the Westmorland swarm of 2020. However, the seismicity catalog of Southern California clearly shows that the swarms do not return that frequently at Westmorland (Figure 4.1b). This disparity can be partially explained by the observation that the 2020 Westmorland swarm released less moment than a typical

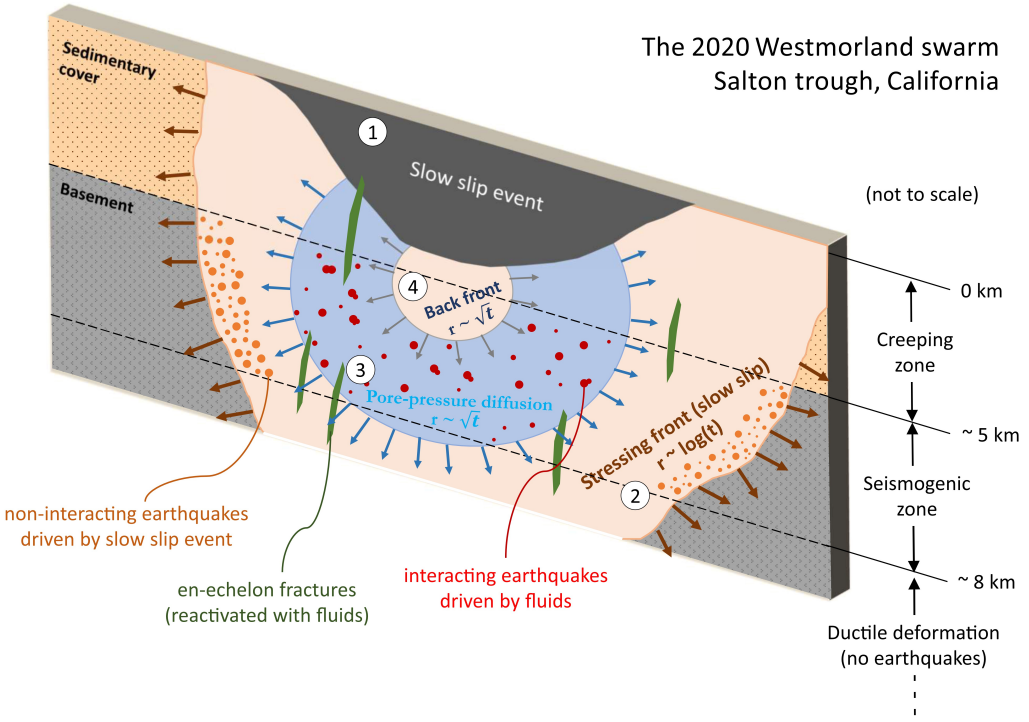

Figure 4.16: A schematic diagram summarizing the mechanics of the 2020 Westmorland swarm. The sequence started with (1) a spontaneous shallow slow slip event, which preceded the swarm by 2 – 15 hours. The slow slip event produced (2) Coulomb stress changes front propagating non-linearly as a logarithm of time, triggering non-interacting earthquakes along the main fault. Behind this stressing front, there was (3) a pore-pressure diffusion front which drove seismicity on the main fault and reactivated seismicity on the en-echelon structures (green). Finally, (4) a propagating back front marked the termination of pore-pressure diffusion and the expansion of the zone of seismic quiescence.

swarm in the area (e.g., Lohman and McGuire, 2007, Wei et al., 2015). Moreover, it may be possible that significant aseismic slip occurs in the period between swarms, either as a result of smaller episodic slow slip events or continuous creep.

4.6.2 Swarm as aftershocks of the slow slip event

The 2020 Westmorland swarm appears quite similar to afterslip-driven sequences of aftershocks (e.g., Perfettini and Avouac, 2007, Perfettini et al., 2018) but with the mainshock replaced by a slow slip event. The observed geodetic deformation associated with the 2020 Westmorland swarm shows rapid onset followed by deceleration (Figure 4.4), similar to the time evolution of afterslip (e.g., Ingleby and Wright, 2017, Marone et al., 1991, Perfettini and Avouac, 2004). The 2020 Westmorland swarm was also observed to expand logarithmically with time (Section 4.5.3), similar to the expansion of afterslip-driven aftershocks following large earthquakes (e.g., Frank et al., 2017, Kato and Obara, 2014, Peng and Zhao, 2009, Tang et al., 2014). For a sequence driven by a slow slip event that can be modeled with a logarithm function, the aftershocks are expected to expand as $\log(t)$ regardless of whether there is a mainshock before the slow slip event or not (Perfettini et al., 2018). Once the slow slip event starts, the mechanisms that govern the evolution of swarms might be the same as those that drive aftershocks.

There are other swarms that have also been interpreted as aftershocks of slow slip events (e.g., Lohman and McGuire, 2007, Martínez-Garzón et al., 2021, Segall et al., 2006), but direct observational evidence in support of that interpretation is rare. This could be a common mechanism for swarms that would have gone unnoticed. Several studies provided evidence of aseismic deformation related to the swarm using radar interferometry, GPS, optical leveling data, or strainmeters (e.g., Kyriakopoulos et al., 2013, Lohman and McGuire, 2007, Wei et al., 2015, Wicks et al., 2011), but none had the time resolution needed to identify if the aseismic event preceded the swarms. Others have inferred aseismic forcing from seismicity data (Llenos and McGuire, 2011, Marsan et al., 2013). Detecting the preceding slow slip event, such as the one observed during the 2020 Westmorland swarm, requires access to high-rate GPS records in the near-field and the relatively sophisticated postprocessing of the geodetic time series. With limited observations thus far, it is uncertain whether the mechanics discussed in this study would generalize to other swarms in the Salton Trough or other tectonic settings worldwide.

4.7 Conclusions

The 2020 Westmorland swarm in the Salton Trough was exceptionally well-recorded by a dense array of seismometers, ground-based GPS/GNSS sites, and space-based radar interferometry, allowing us to describe the earthquake sequence with unprecedented details (Section 4.3). Our study provides evidence of a slow slip event starting between 2 – 15 hours before the swarm sequence (Section 4.4). We demonstrate their causal relationship using static stress triggering analysis (Sections 4.5.1 – 4.5.3) and Dieterich's stress-driven seismicity model based on rate-and-state friction (Sections 4.5.4 – 4.5.6). The model successfully explains the overall spatial and temporal evolution of seismicity, including the time lag between the slow slip event and seismicity, and provides constraints on the rate-and-state friction parameter a and pore pressure (Section 4.5.8). We have also identified pore-pressure diffusion as a secondary driver which sustains the swarm sequence, as supported by the existence of propagating back front and the square root of time expansion of reactivated seismicity along the orthogonal en-echelon structures (Section 4.5.7). Our analysis also allows us to quantify the relative contributions of the different mechanisms described: 45 – 65% of seismicity was driven by the slow slip event, 10 – 35% by inter-earthquake static stress transfer, and 10 – 30% by fluids (Section 4.6.1). Our observations and modeling results are consistent with the interpretation of this swarm as aftershocks of a slow slip event sustained by fluid flow (Section 4.6.2).

Chapter 5

EARTHQUAKE NUCLEATION PROCESS REVEALED BY MODULATION OF SEISMICITY RATE IN CALIFORNIA DRIVEN BY TECTONIC, HYDROLOGICAL, AND TIDAL LOADING

To be submitted as:

K. Sirorattanakul, and J.-P. Avouac. Earthquake nucleation process revealed by modulation of seismicity rate in California driven by tectonic, hydrological, and tidal loading.

Abstract

Seismicity in California is primarily driven by tectonic loading. Stress changes induced by seasonal water storage seem to cause seasonal modulation of seismicity rate. Here, we develop a workflow to identify and quantify regions with significant seasonal modulations of seismicity rate. We find stronger modulation in northern California than in southern California, with a few localized regions associated with hydrothermal systems dominating the response. The seasonal seismicity amplitude shows a clear correlation with seasonal stress amplitudes. The peak seismicity rate occurred 0.5 – 2.5 months after the peak stress rate reflecting the non-instantaneous nature of the earthquake nucleation process. The observed seismicity response to seasonal loading shows that earthquake nucleation is not instantaneous. The observed damped response to the harmonic stress variations due to tides and hydrology is found quantitatively consistent with a nucleation process driven by rate and state friction. We constrain the friction-stress parameter to be of the order of 3-6 kPa.The characteristic time scale of earthquake nucleation is estimated to be between 0.05 and 0.7 yr.

5.1 Introduction

The earthquake rates are known to fluctuate with time according to changes in the driving stress in the Earth's crust. Understanding how seismicity responds to transient stress can elucidate the process controlling earthquake nucleation and can be used to probe friction parameters and effective normal stress (Acosta et al., 2023, Dieterich, 1994, 2007, Segall et al., 2006, Sirorattanakul et al., 2022b). The

transient stress can originate from various sources. One example is the stress change from a large earthquake (a few MPa), which is typically the main driver of aftershock sequences (Dieterich, 1994, King et al., 1994). Other sources of transient stress that could modulate earthquake rates include hydrological surface loading and poroelastic stress associated to seasonal changes in water storage and snowpack (Bettinelli et al., 2008, Carlson et al., 2020, Johnson et al., 2017b, Kang and Knight, 2023, Ueda et al., 2024), Earth tides due to changes of gravitational forces of the Sun and the Moon and ocean loading (Bucholc and Steacy, 2016, Cochran et al., 2004, Scholz et al., 2019, Tanaka et al., 2002, Vidale et al., 1998, Wilcock, 2001), spontaneous slow aseismic slip and postseismic afterslip (Lohman and McGuire, 2007, Perfettini and Avouac, 2004, Sirorattanakul et al., 2022b), and other anthropogenic factors related to geoenergy production (Acosta et al., 2023, Heimisson et al., 2022). Stress changes due to hydrological surface loading are only a few kPa, much smaller than a typical stress drop of 3 MPa for earthquakes, but they are known to significantly modulate earthquake rates in different regions around the world including the Himalayas (Bettinelli et al., 2008, Bollinger et al., 2007), California (Dutilleul et al., 2015, Johnson et al., 2017a,b), New Madrid Seismic Zone (Craig et al., 2017), East African rift (Xue et al., 2020), and Lake Biwa in Japan (Xue et al., 2021). Earth tides also produce stress changes of similar amplitudes, but they are known to modulate earthquake rates only in small areas and often to lesser extent than the modulation from hydrology (Bucholc and Steacy, 2016, Cochran et al., 2004, Vidale et al., 1998, Wang et al., 2022, Wilcock, 2001).

The responses of seismicity to harmonic stress perturbations can be studied using various models. The simplest instantaneous Coulomb failure model (CFM), in which the seismicity rate is assumed to be proportional to the stress rate, predicts larger responses for tidal than seasonal periods. In contrast, the spring-slider rate-and-state model (SRM) accounts for the non-instantaneous nature of earthquake nucleation and predicts similar responses for tidal and annual periods but larger phase lag between peak seismicity rate and peak stress rate for tidal periods (Ader et al., 2014, Beeler and Lockner, 2003). While the SRM is more consistent with the observations than CFM, it still cannot explain the lack of tidal responses. Potential explanations could be that the SRM neglect the finite fault effects (Ader et al., 2014) and the ability to detect periodic modulation is period-dependent (Ader and Avouac, 2013).

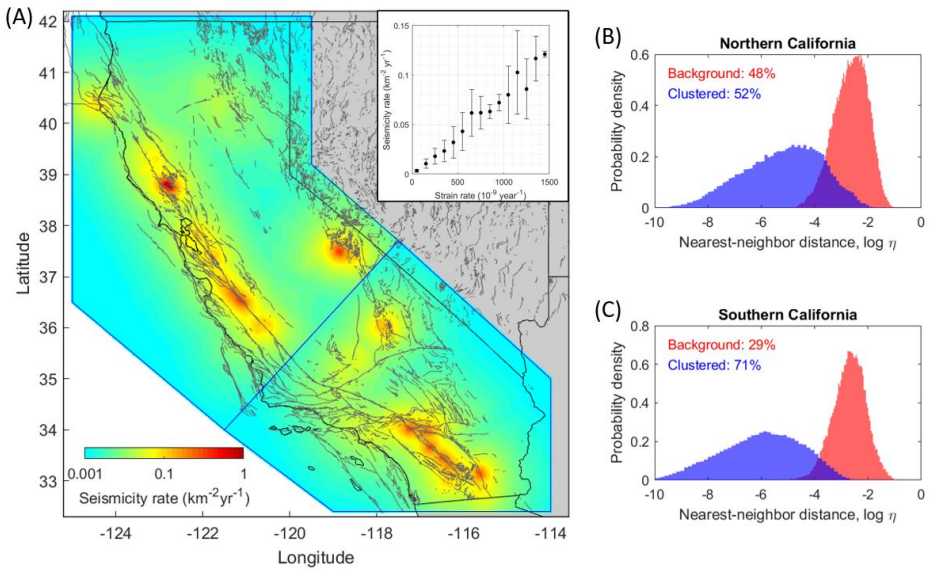

Figure 5.1: Rates of independent earthquakes in California. (A) Earthquakes with magnitude $M \geq 1$ from 2006 – 2023 are taken from the NCSS catalog (NCEDC, 2014) and the HYS catalog (Hauksson et al., 2012) for Northern and Southern California, respective (blue boxes). Aftershocks are removed from the catalogs using the nearest-neighbor distance approach (Zaliapin and Ben-Zion, 2013a) with spatially varying mode separator and the rates of remaining independent background events are shown. The inset shows the correlation between rates of independent earthquakes and the strain rate (second invariant, $J_2 = \sqrt{\epsilon_{xx}^2 + \epsilon_{yy}^2 - 2\epsilon_{xy}^2}$) determined from geodetic measurements (Kreemer et al., 2014). (B-C) The distribution of the nearest-neighbor distances for the independent events and aftershocks for Northern California (excluding events from the Geysers geothermal field for visualization purposes) and Southern California, respectively.

In this study, we analyze the variations in space and time seismicity in California (Figure 5.1) in relation to tectonic, hydrological, and tidal loading. We identify and quantify regions in California with significant seasonal modulations of seismicity rate and explore the extent to which they could be explained by changes in hydrological surface loading. The strong seasonal surface loads in California (Amos et al., 2014, Johnson et al., 2017a,b) along with a well-maintained seismicity catalog (Hauksson et al., 2012, NCEDC, 2014) provide a unique opportunity to investigate whether the response is dominated by a certain area or whether it is a regional response. By evaluating and relating the amplitudes and phases of the driving stress and the responses as seismicity rate variations, we can constrain the earthquake nucleation process.

5.2 Background seismicity and strain rate

We consider earthquakes occurring between 2006 and 2022 in California with magnitude $M \geq 1$ (Figure 5.1A). Since we are interested in earthquakes that are directly induced by periodic stressing and not from stress induced by other large earthquakes, we first identify and remove clustered events such as aftershocks and swarms. We develop an improved declustering method based on nearest-neighbor distance approach. Instead of using one cutoff value to distinguish independent events from the clustered events, we allow this value to vary in space (Figure C.1; Section C.1.2). Consequently, we can separate the overlapping regions of the two modes (Figure 5.1B-C). We evaluate the declustering results a posteriori using the coefficient of variations (CoV) (Kagan and Jackson, 1991), computed as the ratio of the standard deviation and the mean of interevent times. For a perfectly random process (Poissonian), CoV will be very close to 1. In our case, the original catalog contains regions with large CoV exceeding 5. After declustering, the mean CoV value is 1.1 (Figure C.2). Approximately two-third of all $M \geq 1$ events were identified as aftershocks or swarms.

The rates of remaining independent background events are concentrated along mapped faults where tectonic strain rate is high (Figure 5.1). The linear correlation between background seismicity rate and strain rate is consistent with the instantaneous Coulomb model and suggests that the model can explain the long-term seismicity rate, at least to the first order. The non-instantaneous nature of earthquake nucleation is not visible when considering the relation between seismicity rate and strain rate at the decadal timescale of this analysis, which is presumably much larger than the characteristic time of earthquake nucleation.

5.3 Seasonal modulation of seismicity rate

To quantify the amplitudes of seasonal modulation of seismicity rate, we employ the Schuster tests. In particular, we perform a successive walk of unit length steps in the direction according to the time of year each earthquake occurred. The total drifting distance between the origin and the end point of the walk relates to the Schuster p-value and quantifies the probability that seismicity rate is uniform. Larger drifting distance results in smaller the p-value, and hence lower probability that the seismicity rate in uniform. Assuming that the variations is harmonics, the Schuster p-value directly relates to the amplitude of the modulation of the seismicity rate $\alpha = \Delta R/R$, where R is the average seismicity rate and ΔR is half of the peak-to-peak amplitude of the seismicity rate variation (Section C.1.3).

Our analysis reveals multiple regions with strong seasonal modulation of seismicity (Figure 5.2A), but no regions with statistically significant tidal modulation (Figure C.3). The seasonal modulation is much stronger for northern California than in southern California (Figure 5.2A). To the first order, these modulations are driven by the hydrological surface loadings as a result of changes in groundwater levels and snowpacks between the wet and dry seasons, which can cause changes up to 5 – 10 mm of vertical surface displacements (Amos et al., 2014, Johnson et al., 2017a,b). Other indirect effects such as the poroelastic responses are confined to smaller areas such as the sedimentary basins and aquifers and have different phases of peak stress rate (Kang and Knight, 2023), which do not dominate the seasonal stress changes in the regional scale and can generally be neglected. Here, we estimate the seasonal amplitudes of Coulomb stress changes on the optimally oriented plane due to surface loading using a seasonal water storage model from Argus et al. (2022) and a semi-analytical function of a vertical point load acting on an elastic half-space (Section C.1.4). Our calculations reveal larger Coulomb stress amplitudes for northern California than southern California (Figure 5.2B). To further evaluate the consistency of seismicity modulation throughout the different years, we examine the Schuster walk. For northern California (excluding the Geysers area), we find a consistent drift throughout the study period and peak seismicity rate that occurred in mid-August (Figure 5.2C). In contrary, for southern California, no consistent drift is detected and hence the seasonal modulation of seismicity rate, if exists, is not statistically significant (Figure 5.2D).

Rather than being a regional-scale feature, the seasonal response of seismicity rate is localized over a few regions, many of which are related to hydrothermal systems. In the Mendocino County area, the modulation amplitude approaches 25% of background seismicity rate with peak rate occurring in July (Figure 5.2E), consistent with an overall phase for the analysis conducted on the entire northern California (Figure 5.2C). In the Geysers geothermal area, the modulation amplitude is also as large as the Mendocino County, but with a drastically different phases for peak seismicity rate which occurs in February rather than July (Figure 5.2F). This phase for Geysers geothermal area is inconsistent with phase of peak seismicity rate for the surrounding regions in northern California or the phase of peak stress rate at the Geysers geothermal field due to hydrological surface loading (Figure C.4). However, because geothermal energy production peaks in the winter months due to higher demands for energy, the sources of seasonal modulation of seismicity rate in the Geysers geothermal area is probably anthropogenic. Similarly, for Coso

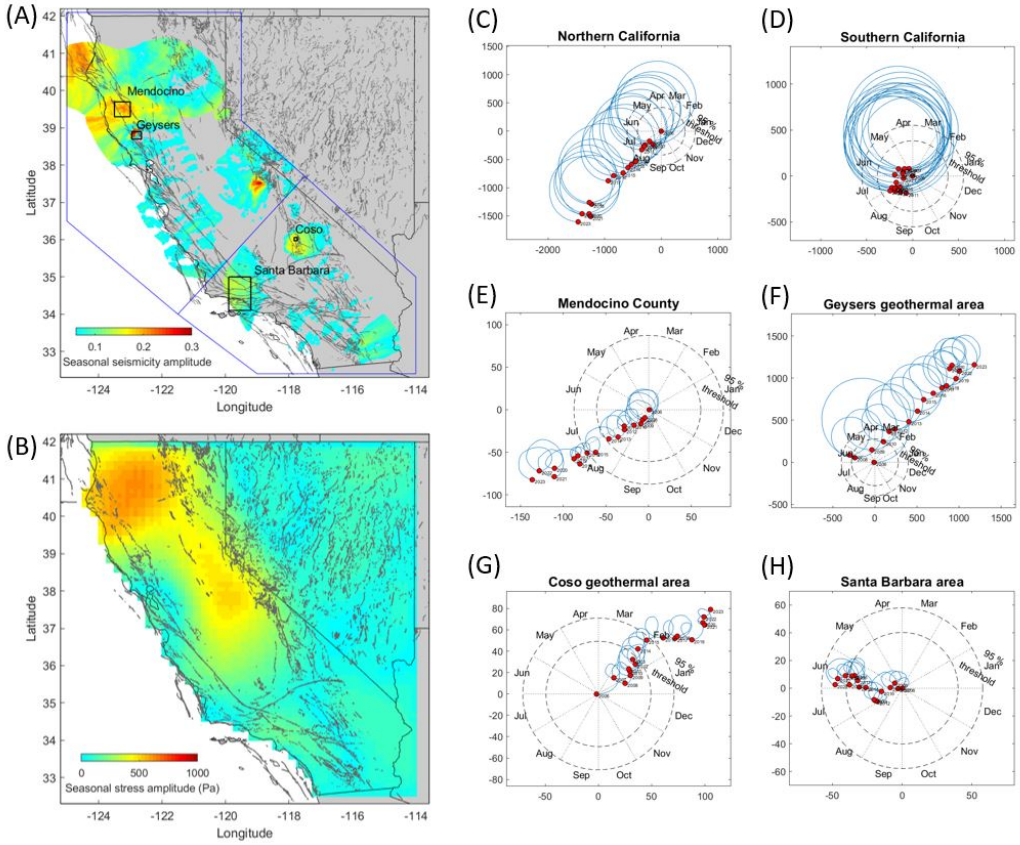

Figure 5.2: Seasonal modulation of seismicity rate and Coulomb stress changes induced by hydrological surface loads. (A) Amplitudes of seasonal modulation of independent earthquake rates determined from the Schuster tests (Ader and Avouac, 2013). Values lower than 0.06 are masked out as they are not statistically significant. (B) Amplitudes of stress due to surface loads at seismogenic depths (5 km) estimated from equivalent water thickness model determined from geodetic measurements (Argus et al., 2022) using analytical solutions (Boussinesq, 1878). (C-H) Schuster walks showing consistent annual modulation of seismicity rates throughout 17 years of observations for the different regions. Seismicity from the Geysers geothermal area is excluded in the Schuster walk for northern California. The circles indicate the detection threshold and a 95% confidence interval.

geothermal area, peak seismicity rate also occurred earlier in the year in the winter months (Figure 5.2G), inconsistent with phases of peak stress rate due to hydrological surface loads (Figure C.4). Therefore, seismicity modulation in the Coso geothermal area is also likely linked to the operations related to geothermal energy production. Finally, the last region explored is the Santa Barbara area, which has hints of seasonal signals, but are considerably weaker than other areas (Figure 5.2H). The Schuster spectrum for all these regions show a true isolated low p-value at annual period with minimal remaining clusters that could have biased our results (Figure C.5). We also test the sensitivity of our results to the cutoff magnitudes and find that the seismicity rate modulation occurs at all magnitudes and not only small ones (Figure C.6). As a result, the bias from spatial and temporal variations of magnitude of incompleteness does not significantly affect our results.

5.4 Relating seismicity modulation to hydrological surface loads

Modeling the response of seismicity to known stress perturbation allows for better understanding of the nucleation process. Using a stress-driven model based on rate-and-state friction formulation, a harmonic stress perturbation of amplitude ΔS can be related to seismicity modulation of amplitude α through the frictional-stress parameter $a\sigma$ as follows: $\Delta S = a\sigma \ln(1+\alpha)$ (Ader et al., 2014, see also Section C.1.5). Our analysis reveals a clear correlation between ΔS and $\ln(1+\alpha)$ with $a\sigma$ ranging between 2 – 6 kPa (Figure 5.3A). Many regions in northern California are subjected to large seasonal surface loading resulting in large enough seismicity modulation that can be confidently detected with the Schuster tests. In contrary, southern California is subjected to smaller seasonal surface loading resulting in seismicity modulation that is too small to be confidently detected. All regions with large seasonal seismicity modulation are subjected to large seasonal surface loading, indicating that surface loading is the primary driver of the seasonal seismicity modulation and that other effects such as poroelastic and thermoelastic stress can be neglected. Furthermore, all regions with large surface loading display large seasonal seismicity modulation suggesting that friction-stress parameter for these regions do not vary by more than an order of magnitude.

In addition to the correlation between the amplitudes of seismicity and stress perturbations, we document a clear phase lag of approximately 0.5 – 2.5 months between the peak seismicity rate and peak stress rate, with the mean being 1.6 months (Figure 5.3B). These lags are consistent throughout all regions in northern California where surface loading dominate the seasonal stress. The Geysers geothermal area is an

exception which has peak seismicity rate arriving prior to peak stress rate suggesting that seasonal seismicity modulation is this area may have been driven by other factors, such as the injection and extraction activities associated with geothermal energy production. These phase lags emphasize the non-instantaneous nature of earthquake nucleation and can also be used as an additional constrain for the nucleation model, especially on the characteristic relaxation time t_a of the seismicity rate following a stress step (i.e., the characteristic duration of an aftershock sequence). Using numerical calculations, we estimate that phase lag of 0.5 – 2.5 months requires t_a of between 0.05 – 0.7 yr (Figure C.8). The amplitudes of stress and the frictional-stress parameter play only a minor role in influencing the amount of phase lag.

To put these parameters into context, using the median values of $t_a \sim 0.3$ yr and $a\sigma \sim 3.5$ kPa, we can estimate the background stress rate $\dot{\tau} = a\sigma/t_a \sim 10$ kPa/yr. With a shear modulus for the Earth's crust $G = 30$ GPa, the background strain rate is approximately 300 nanostrain/yr. This value is consistent with the typical value of strain rates in California (Figure 5.1A).

Furthermore, we can also evaluate the spatial variations of the friction-stress parameter $a\sigma$ (Figure 5.4A). Given the same amount of stress perturbations, regions with larger $a\sigma$ would produce smaller seismicity responses. However, since these areas correspond to also larger t_a, the aftershock sequences would generally have a longer duration. Consequently, the phase lag for the seasonal seismicity would also be expected to be larger, which is qualitatively in agreement with our observations (Figure 5.4B).

5.5 Conclusions and implications for earthquake nucleation

In summary, we present a method to identify and quantify regions in California with significant periodic modulations of seismicity rate. The workflow is flexible and can be adapted to study other settings around the world and for studying harmonic perturbations with other dominating periods. We find stronger seasonal modulation of seismicity rate in northern California than in southern California, concentrating in regions associated with hydrothermal systems. These signals are driven primarily by seasonal variations of the hydrological surface loading. By using a stress-driven model based on rate-and-state friction formulation (Ader et al., 2014, Dieterich, 1994), we can relate the amplitude of seasonal modulation of seismicity to the seasonal stress amplitude and provide constraints on the friction-stress parameter

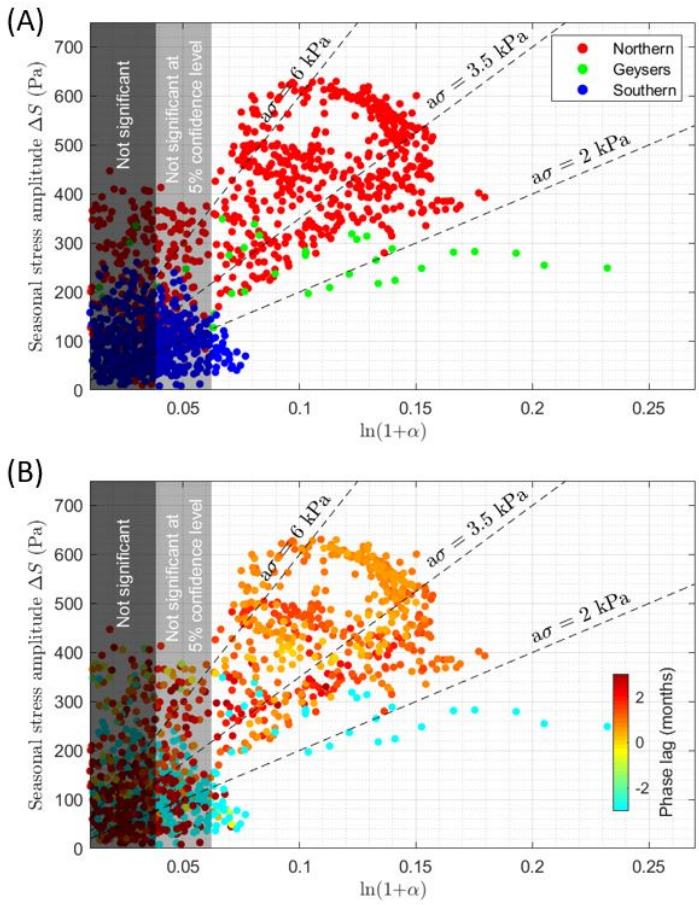

Figure 5.3: Responses of seismicity to seasonal surface loading. Seasonal seismicity amplitudes α is expected to respond to Coulomb seasonal stress amplitudes ΔS through frictional-stress parameter $a\sigma$ as $\Delta S = a\sigma \ln(1+\alpha)$ (Ader et al., 2014). (A) Relationship between α and ΔS color-coded by regions and (B) the duration that peak seismicity rate lags after peak stress rate. The shaded regions represent areas where the detected periodicity is not statistically significant.

governing the earthquake nucleation process. The phase lag between the peak stress rate and peak seismicity rate can be used to constrain the characteristic relaxation time t_a, which governs the non-instantaneous nature of earthquake nucleation. Our analysis suggests friction-stress parameter $a\sigma$ of approximately a few kPa. Using a typical value of $a = 0.01$ from the laboratory experiments (Marone, 1998a), we find the effective normal stress σ of approximately 0.1 MPa. At the seismogenic depth of 5 km, we expect the lithostatic pressure to be approximately 150 MPa. This suggests that the rate-and-state parameter a in natural faults may be much smaller than those typically measured in the laboratory, prevalence of high fluid pore-pressure, or a combination, at least for the areas where the earthquakes occurred.

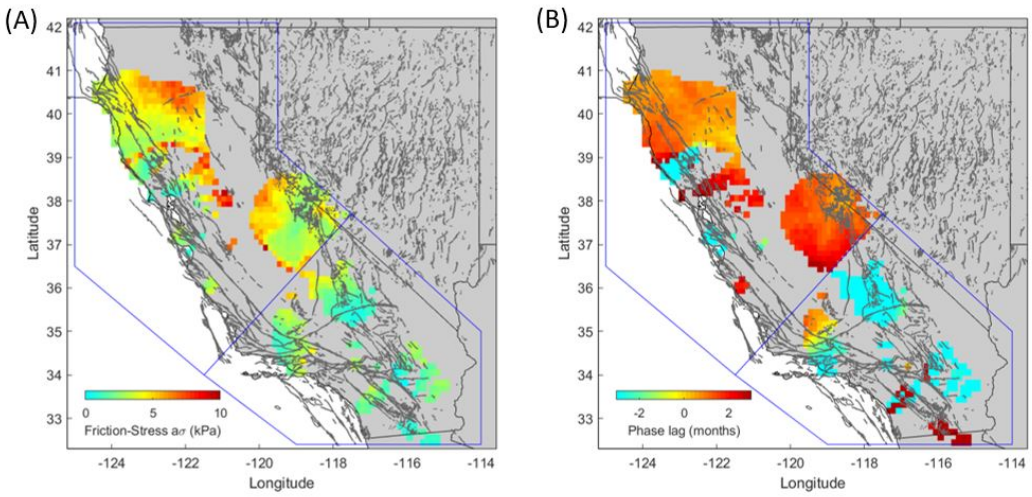

Figure 5.4: Constraining earthquake nucleation process. (A) Spatial distribution of the frictional-stress parameter $a\sigma$ derived from the amplitude of the seasonal seismicity relative to the background seismicity rate and (B) measured phase lag between peak seismicity and peak stress rate. The average $a\sigma$ and phase lag are 3.5 kPa and 1.6 months, respectively

In the upcoming decades, the need for decarbonization and sustainable energy production involves numerous activities that require perturbations of the subsurface reservoirs through injection or extraction of gas or water, which could lead to induced seismicity (Grigoli et al., 2017, Keranen and Weingarten, 2018, Moein et al., 2023). In areas where little is known about their friction properties and stress state, the existence or non-existence of responses of seismicity to tidal and seasonal stress can be used to probe the unknown friction parameter and the stress state of the natural fault at depths. These parameters can then be used as input to seismicity models of choice, allowing the operators to make a more informed decision based on the forecasted seismicity.

Chapter 6

BURSTS OF FAST PROPAGATING SWARMS OF INDUCED EARTHQUAKES AT THE GRONINGEN GAS FIELD

Under review as:

K. Sirorattanakul, J. D. Wilding, M. Acosta, Y. Li, Z. E. Ross, S. J. Bourne, J. van Elk, and J.-P. Avouac. Bursts of fast propagating swarms of induced earthquakes at the Groningen gas field.

Abstract

Gas extraction from the Groningen gas reservoir, located in northeastern Netherlands, has led to a drop in pressure driving compaction and induced seismicity. Stress-based models have shown success in forecasting induced seismicity in this particular context and elsewhere, but they generally assume that earthquake clustering is negligible. To assess earthquake clustering at Groningen, we generate an enhanced seismicity catalog using a deep-learning-based workflow. We identify and locate 1369 events between 2015 and 2022, including 660 newly detected events not previously identified by the standard catalog from the Royal Netherlands Meteorological Institute. Using the nearest-neighbor distance approach, we find that 72% of events are background independent events, while the remaining 28% belong to clusters. The clusters are dominated by swarms (78% of the clustered events, 20% of total seismicity), with only a small fraction being aftershocks (∼8% of total). Among these are five newly identified swarm sequences propagating at high velocities between 3 – 50 km/day along directions that do not follow mapped faults or existing structures and frequently exhibit a sharp turn in the middle of the sequence. The swarms occurred around the time of the maximum compaction rate between November 2016 and May 2017 in the Zechstein salt formation, above the anhydrite caprock, and well-above the directly induced earthquakes that occur within the reservoir and caprock. We suggest that these swarms are related to aseismic deformation within the salt formation rather than fluids. This study suggests that propagating swarms do not always signify fluid migration.

6.1 Introduction

Industrial activities, such as gas extraction, wastewater disposal, hydraulic stimulation, geothermal energy production, carbon dioxide sequestration, and water impoundment from dams can produce substantial stress changes in the Earth's crust that can induce seismicity (Atkinson et al., 2020, Ellsworth, 2013, Grigoli et al., 2017, Keranen and Weingarten, 2018, Moein et al., 2023, Wu et al., 2022). The induced earthquakes can occasionally reach magnitudes of 5 or above, with hypocenters that are often shallower than those of natural seismicity (Hough, 2015), making it capable of damaging nearby structures (Clayton et al., 2016). Management of seismic risks to be within an acceptable level is critical for successful operations.

Induced earthquakes, which exclude background earthquakes driven by tectonics and other natural causes of stress changes, can generally be grouped into two modes based on their clustering behaviors. The first mode includes independent background events that are driven directly by the stress changes due to the large scale human activity, whether from changes in pore pressure as the fluid diffuses (Hubbert and Rubey, 1959, Nur and Booker, 1972) or long-range poroelastic stress changes (Goebel et al., 2017, Segall, 1989, Segall et al., 1994, Zhai et al., 2019). These events are expected to follow a Poisson process, generally non-homogeneous, with time-varying rates governed by stress changes (Acosta et al., 2023, Dahm and Hainzl, 2022, Dempsey and Suckale, 2017, Smith et al., 2022). The second mode includes the clustered events that appear close in space and time with some independent events and often occur as aftershocks, or more occasionally as foreshocks as observed for natural seismicity as well (Ogata, 1988). Mechanistically, these events are triggered by stress changes imparted by a previous earthquake rather than the industrial operations. Aftershocks generally follow well-known patterns, including the decay of their occurrence rates with time as a power law (Omori, 1894, Utsu, 1961) and a scaling in which the largest aftershock is approximately 1.2 magnitude unit lower than the mainshock (Richter, 1958). Clustered events may occasionally deviate from this well-defined pattern and occur as enigmatic bursts of small-magnitude earthquakes without an identifiable mainshock, referred to as swarms (Mogi, 1963). They often exhibit migratory patterns (Audin et al., 2002, Chen and Shearer, 2011, Hainzl and Fischer, 2002) and are a manifestation of underlying aseismic processes such as spontaneous slow slip events (Gualandi et al., 2017a, Jiang et al., 2022, Lohman and McGuire, 2007, Passarelli et al., 2015), fluid pressure diffusion (Audin et al., 2002, Hainzl and Fischer, 2002, Ross and Cochran, 2021, Ruhl et al., 2016, Shapiro et al., 1997, Shelly et al., 2013), or a complex interaction of both (Dublanchet and

De Barros, 2021, Sirorattanakul et al., 2022b, Yukutake et al., 2022). Clustering is generally small in induced seismicity with a proportion of clustered events generally less than 30% (Cochran et al., 2020, Karimi and Davidsen, 2023, Zaliapin and Ben-Zion, 2016), while clusters typically represent up to 70% of natural seismicity (Zaliapin and Ben-Zion, 2013a). Swarms have also been observed in the context of induced seismicity where they are generally ascribed to fluid migration (Ake et al., 2005, Albaric et al., 2014, Baisch et al., 2006, Kwiatek et al., 2019).

In this study, we take advantage of publicly available seismic datasets related to seismicity induced by production in the Groningen gas field in the northeastern Netherlands (Dost et al., 2017, Oates et al., 2022, Willacy et al., 2019) to investigate the degree of clustering and the possible mechanisms involved. We produce an enhanced seismicity catalog for the region using a deep-learning-based workflow. The improved catalog reveals many previously unidentified events, which enables more extensive statistical analysis of earthquake clusters. The newly detected events include five distinct swarm sequences propagating at high velocity between 3 – 50 km/day.

6.2 The Groningen gas field, overview of previous studies of induced seismicity

The Groningen gas field is the largest in Western Europe (Figure 6.1), with an initial gas reserve of approximately 2913 billion cubic meters (BCM) (Burkitov et al., 2016). The gas comprises 85% methane (CH4), 14% nitrogen (N2), and 1% carbon dioxide (CO2) (Burkitov et al., 2016, Stäuble and Milius, 1970). The reservoir lies at a depth of between 2.6 and 3.2 km and spans approximately 35 km east-west and 50 km north-south as a part of the Upper Rotlingend Group composed of interbedded Slochteren sandstone and Ten Boer claystone units. Its thickness varies substantially from 90 m in the southeast to 300 m in the northwest. The coal layers in the underlying Pennsylvanian Carboniferous limestone are the source of the gas. The reservoir is sealed by an overlying thick and impermeable caprock of anhydrite and evaporite layers of the Permian Zechstein group, an aquifer toward the north, and a system of normal faults (de Jager and Visser, 2017). Because of the limited connection with the surrounding groundwater, gas extraction has led to significant pressure depletion from 34.68 MPa, close to hydrostatic pressure (Burkitov et al., 2016), to < 10 MPa (Meyer et al., 2023), which resulted in surface subsidence of almost 40 cm (Smith et al., 2019).

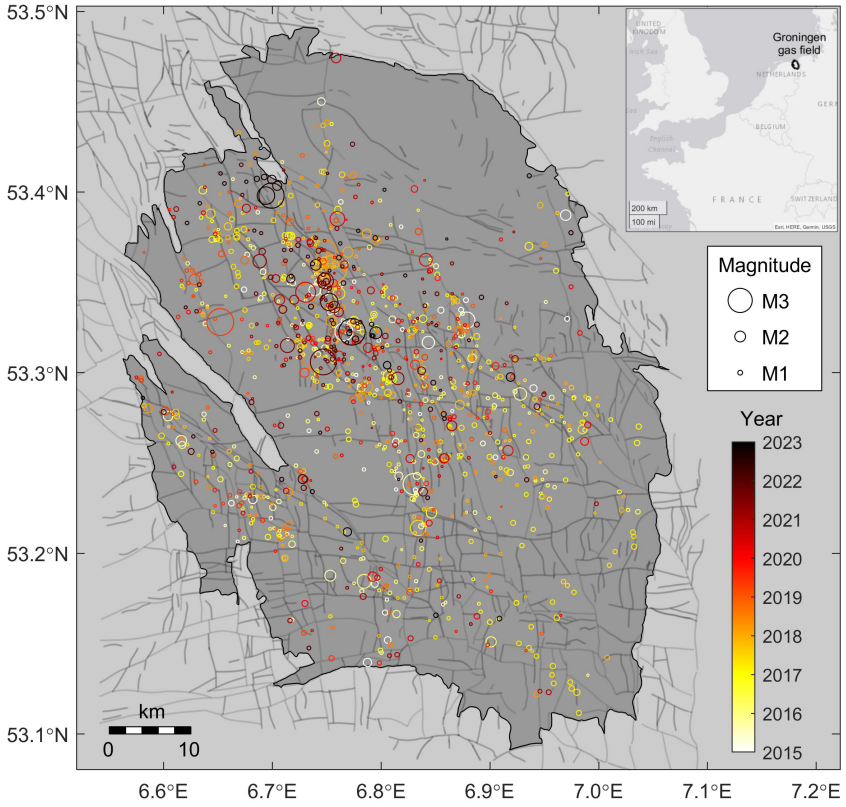

Figure 6.1: Map of induced seismicity in the Groningen gas field from 2015 – 2023 that were detected and located in this study using a deep-learning-based workflow. Circles show events with size representing the local magnitude and color representing the occurrence time. Black line shows the outline of the reservoir. Gray lines show mapped faults. The inset shows the location of the gas field within Europe.

While the field has been in production since 1963, induced seismicity did not start until 1991 (Dost et al., 2017). From 1991 to 2013, the number of earthquakes increased exponentially, prompting significant efforts to deploy additional monitoring instruments. The first regional network in operation since 1995 consisted of eight stations, each with three-component geophones at four different depth levels (50 m, 100 m, 150 m, and 200 m) and a surface accelerometer. Several upgrades of the network followed. In a major upgrade late 2014, 59 additional stations were deployed, significantly improving seismic activity detection (Dost et al., 2017). Most earthquakes align well with one of the > 1100 normal faults mapped by seismic techniques that offset the gas reservoir (Visser and Solano Viota, 2017) and are

located primarily within the reservoir (Willacy et al., 2019) or in the overburden (Smith et al., 2020). They are thought to be driven primarily by poroelastic stresses induced by bulk reservoir volume decrease (Bourne et al., 2014, Candela et al., 2018, Dempsey and Suckale, 2017, Smith et al., 2022) or by stress concentration around faults offsetting the reservoir resulting from compaction (Bourne et al., 2014, Buijze et al., 2017, Van Wees et al., 2018). The largest earthquake to date is the 2012 M_w 3.6 Huizinge earthquake, which sparked public concerns and prompted the operators to ramp down production and eventually shut it down long before exhaustion of the gas reserve (de Waal et al., 2015, Muntendam-Bos et al., 2017, van Thienen-Visser and Breunese, 2015).

In recent years, many researchers have developed computationally efficient models to forecast occurrence rates of induced seismicity based on stress changes from industrial operations (Acosta et al., 2023, Bourne and Oates, 2017, Bourne et al., 2018, Candela et al., 2019, 2022, Dahm and Hainzl, 2022, Dempsey and Suckale, 2017, Heimisson et al., 2022, Kim and Avouac, 2023, Kühn et al., 2022, Langenbruch et al., 2018, Richter et al., 2020, Segall and Lu, 2015, Smith et al., 2022, Zhai et al., 2019). One major limitation of these stress-based models is that they do not account for interactions between earthquakes that may lead to secondary triggering and appear as clustered events. While induced earthquakes tend to have fewer clustered events than natural earthquakes, their proportions can be > 50% depending on the geological settings, which is non-negligible (Zaliapin and Ben-Zion, 2016). A better understanding of clustering behaviors of induced seismicity can lead to further improvements in these models.

6.3 Data and methods

6.3.1 Enhanced seismicity catalog generation

The Royal Netherlands Meteorological Institute (KNMI) has been the authoritative governmental institution responsible for maintaining a seismicity catalog for the area surrounding the Groningen gas field since 1995. To supplement the KNMI catalog, we use a recently developed deep-learning-based workflow to build an enhanced high-resolution seismicity catalog between 2015 and 2022 covering the domain spanning latitude 53.05 – 53.50°N and longitude 6.48 – 7.05°E. As summarized below, the workflow consists of multiple steps, including phase picking, phase association, earthquake location, and magnitude estimation.

Waveform data from seismic stations in the NL and NR networks located within our domain are used in this analysis (Figure D.1). We first apply the PhaseNet automated phase picking algorithm based on a convolutional neural network (Zhu and Beroza, 2019) to detect P- and S-wave arrivals. The algorithm accepts one- or three-component waveform data as input and outputs a list of timestamped P- or S-wave arrival times. We use the standard model included with the PhaseNet distribution, which was trained on California data based on manual picks from seismic analysts at the Northern California Earthquake Data Center but has been shown to effectively generalize to other regions worldwide, including Hawaii (Wilding et al., 2023), Italy (Tan et al., 2021), and Arkansas, USA (Park et al., 2020). The initial iteration of the catalog, spanning from mid-2015 to 2018, includes picking from both surface and borehole seismometers. However, when we expand the catalog to include the first few months of 2015 and from 2019 to 2022, we only apply PhaseNet to surface sensors for computational efficiency. Additionally, for instruments with a sampling rate greater than 100 Hz, we decimate waveform data to 100 Hz per PhaseNet requirements. The output from PhaseNet also has probability labels between 0 and 1, indicating confidence in the pick. We set a probability threshold of 0.3 and remove picks below this confidence threshold.

The P and S arrival picks are then associated into discrete earthquake events using the Gaussian Mixture Model Associator, GaMMA (Zhu et al., 2022). GaMMA probabilistically assigns clusters of P and S picks to individual sources based on identified hyperbolic moveouts and iterates those assignments using the expectation-maximization process. The main parameters controlling the association process are the maximum time ϵ between two picks to be considered as a neighbor of the other and the scalar P- and S-wave velocity used to backproject arrivals. Even though GaMMA uses a uniform velocity model, it can account for travel-time errors in back-projection due to three-dimensional variation of the velocity model by allowing large uncertainty in arrival times during the clustering stage. We test different parameters and identify the best set of parameters as those that include the greatest number of events previously identified by KNMI. The best combination of parameters uses ϵ of 3 seconds, a P-wave velocity of 3.0 km/s, and an S-wave velocity of 1.8 km/s. With this set of parameters, GaMMA identifies 709 out of 739 events in the KNMI catalog over the same spatial and temporal coverage. After the association, we filter out previously unidentified events with fewer than 5 P or S picks and are left with 2591 events. Finally, we manually inspect waveforms of all newly identified

events and remove the spurious picks resulting in 1369 events, including 660 newly detected events (Figures D.2 and D.3).

The events are then located with a modified version of the Hypocenter inversion with Stein Variational Inference and physics-informed neural networks (HypoSVI) program (Smith et al., 2021), adapted to allow for a 3-D velocity model. The velocity model of the Groningen region used in this study was produced by Nederlandse Aardolie Maatschappij (NAM) from seismic reflection, seismic refraction, sonic log and well core samples (Nederlandse Aardolie Maatschappij, 2017). Since HypoSVI inverts for the full posterior distribution of an earthquake location, the algorithm also outputs associated location uncertainties. Compared with the KNMI catalog, we find approximately 40 mismatched events. Most of these events are located near the edges of the velocity model domain by both our algorithm and by KNMI. They are most likely affected by the low number of picks on stations within the velocity model domain and increased picking errors for arrivals with a lower signal-to-noise ratio. To maintain the integrity of the catalog, we manually assign the locations of these events to those provided by KNMI, which can be identified by their depth of exactly 3 km. The events that include the borehole picks can be distinguished by event ID numbers that begin with "100" in contrast to other events that only have picks on surface geophones. Events with picks only from the surface geophones have larger depth uncertainty, as evidenced by several surface-sensor-only events with depths far from the reservoir. These depths can be considered artifacts of the data downsampling process. We have also compared the epicentral (horizontal) locations derived using picks from all sensors and only from surface sensors. They are largely unaffected by excluding the picks from the borehole sensors.

Local earthquake magnitudes (M_L) are calculated with the same procedure used by KNMI (NORSAR, 2018), which can be calculated by using the following equation:

$$M_L = \log_{10} A + 1.33 \cdot \log_{10} R + 0.00139 \cdot R + 0.424 \tag{6.1}$$

where A is amplitude measurement in mm on a simulated Wood-Anderson seismometer of the deepest available borehole sensor for a given station, and R is the source-receiver distance in km. The amplitudes are measured as the peak signal amplitude of the waveform (absolute value). While it is possible to convert local magnitude to moment magnitude using the relation derived by Dost et al. (2018), we restrict our analysis to local magnitude.

6.3.2 Clustering analysis

To analyze the clustering behaviors of seismicity in the Groningen gas field, we apply the nearest-neighbor distance approach (Zaliapin and Ben-Zion, 2013a,b) to the enhanced seismicity catalog. We consider only events located within the boundary of the Groningen gas field that are larger than the completeness magnitude (M_c) of 0.5. For each event j in the catalog, we search for the preceding event i that is most likely to be the parent (mainshock) of event j. The proximity distance between any event pair (i,j) can be quantified using a space-time-magnitude metric normalized by the magnitude of the parent event (Baiesi and Paczuski, 2004, Zaliapin et al., 2008) defined as follows:

$$\eta_{ij} = t_{ij}(r_{ij})^{d_f} 10^{-b(m_i - M_c)} \tag{6.2}$$

where $t_{ij} = t_j - t_i$ is the time between the event pair, r_{ij} is the distance between the epicenters of the event pair, d_f is the fractal dimension of earthquake epicenters taken to be 1.6 (Zaliapin and Ben-Zion, 2013a), b is the Gutenberg-Richter b-value of the frequency-magnitude distribution, and m_i is the magnitude of event i. Since depth uncertainty is large, we do not include depths in the proximity distance calculations.

For each event j, the event i^* with the smallest proximity distance η_{ij} is the nearest neighbor and hence most likely to be the parent of event j. The results can be expanded to two dimensions as rescaled time T_j and rescaled distance R_j, defined as follows (Zaliapin and Ben-Zion, 2013a):

$$\begin{aligned} T_j &= t_{i^*j} 10^{-\frac{b}{2}(m_{i^*} - M_c)} \\ R_j &= (r_{i^*j})^{d_f} 10^{-\frac{b}{2}(m_{i^*} - M_c)}. \end{aligned} \tag{6.3}$$

The distribution of nearest-neighbor distance η_j is expected to be bimodal. The first mode is the independent events represented by a time-stationary, space-inhomogeneous Poisson process concentrating along $\log_{10} T_j + \log_{10} R_j = \text{constant}$. The second mode is the clustered events with considerably smaller T_j and R_j, constituting foreshock-mainshock-aftershock sequences and swarms (Zaliapin and Ben-Zion, 2013a, Zaliapin et al., 2008). The separation between the two modes can be approximated by a 1-D Gaussian mixture model applied on η_j (Hicks, 2011) using Matlab fitgmdist function. The mode separator η_0 is chosen to be where the probability

density function of the two modes intersects. We consider events with $\eta_j \geq \eta_0$ to be independent events and $\eta_j < \eta_0$ to be clustered events (Zaliapin and Ben-Zion, 2013a).

The nearest-neighbor distance approach was originally analyzed for an epidemic-type aftershock sequence (ETAS) model (Ogata, 1988) with an assumption that the background independent events follow a time-stationary, space-inhomogeneous Poisson process (Zaliapin et al., 2008). In the case of induced seismicity, we expect the background Poisson rates of independent events to be inhomogeneous in time as modulated by injection or extraction rates. To test a posteriori the effectiveness of the nearest-neighbor distance approach for induced seismicity and the robustness of the estimated mode separator η_0, we take events with $\eta_j \geq \eta_0$, create 100 shuffled catalogs by randomly permuting the order of the magnitudes and locations, and calculate nearest-neighbor distances for events in these shuffled catalogs, similar to those done in Karimi and Davidsen (2023). Since the shuffling removes any clusters while preserving the seismicity rate and spatial distribution, the distribution of nearest-neighbor distances of these shuffled events reflects the true distribution of the independent mode and hence the majority of events should have $\eta_{\text{shuffled}} \geq \eta_0$ if the chosen η_0 is appropriate. Unlike in Karimi and Davidsen (2023), by shuffling only events with $\eta_j \geq \eta_0$, we reduce bias of the clustered events on the temporal rate of independent events. In principle, we can also completely remove the time clustering by sampling new times from a uniform distribution (Zaliapin and Ben-Zion, 2020) but then we would also remove any time-inhomogeneous nature of the independent events.

We additionally use the Schuster spectrum method (Ader and Avouac, 2013) to verify that, once clustered events are removed based on the chosen value of the mode separator η_0, the remaining events are consistence with a non-homogeneous Poisson process. The method is based on the Schuster tests (Schuster, 1897), which evaluates the amount of seismicity rate variation for a given periodicity. By calculating the Schuster p-value for different periods, we construct a Schuster spectrum and compare with the expectation for a Poisson process. This procedure aids in verification of the quality of the declustering.

To further study the relationship between events, we create a spanning tree by connecting each event to its most likely parent. The strength of each link is inversely proportional to the nearest-neighbor distance η_j. By removing weak links with $\eta_j \geq \eta_0$, we create a spanning forest consisting of single-event trees with no links

and other multievent clusters (Zaliapin and Ben-Zion, 2013a). The independent events previously identified include the singles and the first event from each cluster. We can calculate the average leaf depth for each cluster by averaging the number of links needed to connect events without children to the first event or the root (Zaliapin and Ben-Zion, 2013b). Swarm-like sequences have large average leaf depth, while foreshock-mainshock-aftershock sequences have small average leaf depth.

6.4 Results

6.4.1 Catalog overall properties

Compared to the standard catalog from the Royal Netherlands Meteorological Institute (KNMI), our deep-learning-based workflow enables us to increase the number of detected events between 2015 and 2022 from 739 to 1369. 709 events from the KNMI catalog were identified by our workflow, leaving only 30 events unidentified by our method. 1297 events are located within the horizontal extent of the gas field, which we use for the analysis hereafter.

Despite being automatically generated products, our events display good agreement in both locations and magnitudes with the KNMI catalog (Figure D.4). The horizontal location differences are less than 660 m on average. Most events with large location differences are either located near the edge of the available velocity model or small magnitude events where arrival picks have large uncertainty. The magnitude differences are less than 0.1 magnitude unit on average. Only 78 events (12%) have magnitude differences greater than 0.2 magnitude units. Our catalog also reports depth rather than a fixed depth of 3 km, as the KNMI catalog does. We have refined the depth determination by including time picks from the borehole sensors for the time spanning mid-2015 to 2018, during which we observed a concentration of swarms as detailed below.

The increase in detection is consistent across the period studied. Many new detections are related to small events with signals close to the noise floor. However, a significant portion of new detections are the five bursts of small-magnitude (M_L 0.5 – 1.5) swarm-like sequences that double the earthquake rates between November 2016 and May 2017 (Figure 6.2a), which we discuss further in the "Swarm sequences" Section. Our catalog has the completeness magnitude (M_c) of 0.5 estimated using the maximum curvature method (Wiemer and Wyss, 2000). The b-value slope of the frequency magnitude distribution is determined to be 0.86 by applying the B-Positive method (van der Elst, 2021) to all events with a conservative minimum

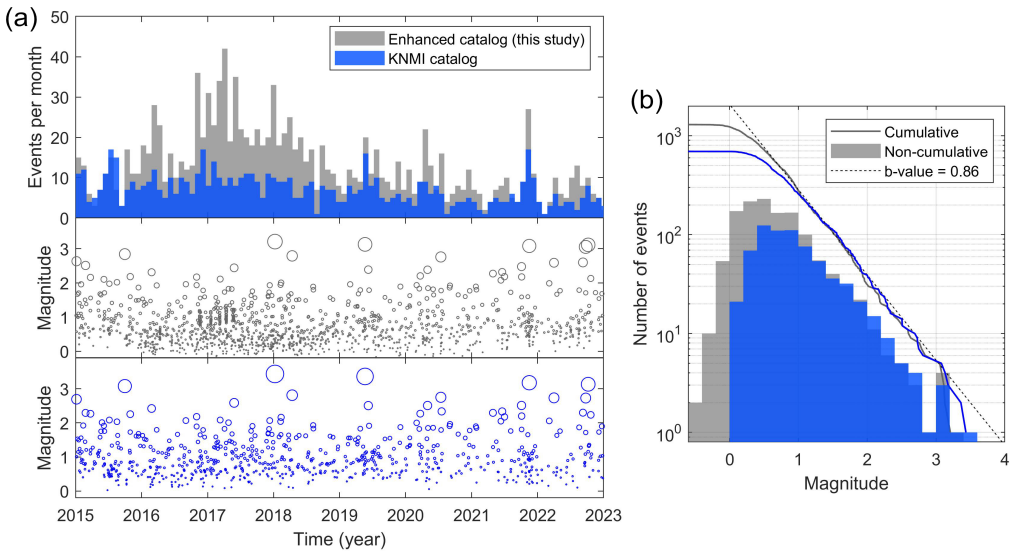

Figure 6.2: Enhanced seismicity catalog. (a) Comparison between our enhanced seismicity catalog and the standard catalog from the Royal Netherlands Meteorological Institute (KNMI). The top panel compares number of detected events per month. The middle panel shows distribution of event magnitude vs. time for the enhanced catalog. The bottom panel is the same as the middle but for the KNMI catalog. (b) Frequency-magnitude distribution from the two catalogs. The dashed line represents the Gutenberg-Richter exponential distribution with the b-value slope of 0.86 estimated from the enhanced catalog using B-Positive method (van der Elst, 2021). The completeness magnitude (M_c) of the enhanced catalog is estimated to be approximately 0.5.

magnitude difference of 0.2 (Figure 6.2b). With these additional events, the enhanced catalog can unlock new insights into the clustering behaviors of earthquakes in the Groningen gas field.

6.4.2 Clustering behaviors

The nearest-neighbor distance approach is applied to 726 events in the enhanced catalog with $M_L \geq 0.5$. The distribution of nearest-neighbor distance η_j expanded in the form of rescaled time T_j and rescaled distance R_j is shown in Figure 6.3a. By fitting η_j with a 1-D Gaussian mixture model, we find the best-fit mode separator of $\log_{10}\eta_0 = -3.05$. We find that 522 events (72%) are independent, while the remaining 204 events (28%) appear to be clustered (Figure 6.3b).

The two-dimensional probability distribution of nearest-neighbor distances of the 100 shuffled catalogs are averaged and shown in Figure 6.3c. Since the rate of independent events vary only gradually during this period, their distribution similarly

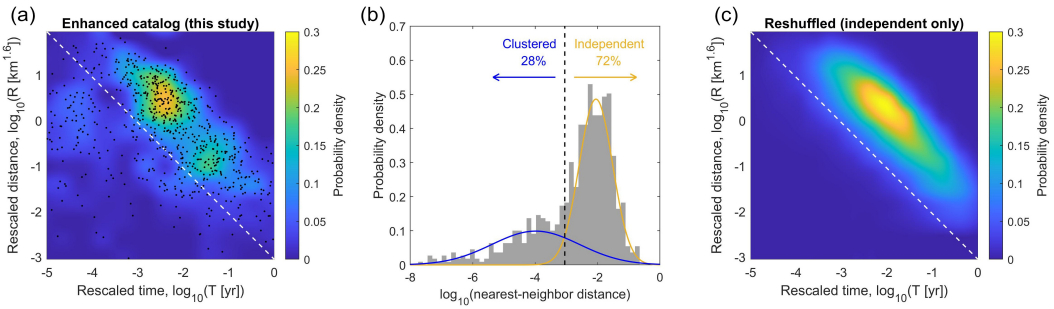

Figure 6.3: Nearest-neighbor clustering analysis performed on our enhanced seismicity catalog with $M_L \geq 0.5$. (a) A joint 2-D distribution of the rescaled time and rescaled distance. Each of the black dots represent proximity of each event to a parent event. (b) Histogram of the nearest-neighbor proximity distance with curves showing the two Gaussian distributions representing the two modes derived from 1-D Gaussian mixture model. (c) The average joint distribution of the rescaled time and rescaled distance derived from 100 catalogs created from reshuffling locations and magnitudes of independent events. The diagonal white dashed lines in panels (a) and (c) and black vertical dashed line in panel (b) mark the mode separator ($\eta_0 = 10^{-3.05}$) used to perform binary classification of events into either independent or clustered.

concentrates along a line with $\log_{10} T_j + \log_{10} R_j$ = constant with almost all reshuffled events (93%) having $\eta_j \geq \eta_0$, validating the approach and the chosen mode separator.

The Schuster spectrum calculated for the non-declustered catalog shows low p-values, lower than expected for a Poisson process, which drifts to even lower value starting at a period of about 2-3 days (Figure D.5a). This pattern shows that the catalog contains clusters (Ader and Avouac, 2013) and we can infer they have durations of a few days or eventually longer. However, if we use only the independent events, the drifting low p-values disappear (Figure D.5b), further validating the choice of the value of the mode separator chosen.

We proceed to analyze the spatiotemporal evolution of the events from each of the two modes (Figure 6.4). The independent events align well with mapped faults and have the seismicity rate that is gradually changing with time. On the other hand, the clustered events show multiple lineations that do not align with mapped faults and occur as short-duration bursts of events in time. The most prominent clusters are the five bursts of small magnitude (M_L 0.5 – 1.5) swarm-like sequences occurring between November 2016 and May 2017. The others appear to be aftershocks of the larger $M_L > 2$ events. By construct, if a sequence has a foreshock, the mainshock will be identified as a clustered event rather than an independent event because the

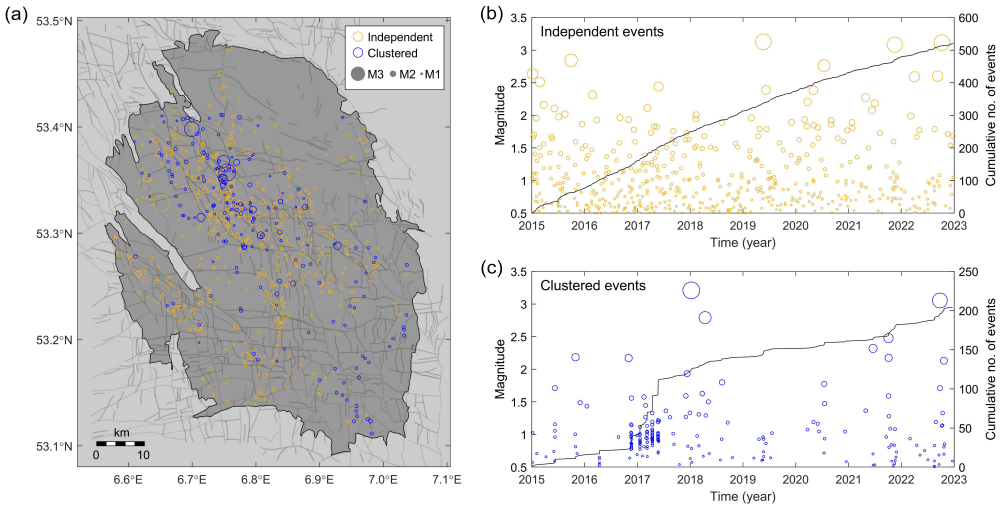

Figure 6.4: Distribution of independent vs. clustered events for $M_L \geq 0.5$ from our enhanced seismicity catalog. (a) Spatial distribution of events color coded by the mode they belong to. (b) Magnitude and cumulative number of events vs. time distribution of the independent events. (c) Same as (b) but for clustered events.

foreshock would be its parent, which explains why some of the larger events are identified as clustered.

The spanning tree created by connecting each event with its nearest neighbor if $\eta_j < \eta_0$ reveals 448 single-event clusters (62% of events) and 73 multievent clusters (38% of events). Their detailed statistics are shown in Figure 6.5. The average size of the multievent clusters is 3.8 events with a standard deviation of 3.6 events. The large standard deviation reflects significant variations in clustering behaviors. All earthquakes with $M_L > 2.5$ are a part of multievent clusters, with the number of events in the cluster growing with mainshock magnitude. On average, the largest aftershock is 1.5 magnitude unit lower than the mainshock, in line with those expected from Båth's law (Richter, 1958). The average leaf depth of these aftershock sequences is 1.3, indicating that most of the events are triggered by the mainshock rather than being aftershocks of aftershocks. On the other end of the spectrum, there are multievent clusters that exist as swarm-like sequences without a clearly identifiable mainshock ($M_{\text{mainshock}} - M_{\text{largest aftershock}} \ll 1$, contradicting Båth's law) and a larger value of average leaf depth up to 8.7. Using an average leaf depth (d_{leaf}) of 2 as a cutoff for binary classification between swarm-like and aftershock-like clusters and considering only clusters with more than 3 events, we find 14 swarm-like clusters ($d_{\text{leaf}} \geq 2$) with a total of 123 events (73% of clustered events) and 9

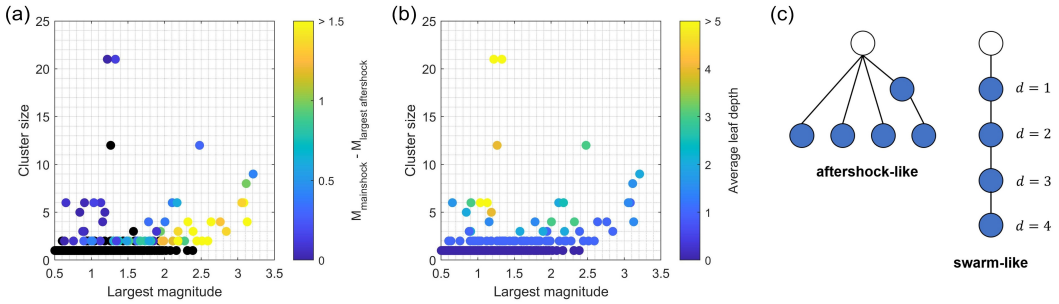

Figure 6.5: Statistics of the identified clusters. (a) Cluster size (number of events) vs. magnitude of the largest event color coded by the magnitude difference between mainshock and largest aftershock. Black circles denote the case with only one event in the cluster or when the largest earthquake is the last one in the sequence. (b) is the same as (a) but color coded by the average leaf depth. (c) A schematic showing aftershock-like and swarm-like sequences. Aftershock-like sequence has smaller average leaf depth than swarm-like sequence, but each event produces more offsprings.

aftershock-like clusters ($d_{\text{leaf}} < 2$) with a total of 46 events (27% of clustered events). Among aftershock-like clusters, the partition between foreshocks, mainshocks, and aftershocks are 11%, 19%, and 70%, respectively. Only 2 of these have any foreshock at all. The analysis suggests that the clustered events are dominated by swarm-like sequences.

6.4.3 Swarm sequences

There were five noticeable swarm-like clusters between November 2016 and May 2017, each lasting 1 to 5 days and consisting of 10 to 20 events, with M_L ranging from 0.66 to 1.56 (Figure 6.6). Outside of this period, we did not find any other noticeable swarm clusters. Upon further investigation of their kinematics, all swarms migrate with velocities ranging from 3 to 50 km/day. We numbered the swarms from 1 to 5 based on the order that they occurred. The migration occurred along one single direction for swarms 1 and 2 and two different orthogonal directions for swarms 3 – 5. For swarms 3 and 4, there exists also ~15 hour pauses with no events before the migration direction switches. The migration directions do not follow mapped faults or other known features of the reservoir. While there are not enough events to determine the exact shape of the migration front, it is possible to model them with $\sqrt{4\pi Dt}$ where D would be an apparent hydraulic diffusivity, and t is time. In the case of fluid-driven swarms, the fitted D would be related to the hydraulic diffusivity of the fault zones (Shapiro et al., 1997), though with a conversion factor that accounts

for the time delays associated with earthquake nucleation (Kim and Avouac, 2023). The swarms in our study have D ranging from 70 – 800 m^2/s, much larger than a commonly accepted range for fluid-driven swarms of 0.005 – 10 m^2/s (Amezawa et al., 2021). In comparison to other swarms around the world, the scaling between migration velocity and duration places them closer to slow-slip events and swarms driven dominantly by slow-slip events than other injection-induced swarms (Danré et al., 2022). We further discuss possible drivers for these swarms in Section 6.5.2.

Another interesting observation is that the swarms occurred at a depth of between 1.5 to 2.5 km. While there could be some uncertainty with the absolute depth locations, they are certainly located toward the shallower side when compared to other earthquakes that are generally thought to be located near the top of the reservoir (Smith et al., 2020, Willacy et al., 2019). As a result, this would place them in the 1 – 2 km thick Zechstein evaporite (salt) above the anhydrite caprock, well above the gas reservoir (Figure 6.7).

6.5 Discussion

6.5.1 Comparison of clustered fraction with other studies

Induced earthquakes are known to have a lower proportion of clustered events than naturally occurring tectonic earthquakes due to high driving stresses from anthropogenic activities in comparison to tectonic loading (Cochran et al., 2018, Martínez-Garzón et al., 2018, Schoenball et al., 2015, Zaliapin and Ben-Zion, 2016). Here, we compile in Table 1 the clustered proportion of seismicity from different regions as reported by previous studies. We find that the clustered events can account for up to 70% of naturally occurring tectonic earthquakes but no more than 30% of induced earthquakes. The estimate of 28% from this study places the Groningen gas field well within the range estimated for other induced seismicity settings. Other studies on the clustered proportion of seismicity from the Groningen gas field provide different estimates of the clustered proportion varying from a few percent up to 27%, which are generally lower than the 28% that we report here (Candela et al., 2019, Muntendam-Bos, 2020, Post et al., 2021, Trampert et al., 2022). Among those that also uses the nearest-neighbor distance approach, Candela et al. (2019) finds 18% of clustered events between 1993 – 2016, while Muntendam-Bos (2020) finds only 6% of clustered events between 1995 – 2018, but the proportion increases to 22% if consider only the period between 2014 – 2018. On the other hand, Post et al. (2021) uses the statistics of the interevent times and finds a larger value of 27% for the clustered proportion. Because the earthquake rates and the clustered proportion of

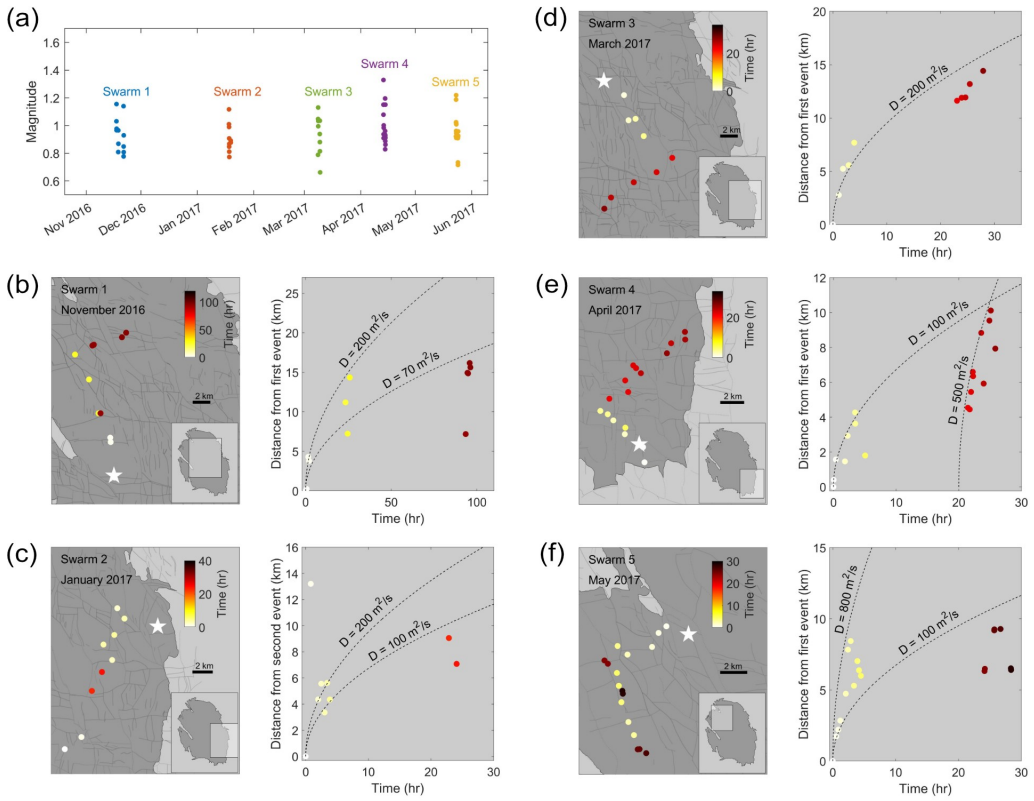

Figure 6.6: Fast propagating earthquake swarms. (a) Magnitude vs. time of the five distinct bursts of swarm-like sequences. (b) – (f) show the spatiotemporal evolution of these five swarms. The white stars mark the second event in swarm 2 and first event in all other swarms. The dashed lines show the predicted expansion for the different values of apparent hydraulic diffusivity D.

induced seismicity can vary in time (Martínez-Garzón et al., 2018, Trugman et al., 2016), it could also explain the differences in the findings from various studies which have used different time window. Furthermore, another difference is that the KNMI catalog used by other studies does not capture the five swarm sequences occurring between November 2016 and May 2017 that were identified in our enhanced catalog. By removing the five swarms, our estimate of the clustered proportion becomes 19%, which is almost equivalent to the estimate from Candela et al. (2019). Additionally, since the clustered proportion can also depend on cutoff magnitude (Zaliapin and Ben-Zion, 2013a), we also calculate the clustered proportion using the different cutoff and find that the clustered proportion generally decreases with larger cutoff and becomes stable at between 18 – 20% as the cutoff exceeds M_L of 1.2 (Figure 6.8).

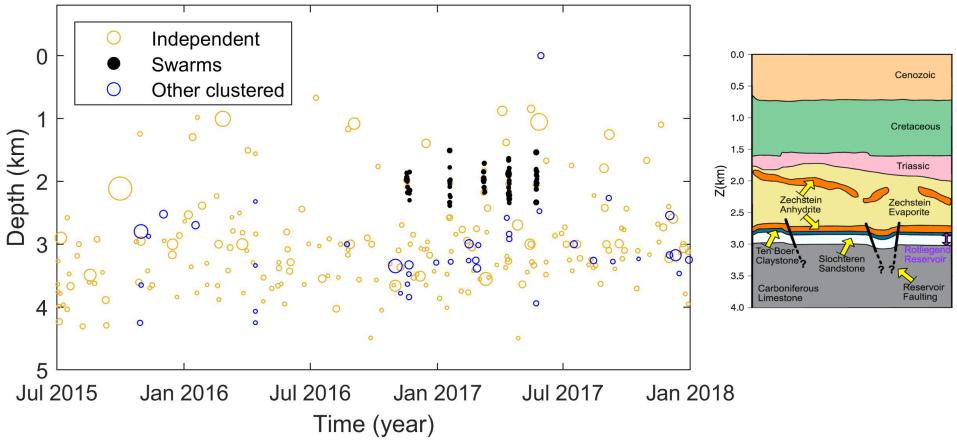

Figure 6.7: Depth distribution of earthquakes with $M_L \geq 0.5$ from our enhanced seismicity catalog with colors identifying whether they are independent, fast propagating swarms shown in Figure 6.6, or other clustered events, along with a schematic showing a depth cross-section of lithologies taken from Smith et al. (2019). Only the time period where we have picks from both surface and borehole sensors are shown. The five swarm sequences are located in the Zechstein evaporite.

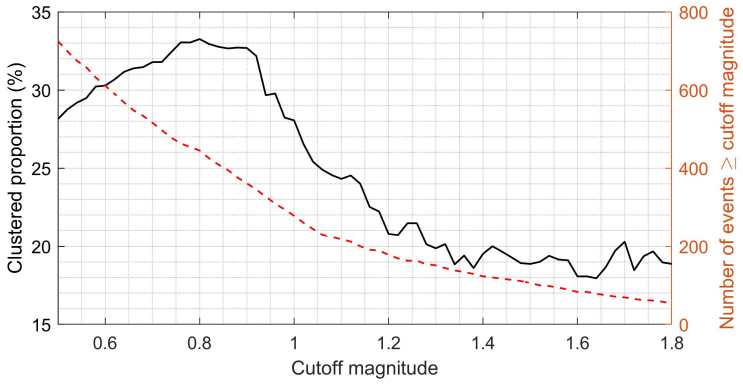

Figure 6.8: Variations of clustered proportion for the different cutoff magnitude. The dashed line shows the number of events larger than or equal to a given cutoff magnitude.

6.5.2 Possible drivers of swarm-like sequences

Although the migration of swarms in the Groningen gas field can be modeled with a square root of time typically associated with fluid pressure diffusion (Shapiro et al., 1997), it is unlikely that fluid plays any dominant role because of the following reasons. First, the migration direction should be along the maximum spatial pressure gradient, which follows the spatial derivative of the compaction rate. This contradicts the observations in which the migration direction seems to align more along the contours of constant compaction (Figure 6.9a). Second, the migration velocity is on the order of 10 km/day, which requires a much higher hydraulic diffusivity than the values typically expected for fluid-driven swarms (Amezawa et al., 2021). Third, while fault slip can enhance permeability, allowing for faster diffusion rates, the migration directions do not follow mapped faults or any known structures. There may be other unmapped faults in which the migration follows as there are focal mechanisms with fault planes not orienting along the mapped faults (Willacy et al., 2019). Nevertheless, because the swarms are located in the Zechstein salt well above the impermeable anhydrite caprock that allows the gas to be preserved for millions of years (Figure 6.7), the faults in the Zechstein evaporite are probably not hydraulically connected to the reservoir. Hence, the swarms cannot be driven by direct fluid contact.

Besides fluids, cascading earthquakes can create an apparent diffusive expansion front (Helmstetter and Sornette, 2002a). However, the swarms consist of only small M_L 0.5 – 1.5 events which would correspond to a rupture dimension of ~15 – 40 m, much smaller than the average distance of ~1 km between events (Figure 6.6). While there could exist a chain of smaller undetectable events that connect the larger ones, this is unlikely as our deep-learning-based workflow should be able to detect some events below M_L 0.5 (Figure 6.2), but we detect none. Therefore, cascade triggering is also unlikely.

These swarms occurred just after the period of accelerated compaction (Figure 6.9b), suggesting they might be related to the large strain rate from such period that could trigger swarms in the Zechstein salt above the reservoir. While seismic events in the salt are rare because salt is highly ductile they can occur in case of large strain rates, for example related to the collapse of mining cavity (Kinscher et al., 2016) or fault creep (Barnea Cohen et al., 2022), or in relation to fluid injection (Lei et al., 2019). In our case, since there are no mining activities in the Zechstein salt and that the salt is likely not hydraulically connected to the reservoir, propagating

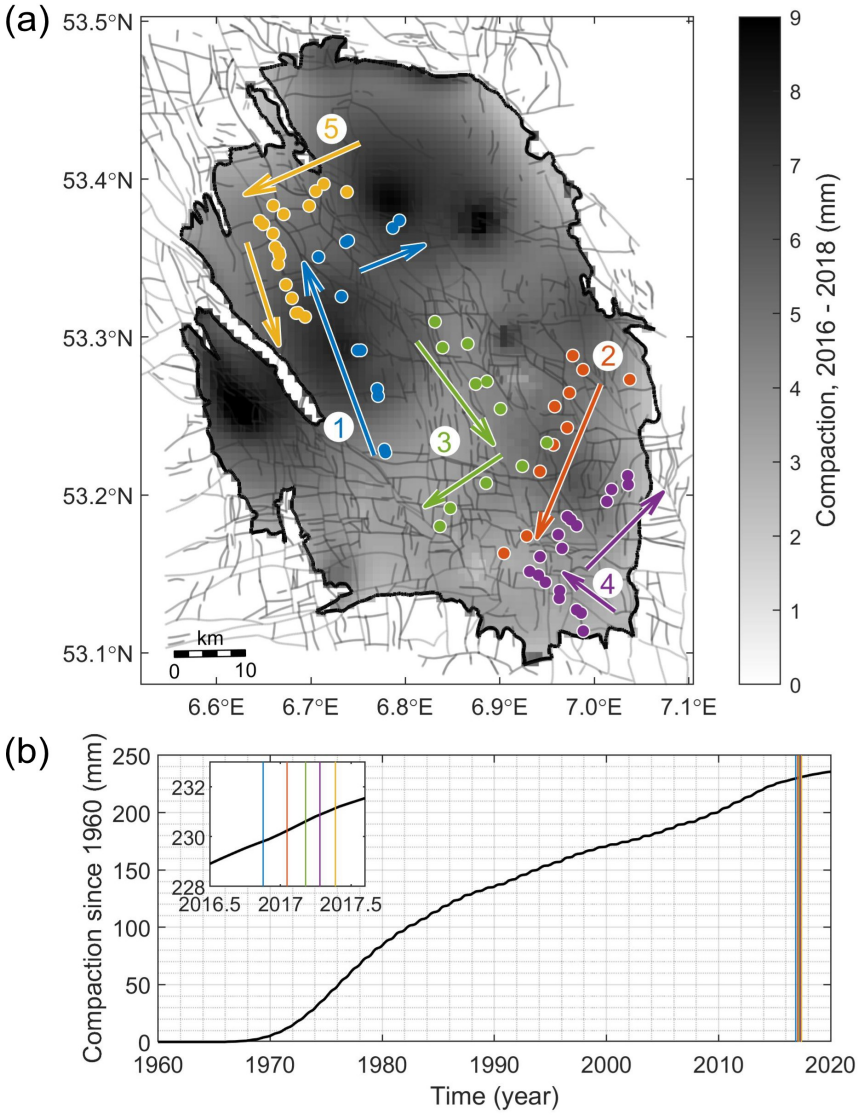

Figure 6.9: Comparison of swarms with reservoir compaction. (a) Spatial distribution of modelled reservoir compaction between 2016 and 2018. The calculation is done using a simple expression $C = C_m \cdot \Delta P \cdot h$ relating compaction C with the compressibility C_m from Smith et al. (2019) constrained with geodetic data, pressure depletion ΔP calculated by Acosta et al. (2023), and the reservoir thickness h. The circles with different colors denote the five different swarms shown in Figure 6.6. (b) Average compaction in the reservoir vs. time. The vertical lines denote the timing of the five swarms. The inset shows a zoomed-in during the time of swarms.

episodes of aseismic deformation is the most probable explanation. While there are no detectable geodetic signals in either GPS on InSAR during the time of the swarms, aseismic creep may locate too deep or being too small to be detected. Swarms that are driven by aseismic slip generally propagate at high velocity in the order of km/hr (Lohman and McGuire, 2007, Sirorattanakul et al., 2022b), which is consistent with the observations of the Groningen swarms. The origin of the aseismic creep can be the incremental growth of the subsidence zone or fluid-driven, with sources located further away within the reservoir depth. When faults are moderately stressed, fluid-induced aseismic creep can outpace the pressure diffusion front and trigger a seismicity front that propagates at velocities that are orders of magnitude larger than the fluid diffusion (Bhattacharya and Viesca, 2019, Sáez et al., 2022, Wynants-Morel et al., 2020). Since these swarms are not driven directly by stress changes from the industrial operations, they are not yet accounted for in induced seismicity forecasting models for the Groningen gas field.

6.6 Conclusions

By applying a deep-learning-based workflow for earthquake detection to seismic data from the Groningen gas field, we identify and locate a total of 1369 events from 2015 – 2022, almost two times more than the standard KNMI catalog. Despite being automatically generated products, the locations and magnitudes of the overlapping events display a high degree of similarity with the KNMI catalog. Analysis of the nearest-neighbor distances reveals that the clusters account for 28% of all events. Among the clustered events, approximately 73% are swarm-like clusters with an average leaf depth of at least 2, while the remaining 27% are aftershocks. The swarm-like clusters include five distinct swarm sequences that migrate at incredibly fast velocities between 3 – 50 km/day along directions that do not follow mapped faults or existing structures and frequently exhibit a sharp turn in the middle of the sequence. Based on the observations of fast velocities and their depths in the Zechstein salt above the reservoir caprock, the swarms are most likely not driven by fluids but rather other aseismic processes such as propagating aseismic creep. The magnitude of these swarms is within the detectable range of the KNMI catalog, but they were not previously identified. With a better catalog, we can enhance our understanding of the mechanics of earthquake clusters and allow us to better incorporate their contributions to seismic hazards into induced seismicity forecasting models.

Chapter 7

CONCLUSIONS AND PERSPECTIVES FOR FUTURE WORK

7.1 Summarizing the main findings of the study

7.1.1 Earthquake nucleation is non-instantaneous

If there is one takeaway that recurs throughout our work, it would be that earthquake nucleation is not instantaneous, not in laboratory experiments nor in natural faults in the real world.

In Chapters 2 and 3, we developed a new experimental methodology to measure the ultraslow slip rate of shear interfaces and demonstrated that frictional interfaces under constant non-zero shear stress are still sliding, though with decaying slip rate down to 10^{-12} m/s, even when the driving force is smaller than the classically defined static friction. Our results reveal the non-stationary nature of the frictional interfaces, contradicting the traditional view of Coulomb friction, but can be explained with a rate- and state-dependent friction formulation. In this latter model, there is no such thing as an instantaneous jump in sliding velocity, and hence, when using the model to explain earthquakes, its nucleation process is not instantaneous. These laboratory experiments are extremely important as they provide a formalism applicable to natural faults.

Moving from the laboratory-scale fault to natural ones, in Chapters 4, 5 and 6, we studied the response of earthquakes to stress perturbations. In Chapter 4, the source of stress perturbations is a spontaneous slow-slip event, and the resulting response is a swarm sequence lasting approximately one week. There is a time delay between the onset of the slow-slip event and the swarm sequence of approximately half a day, pointing out again to the non-instantaneous nature of the earthquake nucleation process. In Chapter 5, the source of stress perturbations is the changes in seasonal surface loading due to hydrology and the response is the seasonal modulation of seismicity rate. While there is a clear correlation between the seasonal amplitudes of the driving stress and the seasonal amplitudes of the modulation of seismicity, the peak seismicity rate occurred slightly after the peak stress rate, ranging from 0.5 – 2.5 months. This time delay also points out again the non-instantaneous nature of the earthquake nucleation process. In Chapter 6, we documented bursts of fast propagating swarms of induced earthquakes, which must be driven by some transient

stresses. Unfortunately, we were not able to isolate the source of these stresses and hence cannot perform similar modeling done in the other chapters.

While the rate-and-state framework (Section 1.3.2) provides a simple explanation for the non-instantaneous nature of the earthquake nucleation, it is not the only possible explanation. The delay in earthquake nucleation could also be captured with mechanisms such as fluid diffusion following a sudden change of pore fluid pressure (Miller, 2020). When these mechanisms are coupled with the Coulomb instantaneous failure model (Section 1.3.1), it can also explain the non-instantaneous nature of the earthquake nucleation.

7.1.2 Response of earthquakes to transient stresses can be used to probe friction and stress state

By modeling the response of earthquakes to transient stresses with the spring-slider rate-and-state model (SRM, Section 1.3.4), we are able to constrain the friction-stress parameter controlling the earthquake nucleation process, which is a product of the rate-and-state friction parameter a and the effective normal stress $\sigma = \sigma_0 - P$. A summary of values obtained from our work is compared against previous studies in Table 7.1.

Study	Frictional-stress parameter, $a\sigma$
The 2020 Westmorland, California swarm (Chapter 4)	1.2 kPa
Seasonal modulation of seismicity rate in California (Chapter 5)	2 - 6 kPa
Inducted seismicity in the Groningen gas field, Netherlands (Acosta et al., 2023)	3 - 7 kPa
Seasonal strain in Himalaya (Bettinelli et al., 2008)	3 - 8 kPa
Reservoir-induced seismicity, Val d'Agri, Italy (Rinaldi et al., 2020)	0.8 kPa
Izu volcanic island swarm, Japan (Toda et al., 2002)	30 kPa
Aftershocks of the 1992 M7.3 Landers, California earthquake (Gross and Kisslinger, 1997)	20 - 40 kPa
Aftershocks of the 2004 M6.0 Parkfield, CA earthquake (Cattania et al., 2015)	3 - 8 kPa

Table 7.1: Comparison of the frictional-stress parameter $a\sigma$ obtained from various studies.

Note that the value from (Gross and Kisslinger, 1997) might be overestimated because the study ignores reloading by postseismic afterslip. Other than that, with the exception of the results from the Izu volcanic island swarm, the ranges of $a\sigma$ are quite narrow, between 0.8 – 8 kPa. Using a typical value of a from laboratory experiments of 0.01 and lithostatic stress at 5 km of σ = 150 MPa, the expected value of $a\sigma$ is 1.5 MPa. Our results suggest that natural faults may have lower a than those typical laboratory values, pore-pressure may be very high resulting in small effective normal stress, or a combination of both. It is also possible that the SRM model underestimates the value of $a\sigma$ because it is zero-dimensional and neglects the finite fault effects, as illustrated in Ader et al. (2014).

7.2 Perspectives for future work

7.2.1 Effects of loading conditions and roughness on interface healing

The experiment methodology developed in Chapters 2 and 3 has provided a unique opportunity to study the healing of shear interfaces, an effect in which the interface becomes strengthened with time. Through a series of preliminary experiments, we started to investigate the effects of loading conditions (varying values of shear and normal stresses) and roughness on interface healing.

In one set of experiments, we subject the specimens with the same inclination angle α to different far-field loads P. Because the friction coefficient is the ratio of shear to normal stress τ_0/σ_0, which depends only on the inclination angles α, i.e., $f = \tau_0/\sigma_0 = \tan\alpha$, the rate-and-state formulation predicts the same slip rate evolution (Equation 1.5). Our measurements reveal that the slip rate evolution from these tests is clearly not the same (Figure 7.1a), contradicting the prediction of the rate-and-state formulation. If we were to continue to use the rate-and-state formulation in its current form, one of the parameters, i.e., a, D_{RS}, or f^*, must be dependent on stress, which is not completely surprising. For example, if D_{RS} were to be interpreted as the average size of contact asperities, we would then expect D_{RS} to increase with normal stress because larger compressive force should squeeze the interface more, and produce larger areas of contact. By combining results from experiments with various normal and shear stresses (by changing the far-field load P and the inclination angle α), we would be able to enhance our understanding of the parameters governing the rate-and-state friction laws.

In another set of experiments, we subject the specimens with the same inclination angle α to the same load P, but with interfaces that are prepared to have different

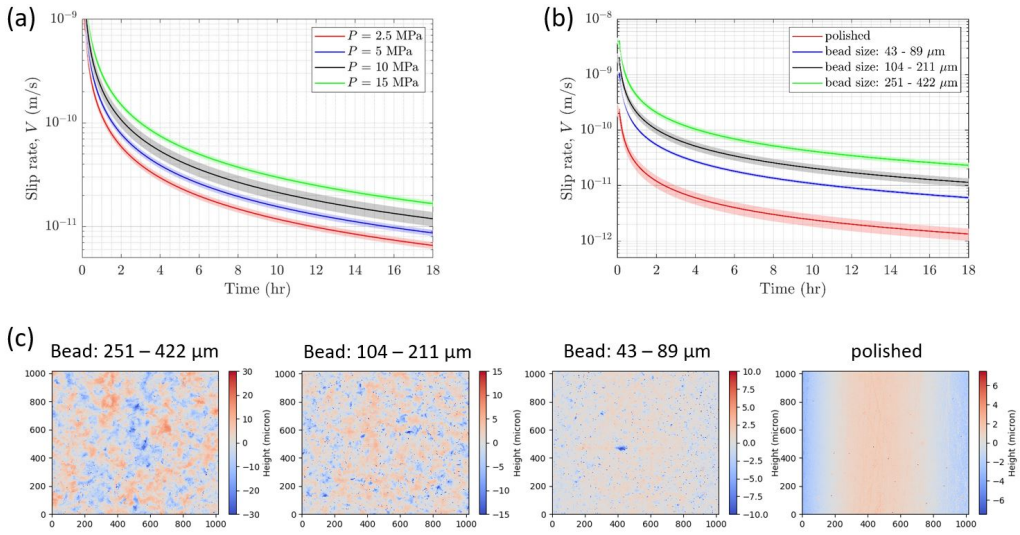

Figure 7.1: Preliminary results from interface healing experiments with different loading conditions and roughness. (a) Tests with different far-field loads P, but with the same inclination angle $\alpha = 26°$. (b) Tests with different roughness. (c) Asperities heights of surfaces with varying roughness (profilometer scan, courtesy of Marie Violay, EPFL).

roughness. To do so, the surfaces are first polished to a near-optical-grade surface finish and then later roughened by blasting the surfaces with glass beads of different sizes. The results from our healing experiments suggest that roughness plays an important role in interface healing (Figure 7.1b).

Moving forward, we are interested in interpreting our interface healing experiments in the context of contact mechanics. By using the profilometer to scan the surfaces (courtesy of Marie Violay at EPFL), we obtain the height distribution of each asperity (Figure 7.1c). By using finite-element-based contact mechanics codes, such as *Tamaas* (Frérot et al., 2020), we can predict contact areas for different loading conditions, allowing us to interpret our results in terms of the average contact sizes and the total real contact areas.

7.2.2 Effects of interface healing on dynamic ruptures

The state of the fault (different amounts of healing or, in specific cases, can be related to maturity) is known to have a profound impact on the dynamics of the subsequent rupture events (Beeler et al., 1998, Marone, 1998a,b). A natural extension of our experiments would be to initiate a spontaneous dynamic rupture after different amounts of healing times. Our preliminary results (conducted by Attilio Lattanzi, myself, Vito Rubino, Nadia Lapusta, and Ares Rosakis) have suggested that the peak friction greatly increases with healing times, which subsequently modifies the rupture arrival time and the supershear transition length (Figure 7.2a).

Similar experiments can be conducted on our fluid injection setup (Gori et al., 2021). Our preliminary results based on numerical modeling have revealed different nucleation behaviors for different initial slip rates V (different amounts of healing) Alghannam et al. (2024). In particular, we find that with the same pressure ramp-up rate, the dynamic rupture occurs at a much lower pressure (earlier time) for the interface that is less healed and hence has higher initial slip rate (Figure 7.2b).

In addition to the behaviors of the dynamic rupture, the state of faults can also influence the characteristics of slip during the nucleation phase. Our preliminary experiments injecting fluids onto bare PMMA interface and surfaces that are embed-

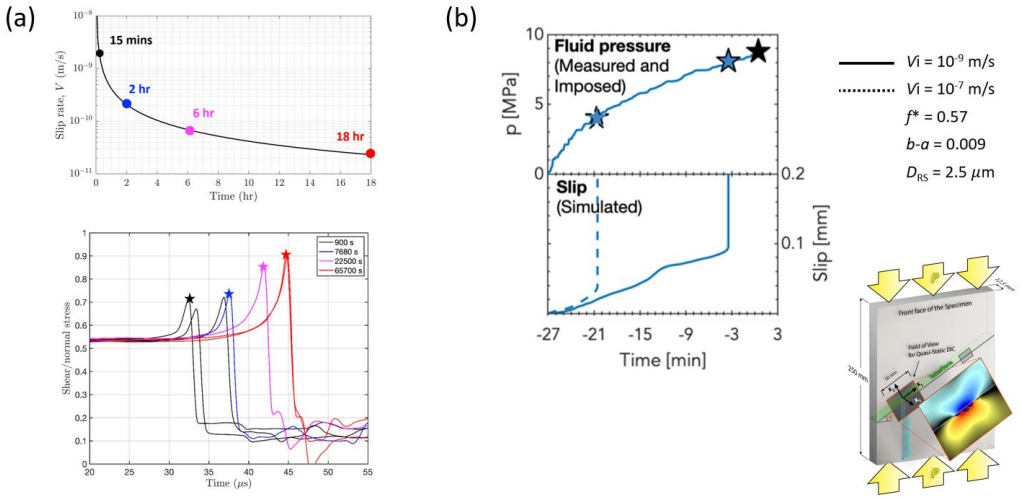

Figure 7.2: Preliminary results on the effects of interface healing on dynamic ruptures. (a) Dynamic ruptures triggered by wire explosion after different healing times have increasing peak friction and delayed arrival times with the increasing healing times. (b) Numerical simulations of the effects of initial slip rate V on the onset of the dynamic rupture. Panel (b) is taken from Alghannam et al. (2024)

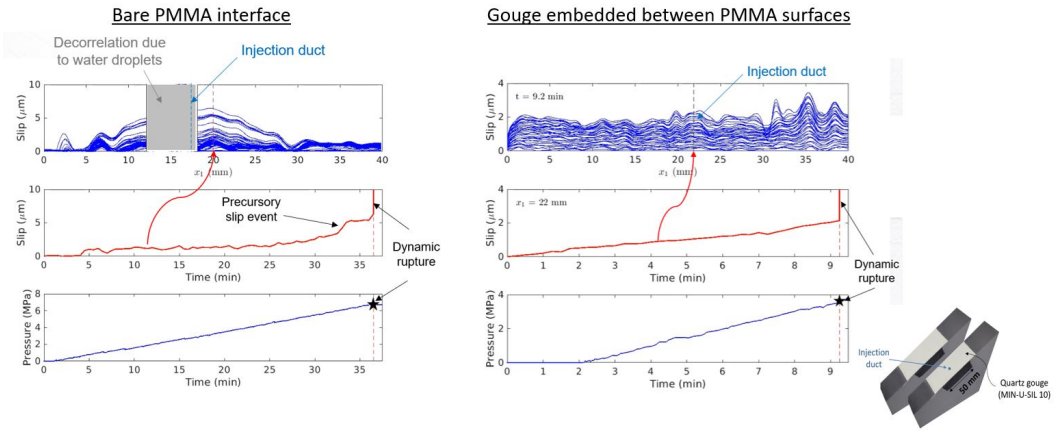

Figure 7.3: Capturing the nucleation process of fluid-induced dynamic fault slip. (Left) Experiment injecting fluid onto bare PMMA interface. The interval between the lines plotted in the top panel is 0.5 min. (Right) Experiment injecting fluid onto the interface embedded with rock gouge (MIN-U-SIL 10). The interval between the lines plotted in the top panel is 0.25 min.

ded with rock gouge reveal vastly different behaviors during nucleation (Figure 7.4). For the bare surface, as we start to pressurize the injected fluid, regions surrounding the injection duct start to slide with the largest accumulated slip occurring near the duct. After 32 minutes, the interface suddenly accelerates for a short amount of time, but not enough to nucleate a dynamic rupture, resulting in a precursory slow-slip event confining to regions close to the fluid injection duct. Then, after another minute or so, the dynamic event nucleates. For the interface embedded with rock gouge, regions across the entire observation window continuously slide relatively uniformly throughout the duration of the experiments. After 9 minutes, the dynamic rupture nucleates. The future work would also include a measurement of this type, but with an injection that starts after different amounts of hold times.

7.2.3 Understanding the driving mechanisms of aftershocks

In this thesis, we have studied the response of earthquakes to transient stresses from a spontaneous slow-slip event, and tidal and seasonal stress. There is another common source of stress that has not yet been explored, which is the postseismic deformation. The richness of the data from the 2019 Ridgecrest earthquake sequences provides a unique opportunity to study the postseismic deformation and use it as a case study to determine whether the aftershock sequences are driven primarily by static stress changes from the mainshock, or from the postseismic afterslip. In that regard, we have started to do some preliminary analysis (Penney et al., 2021) of GPS data and

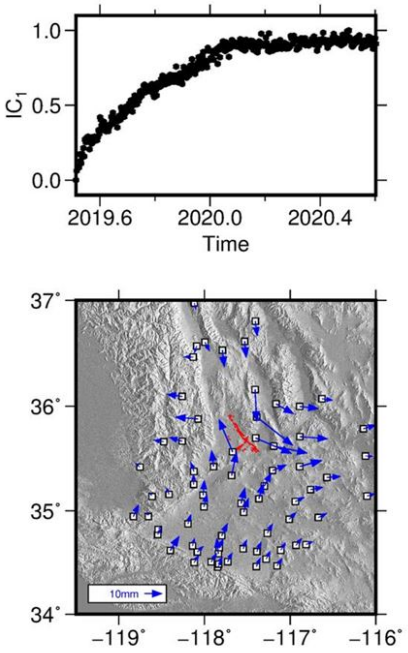

Figure 7.4: Postseismic deformation of the 2019 Ridgecrest earthquakes extracted from GPS data using the independent component analysis. Figure is from Penney et al. (2021)

attempt to extract the postseismic deformation using the independent component analysis from a mixture of signals that could also include deformations due to hydrology and others (Figure 7.4). We intend to continue the research and use the workflow developed in this thesis to learn more about the mechanisms controlling aftershock sequences.

7.2.4 Including finite fault effects, interactions between sources, and slip law

While the spring-slider rate-and-state model (SRM) works well in explaining the response of earthquakes to transient stresses, as evident from the work presented in this thesis, the SRM model has a few limitations. First, the SRM model neglects the finite fault effects. Ader et al. (2014) created earthquake sequences using dynamic modeling and then attempted to model them with the SRM model. They found that the SRM model can underestimate $a\sigma$ as much as 100 times in comparison to the inputs used in dynamic modeling. The lack of finite fault effects could be a cause of unusually low $a\sigma$ reported from studies using the SRM model. Second, the SRM model ignores interactions between sources. For a sequence dominated by cascade triggering from the preceding earthquakes, the SRM model may no longer be suitable. To study the regime at which the approximation is appropriate, one can

utilize simulations of discrete fault networks such as those done in Im and Avouac (2023). Third, the SRM model uses aging law as the state evolution law. There is growing evidence that slip law seems to perform better in many scenarios (e.g., Alghannam et al., 2024). Through numerical studies, we can better understand the limitations of the SRM model and enhance our understanding of the behaviors of the different state evolution laws.

Appendix A

SUPPLEMENTARY MATERIALS FOR CHAPTER 2

A.1 Materials and methods

A.1.1 Specimen preparation

In this study, we investigate two different types of frictional interfaces under shear: (1) bare surfaces of Poly(Methyl Meth-Acrylate) (PMMA) and (2) rock gouge layer embedded in a PMMA sample. The specimens are cut from a PMMA sheet of size 250 mm x 200 mm x 12.5 mm to two equal-sized quadrilateral plates at an oblique inclination angle $\alpha = 26°$ using a computer-numerical-control machine. The inclined mating faces represent the frictional interfaces.

To ensure experimental reproducibility, the mating surfaces of the PMMA specimens are prepared following a well-developed surface finish procedure (Mello, 2012, Mello et al., 2010, Rubino et al., 2019). The interfaces are first polished to near-optical grade finish using a 100 r.p.m. rotating polishing wheel covered with Buehler 12-inch Microcloth and soaked with a mixture of water and Cerium Oxide polishing compound (Buehler MiroMet) in a ratio of 2:1, achieving a typical roughness $R = \frac{1}{L}\int_0^L |z(x)|\,dx \sim 0.016\mu$ m. Then, the interfaces are roughened by blasting with McMaster Carr abrasive glass beads with 70 – 140 mesh size corresponding with the diameter ranging between 104 – 211 microns using a pressure of 75 psi for 3 minutes. A similar procedure performed on a similar material (Homalite-100) generally achieves a typical roughness R ~0.5 μm (Mello, 2012).

The rock gouge layer is incorporated into the PMMA sample using a hybrid configuration (Rubino et al., 2022) and it covers 74% of the center portion of the interface (165 x 12.5 mm^2 out of 222.5 x 12.5 mm^2) (Figure 2.1D). The bare PMMA portion helps to maintain the inclination angle $\alpha = 26°$. The layer of rock gouge has a thickness of 2 mm, and it is composed of a fine quartz gouge power (MIN-U-SIL 10, commercially available from US Silica) with > 99.5% silicon dioxide (SiO_2) and > 96% of grains with a diameter < 10 μm. The field of view captured by the camera (30 x 22 mm^2) falls entirely within the gouge portion at the center of the interface, away from the transitional boundaries between gouge and bare PMMA. Rock gouge is incorporated along the PMMA interface following a similar procedure to that outlined in (Rubino et al., 2022). First, 1 mm of PMMA is removed along the

portion to be filled with gouge, for each mating half. A fine mist of glue is sprayed along this portion, and the specimen is pressed against gouge particles laid on a flat surface at room temperature and humidity. Isopropyl alcohol is used to clean gouge particles on the un-milled portion of bare PMMA. A razor blade is used to shave off excess particles over the milled portion to ensure that the gouge surface is flush with bare PMMA. The glue adheres a thin layer of gouge particles to the PMMA, preventing shear failure from occurring at the gouge-PMMA interface and allowing us to study the frictional behavior of rock gouge.

A.1.2 Loading and image acquisition protocols

To apply shear stress on the frictional interfaces, the two mating halves are first placed into contact and aligned using a specimen holder to ensure parallel loading surfaces and to prevent specimen buckling. The assembly is loaded uniaxially and uniformly using an Instron 300LX with a constant loading rate of 0.2 mm per min (corresponding to vertical strain rates of 1.3 x 10^{-5} s^{-1}, well within the quasi-static regime) until the vertical-load P = 10 MPa is reached. The loading process takes approximately 6 and 10 minutes for specimens with bare PMMA and with interbedded rock gouge surfaces, respectively. The loading time is longer for specimens with rock gouge because more vertical displacement is required to compact the rock gouge layer, due to its granular nature. Both surfaces are inclined at an angle $\alpha = 26°$, at which the vertical load P produces a resolved shear stress of $\tau_0 = P \sin\alpha \cos\alpha$ = 3.94 MPa and a normal stress of $\sigma_0 = P \cos^2\alpha$ = 8.08 MPa. The load is then maintained constant for 18 hours in most experiments and two weeks in one experiment using an automatic load control system.

The central portion of the specimen is monitored using optical imaging with a field-of-view of 30 x 22 mm^2, starting when the vertical load P is reached. To provide the characteristic texture required for performing image correlation, the field-of-view is covered with small black random speckles over a thin white coating produced with Krylon sprays. The average speckle size produced by the Krylon spray spans 5 pixels, with 1 pixel corresponding to approximately 15 µm. Every 5 minutes, 32 images of size 2048 x 1536 $pixels^2$ are taken at a rate of approximately 50 fps using the monochrome camera DMK 37BUX250 by Imaging Source. The camera is equipped with a 50 mm Xenoplan compact series lens (21-1001976) by Schneider Optics and a 10 mm Tamron extension ring (Table A.1). Typically, once the target load is attained, 217 sets of 32 images are acquired every 5 minutes during each test over the 18 hours span duration (Figure A.1). To reduce the noise level, each

set of 32 images is numerically averaged using the software IC Capture Version 2.4 (Imaging Source) and only the averaged images are used for the analysis. To obtain full-field displacements and slip along the interface, the sequence of 217 averaged digital images is analyzed using digital image correlation, as detailed in the next section. Six independent but nominally identical 18-hour experiments are performed for the bare PMMA interface and three for interface embedded with rock gouge to check the repeat. Additionally, one 2-week experiment is conducted for bare PMMA interface.

A.1.3 From optical images to cumulated interfacial slip

To measure slip along the frictional interface, the optical images are analyzed using Digital Image Correlations (DIC) technique (Sutton et al., 2009). Using Correlated Solutions VIC-2D commercial image-matching software, we produce an evolving sequence of full-field displacements for each experiment. The first image in the sequence is used as a reference image in the correlation for bare PMMA, while the last image is used as a reference image in the case of rock gouge to prevent decorrelations due to large displacements in the later images. To preserve the discontinuity of displacements across the interface, the correlation analysis is performed over two domains separated by the interface. For surfaces with rock gouge, the 2-mm gouge layer is treated as an infinitesimal layer and excluded from the correlation. Moreover, to make the correlations computationally amenable, only subregions of size 2048 x 150 px^2 on the different sides of the interface are considered. The correlation uses a subset size of 41 x 41 $pixels^2$ and a step of 1 pixel. The "Fill Boundary" algorithm is used to extrapolate correlated displacements from half a subset size away from the interface to directly at the interface (Table A.2). Using this approach, we can resolve minute full-field displacements as small as 1 x 10^{-3} of the pixel size in the optimal scenario (Rubino et al., 2019), equivalent to 0.015 μm for our field-of-view.

Using full-field displacements, cumulated interfacial slip δ is calculated by taking the differences between the interface-parallel displacements u_1 of pixels immediately below and above the interface, i.e., $\delta(x_1, t) = u_1(x_1, x_2 = 0^-, t) - u_1(x_1, x_2 = 0^+, t)$. To describe the macroscopic frictional behavior of the interface, the mean cumulated slip is calculated for each time frame, i.e., $\bar{\delta} = \frac{1}{L}\int_0^L \delta(x_1, t)\, dx_1$.

A.1.4 Uncertainty quantification of slip measurements

To quantify measurement uncertainties, we perform an experiment on a PMMA sample without an interface, under the same loading conditions as the regular experiments and we measure slip along the mathematical line where an interface lies in the regular experiment following the same analysis procedure. Since there is no physical interface in this case, any measured slip is due to the DIC measurement accuracy or to the viscoelastic relaxation of PMMA over the distance across which slip is computed, which is of 1 pixel (15 μm). The DIC measurement accuracy is affected by a number of factors, such as the electronic noise of the camera sensor, lighting variations during the observation time window, vibrations of the optical table, suboptimal speckle pattern, or interpolation methods used during correlations (Rubino et al., 2019). In our case, we find that DIC measurement errors and viscoelastic relaxation contribute to less than 0.05 μm of the mean cumulated slip (Figure A.2). The existence of a sharp discontinuity in displacements across the interface, rather than a gradual one, also dismisses shear-induced deformation of the material near the interface as a possible alternative explanation of the measured slip (Figure A.3).

A.1.5 Fitting the slip measurements

According to rate-and-state friction formulations (Bhattacharya et al., 2022, Blanpied et al., 1995, Dieterich, 1979, Marone, 1998a, Rice and Ruina, 1983, Rice et al., 2001, Ruina, 1983, Tullis and Weeks, 1986), which have been developed based on previous laboratory experiments sliding two rock surfaces or gouge layer, friction coefficient depends on slip rate $V(t)$ and has memory effects captured by an evolving state variable $\theta(t)$. One example is:

$$f = f^* + a \ln\left(\frac{V(t)}{V^*}\right) + b \ln\left(\frac{V^*\theta(t)}{D_{RS}}\right) \tag{A.1}$$

where t is time, f is the evolving friction coefficient, f^* is a reference friction coefficient at reference slip rate V^*, D_{RS} is the critical slip distance, and a and b are nondimensional parameters quantifying the direct and evolutionary effects, respectively.

The velocity-dependent term (direct effect) is universally positive ($a > 0$) and can be interpreted as the breaking of asperities from a thermally activated Arrhenius process (Rice et al., 2001). The state-dependent term (evolutionary effect) is interpreted as the logarithmic growth of the real area of contact due to thermally activated creep

(Ben-David et al., 2010, Berthoud et al., 1999, Dieterich and Kilgore, 1994, Ikari et al., 2016, Perfettini and Molinari, 2017). Two typical choices for the state evolution law include the "aging law" (Dieterich, 1979) and the "slip law" (Ruina, 1983), respectively:

$$\frac{d\theta}{dt} = 1 - \frac{V(t)\theta(t)}{D_{RS}} \tag{A.2}$$

$$\frac{d\theta}{dt} = -\frac{V(t)\theta(t)}{D_{RS}} \ln\left(\frac{V(t)\theta(t)}{D_{RS}}\right). \tag{A.3}$$

At steady state, i.e., $d\theta/dt = 0$, both state evolution laws converge and $\theta = D_{RS}/V$ reflects the contact age. Moreover, the friction coefficient becomes purely slip rate-dependent:

$$f = f^* + (a - b) \ln\left(\frac{V}{V^*}\right). \tag{A.4}$$

If $a < b$, the friction coefficient at steady state decreases with slip rate and the interface is said to be "velocity-weakening." On the contrary, if $a > b$, friction increases with slip rate, and the interface is "velocity-strengthening." If $a = b$, friction does not change with slip rate and the interface is "velocity-neutral." Stability analysis shows that unstable slip can only occur for a velocity-weakening interface (Rice and Ruina, 1983, Scholz, 2019).

A drawback of the logarithmic form (Equation A.1) is that the stress is not defined for $V = 0$. The logarithmic form was derived from purely empirical considerations to match experimental observations (Dieterich, 1979, 1981, Ruina, 1983). This form is consistent with an Arrhenius rate process at contact junctions in the range for which forward microscopic jumps, in the direction of shear stress, are overwhelmingly more frequent than backward jumps, and hence the backward jumps are ignored. Such an interpretation has been implicit or explicit in a number of studies (Baumberger, 1997, Berthoud et al., 1999, Brechet and Estrin, 1994, Chester, 1994, Heslot et al., 1994, Nakatani, 2001, Persson, 1998, Sleep, 1997, Stesky, 1978).

Accounting for backward jumps, which are expected to be comparable to forward jumps near zero shear stress and zero slip rate, gives (Lapusta et al., 2000):

$$f = a \sinh^{-1}\left(\frac{V(t)}{2V^*}\exp\left(\frac{f^* + b\ln\left(\frac{V^*\theta(t)}{D_{RS}}\right)}{a}\right)\right). \tag{A.5}$$

This physically based regularized form highlights that exactly zero velocities are only expected at zero shear stress, with any non-zero shear stress giving rise to some slip rate. Note that this regularized form is indistinguishable from the logarithmic one in the range of experimental observations, and so we will continue using the logarithmic form in our analysis. Another way to regularize the rate-and-state formulation (Equation A.1) is to impose a linearization of friction coefficient with slip rate when the slip rate drops below some threshold value Vlinear (Aagaard et al., 2019):

$$f = \begin{cases} f^* + a\ln\left(\frac{V(t)}{V^*}\right) + b\ln\left(\frac{V^*\theta(t)}{D_{RS}}\right) & \text{if } V \geq V_{\text{linear}} \\ f^* + a\ln\left(\frac{V_{\text{linear}}}{V^*}\right) + b\ln\left(\frac{V^*\theta(t)}{D_{RS}}\right) - a\left(1 - \frac{V(t)}{V_{\text{linear}}}\right) & \text{if } V < V_{\text{linear}}. \end{cases} \tag{A.6}$$

The threshold value V_{linear} is typically chosen as 10^{-12} m/s.

Our slip measurements reveal that both bare PMMA surface and those embedded with rock gouge continue to slide over the duration of the experiments even though the friction coefficient is smaller than its static value. Rate-and-state friction predicts that all interfaces are always sliding24 and could potentially explain our observations. Rewriting Equation A.1 to solve for $V(t)$ yields:

$$V(t) = V^* \exp\left(\frac{f - f^*}{a}\right)\left(\frac{V^*\theta(t)}{D_{RS}}\right)^{-\frac{b}{a}}. \tag{A.7}$$

In general, no closed-form solutions exist for systems of equations (Equation A.2 and A.7) or (Equation A.3 and A.7). While it is possible to fit the slip measurements by using a grid search and fully evolve the state variable through a finite difference scheme, the number of free parameters results in many possible solutions. In the following subsections, we present two particular cases where there exists a closed-form expression for $\theta(t)$, $V(t)$ and $\delta(t)$.

A.1.6 Closed-form expression of slip when $a = b$

Motivated by the approximately velocity-neutral behavior of PMMA, we can assert a special case where $a = b$. In such case, Equation A.7 simplifies to:

$$V(t) = \exp\left(\frac{f - f^*}{a}\right)\frac{D_{\mathrm{RS}}}{\theta(t)} \tag{A.8}$$

and, hence, the state evolution laws (Equations A.2 and A.3) become:

$$\frac{d\theta}{dt} = 1 - \exp\left(\frac{f - f^*}{a}\right) \tag{A.9}$$

$$\frac{d\theta}{dt} = -\frac{f - f^*}{a}\exp\left(\frac{f - f^*}{a}\right). \tag{A.10}$$

The state variable θ is generally envisioned to be related to the contact time. For the experiments conducted in this study, $\theta = 0$ would correspond to the time we place the two halves of the specimen in contact with one another, which we could arbitrarily set to be at $t = 0$. With this initial condition, integrating Equations A.9 and A.10 would lead to the following expressions for the state variable:

$$\theta(t) = \left(1 - \exp\left(\frac{f - f^*}{a}\right)\right)t \tag{A.11}$$

$$\theta(t) = -\left(\frac{f - f^*}{a}\right)\exp\left(\frac{f - f^*}{a}\right)t. \tag{A.12}$$

Substituting Equations A.11 and A.12 into A.8 yields expressions for slip rate as a function of time:

$$V(t) = \frac{D_{\mathrm{RS}}}{\exp\left(\frac{f^* - f}{a}\right) - 1}t^{-1} \tag{A.13}$$

$$V(t) = \frac{aD_{\mathrm{RS}}}{f^* - f}t^{-1} \tag{A.14}$$

which we can integrate to get the evolution of slip, $\delta(t)$:

$$\delta(t) = \frac{D_{\mathrm{RS}}}{\exp\left(\frac{f^* - f}{a}\right) - 1}\ln t + C \tag{A.15}$$

$$\delta(t) = \frac{aD_{\mathrm{RS}}}{f^* - f} \ln t + C \tag{A.16}$$

where C is an integration constant.

Hence, assuming that the interface is approximately velocity-neutral, we can perform a least-square inversion of the slip observations using the general logarithmic form:

$$\delta(t) = C_1 \ln t + C_2. \tag{A.17}$$

The best-fit parameter C_1 can then be used to constrain frictional parameters a, D_{RS} and f^* since $C_1 = D_{RS}/(\exp(\frac{f^*-f}{a}) - 1)$ for the aging law and $C_1 = aD_{RS}/(f^* - f)$ for the slip law, respectively. The parameter C_2 is related to the initial condition of the system.

We find the best-fit parameters through a standard linear least-square inversion and explore the surrounding parameter space through a grid search. For bare PMMA surfaces, the search range is between 0 and 1.5 μm for C_1 and between -100 and 100 $\mu\mu$m for C_2. For surfaces embedded with rock gouge, the search range is between 0 and 50 μm for C_1 and between -1000 and 1000 μm for C_2. The grid search results are shown in Figures A.4 to A.7 and Tables A.3 and A.4.

We note that for these specific conditions, a decelerating fault implies that f^* must be larger than f. Indeed, taking the temporal derivatives of Equations A.13 and A.14 yields

$$\frac{\partial V}{\partial t} = -\frac{D_{\mathrm{RS}}}{\exp\left(\frac{f^*-f}{a}\right) - 1} t^{-2} \tag{A.18}$$

$$\frac{\partial V}{\partial t} = -\frac{aD_{\mathrm{RS}}}{f^* - f} t^{-2} \tag{A.19}$$

which shows that $\partial V/\partial t$ can only be negative when $f^* > f$ (given positive D_{RS} and a) in both cases.

A.1.7 Closed-form expression of slip when $\theta \sim t$

A different simplification arises in the aging law framework when the state variable is approximately equal to time. Motivated by slow slip rate expected from the experiment, we can explore the limiting case where $V\theta/D_{RS} \ll 1$. In this case, the aging law reduces to $d\theta/dt = 1$ and the state variable integrates to $\theta(t) = t + t_0$, for some integration constant t_0. The expressions for slip rate and slip become, respectively:

$$V(t) = V^* \exp\left(\frac{f - f^*}{a}\right)\left(\frac{V^*(t - t_0)}{D_{\mathrm{RS}}}\right)^{-\frac{b}{a}} \tag{A.20}$$

$$\delta(t) = \left(\frac{a}{a-b}\right) V^* \exp\left(\frac{f - f^*}{a}\right)\left(\frac{V^*}{D_{\mathrm{RS}}}\right)^{-\frac{b}{a}} (t - t_0)^{1-\frac{b}{a}} + C. \tag{A.21}$$

The slip observations can then be fitted with a power-law relationship of the form:

$$\delta(t) = C_1(t - t_0)^{C_3} + C_2 \tag{A.22}$$

from which b/a can be inferred from $C_3 = 1 - b/a$ and the frictional parameters a, D_{RS} and f^* can be constrained from $C_1 = \left(\frac{a}{a-b}\right) V^* \exp\left(\frac{f-f^*}{a}\right)\left(\frac{V^*}{D_{\mathrm{RS}}}\right)^{-\frac{b}{a}}$. As before, we find the best-fit parameters through a standard linear least-square inversion and explore the surrounding parameter space through a grid search. For bare PMMA surfaces, the search range is between -50 and 50 μm/s$^{1-b/a}$ for C_1, between -200 and 200 µm for C_2, between -0.5 and 0.5 for C_3, and between -10 hr and the time t where we have the first image for t_0. For surfaces embedded with rock gouge, the search range is between -500 and 500 μm/s$^{1-b/a}$ for C_1, between -2000 and 2000 µm for C_2, between -0.5 and 0.5 for C_3, and between -10 hr and the time t where we have the first image for t_0. The grid search results are shown in Figures A.8 to A.12 and Tables A.5 and A.6.

There are ranges of parameters that would be unphysical according to the rate-and-state formulation. Since we expect a, V^*, f^*, and D_{RS} to be positive, we cannot have a velocity-strengthening interface ($b < a$) and $C_1 < 0$ or a velocity-weakening interface ($b > a$) and $C_1 > 0$ (see Figures A.9 and A.11). This also ensures that slip accumulates monotonically over time. We also find that for any set of $C_1 > 0$ and $C_3 > 0$, there exists another pair of $C_1 < 0$ and $C_3 < 0$ that can fit the data almost

as well (see Figure A.12), demonstrating that the fitting exercise is ill-posed even when making simplifying assumptions to reduce the number of fitting parameters.

To a posteriori test whether the $V\theta/D_{RS} \ll 1$ approximation is indeed appropriate, we can first rewrite it as follows:

$$\frac{V\theta}{D_{\mathrm{RS}}} = \frac{C_1(1-\frac{b}{a})(t+t_0)^{1-\frac{b}{a}}}{D_{\mathrm{RS}}}. \tag{A.23}$$

As noted previously, because $C_1 > 0$ for $b < a$ and $C_1 < 0$ for $b > a$, $C_1\left(1-\frac{b}{a}\right)$ is always positive. Therefore, $V\theta/D_{RS}$ will grow over time for $b < a$ and decay over time for $b > a$. As such, $V\theta/D_{RS} \ll 1$ will become increasingly true for a velocity-weakening interface. Since we infer our interface to be weakly velocity-weakening, the approximation is deemed appropriate. We have also computed $V\theta/D_{RS}$ for the V inferred from our observations and for a typical value of $D_{RS} \sim 10$ μm, we find $V\theta/D_{RS}$ drops to below 0.1 after 1 hr (see Figure A.13). Note that it is not necessary to have small $V\theta/D_{RS}$ from the beginning. As soon as the approximation is true, we find θ growing as t with some offset t_0 that records the initial process when $V\theta/D_{RS}$ may not necessarily be much smaller than 1.

A.2 Supplementary figures

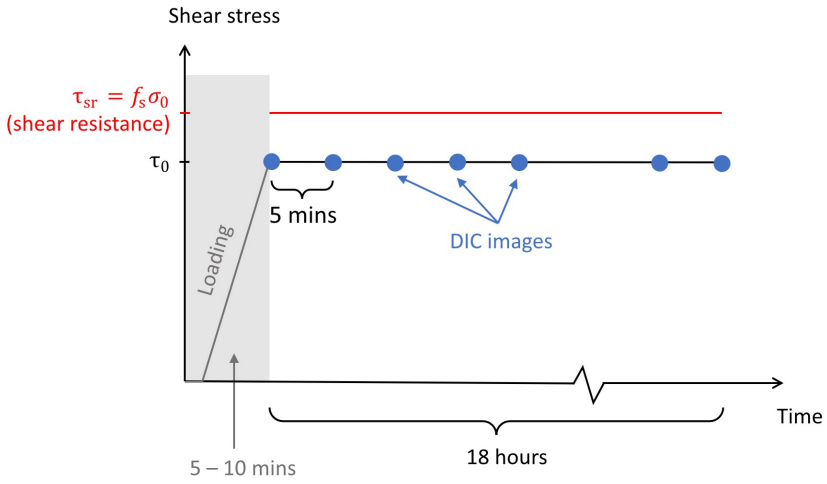

Figure A.1: A schematic summarizing the experimental procedure. For each test, a specimen with an inclination angle α is loaded uniaxially to a preset load P = 10 MPa with resolved normal stress $\sigma_0 = P\cos^2\alpha$ = 8.08 MPa and resolved shear stress $\sigma_0 = P\sin\alpha\cos\alpha$ = 3.94 MPa. The load is maintained for 18 hours (6.48 x 104 seconds), and optical images are taken every 5 minutes.

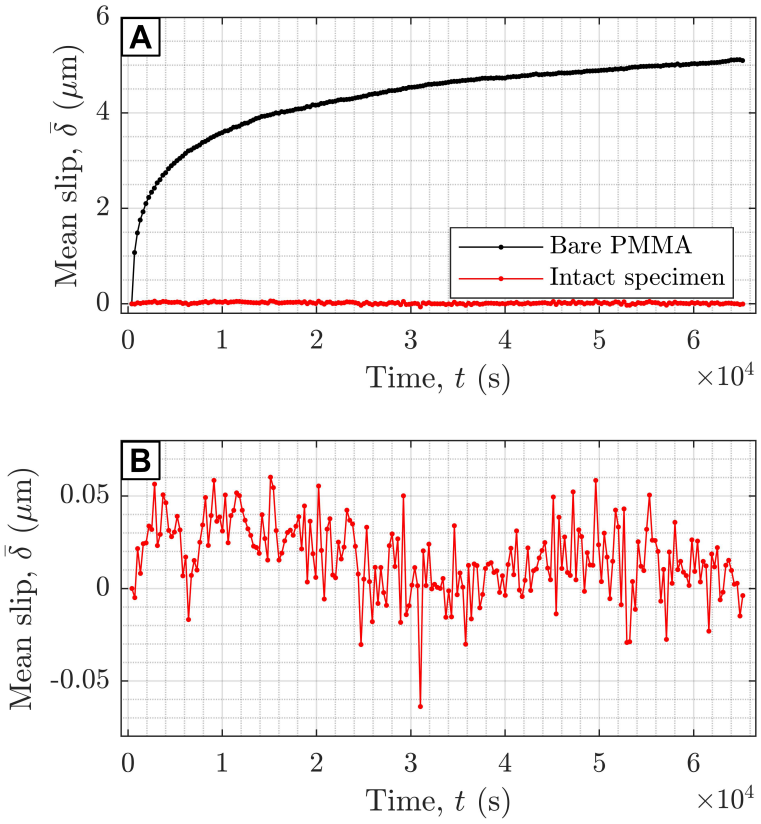

Figure A.2: Comparison of bare PMMA test (with interface) with an intact specimen (no interface). (A) Mean accumulated slip $\bar{\delta}$ measured using identical experimental procedures and data analysis for a specimen with bare PMMA interface and a reference intact specimen without any interface indicating potential bulk effects and/or experimental error. (B) is the zoomed in version of (A). The comparison clearly shows the slip measured along nominally stationary PMMA interfaces is much larger than the experimental error and bulk effects (standard deviation < 0.02 μm).

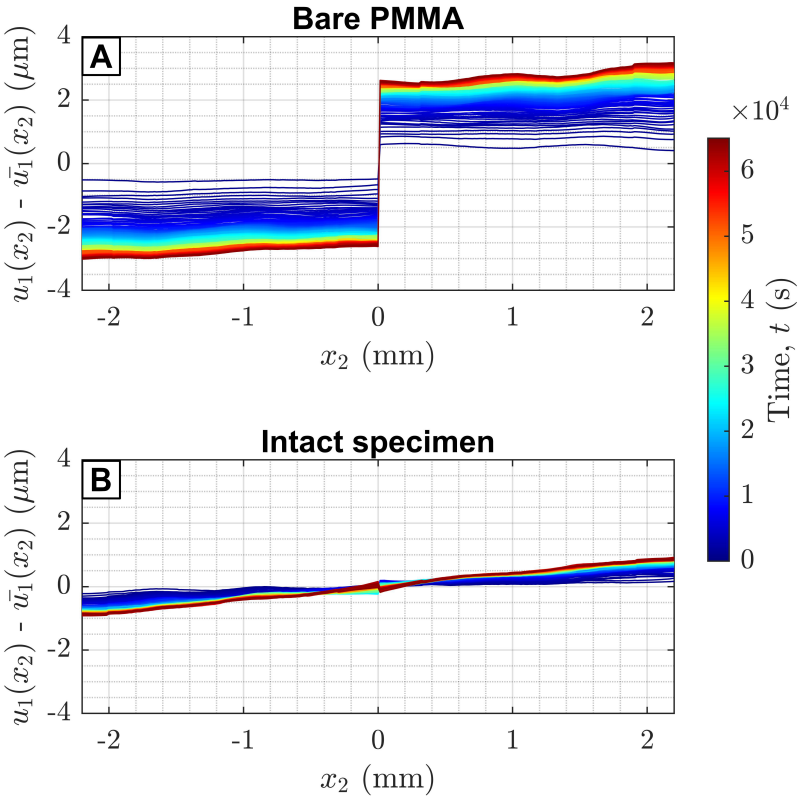

Figure A.3: Minimal shear-induced deformation of material near the interface. (A) A representative profile of the measured fault-parallel displacement u_1 across the direction x_2 (perpendicular to the interface) for bare PMMA surface, color coded by time. (B) is similar to (A) but for an intact specimen. The mean displacement ($\bar{u_1}$) for each profile is subtracted to remove any rigid body translation that may be due to some small vibration of camera or the optical table allowing for better visualization. The profile in (A) looks more like a step function than an S-shape, dismissing shear-induced deformation of material near interface from contributing in any significant way to the observed accumulated slip $\delta(t)$.

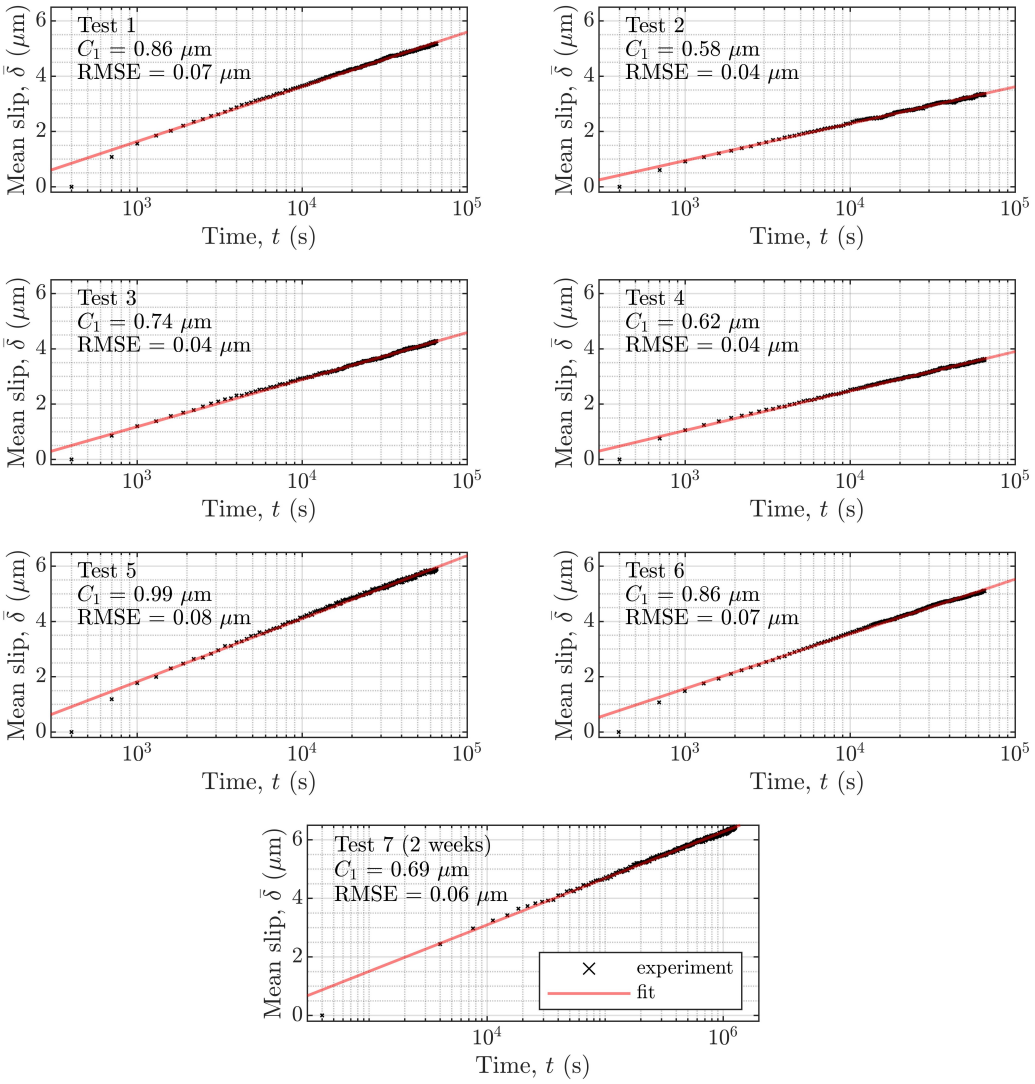

Figure A.4: Fitting the mean cumulated slip $\bar{\delta}$ of bare PMMA interfaces with logarithmic functions ($\bar{\delta} = C_1 \log t + C_2$). The interfaces are re-polished and re-beadblasted for each individual test to maintain experimental repeatability (See also Table A.3). The bare PMMA tests shown in the main text are test 1 (18 hr) and test 7 (2 weeks).

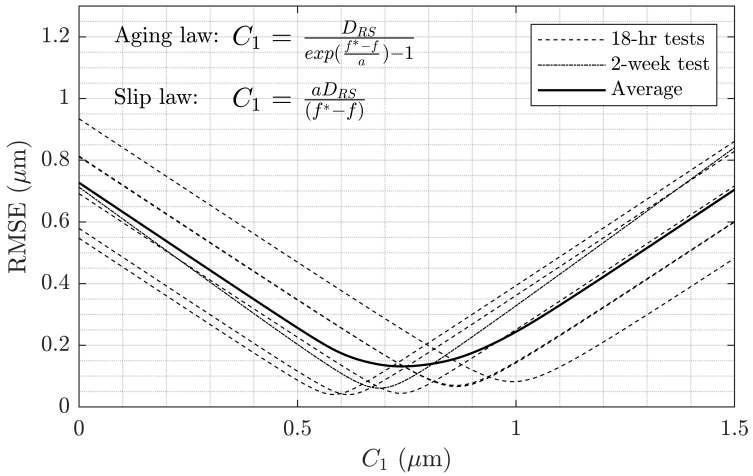

Figure A.5: Parameter space exploration fitting the mean cumulated slip $\bar{\delta}$ of bare PMMA interfaces with logarithmic functions ($\bar{\delta} = C_1 \log t + C_2$). The root-mean-square error (RMSE) is shown for each individual experiment and as an average of all 7 tests (six 18-hr tests and one 2-week test). The logarithmic form arises from the velocity-neutral approximation ($a = b$). The fitting parameter C_1 can be explained with a combination of rate-and-state parameters. Their exact form depends on the choice of state evolution law (aging law or slip law) (See also Table A.3).

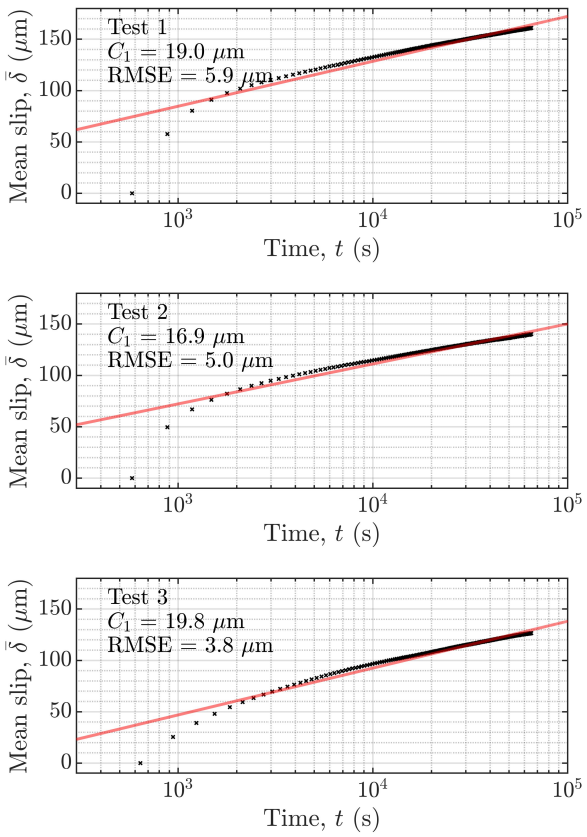

Figure A.6: Fitting the mean cumulated slip $\bar{\delta}$ of interfaces embedded with rock gouge with logarithmic functions ($\bar{\delta} = C_1 \log t + C_2$). The interfaces are re-polished and re-beadblasted for each individual test to maintain experimental repeatability (See also Table A.4). The rock gouge test in the main text is test 1 (18 hr).

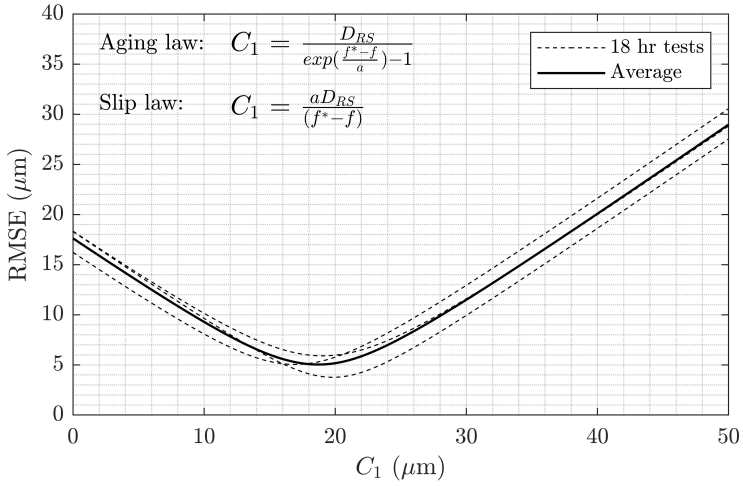

Figure A.7: Parameter space exploration fitting the mean cumulated slip $\bar{\delta}$ of interfaces embedded with rock gouge with logarithmic functions ($\bar{\delta} = C_1 \log t + C_2$). The root-mean-square error (RMSE) is shown for each individual experiment and as an average of all three 18-hr tests. The logarithmic form arises from the velocity-neutral approximation ($a = b$). The fitting parameter C_1 can be explained with a combination of rate-and-state parameters. Their exact form depends on the choice of t state evolution law (aging law or slip law) (See also Table A.4).

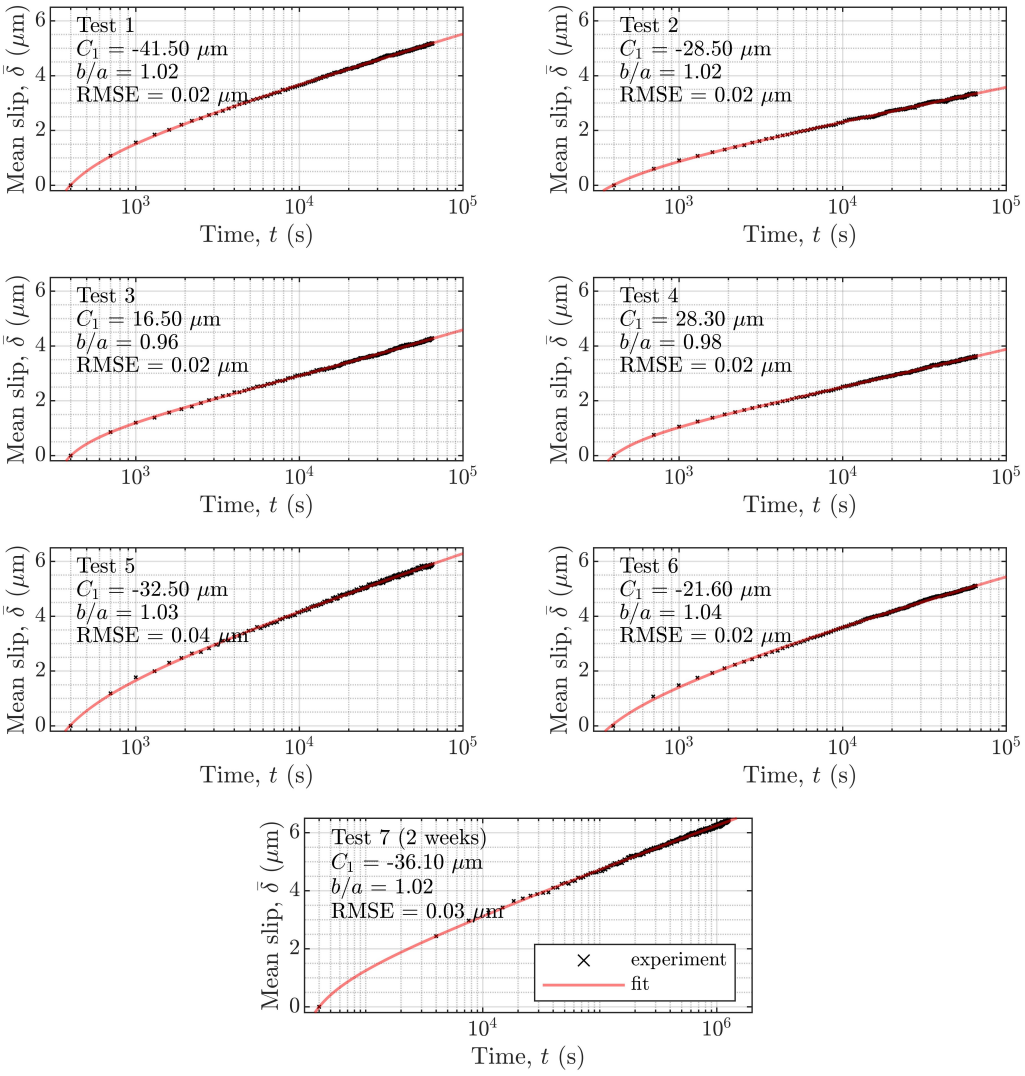

Figure A.8: Fitting the mean cumulated slip $\bar{\delta}$ of bare PMMA interfaces with power laws ($\bar{\delta} = C_1(t - t_0)^{1-b/a} + C_2$). The interfaces are re-polished and re-beadblasted for each individual test to maintain experimental repeatability (See also Table A.5). The bare PMMA test shown in the main text is test 1 (18 hr) and test 7 (2 weeks).

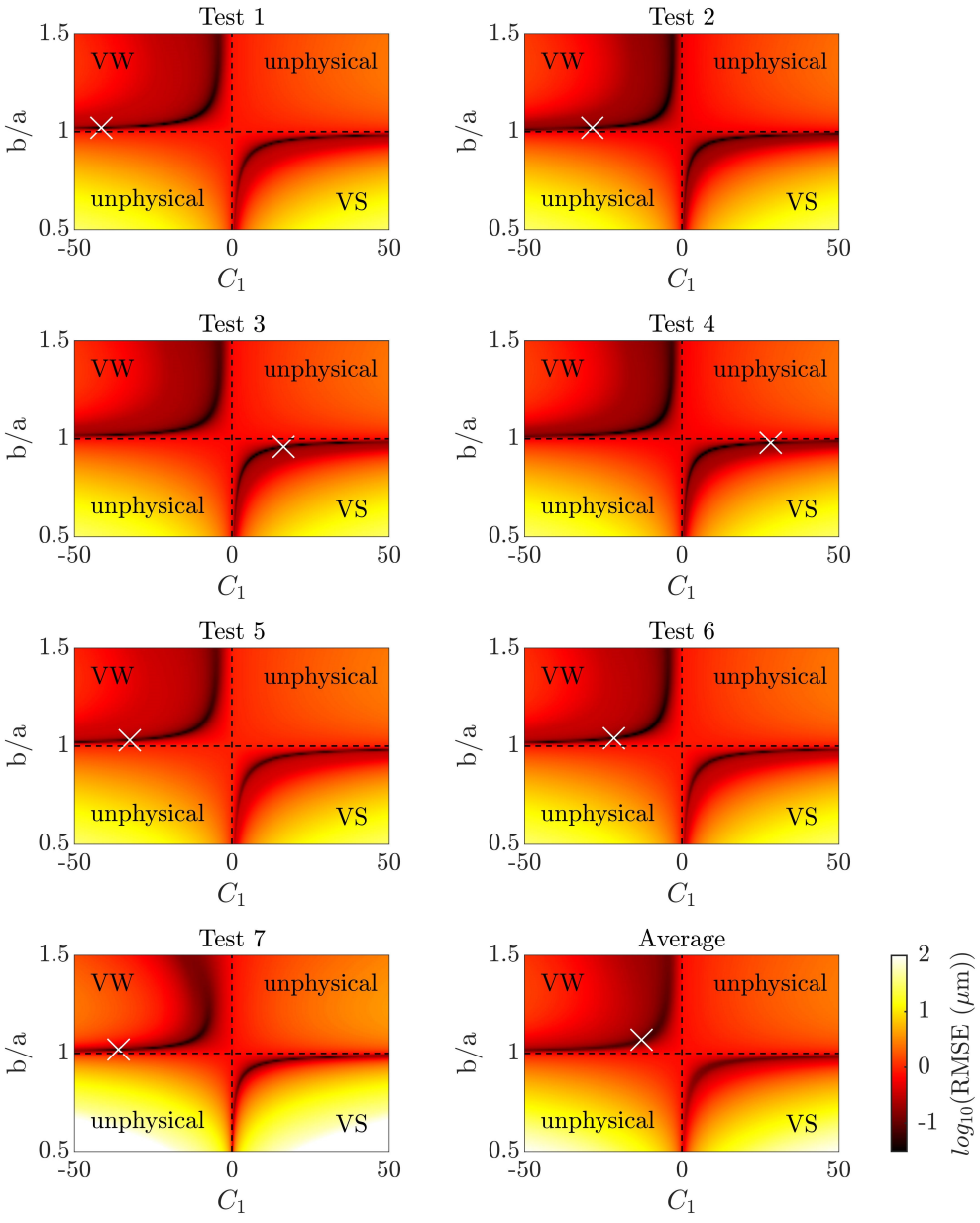

Figure A.9: Parameter space exploration fitting the mean cumulated slip $\bar{\delta}$ of bare PMMA interfaces with power laws ($\bar{\delta} = C_1(t - t_0)^{1-b/a} + C_2$). The root-mean-square error (RMSE) is shown for each individual experiment and as an average of all seven tests (six 18-hr tests and one 2-week test). The power law form arises from the aging law with $V\theta/D_{RS} \ll 1$, in which case the state variable θ is approximately the time t offset by some constant t_0. The fitting parameter C_1 can be explained with a combination of rate-and-state parameters, i.e., $C_1 = \left(\frac{a}{a-b}\right) V^* \left(\frac{V^*}{D_{RS}}\right)^{-b/a} \exp\left\{\left(\frac{f-f^*}{a}\right)\right\}$ with unit being $\mu m/s^{1-b/a}$ (See also Table A.5). The bare PMMA test shown in the main text is test 1 (18 hr) and test 7 (2 weeks).

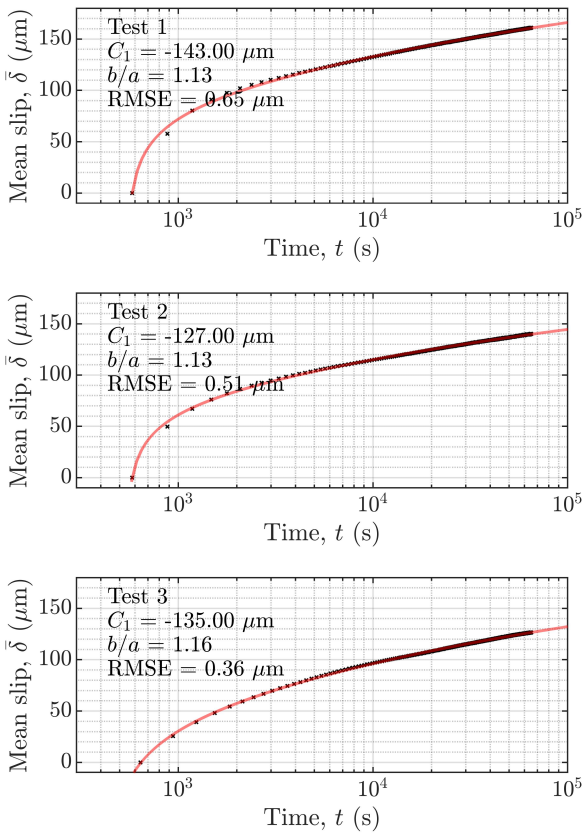

Figure A.10: Fitting the mean cumulated slip $\bar{\delta}$ of interfaces embedded with rock gouge with power laws ($\bar{\delta} = C_1(t - t_0)^{1-b/a} + C_2$). The interfaces are re-polished and re-beadblasted for each individual test to maintain experimental repeatability (See also Table A.6). The rock gouge test in the main text is test 1 (18 hr).

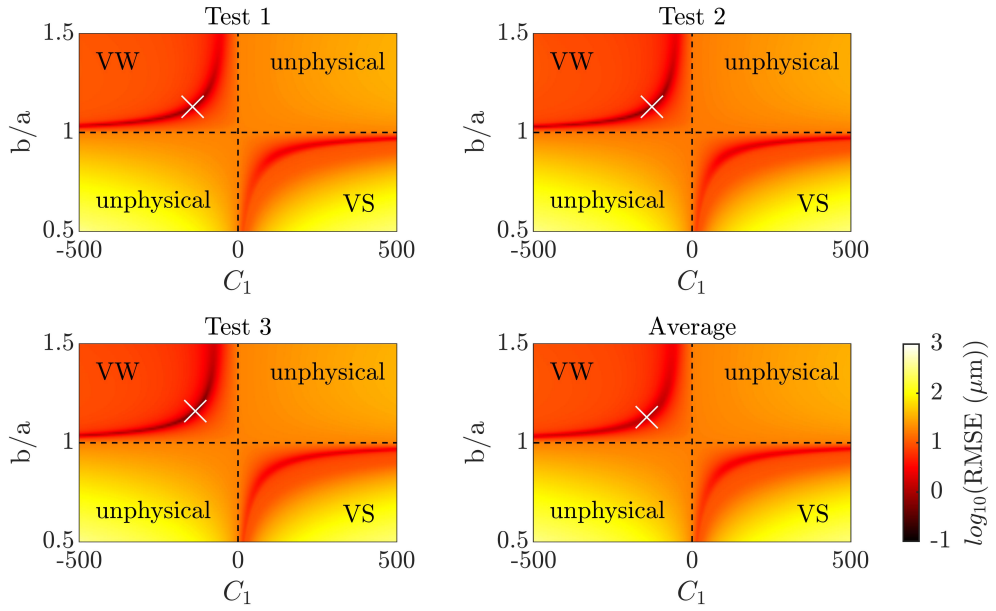

Figure A.11: Parameter space exploration fitting the mean cumulated slip $\bar{\delta}$ of interfaces embedded with rock gouge with power laws ($\bar{\delta} = C_1(t - t_0)^{1-b/a} + C_2$). The root-mean-square error (RMSE) is shown for each individual experiment and as an average of all three 18-hr tests. The power law form arises from aging law with $V\theta/D_{RS} \ll 1$, in which case the state variable θ is approximately the time t offset by some constant t_0. The fitted parameter C_1 can be explained with a combination of rate-and-state parameters, i.e., $C_1 = \left(\frac{a}{a-b}\right) V^* \left(\frac{V^*}{D_{RS}}\right)^{-b/a} \exp\left\{\left(\frac{f-f^*}{a}\right)\right\}$ with unit being $\mu m/s^{1-b/a}$ (See also Table A.6). The rock gouge test in the main text is test 1 (18 hr).

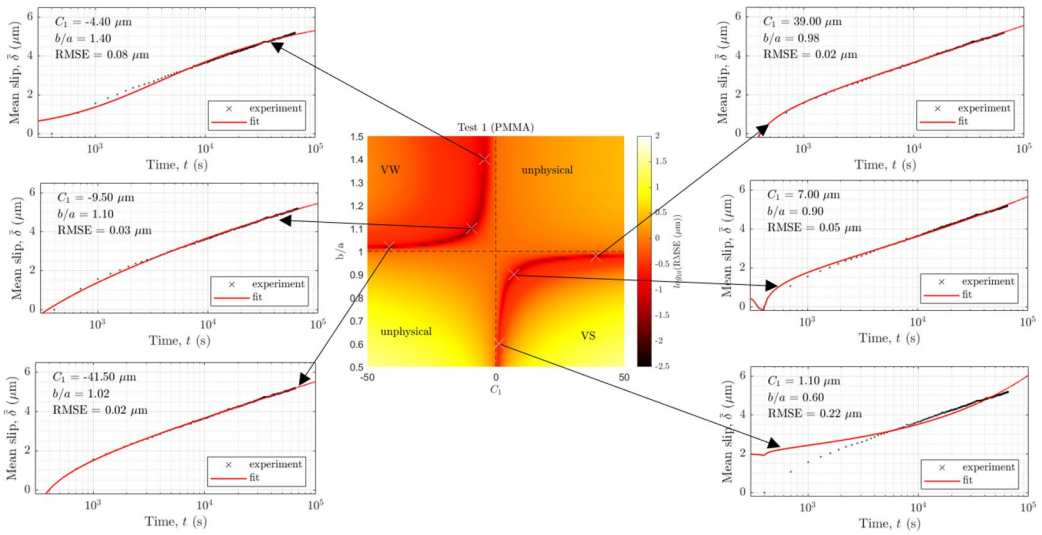

Figure A.12: Evaluating the fitting quality of power laws ($\bar{\delta} = C_1(t - t_0)^{1-b/a} + C_2$) for mean cumulated slip $\bar{\delta}$ of bare PMMA interface from test 1. While there are parameters with velocity-strengthening and velocity-weakening that result in a small RMSE, visual inspection of the fit favors velocity-neutral parameters.

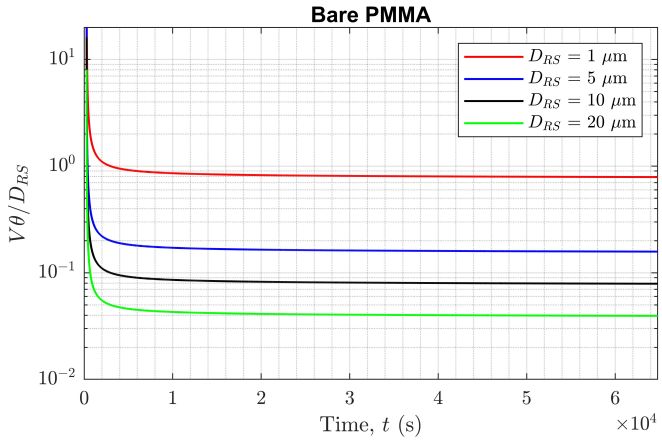

Figure A.13: Evaluating a posterior the $V\theta/D_{RS} \ll 1$ approximation. Calculations of $V\theta/D_{RS}$ using the best-fit V and t_0 from bare PMMA test 1 for different possible values of D_{RS}. For a typical value of D_{RS} = 5 μm, $V\theta/D_{RS} < 0.1$ after the first hour.

A.3 Supplementary tables

Camera	Imaging Source monochrome camera DMK 37BUX250
Image size	3 MP, 2048 x 1536 px^2
Lens	Schneider Optics Xenoplan compact series (21-1001976) with 10 mm extension ring
Focal length	50 mm
Aperture	f/2.8
Field of view	30 x 22.5 mm^2
Image scale	68.3 px/mm
Stand-off distance	300 mm
Image acquisition rate	32 frames at 50 fps every 5 mins
Exposure time	0.02 s
Patterning technique	base coat of Krylon white paint with small black and white speckles on top
Pattern feature size	5 px

Table A.1: Digital image correlations (DIC) hardware parameters used in this study.

DIC software	Correlated Solutions VIC-2D (version 6.2.0)
Image filtering	32 frames numerically averaging
Reference image	single reference image (standard correlation)
Interpolant	continuous splines (8-tap)
Matching criterion	zero-normalized squared differences
Subset / Element size	41 px (approximately 0.6 mm)
Step size	1 px (approximately 15 μm)
Subset shape function	affine
Subset weights	Gaussian

Table A.2: Digital image correlations (DIC) analysis parameters used in this study.

Test no.	Interface type	Duration	C_1 (μm)	C_2 (μm)	RMSE (μm)	% misfit
1	Bare PMMA	18 hr	0.86	2.74	0.07	1.6%
2	Bare PMMA	18 hr	0.58	1.69	0.04	1.4%
3	Bare PMMA	18 hr	0.74	2.13	0.04	1.1%
4	Bare PMMA	18 hr	0.62	1.84	0.04	1.3%
5	Bare PMMA	18 hr	0.99	3.09	0.08	1.6%
6	Bare PMMA	18 hr	0.86	2.67	0.07	1.6%
7	Bare PMMA	2 weeks	0.68	2.44	0.06	1.1%

Table A.3: Best-fitting parameters and the corresponding root-mean-squared errors (RMSEs) obtained from fitting mean cumulated slip $\bar{\delta}$ of bare PMMA interfaces with logarithmic functions ($\bar{\delta} = C_1 \log t + C_2$). There are two fitting parameters, one physical parameter (C_1) and one initial condition (C_2).

Test no.	Interface type	Duration	C_1 (μm)	C_2 (μm)	RMSE (μm)	% misfit
1	Rock gouge	18 hr	19.0	109.1	5.9	4.1%
2	Rock gouge	18 hr	16.9	93.9	5.0	4.0%
3	Rock gouge	18 hr	19.8	72.3	3.8	3.4%

Table A.4: Best-fitting parameters and the corresponding root-mean-squared errors (RMSEs) obtained from fitting mean cumulated slip $\bar{\delta}$ of interfaces embedded with rock gouge with logarithmic functions ($\bar{\delta} = C_1 \log t + C_2$). There are two fitting parameters, one physical parameter (C_1) and one initial condition (C_2).

Test no.	Interface type	Duration	C_1 (μm/s$^{1-b/a}$)	b/a	C_2 (μm)	t_0 (hr)	RMSE (μm)	% misfit
1	Bare PMMA	18 hr	-41.5	1.02	44.35	0.07	0.02	0.5%
2	Bare PMMA	18 hr	-28.5	1.02	30.24	0.06	0.02	0.7%
3	Bare PMMA	18 hr	-16.5	0.96	-14.26	0.09	0.02	0.6%
4	Bare PMMA	18 hr	-28.3	0.98	-26.37	0.08	0.02	0.7%
5	Bare PMMA	18 hr	-32.5	1.03	35.71	0.07	0.04	0.8%
6	Bare PMMA	18 hr	-21.6	1.04	24.35	0.06	0.02	0.5%
7	Bare PMMA	2 weeks	-36.0	1.02	38.41	0.07	0.04	0.7%

Table A.5: Best-fitting parameters and the corresponding root-mean-squared errors (RMSEs) obtained from fitting mean cumulated slip $\bar{\delta}$ of bare PMMA interfaces with power laws ($\bar{\delta} = C_1(t - t_0)^{1-b/a} + C_2$).There are four fitting parameters, two physical parameters (C_1) and two initial conditions (C_2).

Test no.	Interface type	Duration	C_1 (μm/s$^{1-b/a}$)	b/a	C_2 (μm)	t_0 (hr)	RMSE (μm)	% misfit
1	Rock gouge	18 hr	-143	1.13	259	0.15	0.65	0.5%
2	Rock gouge	18 hr	-127	1.13	227	0.15	0.51	0.4%
3	Rock gouge	18 hr	-135	1.16	212	0.12	0.36	0.3%

Table A.6: Best-fitting parameters and the corresponding root-mean-squared errors (RMSEs) obtained from fitting mean cumulated slip $\bar{\delta}$ of interfaces embedded with rock gouge with power laws ($\bar{\delta} = C_1(t - t_0)^{1-b/a} + C_2$).There are four fitting parameters, two physical parameters (C_1) and two initial conditions (C_2).

Appendix B

SUPPLEMENTARY MATERIALS FOR CHAPTER 4

B.1 Extracting deformation related to the swarm

The following text supplements Section 4.3.2 on the extended descriptions of the steps used to extract deformation related to the swarm from the GPS position time series and related justifications.

We first work with the daily sampled position time series and start by fitting the observations (Figure B.4) using least square minimizations to find the optimized parameters of the trajectory model (Bevis and Brown, 2014):

$$\begin{aligned} x(t) = x_0 + v_0 t + A_1^{\sin} \sin(f_1 t + \phi_1) + A_2^{\sin} \sin(f_2 t + \phi_2) \\ + \sum_{i=1}^{n_{\text{instr}}} A_i^{\text{instr}} H(t - t_i) \\ + \sum_{i=1}^{n_{\text{eq}}} H(t - t_i) \left[A_i^{\text{co}} + A_i^{\text{post}} \left(1 - e^{\frac{t - t_i}{\tau_i}} \right) \right]. \end{aligned} \tag{B.1}$$

The trajectory model uses a set of analytical functions based on the commonly observed geodetic deformations. This includes the following:

- the initial position x_0 at $t = 0$
- a linear function representing the long-term tectonics motion with a displacement rate v_0
- a sinusoidal function with amplitude $A_1^{\sin}$, an annual period $T_1 = 1/f_1$ and an initial phase of ϕ_1 representing annual variation
- a sinusoidal function with amplitude $A_2^{\sin}$, a half-year period $T_2 = 1/f_2$ and an initial phase of ϕ_2 representing semi-annual seasonal variation
- Heaviside step functions representing offsets with amplitude A_i^{instr} due to instrumentations such as station maintenance at $t = t_i$
- Heaviside step functions representing offsets with amplitude A_i^{co} due to earthquakes (co-seismic displacements) at $t = t_i$, and

- exponential decays of amplitude A_i^{post} and a characteristic relaxation time of τ_i after the earthquakes occurring at $t = t_i$.

To determine when co-seismic or instrumental steps are expected, we use the list of potential steps provided by the Nevada Geodetic Laboratory (Blewitt et al., 2018, http://geodesy.unr.edu/NGLStationPages/steps.txt, last accessed November 14, 2020). An earthquake with magnitude M is considered to potentially cause a step at a given station if the distance between the epicenter and the station in km is less than $10^{(M/2\tilde{}0.79)}$. The first iteration of trajectory model fitting utilizes all steps in the NGL steps file. The quality of the fits is then assessed, and steps that are too small (< 3 mm) are removed to reduce the number of fitting parameters. Additional steps for local effects not documented in the NGL steps file are added as appropriate. The final list of steps used can be found in Supporting Table B.1.

We use the trajectory model only to estimate the long-term trend and the co-seismic and instrumental steps. The technique is inappropriate for modeling seasonal signals because they are not precisely harmonic and generally show interannual variability. The detrended time series thus contain the transient geodetic signal that we are interested in, along with seasonal variations and other smaller signals.

If the transient geodetic signal due to the swarm dominates the data variance, a Principal Component Analysis (PCA) decomposition (Kositsky and Avouac, 2010) can be used to extract it. Since the deformations during the swarm are small, we use the modified variational Bayesian Independent Component Analysis (vbICA) decomposition (Gualandi et al., 2016), a blind source separation technique, to isolate various non-linear signals remaining in the detrended time series. The vbICA decomposition separates the signals by simultaneously maximizing statistical independence of the signals' probability density function (pdf) and minimizing misfit with the data without any presumed analytical forms. The method uses a Bayesian framework which requires a priori assumptions of the sources' pdf taken to be a mixture of Gaussians (MoG). Here, we use 4 Gaussians as recommended by Choudrey and Roberts (2003), governed by a similar set of hyper-parameters to Gualandi et al. (2020) (Table B.2). Each signal isolated ($i = 1, 2, \ldots, R$) is an independent component (IC) that includes a stationary spatial function ($U_{M\times R}$) explaining the amplitude of the signal for the different position time series ($m = 1, 2, \ldots, M$), the relative strength of the signal comparing to other signals ($S_{R\times R}$), and a time function ($V_{T\times R}$) describing signal's variation with time ($t = 1, 2, \ldots, T$). Simple matrix multiplication of the spatial distributions, the relative strengths, and

the time functions provides the original time series reconstruction. The unmodeled part is then regarded as noises and depicted using a noise matrix (N).

The decomposition, as discussed, can be written in a formulation similar to the Principal Component Analysis (PCA) as follow:

$$X_{M\times T} = U_{M\times R} S_{R\times R} V^T_{R\times T} + N_{M\times T} \approx U_{M\times R} S_{R\times R} V^T_{R\times T}. \tag{B.2}$$

The modified vbICA that we use here (Gualandi et al., 2016) is based on the original vbICA method (Choudrey and Roberts, 2003) but also takes into account data uncertainties and missing data (Chan et al., 2003) and has recently been successfully applied to daily sampled GPS position time series (e.g., Gualandi et al., 2017a, 2020, Larochelle et al., 2018, Michel et al., 2019, Serpelloni et al., 2018). The number of ICs to retain is chosen by the Automatic Relevance Determination (ARD) criterion (Gualandi et al., 2016), which evaluates the ratio between the maximum and the minimum a posteriori sources' variance. When this variances ratio is large, the IC with the smallest posterior variance can be discarded as noises. We increase the number of ICs until we see a jump in this variances ratio. Though MoG allows for flexibility in explaining multimodal pdf commonly observed in geophysical signals (Gualandi et al., 2016), its performance for estimating linear function is not optimal, which is why the data have to be detrended.

In our first vbICA decomposition, we concentrate on extracting the remaining non-linear signals unrelated to the swarm, such as the seasonal signals and the common mode motion. The input data include daily sampled position time series between 2016 and 2020.9 from 113 regional GPS stations between latitude 32 – 34°N and longitude 115 – 117°W. 33 stations were excluded due to insufficient temporal coverage (< 50%) or strong local site effects (large anomalous displacements > 10 mm not presented in any of the neighboring stations). The broader spatial coverage allows for better estimation of the common-mode jitter, which has a spatial wavelength of hundreds of km, while the longer temporal coverage allows for better estimation of seasonal variations due to hydrological cycles that have an annual period. Using narrower spatial and temporal coverage would prevent these larger-scale deformations from being accurately extracted. For 28 stations within 35 km from the center of the Westmorland swarm, data points after 2020.732 (September 25, 2020) were removed to prevent the deformations during the swarm from contaminating the larger-scale signal extractions. As we increase the number of ICs from 11 to 12, we observe a

big jump in the ratio of the variances (Figure B.5), and hence we choose to limit the maximum number of ICs to 11 based on the ARD criterion. Furthermore, when we have more than 8 ICs, some ICs contain residuals of co-seismic steps, which is unphysical (Figure B.6). Therefore, we prefer to decompose the time series into 8 ICs. We have also tested the different choices of priors and found the current set (Table B.2) appropriate as they maximize the number of ICs without co-seismic step residuals. From the 8 ICs decomposed, we associate ICs 1, 2, 4 to common-mode jitter, IC 3 to post-seismic relaxation following the 2019 Ridgecrest earthquakes, IC 5 to precipitation response, ICs 6, 7 to seasonal variations due to hydrological cycles, and IC 8 to operations of Brawley geothermal power plants (Figure B.7). These 8 ICs combined explain over 70% of the data variances (Figure B.8), leaving out the average root mean square misfit of 2.1 mm. IC 4 has a larger gradient at the time of the swarm. Since data during the swarm from stations near the swarm are not included, this gradient is unlikely to be related to the swarm. Moreover, the spatial function U_4 of IC 4 shows the same signal's amplitude across the region instead of having a larger amplitude for stations near the swarm in the case that the signals are related to the swarm. We have also repeated the study with numbers of ICs ranging from 6 to 8 and found our results independent of these choices.

Since the data during the swarm from stations < 35 km from Westmorland were not included in the vbICA decomposition, the corresponding displacements at these stations are extrapolated based on the displacement pattern determined for each component at the stations further away. The signal reflects only larger-scale processes unrelated to the swarm. We remove all 8 ICs from the original detrended position time series to obtain residuals that contain only the deformation due to the swarm. For the ICs related to common-mode jitter, we use the best least-squares fit rigid body motion instead of directly using the spatial distribution from vbICA decomposition.

With larger-scale variations removed from the position time series, we run the vbICA decomposition again using only the position time series near the time of the swarm between 2020.65 and 2020.81 (August 27 – October 24, 2020) from 17 stations within 35 km from the center of the Westmorland swarm. This time, the purpose of the vbICA decomposition is to extract the dominant signal related to the swarm and remove uncorrelated noises. Station P499 is excluded from the analysis due to a potential instrumental offset resulting from maintenance right before the swarm (see details at https://www.unavco.org/instrumentation/networks/status/nota/maintenance/P499).

We find that regardless of the number of ICs chosen, the first IC dominates (Figure B.9) and by itself explains over 77.2% of data variance (Figure B.10). The other ICs contribute at most 3% of data variance. Therefore, we keep only this first IC and associate it with the swarm.

Our result shows that the transient geodetic signal related to the swarm started within one day from the onset of the swarm. Hence, the time resolution provided by the daily data is not sufficient to determine whether the geodetic deformation preceded the swarm or was coeval. This prompted us to use instead the 5-min sampled position time series, also processed by the Nevada Geodetic Laboratory (Blewitt et al., 2018). Although these 5-min sampled position time series provide a much higher time resolution, the uncertainties associated with each data point are much larger. Therefore, performing vbICA decomposition directly on the 5-min sampled position series does not provide the best possible result.

To extract the deformation from the 5-min sampled position time series, we first write the desired decomposition using similar notation as Equation B.2:

$$X_{M\times T,\text{5min}} \approx U_{M\times R,\text{5min}} S_{R\times R,\text{5min}} V^T_{R\times T,\text{5min}}. \tag{B.3}$$

Recall that we already have the vbICA decomposition for the daily sampled time series:

$$X_{M\times T,\text{daily}} \approx U_{M\times R,\text{daily}} S_{R\times R,\text{daily}} V^T_{R\times T,\text{daily}}. \tag{B.4}$$

If we further assert that the spatial function derived from the daily sampled position time series is generalizable to the 5-min sampled position time series, i.e., $U_{M\times R,\text{5min}} S_{R\times R,\text{5min}} = U_{M\times R,\text{daily}} S_{R\times R,\text{daily}}$, we can rearrange Equations B.3 and B.4 and solve for the time function for the 5-min sampled position time series $V_{T\times R,\text{5min}}$ using a simple projection (Figure B.11).

This can be formulated as follows:

$$V_{T\times R,\text{5min}} \approx X^T_{T\times M,\text{5min}} U_{M\times R,\text{5min}} S^{-1}_{R\times R,\text{5min}} \approx X^T_{T\times M,\text{5min}} U_{M\times R,\text{daily}} S^{-1}_{R\times R,\text{daily}}. \tag{B.5}$$

Since 5-min sampled position time series are rather noisy, the extracted time function $V_{T\times R,\text{5min}}$ has to be filtered. We use a low-pass Savitzky-Golay filter (Savitzky and

Golay, 1964) based on a moving polynomial fit to mitigate high-frequency noises. This filtering technique is non-causal and, therefore, does not temporally shift the onset of geodetic deformation. The choice of this filter is justified in Section 4.5.4.

B.2 Quantifying the uncertainty of the geodetic slip inversion

The following text supplements Section 4.4.2 on the extended descriptions of the sensitivity test to quantify the uncertainty of the results from geodetic slip inversion.

First, we explore various fault geometries by independently varying the dip angles of F1 and F2. The weighting and smoothing parameters are the same as the preferred slip model. We find that the misfit between the predicted displacements from our slip model and the data vary by < 15% and show no systematic patterns with the misfits of the various subsets of data (GNSS, InSAR ascending, or InSAR descending) are considered (Figures B.14 and B.15). Therefore, without further evidence that the faults dip, we prefer to keep the faults in our model vertical for simplicity.

Then, we assess the resolution of our geodetic slip inversion by using a standard checkerboard resolution test (Lévěque et al., 1993). We simulate data from a synthetic slip model with a checkerboard-like pattern. For simplicity, we did not add any instrumental noises. We then perform slip inversion on these simulated data and assess the extent to which we recover the synthetic checkerboard-like pattern. Here, the weighting and smoothing parameters are picked to best recover the checkerboard pattern. Since the data uncertainty depends on the slip patterns themselves, using the same weighting and smoothing parameters with our preferred slip model is not appropriate. The results show that we can reliably recover the checkerboard pattern, at the kilometer scale (~2 km in horizontal, ~5 km in vertical), over the entire range of our fault model (Figure B.16).

Lastly, we assess the variances of our slip model by using a jackknife test (Efron and Stein, 1981). We randomly remove 20% of the input data and perform inversions on this reduced dataset 100 times. The weighting and smoother parameters used here are the same as those used for the preferred slip model. Most of the main features persist throughout the test, though some uncertainties exist for shallow patches on F1 (Figure B.17).

B.3 Temporal variations of seismicity clustering

The following text supplements Section 4.5.5 on the extended descriptions of temporal variations of seismicity clustering.

We expand the discussion of aggregated statistics of the entire catalog and investigate how these statistics vary temporally. To do so, we bin the seismicity using a moving window of 100 events with sliding steps of 10. For each bin, we calculate the fraction of the clustered events determined from the Gamma distribution (Hainzl et al., 2006) and, additionally, the coefficient of variations (CoV), defined as the standard deviation divided by the mean of interevent times (Kagan and Jackson, 1991). The CoV values can be interpreted as follows:

- CoV = 1: a perfectly Poissonian random process
- CoV > 1: a clustered process
- CoV < 1: a quasi-periodic process
- CoV = 0: a perfectly periodic process.

With such a small bin, the seismicity rates do not vary much, and hence clustering due to inhomogeneity of seismicity rates is effectively removed. Any remaining clustering in these small bins would indicate deviation from the inhomogeneous Poisson process. Our results (Figure B.31) show that CoVs are consistently < 1 during the first day of the swarm. In this period, the process is more quasi-periodic than Poissonian. Adding the ~10% of missing events during this period (Section 4.5.5 and Figure B.30) can convert this quasi-periodic process back to the Poisson process. During the latter phase of the swarm, we occasionally find CoV > 1 (e.g., on October 3 and October 5, 2020), indicating that the process is clustered beyond those resulting from the inhomogeneity of seismicity rates. Therefore, a secondary mechanism is required to explain this latter phase of the swarm (Section 4.5.7).

B.4 Seismicity declustering

The following text supplements Section 4.5.8 on the extended descriptions of seismicity declustering.

We first employ a magnitude cutoff and work only with events that are larger than the completeness magnitude M_c. To remove biases from varying detection levels between day and night, we pick a conservatively large M_c of 1.4. Then, we evaluate distances between a parent event i and all possible daughter events j that occurred after the parent event. Given larger uncertainties for depths, we use only the epicentral locations and discard information related to depths. We use a

space-time-magnitude metric normalized by the magnitude m_i of the parent event (Baiesi and Paczuski, 2004, Zaliapin et al., 2008), defined as follows:

$$\eta_{ij} = t_{ij}(r_{ij})^D 10^{-b(m_i - M_c)} \quad \text{where } t_j > t_i \tag{B.6}$$

where t_{ij} is the time between events and is defined as $t_j - t_i$, r_{ij} is the spatial distances between earthquake epicenters, D is the fractal dimension of earthquake epicenters taken to be 1.6, and b is the Gutenberg-Richter b-value evaluated using the maximum likelihood estimate (Aki, 1965) to be 0.99. For each parent event i, the smallest of these η_{ij} is the nearest-neighbor distance.

For natural seismicity, the distribution of η_i is expected to be bimodal, with one mode corresponding to the background seismicity and another to clustered events related to aftershock activities (Zaliapin and Ben-Zion, 2013a, Zaliapin et al., 2008). A two-dimensional expansion of η_i can provide further visualization of the clustering behaviors. The expansion includes the rescaled time T_i and rescaled distance R_i (Zaliapin and Ben-Zion, 2013a), defined as follows:

$$\begin{aligned} T_i &= t_{ij'} 10^{-0.5b(m_i - M_c)/2} \\ R_i &= (r_{ij'})^D 10^{-0.5b(m_i - M_c)/2} \end{aligned} \tag{B.7}$$

where j' is the daughter event j that is the nearest neighbor to the parent event i neighbor distance.

The declustering results are shown in Figure B.35. We remove the 1996 clustered events (aftershocks) with $\eta_i \leq 10^{-4}$ and are left with 473 background events.

B.5 Periodicity detection

The following text supplements Section 4.5.8 on the extended descriptions of the determination of seismicity rate variation for a given periodicity.

To test whether we observe a significant period behavior for a period T, we first phase the seismicity based by converting the epicentral times t_i to a corresponding phase angles $\theta_i = 2\pi t_i / T$. Then, we perform a 2D walk of successive unit-length steps in the direction of those phase angles. After a total of N steps (earthquakes), the total distance D between the start and end points of the walk is related to the Schuster p-value (Schuster, 1897) as follows:

$$p = e^{-D^2/N}. \tag{B.8}$$

The p-value represents the probability of the null hypothesis that the events are drawn from a uniform seismicity rate. The periodicity will be considered significant if the p-value is smaller than the cutoff value (Ader and Avouac, 2013):

$$p_{\text{cutoff}} = \frac{T}{t} \tag{B.9}$$

where t is the total time span of the seismicity catalog. Note that the cutoff p-value depends on the period tested.

For a sinusoidal varying seismicity rate, we can relate the Schuster p-value to the amplitude α of seismicity rate variation using the following (Ader and Avouac, 2013):

$$-\ln p = 1 + \frac{N\alpha^2}{4}. \tag{B.10}$$

Using the declustered catalog (Section B.4), we can run a Schuster test for a different period and generate a Schuster spectrum (Ader and Avouac, 2013), as shown in Figure B.36. For an annual period, $p = 10^{-3.3}$, equating to α of 0.24. The Schuster walk (Figure B.37) shows a systematic drift with a peak seismicity rate between July and August. For a semi-diurnal (12-hr) period, $p = 10^{-1.6}$, which is larger than the $p_{\text{cutoff}} = 10^{-3.9}$, meaning that the Schuster test does not reject the null hypothesis that the observed seismicity rate is uniform. Using p_{cutoff}, the tidal response at a 12-hr period, if it exists, would have $\alpha < 0.26$.

Using Dieterich's model (Dieterich, 1994, Heimisson and Segall, 2018), the amplitudes α of seismicity rate variations for a period T can be related to the amplitudes of periodic stressing $\Delta\tau$ according to (Ader et al., 2014):

$$\frac{R(t)}{r} = 1 + \alpha \cos\left(\frac{2\pi t}{T}\right) = e^{\frac{\Delta\tau}{a\sigma}} \tag{B.11}$$

where $R(t)$ is the seismicity rate at time t, r is the background seismicity rate, a is the frictional rate-and-state parameter governing the nucleation process, and σ is the effective normal stress. With known amplitudes α of seismicity rate variations and the amplitudes of the periodic stressing $\Delta\tau$, we can estimate the parameters $a\sigma$ as discussed in Section 4.5.8.

B.6 Tidal strain calculation

The following text supplements Section 4.5.8 on the extended descriptions of the calculation of the tidal strain.

We first use *Solid* software (Milbert, 2018) to compute time series surface displacements due to solid Earth tides at gridded points. Then, we calculate the corresponding time series of surface two-dimensional tidal strains. Assuming plane strain approximation (no vertical strains, i.e., $\epsilon_{zz} = 0$), which is valid for a shallow crust, we relate strains ϵ_{ij} to stresses σ_{ij} using the following set of equations:

$$\begin{bmatrix} \sigma_{xx} \\ \sigma_{yy} \\ \sigma_{xy} \end{bmatrix} = \frac{E}{(1+\nu)(1-2\nu)} \begin{bmatrix} 1-\nu & \nu & 0 \\ \nu & 1-\nu & 0 \\ 0 & 0 & 1-2\nu \end{bmatrix} \begin{bmatrix} \epsilon_{xx} \\ \epsilon_{yy} \\ \epsilon_{xy} \end{bmatrix} \tag{B.12}$$

$$\sigma_{zz} = \frac{E\nu}{(1+\nu)(1-2\nu)}(\epsilon_{xx} + \epsilon_{yy})$$

$$\sigma_{xz} = \sigma_{yz} = 0$$

where positive x-direction is easting, positive y-direction is northing, positive z-direction is vertically upward, E is the elastic modulus assumed to be 75 GPa, and ν is the Poisson's ratio assumed to be 0.25.

Then, using the stress tensor components, we can calculate stresses acting on a fault plane, assumed here to be parallel to the southern San Andreas fault (vertical right-lateral strike-slip striking 162°). Then, we can calculate the time series of Coulomb stress changes (Figure B.38). Using a fast Fourier transform (FFT), we find the amplitude of periodic stress changes at the semi-diurnal (12-hr) period to be 0.6 kPa (Figure B.39).

B.7 Supplementary figures

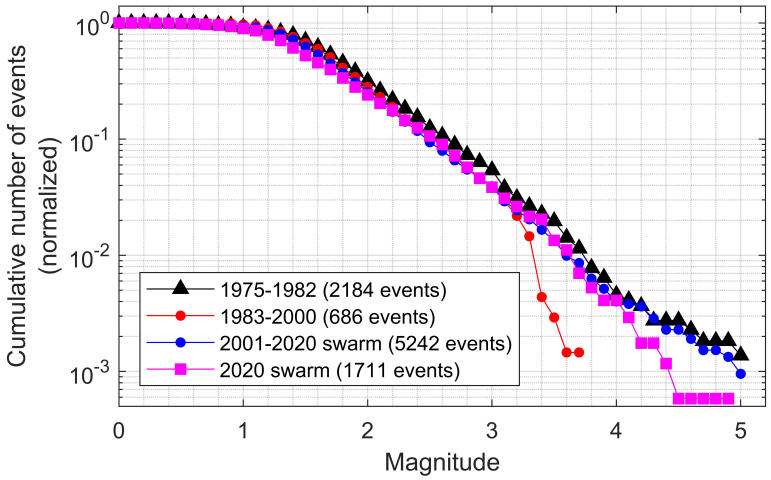

Figure B.1: Frequency-magnitude distribution of earthquakes from the Southern California Seismic Network (SCSN) catalog (Hutton et al., 2010) separated into different time intervals based on establishing the SCSN network of seismometers. The cumulative numbers of events are normalized by the total number of earthquakes within the time interval of interest. During the 2020 swarm, large events were missing compared to what we expect from the Gutenberg-Richter law (Gutenberg and Richter, 1944).

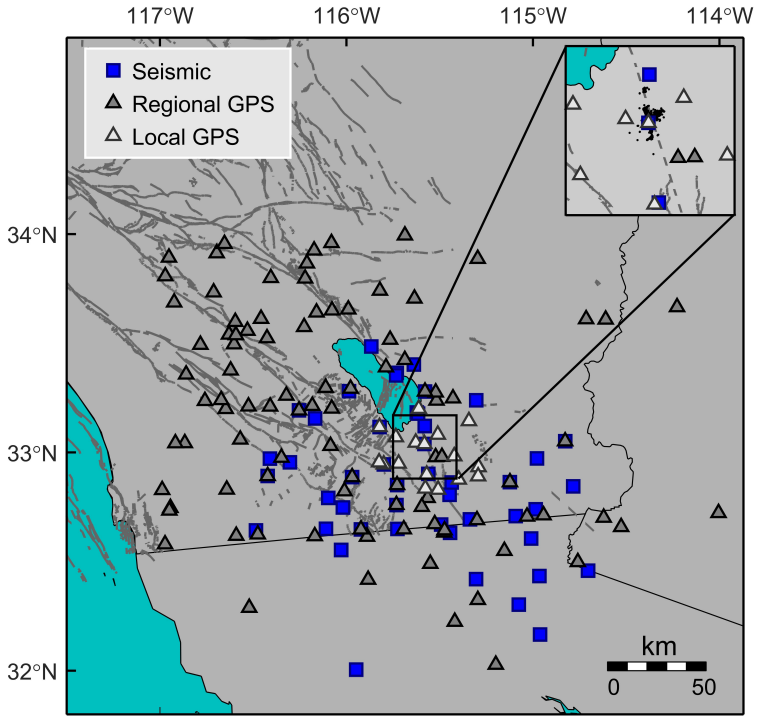

Figure B.2: Distribution of seismic (squares) and GPS stations (triangles) used in this study. Data from all GPS stations (regional and local) processed by Nevada Geodetic Laboratory (Blewitt et al., 2018) are used in the initial vbICA decomposition (Gualandi et al., 2016) to extract large-scale deformations unrelated to the swarm. Only data from local stations (white triangles) are used when extracting deformation related to the swarm. Two stations near the proximity of the swarm are shown as black as they either have no data during the swarm or data during the swarm were affected by station maintenance. Relocated seismicity from this study during the 2020 Westmorland swarm (Sirorattanakul et al., 2022a) is shown as black dots in the inset.

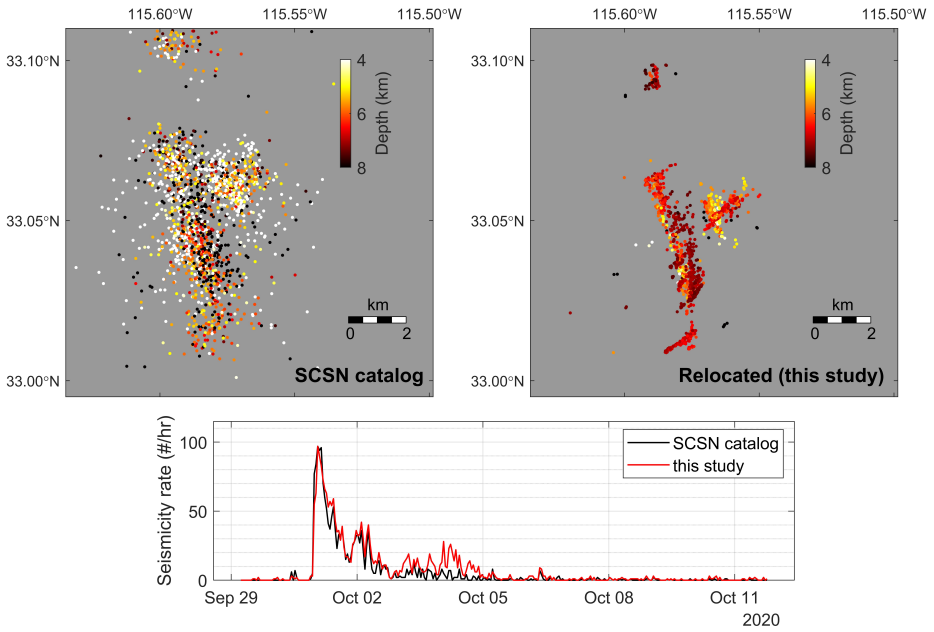

Figure B.3: Comparison between the SCSN catalog (Hutton et al., 2010) and relocated seismicity catalog from this study (Sirorattanakul et al., 2022a). The top panels show the spatial distribution of seismicity color-coded by depth for the SCSN catalog (left) and relocated catalog generated from this study (right). The bottom panel shows the time evolution of the seismicity rate. For the catalog from this study, we consider all detected events, including those non-relocated. Additional events in the catalog we produce in this study are mostly related to the latter phase of the swarm sequence, where fluids play a significant role (Section 4.5.7 in the main text).

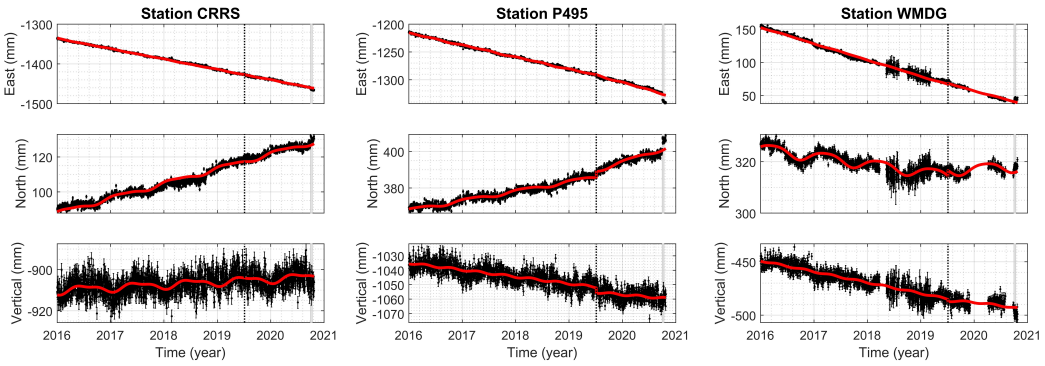

Figure B.4: Comparison of daily sampled GPS position time series pre-processed by Nevada Geodetic Laboratory (black) and the best-fit trajectory model (red) for 3 stations with the largest deformation related to the 2020 Westmorland swarm. For each station, the panels show eastward, northward, and upward displacements. The vertical black lines denote steps due to earthquakes. The vertical gray shaded area brackets the 2020 Westmorland swarm.

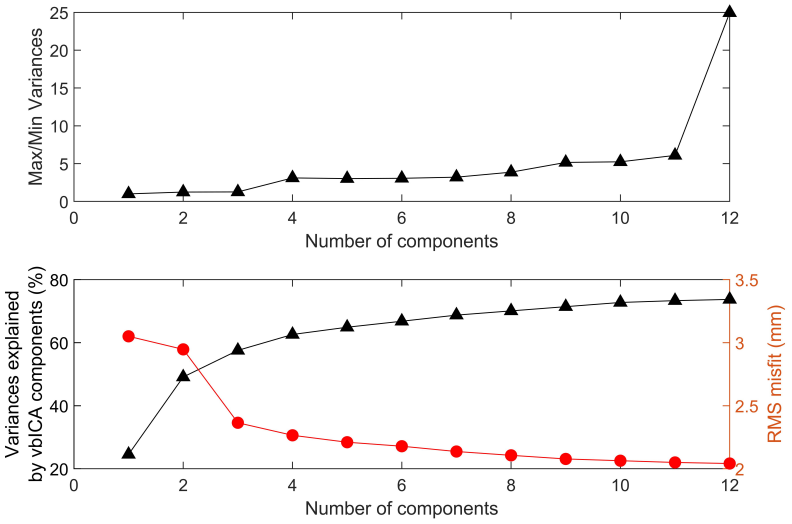

Figure B.5: Statistics of vbICA for the different number of total decomposed components. The top panel shows the ratio between the maximum and the minimum a posteriori variance of the components. The bottom panel shows variances explained by the vbICA components (black), and the root mean square (RMS) misfit between the vbICA construction and the data (red).

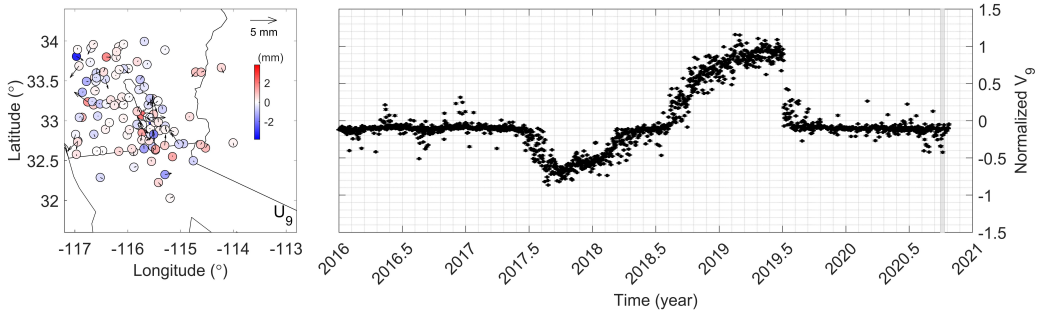

Figure B.6: Spatial and time function of IC9 when decomposing data from 113 regional stations into 9 ICs using vbICA. The left panel shows the spatial functions with arrows indicating horizontal motion and colors indicating vertical motion, while the right panel shows the time function describing the time-evolving amplitudes of these motions. The vertical gray shaded area in the right panel brackets the 2020 Westmorland swarm. This IC shows residuals of co-seismic steps during the M7.1 Ridgecrest, California earthquakes (2019.51) that are not completely removed using the trajectory model.

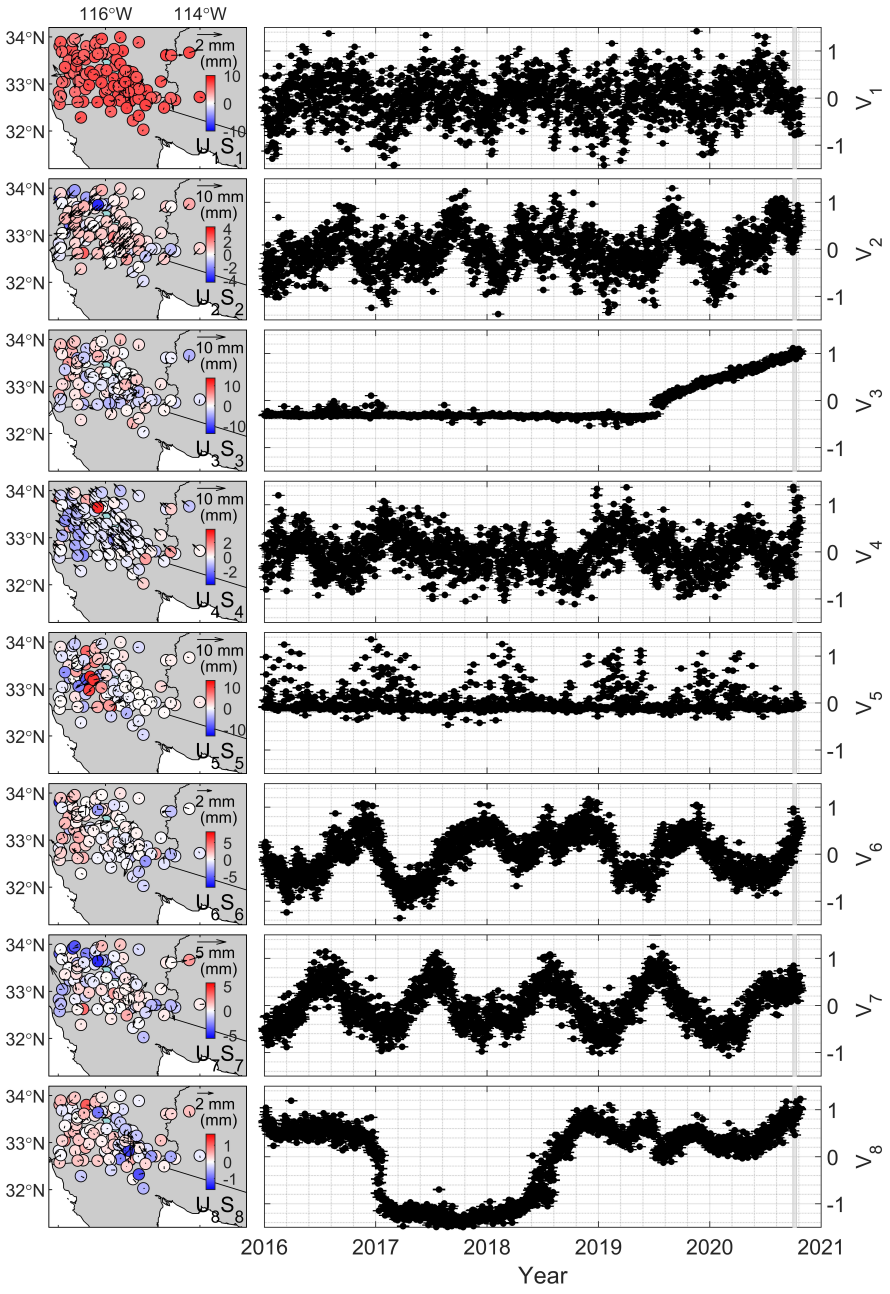

Figure B.7: Spatial and time functions of the 8 independent components (ICs) representing regional-scale signals not related to the swarm extracted using vbICA decomposition performed on detrended daily position time series from 113 regional stations. For each component i, the left panel shows the spatial function $U_i S_i$ with arrows indicating horizontal motion and colors indicating vertical motion, while the right panel shows the time function V_i describing the time-evolving amplitudes of these motions. The vertical gray shaded area in the right panels brackets the 2020 Westmorland swarm. ICs 1, 2, and 4 are associated with the common-mode jitter. IC 3 is associated with post-seismic relaxation following the 2019 Ridgecrest earthquakes. IC 5 is associated with precipitation response. ICs 6 and 7 are associated with hydrological cycles. IC 8 is associated with the operations of Brawley geothermal power plants.

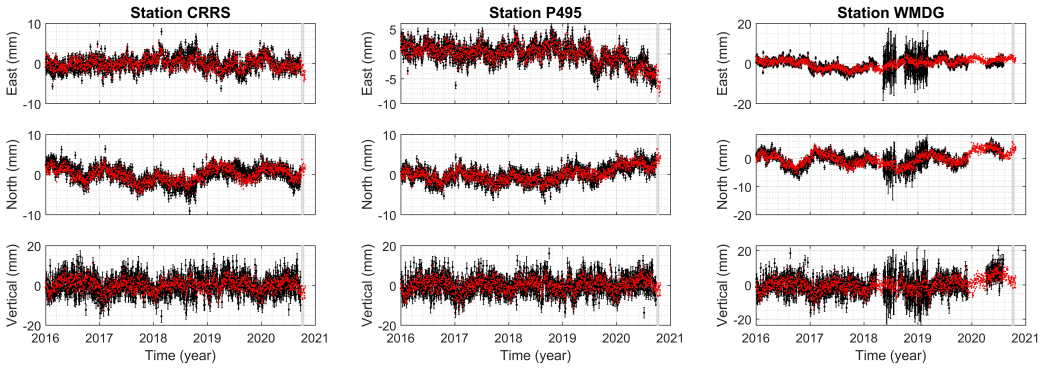

Figure B.8: Comparison of regional-scale vbICA reconstruction (red) and detrended daily sampled GPS position time series (black) for 3 stations with the largest deformation related to the 2020 Westmorland swarm. For each station, the panels show eastward, northward, and upward displacements. The vertical gray shaded area brackets the 2020 Westmorland swarm. Data near the time of the swarm from 28 stations within 35 km from the center of the 2020 Westmorland swarm are not included in the vbICA decomposition, and hence the deformation due to the swarm is not visible here.

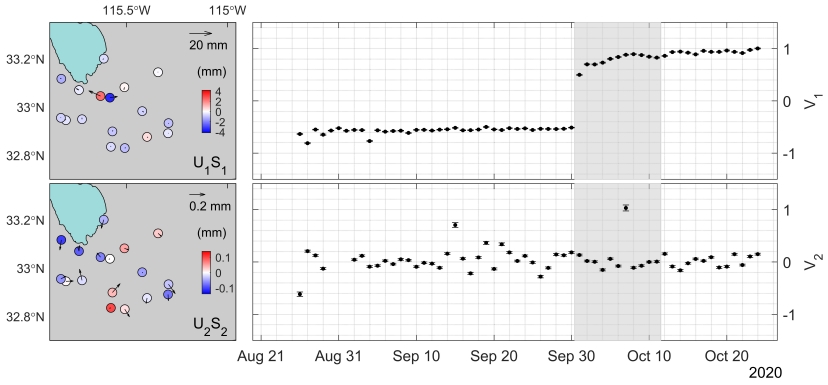

Figure B.9: Spatial and time functions of the 2 independent components (ICs) extracted using a local-scale vbICA decomposition performed on 18 local stations already corrected for regional deformations. For each component i, the left panel shows the spatial function $U_i S_i$ with arrows indicating horizontal motion and colors indicating vertical motion, while the right panel shows the time function V_i describing the time-evolving amplitudes of these motions. The water body (cyan) shown in the left panels is the Salton Sea. The vertical gray shaded area in the right panels brackets the 2020 Westmorland swarm. Only the first IC is associated with the 2020 Westmorland swarm.

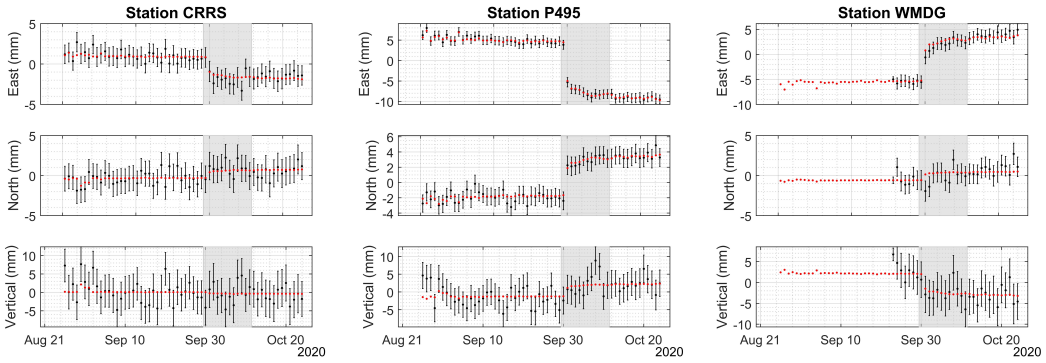

Figure B.10: Comparison of vbICA reconstruction (red) and daily sampled GPS position time series corrected for regional deformations (black) for 3 stations with the largest deformation related to the 2020 Westmorland swarm. For each station, the panels show eastward, northward, and upward displacements. The vertical gray shaded area brackets the 2020 Westmorland swarm.

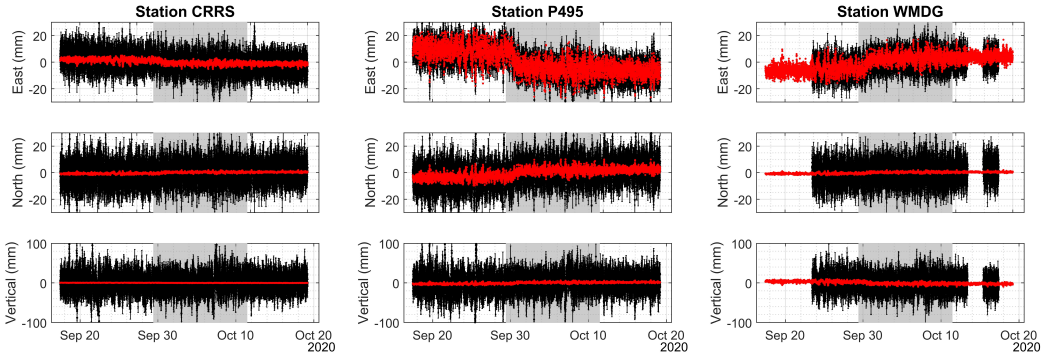

Figure B.11: Comparison of vbICA reconstruction (red) and raw 5-min sampled position time series (black) for 3 stations with the largest deformation related to the 2020 Westmorland swarm. For each station, the panels show eastward, northward, and upward displacements. The vertical gray shaded area brackets the 2020 Westmorland swarm.

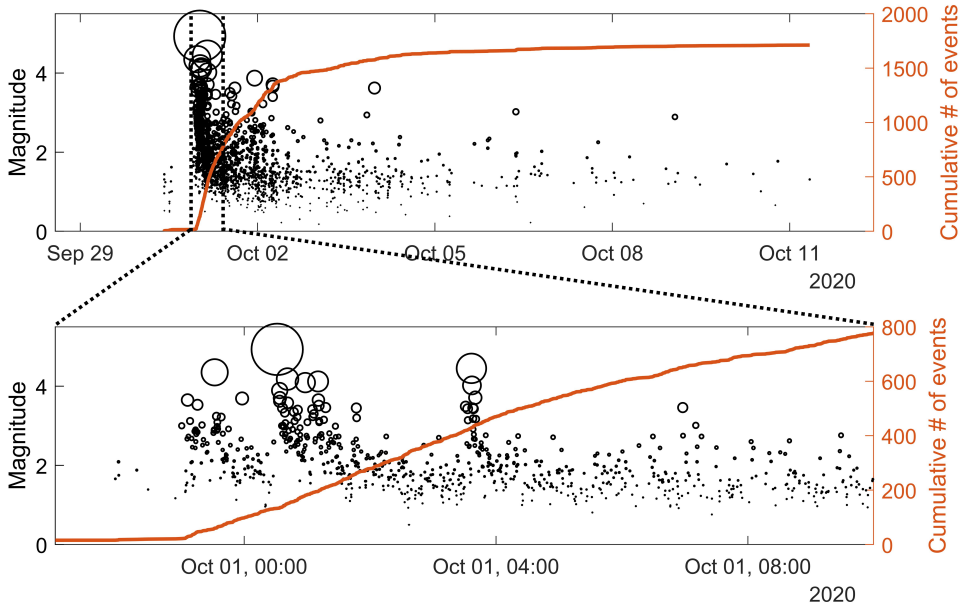

Figure B.12: Seismicity magnitude-time distribution from the Southern California Seismic Network (SCSN) catalog (Hutton et al., 2010). The bottom panel is the zoomed-in version of the top panel. There were several clustered events about half a day before the main swarm activity. The large earthquakes were all within the first 6 hr of the swarm.

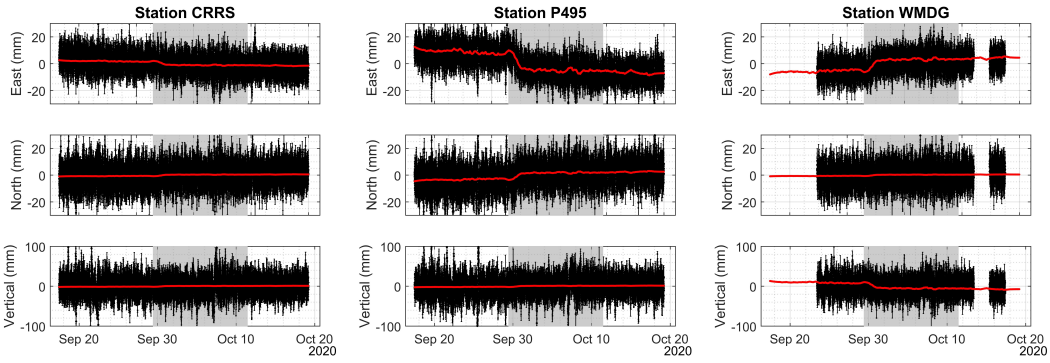

Figure B.13: Comparison of the surface displacements predicted from the preferred slip model (red) and raw 5-min sampled position time series (black) for 3 stations with the largest deformation related to the 2020 Westmorland swarm. For each station, the panels show eastward, northward, and upward displacements. The vertical gray shaded area brackets the 2020 Westmorland swarm.

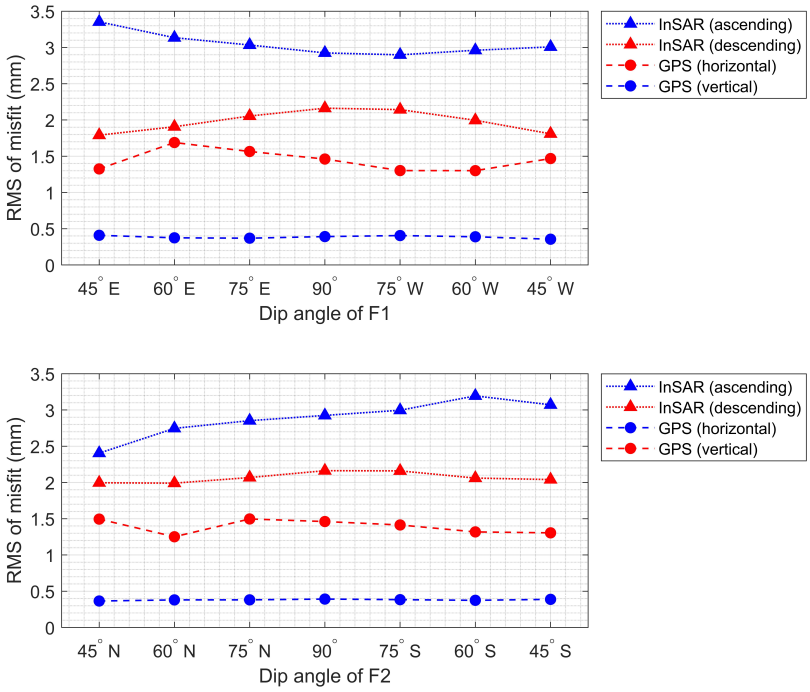

Figure B.14: Sensitivity of the geodetic inversion to the assumed subfault dip angles. The top panel shows the root-mean-square of the misfit for each data type given different dip angles of fault F1 while fault F2 is kept vertical. The bottom panel shows the root-mean-square of the misfit for each data type given different dip angles of fault F2 while fault F1 is kept vertical. The same weighting and smoothing parameters with the preferred slip model are used.

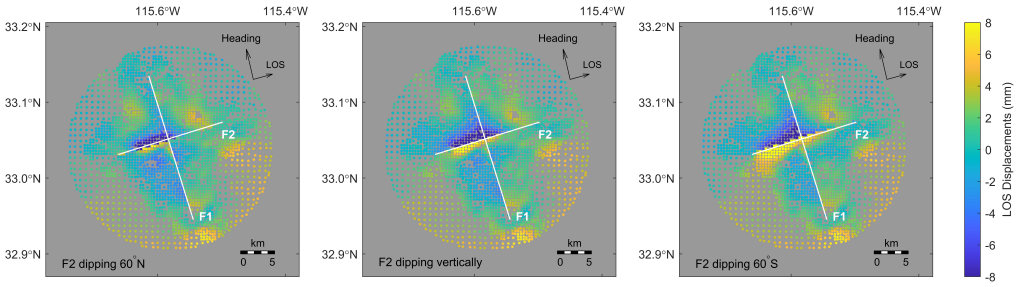

Figure B.15: Sensitivity of the geodetic inversion to the assumed dip angles of fault F2. The panels show residuals of observed Line-Of-Sight (LOS) displacements along the ascending track that are not captured by fault models with different dip angles for F2. The same weighting and smoothing parameters with the preferred slip model are used.

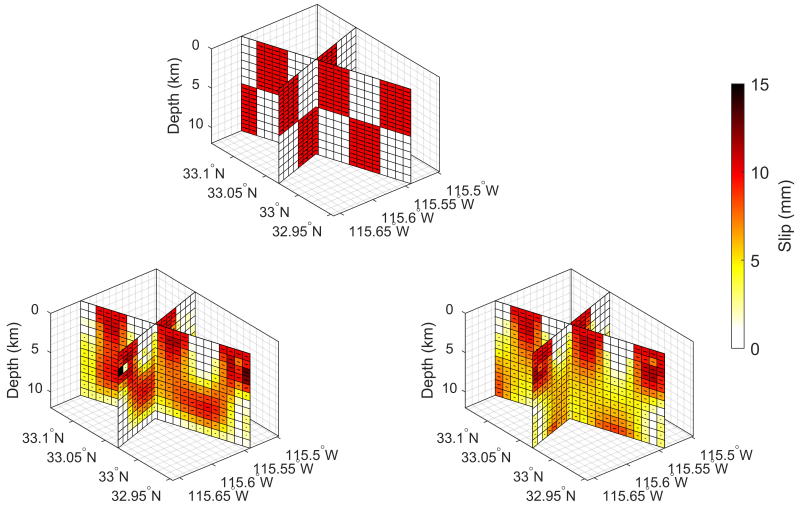

Figure B.16: Checkerboard resolution test. The top panel shows the assumed slip model used to generate synthetic displacement data. No noises are added. The bottom panels show the slip model recovered from inverting the synthetic displacements with (left) and without (right) zero-slip boundary conditions.

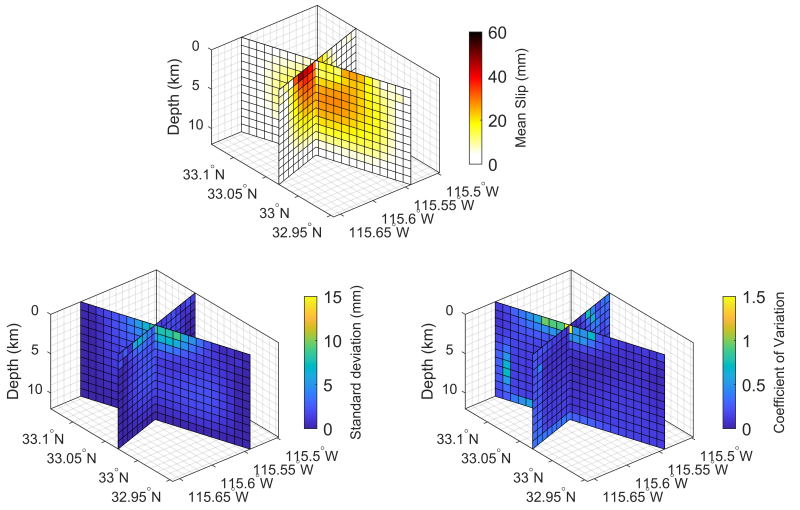

Figure B.17: Variances estimation using Jackknife test. The top panel shows the mean slip from 100 slip models inverted using 80% of randomly selected input data (without replacements). The bottom panels show the standard deviation (left) and the coefficient of variation (right, defined as the standard deviation divided by the mean) of these models.

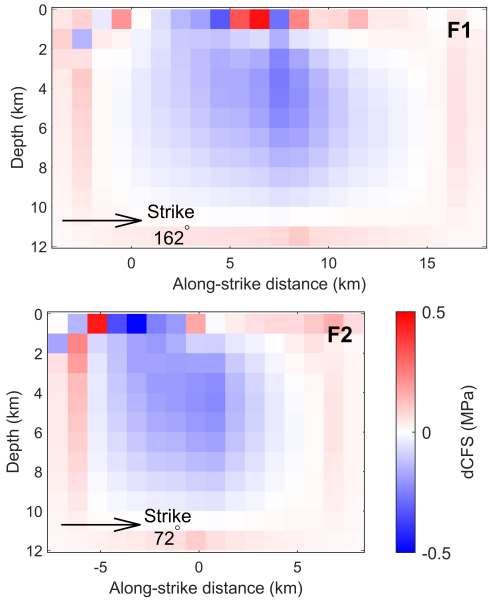

Figure B.18: Coulomb Failures Stress changes (dCFS) on fault planes F1 and F2 calculated from the total geodetically resolved slip.

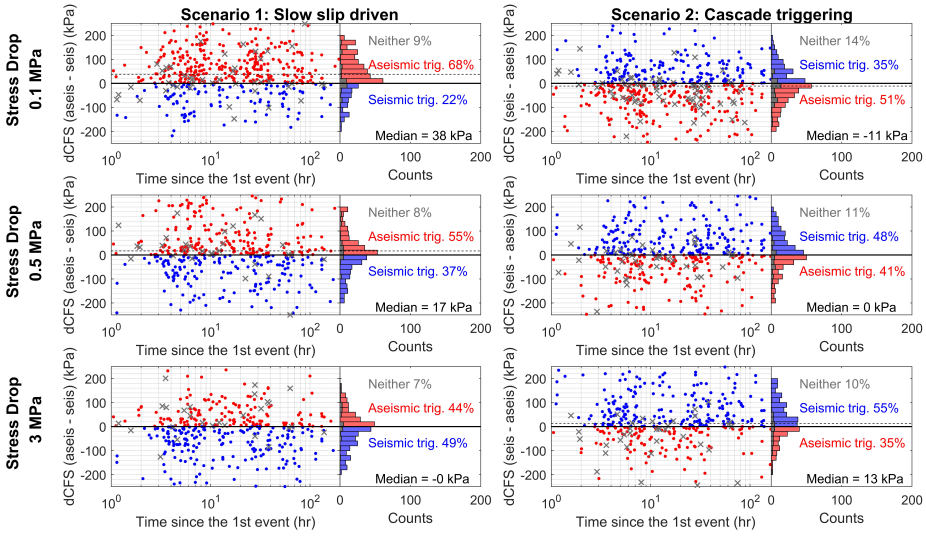

Figure B.19: Sensitivity of static stress triggering analysis (Section 4.5.1) to the assumed stress drop. The left panels are similar to Figure 4.8c in the main text, and the right panels are similar to Figure 4.8f in the main text but with different values of assumed stress drop.

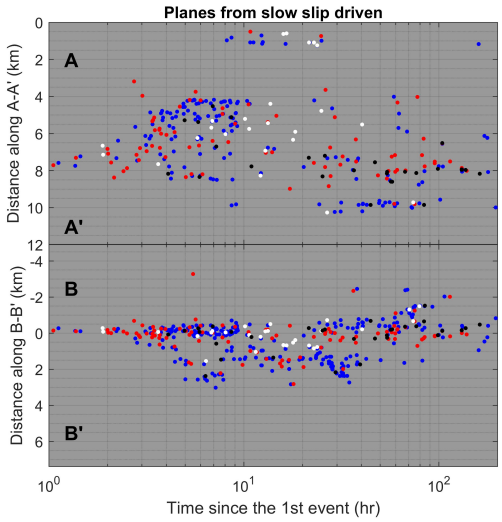

Figure B.20: Spatio-temporal distribution of relocated events with a matching SCSN focal mechanism color-coded by the faulting types: left-lateral strike-slip (blue), right-lateral strike-slip (red), normal (white), and reverse (black). The top panel includes only the events within a 1 km distance from the 162°-striking main fault F1 (similar to Figure 4.5f), while the bottom panel includes all events (similar to Figure 4.5g).

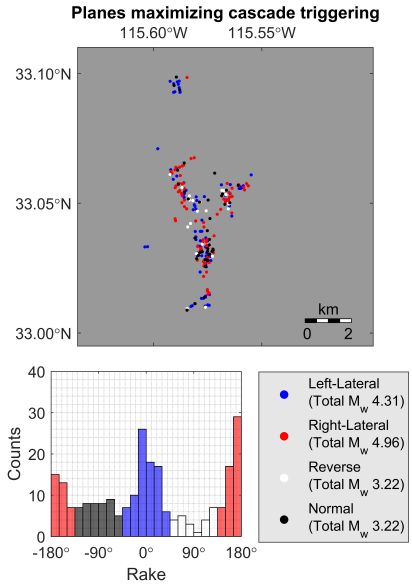

Figure B.21: Same as Figure 4.9 in the main text, but with faulting types chosen from the nodal planes promoted by dCFS from the cascade triggering (scenario 2 in Figure 4.8).

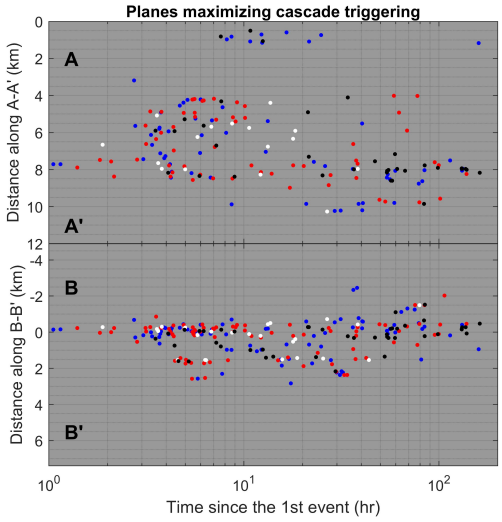

Figure B.22: Same as Figure B.20, but with faulting types chosen from the nodal planes promoted by dCFS from the cascade triggering (scenario 2 in Figure 4.8).

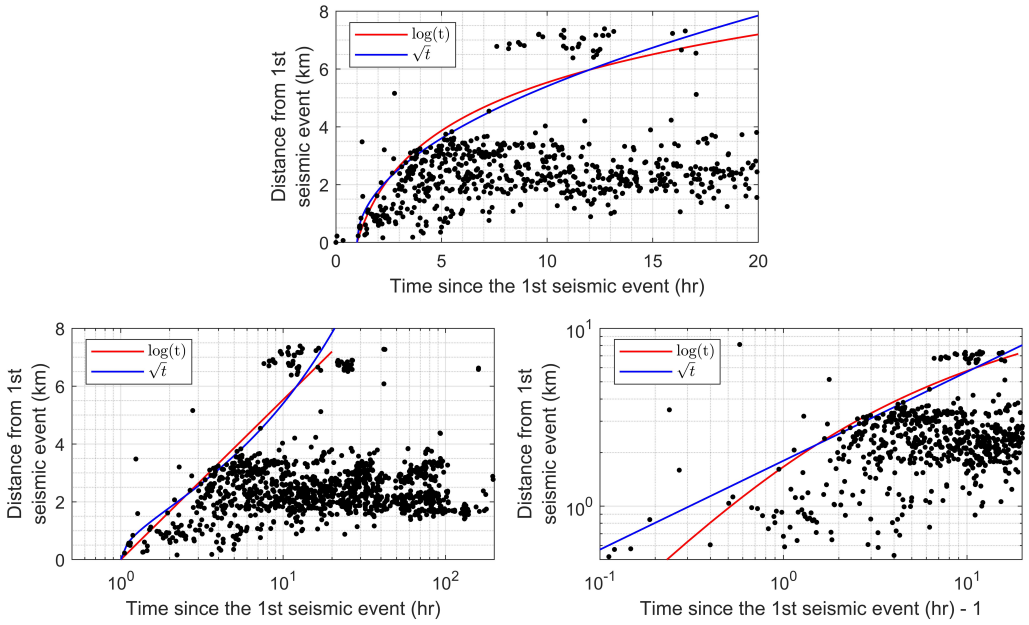

Figure B.23: Comparison between the two non-linear functions, $\sqrt{t}$ and $\log(t)$, in explaining the expansion of seismicity observed in our high-resolution relocated seismicity catalog. The plots show different scales: linear, semilog, and log-log. These results indicate that we cannot confidently distinguish between the two functions using only the observed seismicity alone. In the log-log plot, the time since the first seismic event is subtracted by 1 so that the first event would occur at the distance of $c_1 \log_{10}(1) = 0$ km.

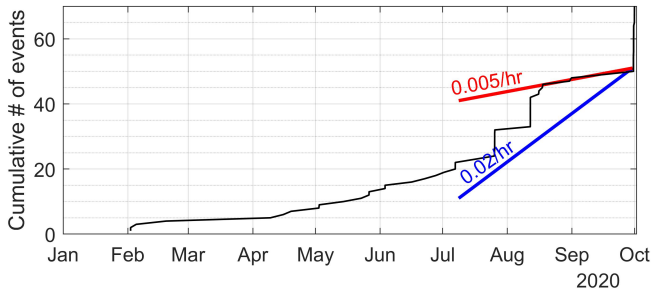

Figure B.24: The cumulative number of events from the Southern California Seismic Network (SCSN) catalog (Hutton et al., 2010) over the local area where the swarm occurred (latitude between 32.98°N and 33.12°N, longitude between 115.65°W and 115.50°W). Given that this study analyzes seismicity in a small area, the detection level does not vary much spatially, and hence no magnitude cutoff is employed. The background seismicity rate right before the 2020 Westmorland swarm is estimated from the slope of the curve to be 0.005 event/hr.

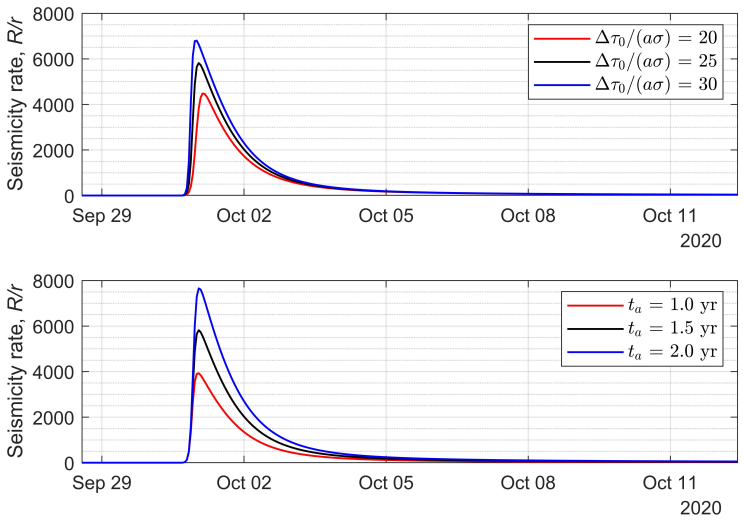

Figure B.25: Sensitivity test of Dieterich's model (Dieterich, 1994, Heimisson and Segall, 2018) used in this study (Section 4.5.4) assuming a fixed $t_a = 1.5$ yr for the top panel and a fixed $\Delta\tau_0/a\sigma = 25$ for the bottom panel. The parameter $\Delta\tau_0/a\sigma$ governs the time lag between the slow slip event and seismicity, while the parameter t_a governs the amplitudes of seismicity rate increased. The evolution of stress changes is approximated with the exponential function (Figure 4.11e).

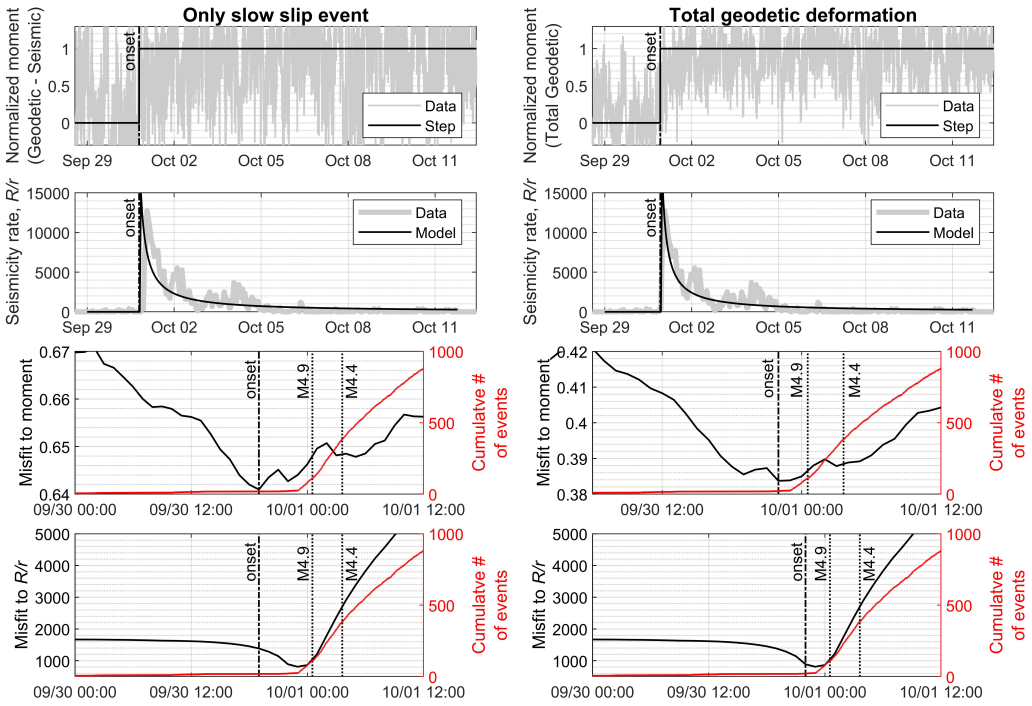

Figure B.26: Same as Figure 4.11, but the moment release and hence the stress changes are approximated by a Heaviside step function instead of an exponential function.

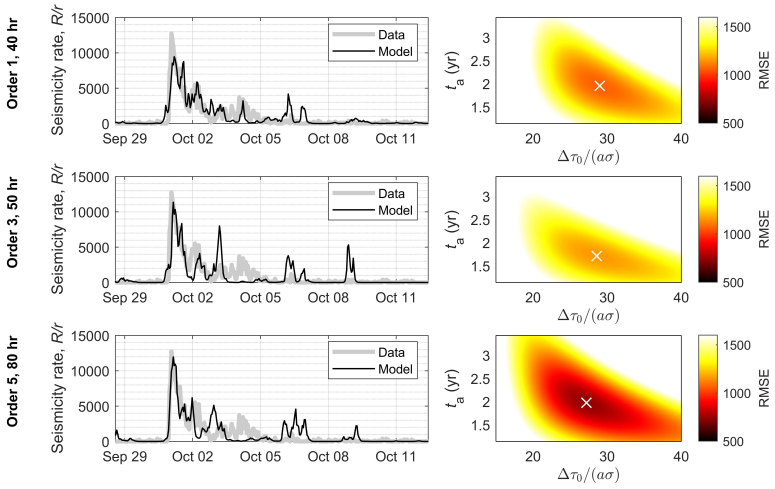

Figure B.27: Sensitivity of modeled seismicity rate driven by stress changes from the slow slip event to the different polynomial orders and window size of the Savitzky-Golay filter used. For a filter with a given polynomial order and window size, the left panel shows the best fit seismicity rate, and the right panel shows the root-mean-squared error (RMSE) from the parameters grid search with the white cross denoting the best t_a and $\Delta\tau_0/a\sigma$. The three choices of the filters shown here are selected from the local minima of the normalized mean squared error (MSE) from Figure 4.12c in the main text.

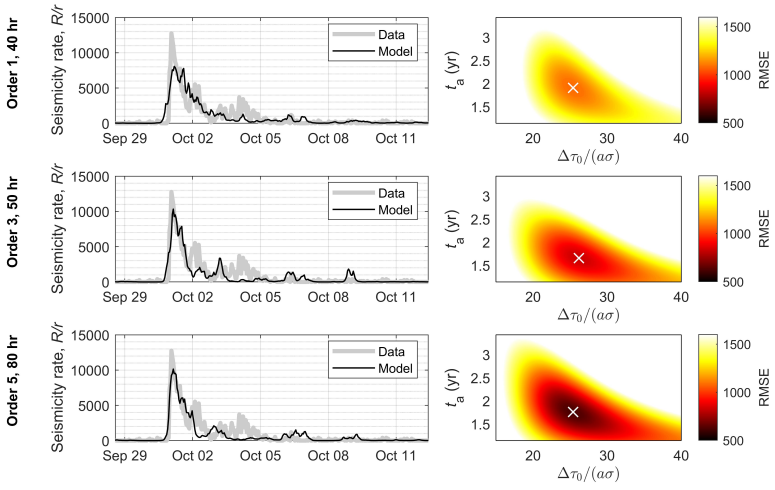

Figure B.28: Same as Figure B.27 but use the modeled seismicity rate driven by stress changes from the total geodetically resolved slip. The three choices of filters shown here are selected from the local minima of the normalized mean squared error (MSE) from Figure 4.12h in the main text.

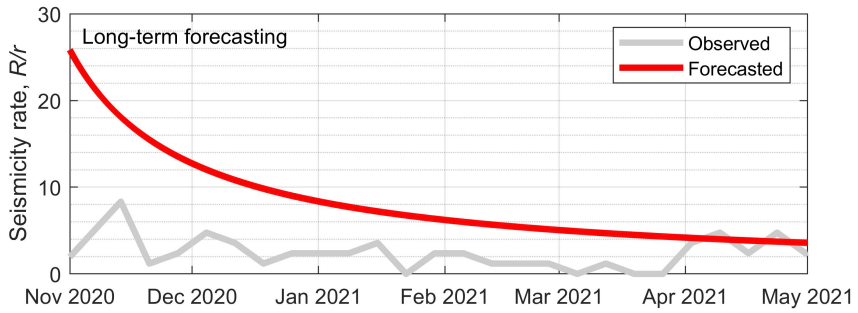

Figure B.29: Long-term forecasting of seismicity rate assuming that the stress changes during the swarm event dominate the long-term stress changes. The observed long-term seismicity rate is calculated over the Westmorland area (latitude 32.98 – 33.12°N, longitude 115.50 – 115.65°W) using the SCSN catalog (Hutton et al., 2010) and rescaled to our catalog. The long-term forecasting uses the total geodetic moment release fitted with an exponential function (Figure 4.11e in the main text) and associated best-fit parameters $\tau_0/a\sigma = 23$ and $t_a = 2$ yr (Table 4.2). The results show an elevated seismicity rate above the background rate prior to the swarm event ($R/r > 1$) even after several months. Our forecasts are overestimated possibly because of stress release from events driven by pore-pressure diffusion (Figure 4.15 and Section 4.5.7) not accounted for in our forecasting model.

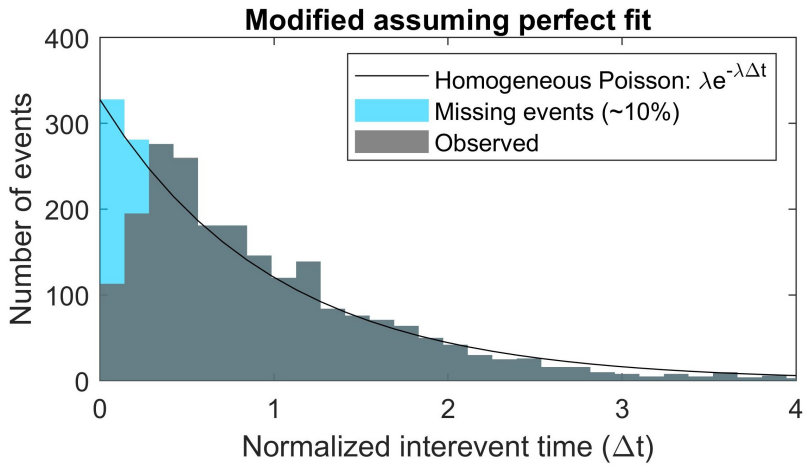

Figure B.30: Distribution of the modified interevent times, calculated by removing the inhomogeneity of the seismicity rates by assuming that Dieterich's model (Dieterich, 1994, Heimisson and Segall, 2018) achieves a perfect fit. We find that the swarm does not perfectly follow the inhomogeneous Poisson process. About 10% of events with short interevent times are missing, probably due to missed detections near the peak seismicity rate when average interevent times are less than 15 seconds.

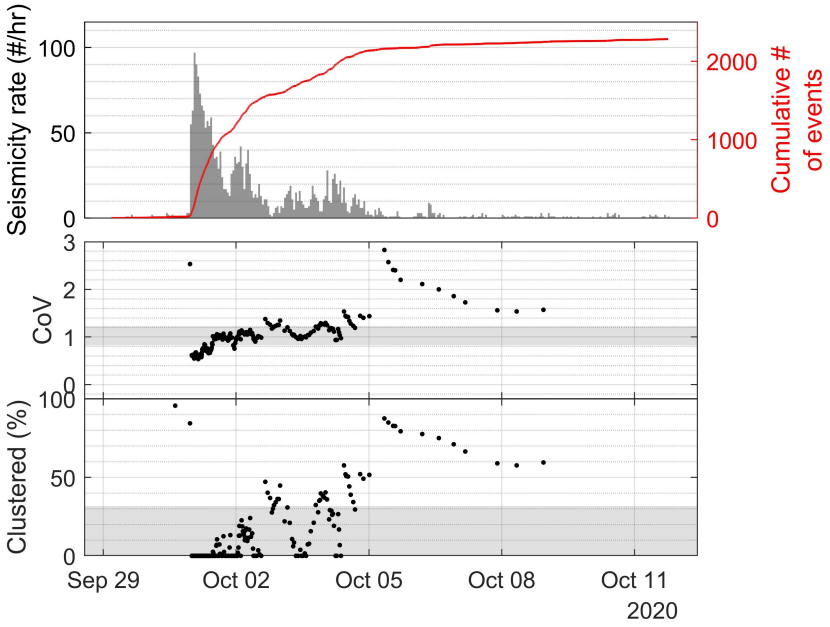

Figure B.31: Temporal variation of point process statistics. (top) Time series of the observed seismicity rate and corresponding cumulative number of events. All detected events from this study, including those non-relocated, are used. (middle) Coefficient of variations (CoVs) and (bottom) clustering percentage estimated from the Gamma distribution (Hainzl et al., 2006) for a moving window of 100 events and sliding steps of 10 events. The gray areas in the middle and the bottom panels represent a range of values consistent with a 95% confidence interval of a process being Poissonian.

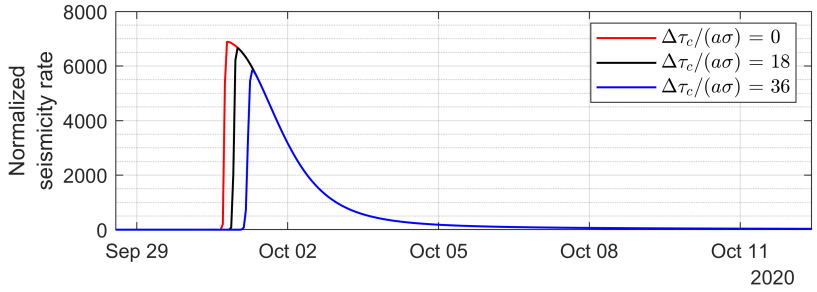

Figure B.32: Sensitivity test of a stress-driven model based on Dieterich's nucleation with a critical stress threshold (Equation 4.5, Section 4.5.6) assuming $t_a = 1.1$ yr, $\Delta\tau_0/a\sigma = 74$, and an exponential stress transfer (Figure 4.11e). A larger critical stress threshold $\Delta\tau_c/a\sigma$ corresponds to a larger time lag between the slow slip event and seismicity.

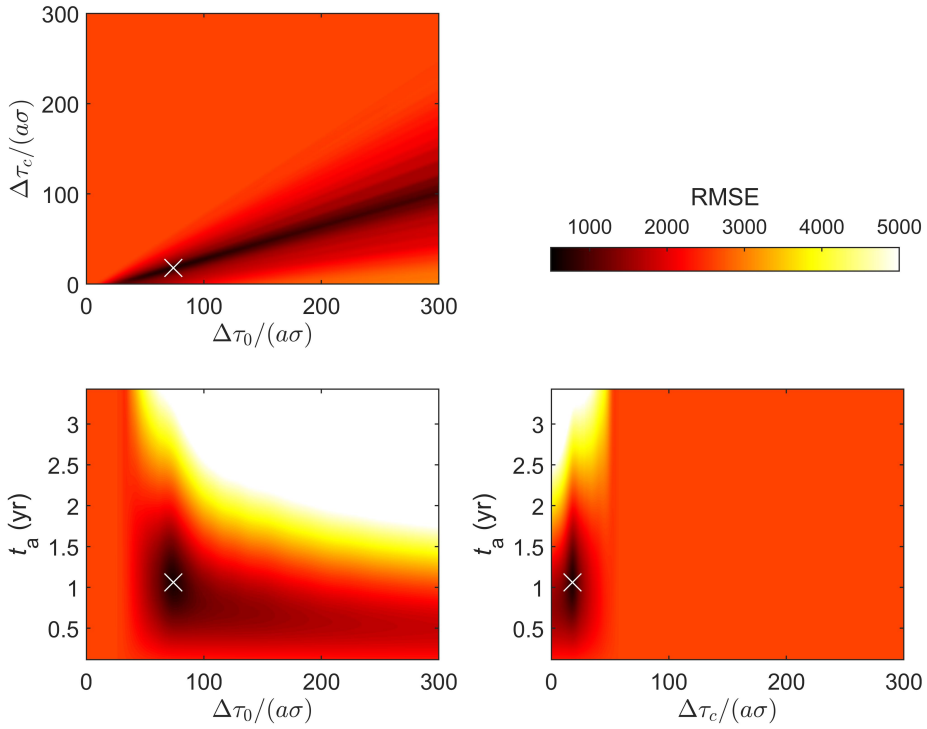

Figure B.33: Root-mean-square error (RMSE) calculated over the first seismicity peak (up to the first day of the swarm) for different values of t_a, $\tau_0/a\sigma$, and $\tau_c/a\sigma$. Each panel shows a slice of RMSE from the full grid search assuming the third parameter not shown in the plot is at the optimum value

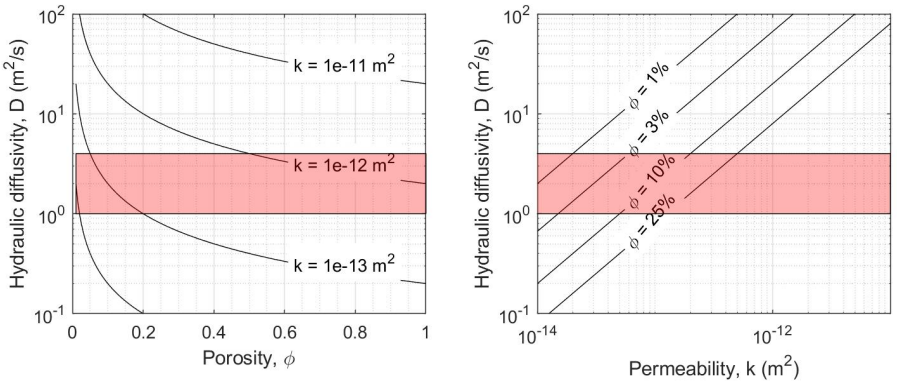

Figure B.34: Possible ranges of porosity and permeability for the hydraulic diffusivity between 1 - 4 m^2/s found in this study (red regions). Diffusivity (D), porosity (ϕ), and permeability (k) are related by $D = k/(\phi\mu\beta)$ with the fluid's viscosity μ and compressibility β.

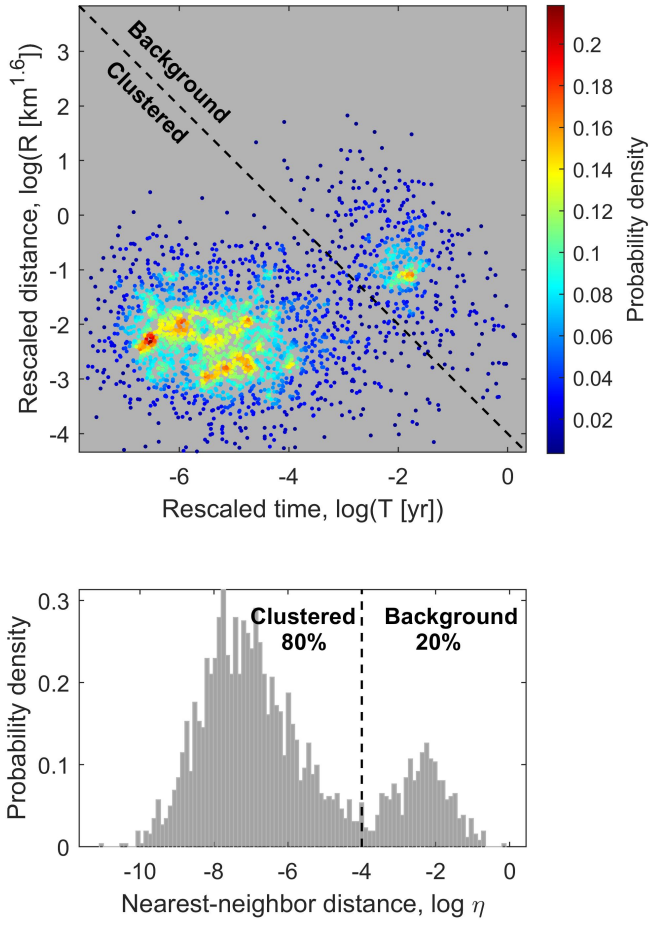

Figure B.35: Distribution of events near the Westmorland area (latitude 32.98 – 33.12°N, longitude 115.50 – 115.65°W) from the Quake Template Matching (QTM) catalog (Ross et al., 2019a) in rescaled space-time (top) and histogram of the corresponding nearest-neighbor distance (bottom). The distribution of η_i is bimodal with the two modes separated with $\eta_{\text{cutoff}} = 10^{-4}$. Events with $\eta_i < \eta_{\text{cutoff}}$ are aftershocks, while the rest are mainshocks. The method is based on Zaliapin and Ben-Zion (2013a).

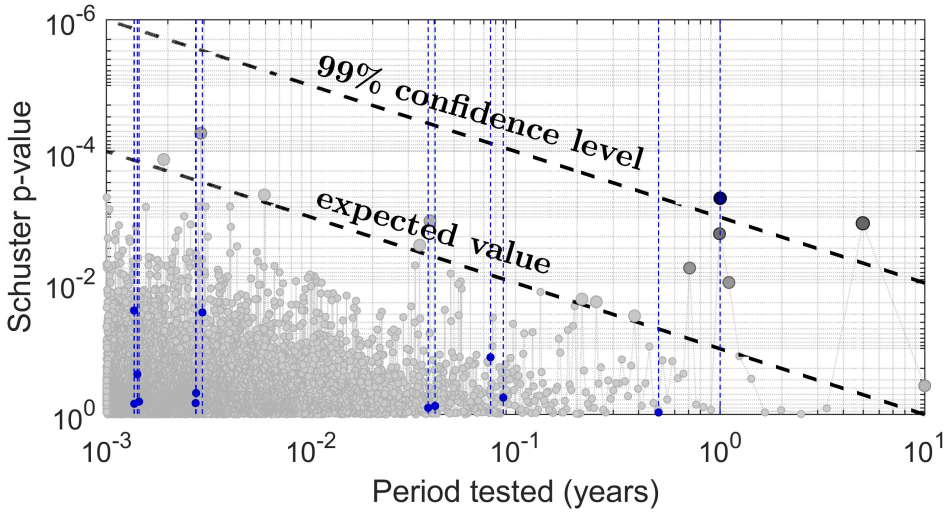

Figure B.36: Schuster spectrum for the declustered seismicity near Westmorland, California, from the Quake Template Matching (QTM) catalog (Ross et al., 2019a). The Schuster p-value reflects the probability that a periodic behavior is observed by chance. The "expected value" denotes the detection threshold T/t, which changes with period T and catalog length t (Ader and Avouac, 2013). The p-values corresponding to tidal periods are shown in blue.

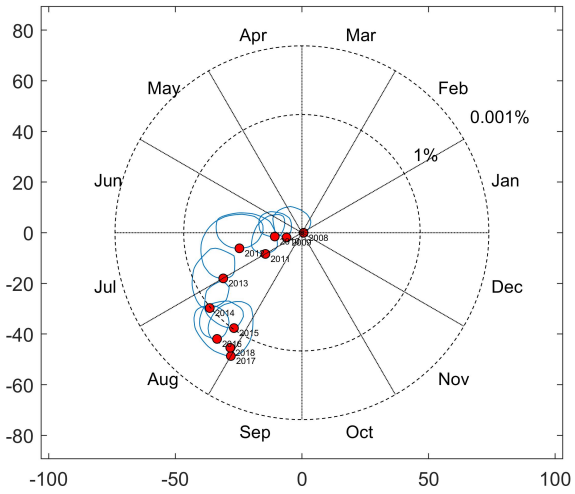

Figure B.37: A Schuster walk of successive unit-length for the declustered seismicity near Westmorland, California, from the Quake Template Matching (QTM) catalog (Ross et al., 2019a) and an annual period. The circles denote the p-value (probability that the seismicity rate is uniform). The drift direction reflects the time of year with the maximum seismicity rate.

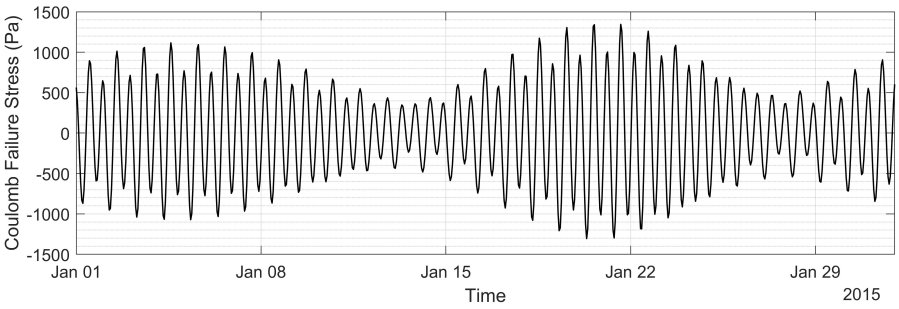

Figure B.38: Coulomb Failures Stress changes (dCFS) due to solid Earth tides calculated using surface displacements at gridded points from Solid software (Milbert, 2018) for Westmorland, California, on a fault plane parallel to the southern San Andreas fault (vertical right-lateral strike-slip striking 162°). Plane strain approximation is used.

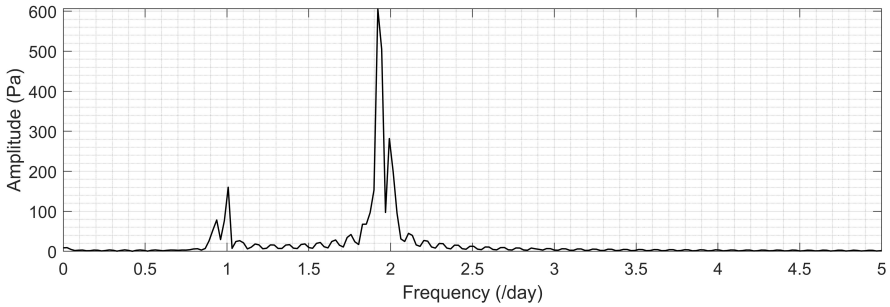

Figure B.39: Fast Fourier transform (FFT) of Coulomb Failures Stress changes (dCFS) due to solid Earth tides shown in Figure B.38.

B.8 Supplementary tables

AZQZ 19JUL06 2 562.341 386.880 7.1 ci38457511
AZQZ 20JAN31 3 Unknown
AZRY 19JUL06 2 562.341 263.283 7.1 ci38457511
BLYT 19JUL06 2 562.341 356.600 7.1 ci38457511
CAC1 19JUL06 2 562.341 244.706 7.1 ci38457511
CAC1 20JAN16 3 Unknown
CACJ 19JUL06 2 562.341 341.568 7.1 ci38457511
CACM 19JUL06 2 562.341 364.648 7.1 ci38457511
CACM 16DEC05 3 Unknown
CACT 19JUL06 2 562.341 277.322 7.1 ci38457511
CACX 19JUL06 2 562.341 393.628 7.1 ci38457511
CAGW 19JUL06 2 562.341 418.514 7.1 ci38457511
CAGW 18JUN06 3 Unknown
CANI 19JUL06 2 562.341 340.082 7.1 ci38457511
CAOR 19JUL06 2 562.341 379.946 7.1 ci38457511
CARA 19JUL06 2 562.341 310.568 7.1 ci38457511
CMPO 19JUL06 2 562.341 356.702 7.1 ci38457511
COAG 19JUL06 2 562.341 395.088 7.1 ci38457511
DAEX 19JUL06 2 562.341 442.428 7.1 ci38457511
DAEX 16JAN25 3 Unknown
DESC 19JUL06 2 562.341 338.487 7.1 ci38457511
DHLG 19JUL06 2 562.341 312.259 7.1 ci38457511
DSSC 19JUL06 2 562.341 240.480 7.1 ci38457511
ERRG 19JUL06 2 562.341 336.983 7.1 ci38457511
FSHB 19JUL06 2 562.341 354.836 7.1 ci38457511
GLRS 19JUL06 2 562.341 336.413 7.1 ci38457511
GMPK 19JUL06 2 562.341 394.969 7.1 ci38457511
HNPS 19JUL06 2 562.341 291.368 7.1 ci38457511
HOOT 19JUL06 2 562.341 305.518 7.1 ci38457511
IDOG 19JUL06 2 562.341 252.874 7.1 ci38457511
IDQG 19JUL06 2 562.341 254.888 7.1 ci38457511
IID2 19JUL06 2 562.341 414.364 7.1 ci38457511
JAS1 19JUL06 2 562.341 331.870 7.1 ci38457511
JAS1 18AUG09 3 Unknown
KYVW 19JUL06 2 562.341 242.851 7.1 ci38457511
LKHG 19JUL06 2 562.341 292.047 7.1 ci38457511
MONP 19JUL06 2 562.341 337.720 7.1 ci38457511
MTGG 19JUL06 2 562.341 298.828 7.1 ci38457511
MVFD 19JUL06 2 562.341 301.046 7.1 ci38457511
NSSS 19JUL06 2 562.341 359.383 7.1 ci38457511
OTAY 19JUL06 2 562.341 356.855 7.1 ci38457511
P003 19JUL06 2 562.341 473.148 7.1 ci38457511
P003 18OCT19 3 Missing maintenance

P066 19JUL06 2 562.341 374.423 7.1 ci38457511
P479 19JUL06 2 562.341 263.888 7.1 ci38457511
P480 19JUL06 2 562.341 331.147 7.1 ci38457511
P481 19JUL06 2 562.341 358.724 7.1 ci38457511
P482 19JUL06 2 562.341 293.814 7.1 ci38457511
P483 19JUL06 2 562.341 315.833 7.1 ci38457511
P484 19JUL06 2 562.341 280.856 7.1 ci38457511
P485 19JUL06 2 562.341 304.764 7.1 ci38457511
P486 19JUL06 2 562.341 302.552 7.1 ci38457511
P487 19JUL06 2 562.341 312.435 7.1 ci38457511
P488 19JUL06 2 562.341 317.776 7.1 ci38457511
P489 17SEP20 1 Antenna Code Changed
P489 19JUL06 2 562.341 306.917 7.1 ci38457511
P490 19JUL06 2 562.341 271.831 7.1 ci38457511
P491 19JUL06 2 562.341 274.427 7.1 ci38457511
P492 19JUL06 2 562.341 353.719 7.1 ci38457511
P493 19JUL06 2 562.341 352.814 7.1 ci38457511
P494 19JUL06 2 562.341 376.082 7.1 ci38457511
P495 19JUL06 2 562.341 352.787 7.1 ci38457511
P496 19JUL06 2 562.341 382.832 7.1 ci38457511
P497 19JUL06 2 562.341 375.471 7.1 ci38457511
P498 19JUL06 2 562.341 369.642 7.1 ci38457511
P499 19JUL06 2 562.341 365.742 7.1 ci38457511
P501 19JUL06 2 562.341 379.976 7.1 ci38457511
P502 19JUL06 2 562.341 368.718 7.1 ci38457511
P503 19JUL06 2 562.341 357.917 7.1 ci38457511
P504 19JUL06 2 562.341 301.478 7.1 ci38457511
P505 19JUL06 2 562.341 314.093 7.1 ci38457511
P506 17JUL28 1 Antenna Code Changed
P506 19JUL06 2 562.341 355.020 7.1 ci38457511
P507 19JUL06 2 562.341 338.798 7.1 ci38457511
P508 19JUL06 2 562.341 343.752 7.1 ci38457511
P509 20JAN13 1 Receiver Make and Model Changed
P509 19JUL06 2 562.341 383.745 7.1 ci38457511
P510 19JUL06 2 562.341 357.801 7.1 ci38457511
P511 19JUL06 2 562.341 296.654 7.1 ci38457511
P584 19JUL06 2 562.341 216.910 7.1 ci38457511
P600 19JUL06 2 562.341 246.667 7.1 ci38457511
P601 19JUL06 2 562.341 244.377 7.1 ci38457511
P607 19JUL06 2 562.341 277.977 7.1 ci38457511
P608 19JUL06 2 562.341 263.451 7.1 ci38457511
P740 19JUL06 2 562.341 258.275 7.1 ci38457511
P741 19JUL06 2 562.341 264.655 7.1 ci38457511
P742 19JUL06 2 562.341 268.790 7.1 ci38457511
P744 19JUL06 2 562.341 379.143 7.1 ci38457511

P797 19JUL06 2 562.341 264.738 7.1 ci38457511
PB1Y 19JUL06 2 562.341 388.855 7.1 ci38457511
PHJX 19JUL06 2 562.341 410.505 7.1 ci38457511
PIN1 19JUL06 2 562.341 261.586 7.1 ci38457511
PIN2 19JUL06 2 562.341 261.606 7.1 ci38457511
PJZX 19JUL06 2 562.341 404.850 7.1 ci38457511
PMOB 19JUL06 2 562.341 276.649 7.1 ci38457511
POBG 19JUL06 2 562.341 239.636 7.1 ci38457511
POTR 19JUL06 2 562.341 362.446 7.1 ci38457511
PTEX 19JUL06 2 562.341 399.612 7.1 ci38457511
QUEX 19JUL06 2 562.341 422.898 7.1 ci38457511
RAAP 19JUL06 2 562.341 309.643 7.1 ci38457511
RUNG 19JUL06 2 562.341 393.179 7.1 ci38457511
SA63 19JUL06 2 562.341 445.755 7.1 ci38457511
SA63 17SEP03 3 Unknown
SGLG 19JUL06 2 562.341 387.326 7.1 ci38457511
SGPS 19JUL06 2 562.341 222.340 7.1 ci38457511
SLHG 19JUL06 2 562.341 311.930 7.1 ci38457511
SLMS 19JUL06 2 562.341 312.940 7.1 ci38457511
SNTE 19JAN01 3 Unknown
THMG 19JUL06 2 562.341 273.607 7.1 ci38457511
TMAP 19JUL06 2 562.341 270.736 7.1 ci38457511
USGC 19JUL06 2 562.341 334.774 7.1 ci38457511
WIDC 19JUL06 2 562.341 231.862 7.1 ci38457511
WMDG 19JUL06 2 562.341 355.625 7.1 ci38457511
WWFG 19JUL06 2 562.341 333.092 7.1 ci38457511
WWMT 19JUL06 2 562.341 219.394 7.1 ci38457511
YUHG 19JUL06 2 562.341 379.839 7.1 ci38457511

Table B.1: List of steps for trajectory model fitting used in this study. The format of the columns follows the steps master file from Nevada Geodetic Laboratory (Blewitt et al., 2018, http://geodesy.unr.edu/NGLStationPages/steps.txt, last accessed November 14, 2020). The headers are as follows. Column 1: 4-character ID of GPS station. Column 2: date of possible step in YYMMMDD format. Column 3: step type, 1 = maintenance, 2 = earthquakes, 3 = others. For earthquakes, there are additional columns. Column 4: threshold distance affected by the earthquake in km. Column 5: distance between the station and the epicenter in km. Column 6: event magnitude. Column 7: USGS event ID.

Hyper-parameters	Value
$b_{\alpha 0}$	10^5
$c_{\alpha 0}$	0.1
b_0	10
c_0	0.1
$b_{\lambda 0}$	10^3
$c_{\lambda 0}$	10^{-3}

Table B.2: Hyper-parameters used as a priori assumptions for vbICA decomposition (Gualandi et al., 2016). The vbICA operates on a more traditional formulation of blind source separations which writes $X = A\Sigma + N$, where A is the mixing matrix, Σ is the source matrix, and N is the noise matrix. Note that this is equivalent to the notation presented in Equation B.2 since we can always decompose a matrix into a unit column norm matrix and a diagonal matrix, and hence, we can write $X = A\Sigma + N = (US_A)(S_\Sigma V^T) + N = USV^T + N$. The hyper-parameters are the precision (inverse of the variance) of each Gaussian source in Σ which can be described using a Gamma distribution with the width b and scale c for the mixing matrix ($b_{\alpha 0}$,$c_{\alpha 0}$), the sources (b_0,c_0), and the noise ($b_{\lambda 0}$,$c_{\lambda 0}$).

Ascending track 166 frame 105				Descending track 173 frame 480			
Image	Year	Month	Day	Image	Year	Month	Day
20200909	2020	9	9	20200903	2020	9	3
20200921	2020	9	21	20200909	2020	9	9
20201003	2020	10	3	20200915	2020	9	15
20201015	2020	10	15	20200921	2020	9	21
20201027	2020	10	27	20200927	2020	9	27
				20201003	2020	10	3
				20201009	2020	10	9
				20201015	2020	10	15
				20201027	2020	10	27

Table B.3: List of SAR imagery used in this study. The first two images and the first five images from ascending and descending track, respectively, are those acquired prior to the main event. Interferograms are generated between these images and those acquired after the event.

Appendix C

SUPPLEMENTARY MATERIALS FOR CHAPTER 5

C.1 Materials and methods

C.1.1 Seismicity catalogs

For Northern California, we use the standard NCSS earthquake catalog available through the Northern California Earthquake Data Center (NCEDC) managed by UC Berkeley Seismological Laboratory (NCEDC, 2014). For Southern California, we use the routinely published waveform relocated earthquake catalog (Hauksson et al., 2012) available through the Southern California Earthquake Data Center (SCEDC) managed by California Institute of Technology (Caltech). We consider all earthquakes occurred between 2006 and 2022 (inclusive) with magnitude $M \geq 1$.

C.1.2 Seismicity declustering

Aftershocks are driven by the mainshocks and can obscure periodicity analysis. They can be identified by using a modified nearest-neighbor distance approach (Zaliapin and Ben-Zion, 2013a). For each event j in the catalog, we search for the preceding nearest-neighbor event i that is most likely to be the parent (mainshock) of event j with the minimum proximity distance η_{ij}, defined using a space-time-magnitude metric (Baiesi and Paczuski, 2004, Zaliapin et al., 2008) as follows:

$$\frac{d\theta}{dt} = -\frac{V(t)\theta(t)}{D_{RS}} \ln\left(\frac{V(t)\theta(t)}{D_{RS}}\right) \tag{C.1}$$

where $t_{ij} = t_j - t_i$ is the time between the two events, r_{ij} is the distance between the epicenters of the two events, d_f is the fractal dimension of earthquake epicenters, b is the Gutenberg-Richter b-value of the frequency-magnitude distribution, m_i is the magnitude of event i, and M_c is the completeness magnitude. For simplicity, we exclude depths in our analysis. We choose $d_f = 1.6$, $b = 1$, and $M_c = 1.0$. The proximity distance η_{ij} can be visualized in a two-dimensional plot using the rescaled time T_j and the rescaled distance R_j (Zaliapin and Ben-Zion, 2013a):

$$\begin{aligned} T_j &= t_{i^*j} 10^{-0.5b(m_{i^*} - M_c)/2} \\ R_j &= (r_{i^*j})^{d_f} 10^{-0.5b(m_{i^*} - M_c)/2}. \end{aligned} \tag{C.2}$$

The distribution of the nearest-neighbor distance η_j is expected to be a mixture of two Gaussians representing the two modes: independent and clustered events. Because the productivity of the background events is expected to vary spatially, we expect the optimal mode separator η_0 to also vary spatially. To determine how η_0 vary spatially, we first sample points in the space by applying the quadtree algorithm to the observed seismicity (higher density of points where seismicity rates are high), consider 2,000 nearest events, and fit the distribution of η_j with 1-D Gaussian mixture model to obtain η_0 at that location. The Gaussian mixture model fitting is manually evaluated. If the fit is not satisfying, we determine the clustered fraction using Gamma distribution (Hainzl et al., 2006) and η_0 is then chosen so that the number of events with $\eta_j < \eta_0$ equals to the clustered fraction. $\eta_0(x, y)$ at any arbitrary point in space can be obtained through interpolation (Figure C.1). Any event j with $\eta_j \geq \eta_0(x_j, y_j)$ is considered a background event and is kept for subsequent analysis.

To evaluate the quality of the declustering method, we utilize a measure based on point process such as the coefficient of variation (CoV) (Kagan and Jackson, 1991), defined as the ratio of standard deviation and the mean of the interevent times. For a regular process with constant recurring interval, CoV < 1. For a random Poissonian process, CoV = 1. For clustered process, CoV > 1. As a result, regions with aftershocks have larger CoV, while a proper declustered catalog should have CoV of approximately 1. By evaluating a posteriori, the spatial distribution of CoV of the declustered catalog in comparison to the original catalog (Figure C.2), we can refine the chosen $\eta_0(x, y)$.

C.1.3 Periodicity detection

To test whether a periodic modulation of seismicity rate exists, we employ the Schuster tests. For a testing period T, we first convert the earthquake occurrence time t_i to a corresponding phase angle as follows: $\theta_i = 2\pi t_i/T$. Then, we perform a 2D successive Schuster walk of unit-length steps in the direction according to the computed phase angles. After a total of N steps (earthquakes), the Schuster p-value can be computed using the total drifting distance between the origin and the end point of the walk as follows (Schuster, 1897):

$$p = e^{-D^2/N}. \tag{C.3}$$

The Schuster p-value quantifies the probability of the null hypothesis that seismicity rate is uniform and follows a random Poisson point process. The null hypothesis can be rejected if the p-value is smaller than the cutoff value $p_{\text{cutoff}} = T/t_{\text{catalog length}}$, which depends on the testing period T (Ader and Avouac, 2013). For a traditional 95% confidence to reject the null hypothesis, the cutoff value becomes $p_{95} = 0.05 \cdot p_{\text{cutoff}} = 0.05 \cdot T/t_{\text{catalog length}}$. The drifting direction reflects the phases at which seismicity rate is maximum. The consistency of the drifts between the different cycles can be visually evaluated with the Schuster walk.

By performing Schuster tests for all the periods, we can construct a Schuster spectrum. Sampling the spectrum using a frequency step of $t_{\text{catalog length}})/T_{\text{min}}$ is the most optimal as it is fine enough to avoid missing some periods while preventing oversampling which could lead to unnecessarily long computation time. Evaluating Schuster p-value without visualizing the Schuster walk or building a spectrum is precarious as the drifting may be dominated by earthquake clusters that may not be completely removed during the declustering process. A true periodicity detection would result in an isolated low p-value at a particular period, while imperfect declustering would result as drifting low p-values around the characteristic decay of aftershocks.

If the seismicity rate modulation is harmonics, the Schuster p-value is related to the modulation amplitude α as follows (Ader et al., 2014):

$$\alpha = \sqrt{-\frac{4(\ln p + 1)}{N}}. \tag{C.4}$$

Because there is a cutoff p-value for the periodicity detection to be significant, there is a corresponding threshold for the modulation amplitude required for periodicity to be detected, which depends on the catalog length and the number of events considered. For the spatial distribution of α shown in Figure 5.2, each gridded point is a result of a Schuster test performed on 2000 nearest events resulting in $\alpha_{\text{threshold}} = 0.06$ and $\alpha_{95} = 0.10$.

C.1.4 Seasonal stress due to surface loading

The changes in seasonal water storage used in this study is modelled using a combination of surface displacements data from Global Navigation Satellite System (GNSS) stations and gravity data from a pair of Gravity Recovery and Climate Experiment (GRACE) satellites (Argus et al., 2022). The spatial distribution of the

seasonal modulation amplitude of the equivalent water thickness is shown in Figure C.7. Consequently, changes of water thickness Δh results in changes of vertical load $\rho_{\text{water}} g \Delta h$ and hence the stress state of the Earth's crust. The vertical loads are assumed to be applied on Earth's surface and can be converted to multiple point force acting at some regular grid with a spacing of 2.5 km. The total stress changes in the elastic half-space are then a superposition of analytical solutions from individual vertical point forces. Assuming that the force N is applied at the origin of the half-space, the stress changes (compression, positive) can be calculated as follows (Boussinesq, 1878, Jaeger et al., 2007):

$$
\begin{aligned}
\sigma_{xx}(x,y,z) &= \frac{N}{2\pi}\left[\frac{3x^2z}{r^5} + \frac{(1-2\nu)(y^2+z^2)}{r^3(z+r)} - \frac{(1-2\nu)z}{r^3} - \frac{(1-2\nu)x^2}{r^2(z+r)^2}\right] \\
\sigma_{yy}(x,y,z) &= \frac{N}{2\pi}\left[\frac{3y^2z}{r^5} + \frac{(1-2\nu)(x^2+z^2)}{r^3(z+r)} - \frac{(1-2\nu)z}{r^3} - \frac{(1-2\nu)y^2}{r^2(z+r)^2}\right] \\
\sigma_{zz}(x,y,z) &= \frac{N}{2\pi}\left[\frac{3z^3}{r^5}\right] \\
\sigma_{xy}(x,y,z) &= \frac{N}{2\pi}\left[\frac{3xyz}{r^5} - \frac{(1-2\nu)xy(z+2r)}{r^3(z+r)^2}\right] \\
\sigma_{yz}(x,y,z) &= \frac{N}{2\pi}\left[\frac{3yz^2}{r^5}\right] \\
\sigma_{xz}(x,y,z) &= \frac{N}{2\pi}\left[\frac{3xz^2}{r^5}\right]
\end{aligned}
\tag{C.5}
$$

where r is the distance between the origin and point (x, y, z) in which the stress changes are evaluated. The stress changes are evaluated at a seismogenic depth of 5 km where most earthquakes occurred in California.

To evaluate whether stress changes are more favorable for failure along a particular plane, we use the Coulomb stress change defined as $\Delta S = \Delta\tau - \mu\Delta\sigma$, where $\Delta\tau$ and $\Delta\sigma$ is the shear stress change and normal stress change on the failure plane, respectively. The coefficient of friction is chosen to be 0.4 to approximately account for poroelastic effects (King et al., 1994). We calculate ΔS on optimally oriented fault plane. To do so, we first calculate the principal stress changes $\Delta\sigma_1$, $\Delta\sigma_2$, and $\Delta\sigma_3$. Then, ΔS on the optimally oriented plane is (King et al., 1994):

$$\begin{aligned}\Delta\sigma_{\text{optimal}} &= \frac{1}{2}(\Delta\sigma_1 + \Delta\sigma_3) - \frac{1}{2}(\Delta\sigma_1 - \Delta\sigma_3)\cos 2\beta \\ \Delta\tau_{\text{optimal}} &= \frac{1}{2}(\Delta\sigma_1 - \Delta\sigma_3)\sin 2\beta \\ \Delta S_{\text{optimal}} &= \Delta\sigma_{\text{optimal}} - \mu\Delta\tau_{\text{optimal}}\end{aligned} \tag{C.6}$$

where the optimally oriented plane is oriented at an angle $\beta = \frac{1}{2}\arctan(-\mu)$ from the σ_1 axis.

C.1.5 Relating stress to seismicity

To relate seismicity to stress, we employ a model based on rate-and-state friction formulation. In this model, friction coefficient evolves with slip velocity V and the state of the fault θ according to the following (Dieterich, 1979, Marone, 1998a, Ruina, 1983):

$$\mu = \mu^* + a\ln\left(\frac{V(t)}{V^*}\right) + b\ln\left(\frac{V^*\theta}{D_{RS}}\right) \tag{C.7}$$

where μ^* is the steady-state reference friction coefficient at reference slip rate V^*, a and b are non-dimensional material constants, and D_{RS} is the critical slip distance. The state θ has a unit of time and can be evolved using several state evolution laws, such as the following (Dieterich, 1979):

$$\frac{d\theta}{dt} = 1 - \frac{V\theta}{D_{RS}}. \tag{C.8}$$

In this case, the state θ reflects the contact age and can be interpreted as related to the time since the last earthquake. For a population of faults that are critically stressed, the formulation can be used to described the response of seismicity to an evolving Coulomb stress perturbation $\Delta S(t)$ according to the following equation (Dieterich, 1994):

$$\frac{R(t)}{r} = \frac{e^{\frac{\Delta S(t)}{a\sigma}}}{1 + \frac{1}{t_a}\int_0^t e^{\frac{\Delta S(x)}{a\sigma}}\,dx} \tag{C.9}$$

where $t_a = a\sigma/\dot{S}$ is the characteristic relaxation time of the seismicity following a stress step (i.e., the characteristic duration of an aftershock sequence), $\dot{S}$ is the

background stress rate, and $a\sigma$ is the product of the rate-and-state parameter a and normal stress σ, which represents the friction-stress parameter governing earthquake nucleation. This formulation accounts for the non-instantaneous nature of earthquake nucleation and successfully explains a number of time-dependent behaviors of earthquakes that cannot be explained by the Coulomb instantaneous failure model, such as the presence of both locked and slowly creeping segments of natural faults (Bürgmann et al., 2000, Perfettini et al., 2010), correlation of earthquakes with periodic loadings (Ader et al., 2014, Beeler and Lockner, 2003), the slow-slip driven earthquake swarms (Lohman and McGuire, 2007, Sirorattanakul et al., 2022b), and seismicity induced by gas extraction (Acosta et al., 2023). For the case of harmonic stress perturbations, Equation C.9 reduces the following:

$$\Delta S = a\sigma \ln(1 + \alpha). \tag{C.10}$$

C.2 Supplementary figures

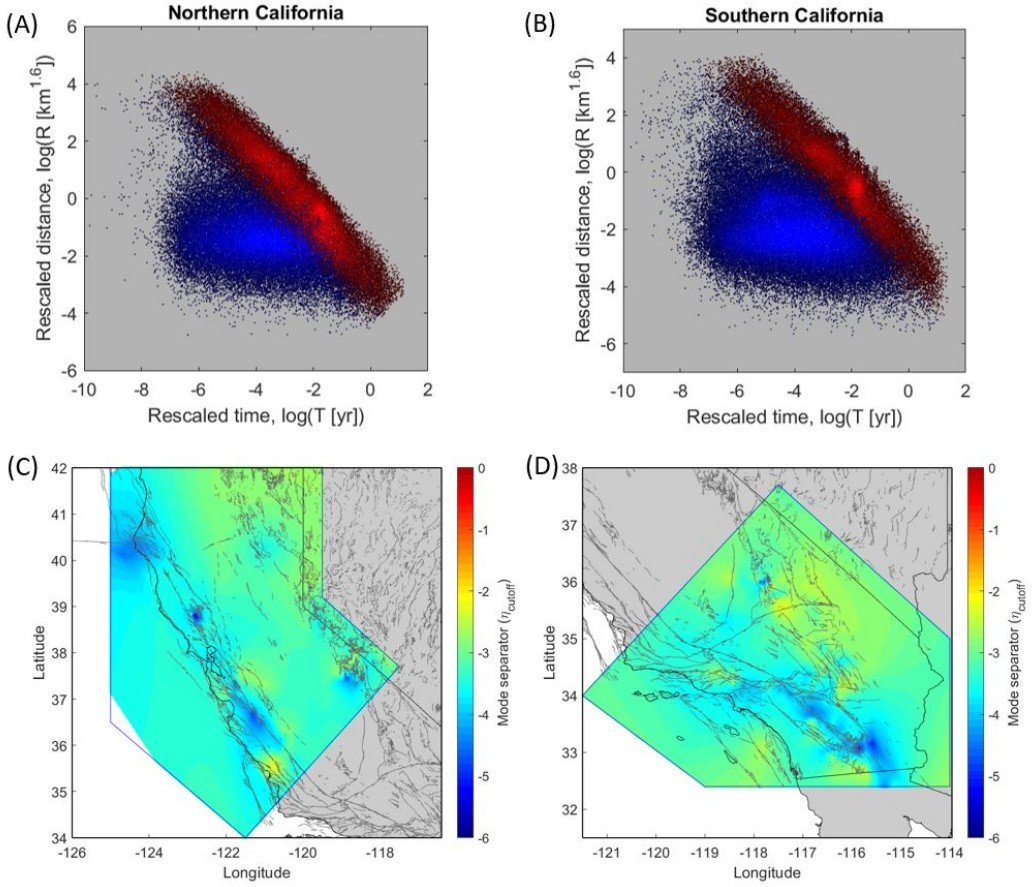

Figure C.1: Identifying aftershocks using nearest-neighbor distances. (A-B) Distribution of rescaled time and rescaled distance for earthquakes in Northern and Southern California. Red represents to the independent earthquakes, while blue represents aftershocks. (C-D) Spatial distribution of mode separator used to separate independent earthquakes from aftershocks.

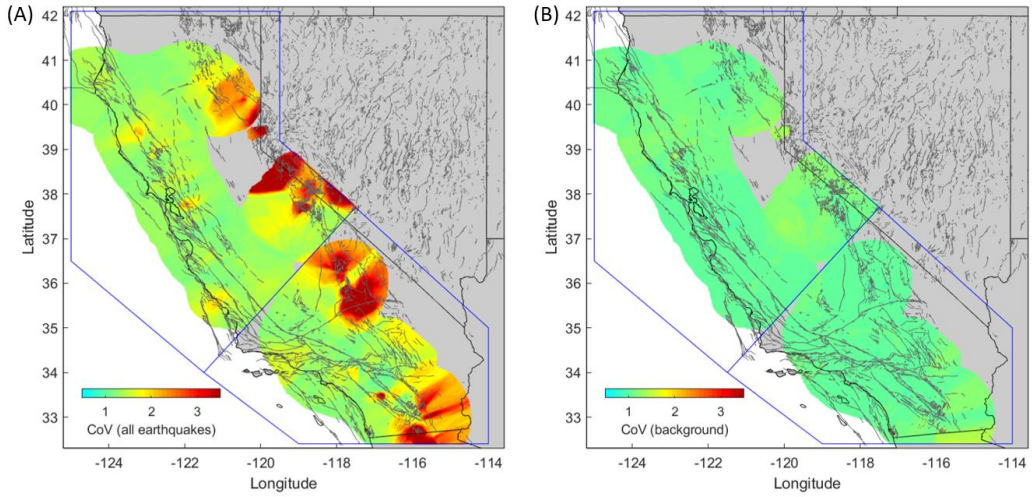

Figure C.2: Clustering statistics of earthquakes in California. (A) The coefficient of variations (CoV) of all earthquakes with magnitude $M \geq 1$. CoV quantifies the clustering in the point process and is defined as the ratio of standard deviation and the mean of interevent times. A Poisson process would have CoV of 1, while regular process would have CoV < 1 and clustered process would have CoV > 1. (B) CoV for the independent earthquakes after declustering.

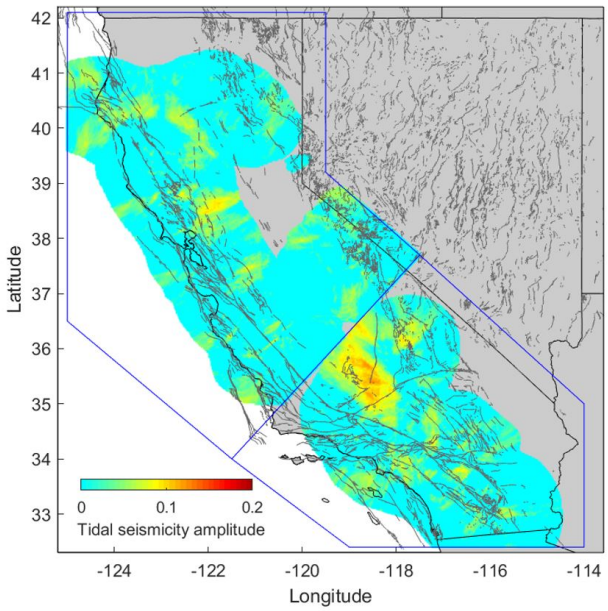

Figure C.3: Tidal modulation of seismicity rate. Amplitudes of tidal modulation of independent earthquake rates determined from the Schuster tests (Ader and Avouac, 2013). Values lower than 0.13 are not statistically significant.

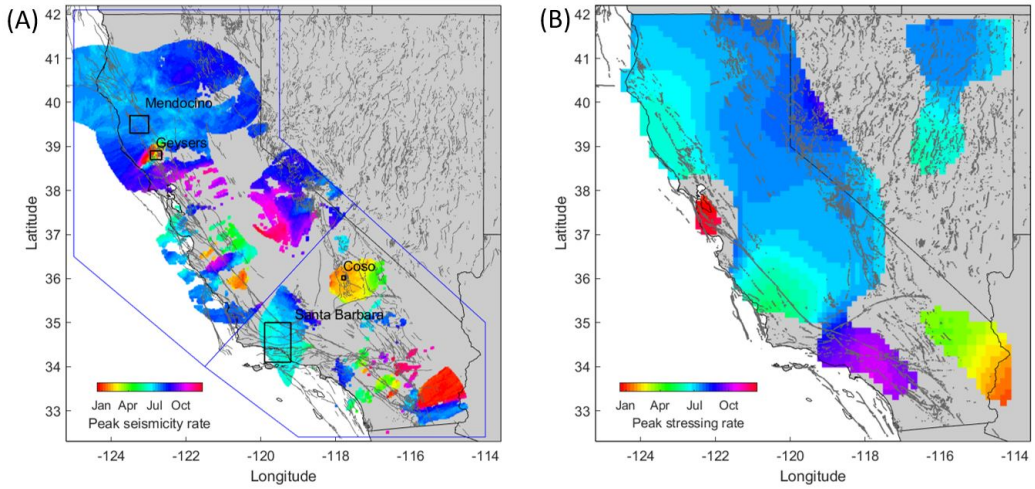

Figure C.4: Phases of peak seismicity rate and stressing rate. (A) Phases of peak seismicity rate determined from the Schuster walk. Regions with seasonal seismicity amplitude smaller than the detection threshold of 0.06 are masked out. (B) Phases of peak stressing rate determined by the best-fitting sinusoidal function to the time series of Coulomb stress changes. Regions with seasonal stress amplitudes smaller than 200 Pa are masked out.

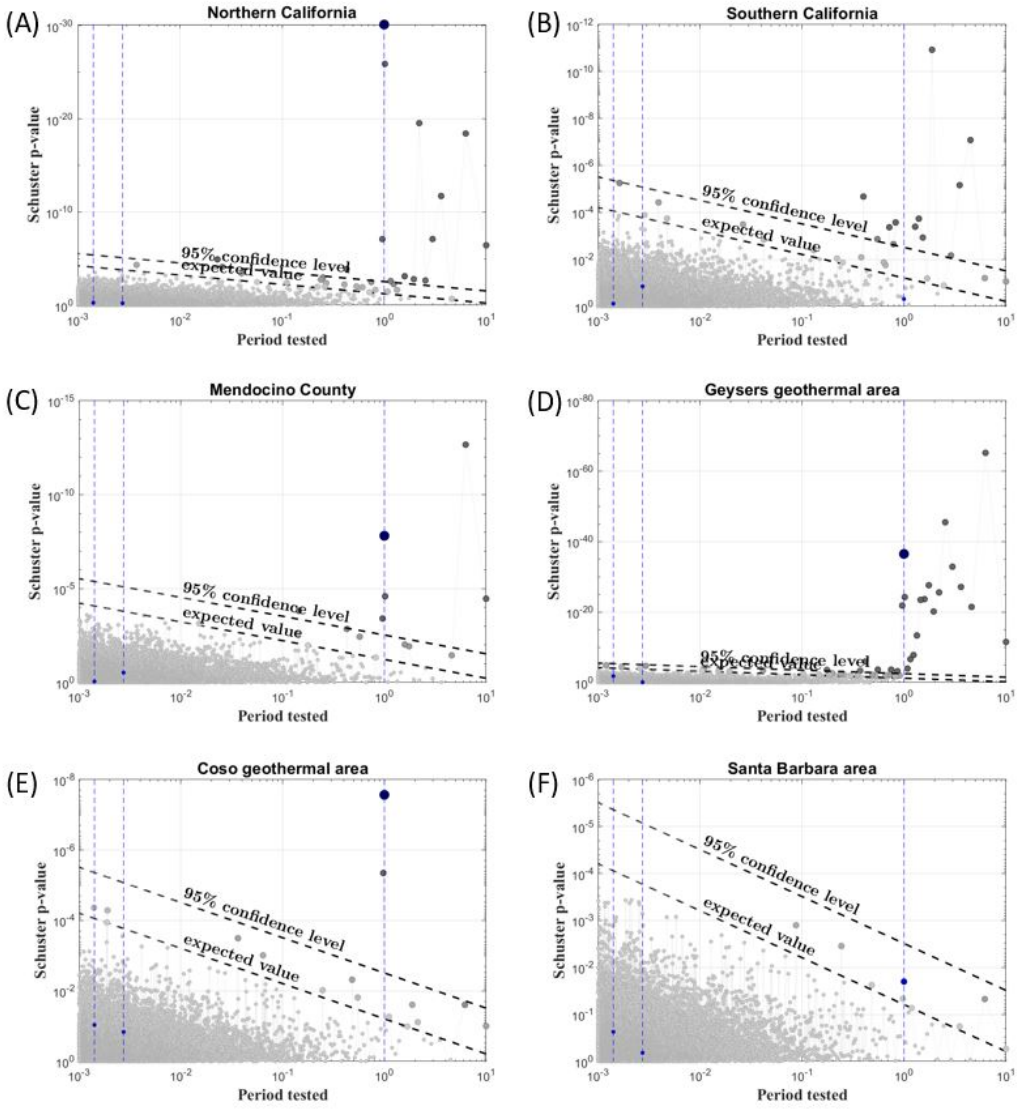

Figure C.5: Schuster spectrum for the selected regions shown in Figure 5.2C-H. Isolated p-value reflects periodicity detection, while drifting low p-value reflects the imperfection of the declustering method.

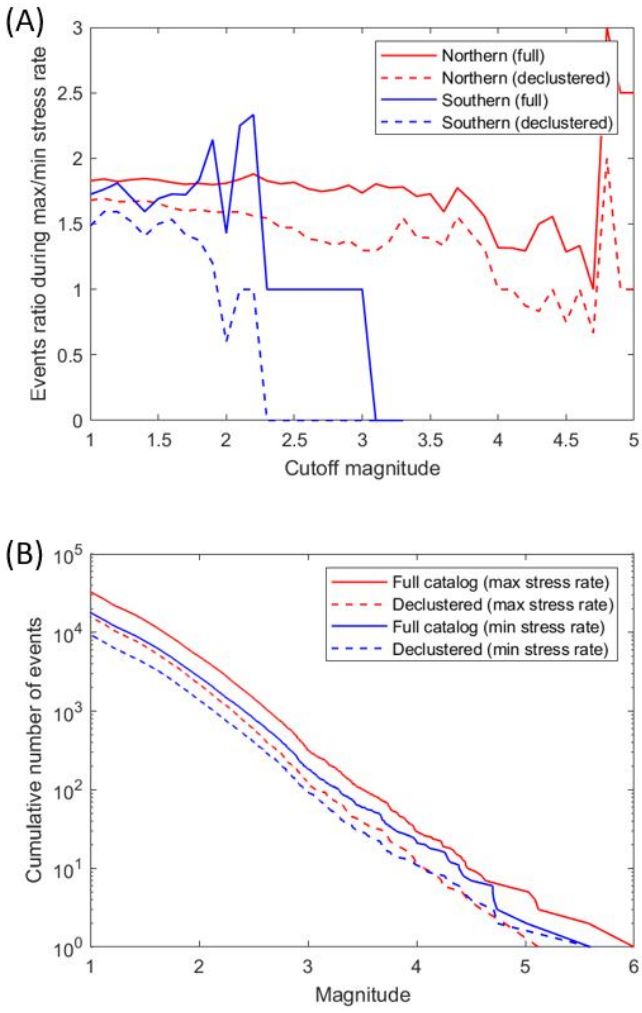

Figure C.6: Sensitivity of seasonal modulation to completeness magnitudes. (A) Ratio of number of events occurring within 1.5 months from the peak stress rate and those within 1.5 months from the minimum stress rate. Only regions with seasonal stress amplitudes > 200 Pa are considered. For large enough samples, the ratio is independent of the cutoff magnitude. (B) The cumulative frequency-magnitude distribution of events occurred within 1.5 months from peak stress rate and 1.5 months from the minimum stress rate. The excess events during peak stress rate include events of all magnitudes and not just the smaller ones.

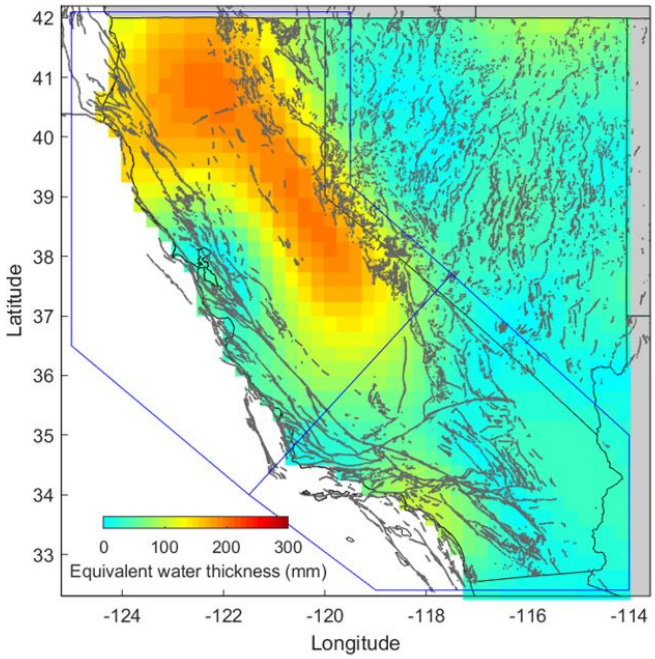

Figure C.7: Seasonal amplitudes of the equivalent water thickness. The equivalent water thickness is estimated from geodetic measurements (Argus et al., 2022).

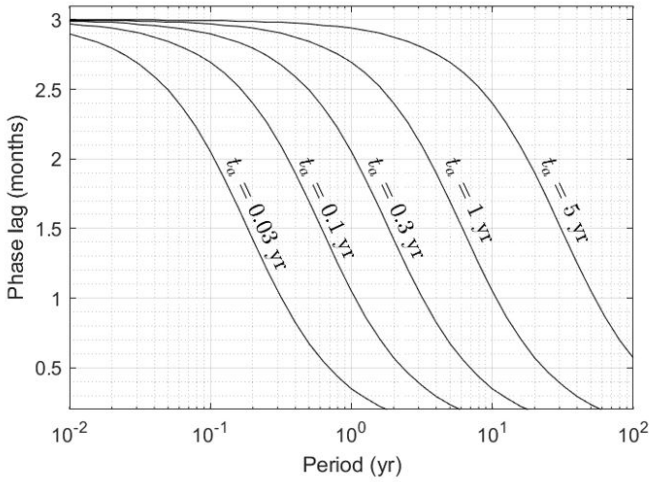

Figure C.8: Predicted phase lag using the spring-slider rate-and-state model. Phase lag between peak seismicity rate and peak stress rate for the different perturbation periods and different value of the characteristic time t_a. The perturbations are assumed to be harmonics with amplitudes of 300 Pa. The friction-stress parameter $a\sigma$ is chosen to be the median value of 3.5 kPa from our analysis.

Appendix D

SUPPLEMENTARY MATERIALS FOR CHAPTER 6

D.1 Supplementary figures

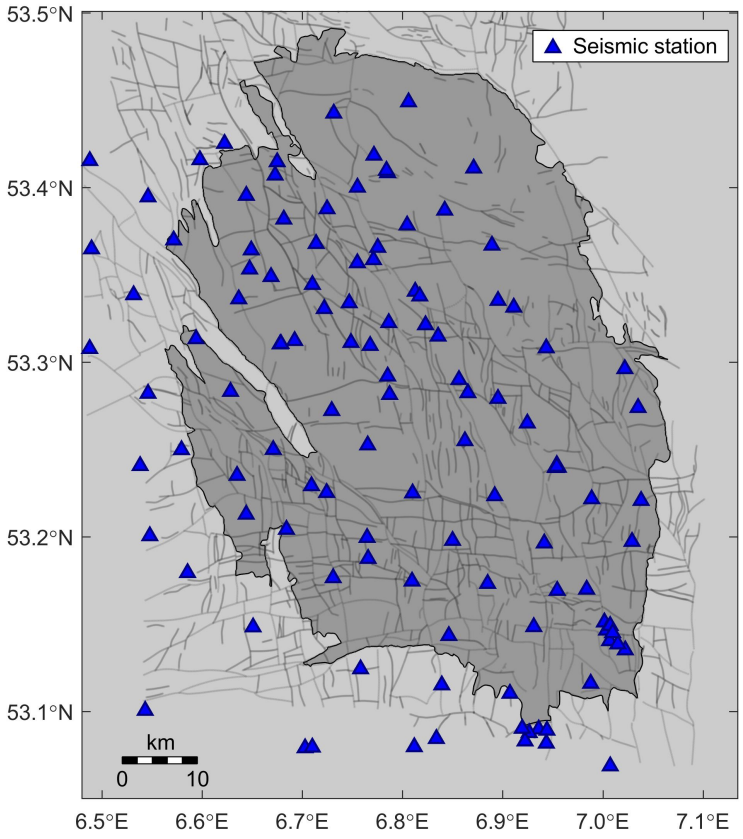

Figure D.1: Locations of seismic stations from NL and NR networks located within the boundary of the available 3D velocity model (approximately between longitude of 6.48°E and 7.05°E and between latitude of 53.05°N and 53.5°N) used in this study.

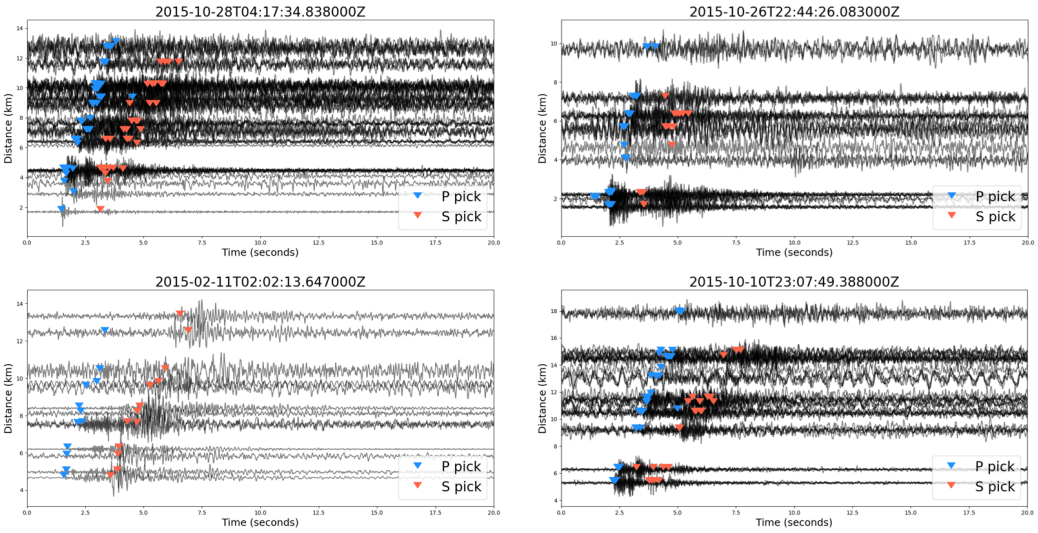

Figure D.2: Examples of P and S picks from selected four new events that were previously unreported in the KNMI catalog.

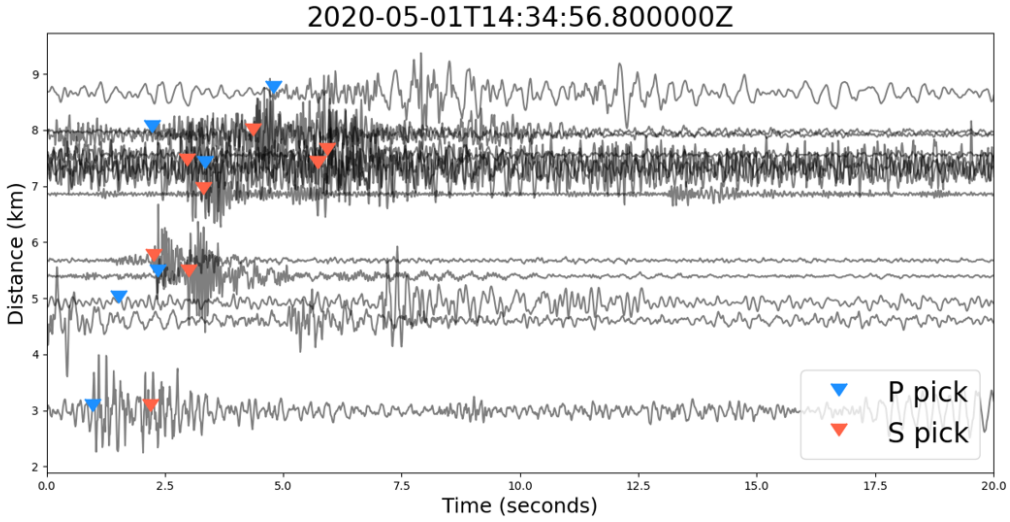

Figure D.3: An example of a spurious detection identified by the machine learning algorithm due to instrumental and cultural noises. These are removed from our catalog during the step when we manually inspected the waveforms of each identified event.

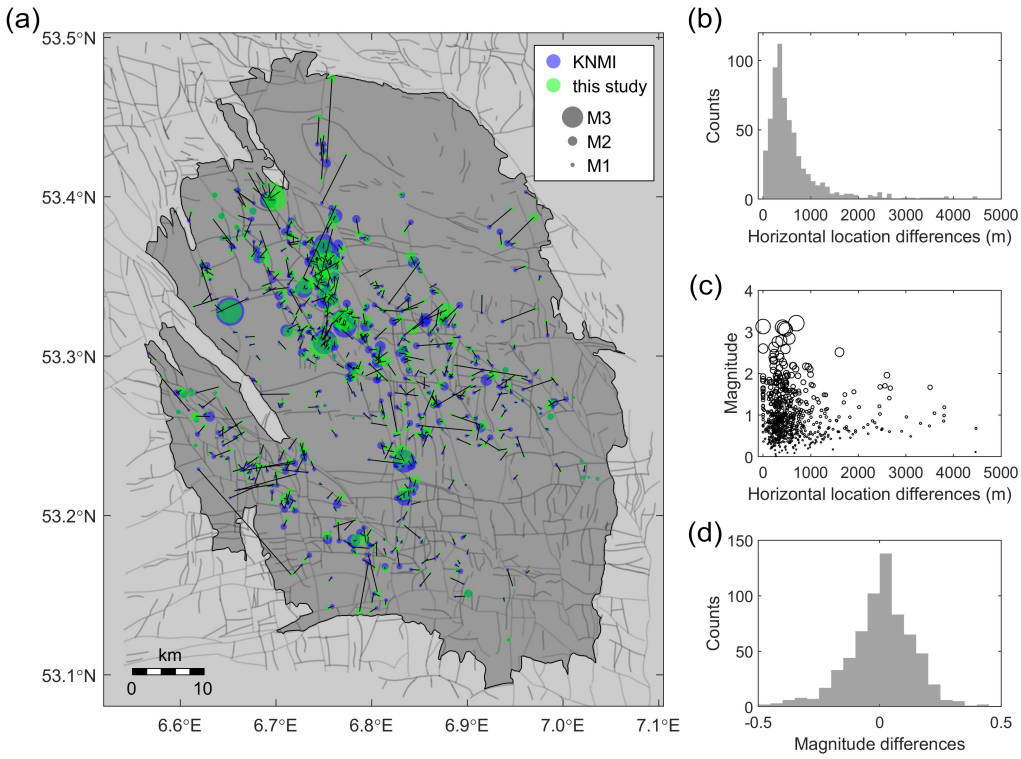

Figure D.4: Comparison between the enhanced seismicity catalog from this study with the standard catalog from the Royal Netherlands Meteorological Survey (KNMI). (a) Events are denoted with circles color coding by the catalog that they are from. The black lines connect the same event from the two different catalogs. (b) Histogram of the horizontal location differences. (c) The horizontal location differences vs. magnitudes from our enhanced catalog. The differences are largest for small events whose uncertainty of arrival time picks is high. (d) Histogram showing differences in magnitudes from the two catalogs. Only events that exist in both catalogs are shown here.

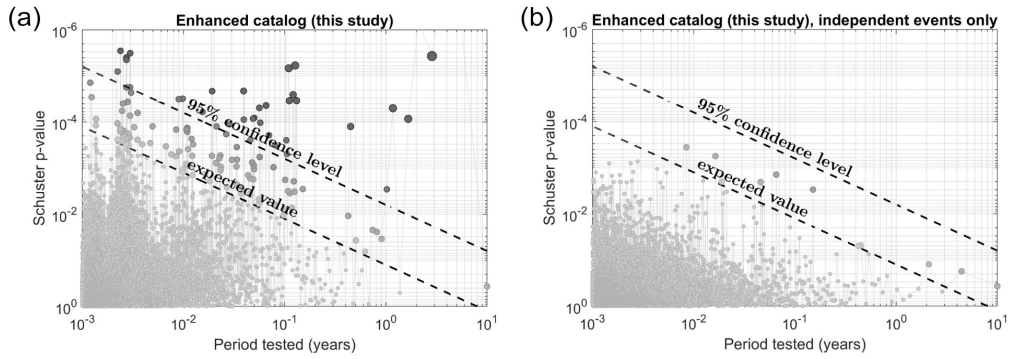

Figure D.5: Schuster analysis for detection of periodic modulation of seismicity rate. (a) The Schuster spectrum is for all events in the entire enhanced catalog with $M_L \geq 0.5$. (b) is similar to (a), but only for the independent events. The lower the p-value, the larger the periodic modulation. The two diagonal black dashed lines represent the expected p-value for catalogs without any periodic modulation (purely Poissonian process) and a threshold at which lower p-value means that the periodicity is detected at the 95% confidence level.

Bibliography

B. Aagaard, M. Knepley, and C. Williams. Pylith user manual version 2.2.1, 2019.

M. Acosta and M. Violay. Mechanical and hydraulic transport properties of transverse-isotropic Gneiss deformed under deep reservoir stress and pressure conditions. *International Journal of Rock Mechanics and Mining Sciences*, 130: 104235, 2020. doi: 10.1016/j.ijrmms.2020.104235.

M. Acosta, R. Maye, and M. Violay. Hydraulic transport through Calcite bearing faults with customized roughness: Effects of normal and shear loading. *Journal of Geophysical Research: Solid Earth*, 125(8), 2020. doi: 10.1029/2020JB019767.

M. Acosta, J.-P. Avouac, J. D. Smith, K. Sirorattanakul, H. Kaveh, and S. J. Bourne. Earthquake nucleation characteristics revealed by seismicity response to seasonal stress variations induced by gas production at Groningen. *Geophysical Research Letters*, 50(19):e2023GL105455, 2023. doi: 10.1029/2023GL105455.

T. J. Ader and J.-P. Avouac. Detecting periodicities and declustering in earthquake catalogs using the Schuster spectrum, application to Himalayan seismicity. *Earth and Planetary Science Letters*, 377-378:97–105, 2013. doi: 10.1016/j.epsl.2013.06.032.

T. J. Ader, N. Lapusta, J.-P. Avouac, and J.-P. Ampuero. Response of rate-and-state seismogenic faults to harmonic shear-stress perturbations. *Geophysical Journal International*, 198(1):385–413, 2014. doi: 10.1093/gji/ggu144.

D. Agnew. Earth Tides. In *Treatise on Geophysics*, pages 151–178. Elsevier, 2007. doi: 10.1016/B978-0-444-53802-4.00058-0.

D. C. Agnew. Strainmeters and tiltmeters. *Review of Geophysics*, 24(3):469–700, 1986. doi: 10.1029/RG024i003p00579.

J. Ake, K. Mahrer, D. O'Connell, and L. Block. Deep-Injection and Closely Monitored Induced Seismicity at Paradox Valley, Colorado. *Bulletin of the Seismological Society of America*, 95(2):664–683, 2005. doi: 10.1785/0120040072.

K. Aki. Maximum likelihood estimate of b in the formula log N = a-bM and its confidence limits. *Bulletin of the Earthquake Research Institute, University of Tokyo*, 43:237–239, 1965.

J. Albaric, V. Oye, N. Langet, M. Hasting, I. Lecomte, K. Iranpour, M. Messeiller, and P. Reid. Monitoring of induced seismicity during the first geothermal reservoir stimulation at Paralana, Australia. *Geothermics*, 52:120–131, 2014. doi: 10.1016/j.geothermics.2013.10.013.

M. Alghannam, S. Larochelle, N. Lapusta, V. Rubino, K. Sirorattanakul, A. Lattanzi, and A. J. Rosakis. Reproducing the lab-observed dependence of rupture nucleation on fluid pressurization rate in rate-and-state simulations. *Under Review at Philosophical Transactions of the Royal Society A*, 2024.

Z. Altamimi, P. Rebischung, L. Métivier, and X. Collilieux. ITRF2014: A new release of the International Terrestrial Reference Frame modeling nonlinear station motions. *Journal of Geophysical Research: Solid Earth*, 121(8):6109–6131, 2016. doi: 10.1002/2016JB013098.

Y. Amezawa, T. Maeda, and M. Kosuga. Migration diffusivity as a controlling factor in the duration of earthquake swarms. *Earth, Planets and Space*, 73(1):148, 2021. doi: 10.1186/s40623-021-01480-7.

G. Amontons. De la resistance cause'e dans les machines (About resistance and force in machines). *Mem l'Acedemie R A*, pages 257–282, 1699.

C. B. Amos, P. Audet, W. C. Hammond, R. Bürgmann, I. A. Johanson, and G. Blewitt. Uplift and seismicity driven by groundwater depletion in central California. *Nature*, 509(7501):483–486, 2014. doi: 10.1038/nature13275.

J.-P. Ampuero and A. M. Rubin. Earthquake nucleation on rate and state faults – Aging and slip laws. *Journal of Geophysical Research: Solid Earth*, 113(B1): 2007JB005082, 2008. doi: 10.1029/2007JB005082.

D. F. Argus, R. G. Gordon, and C. DeMets. Geologically current motion of 56 plates relative to the no-net-rotation reference frame: NNR-MORVEL56. *Geochemistry, Geophysics, Geosystems*, 12(11), 2011. doi: 10.1029/2011GC003751.

D. F. Argus, H. R. Martens, A. A. Borsa, E. Knappe, D. N. Wiese, S. Alam, M. Anderson, A. Khatiwada, N. Lau, A. Peidou, M. Swarr, A. M. White, M. S. Bos, M. Ellmer, F. W. Landerer, and W. P. Gardiner. Subsurface water flux in California's Central Valley and its source watershed from space geodesy. *Geophysical Research Letters*, 49(22):e2022GL099583, 2022. doi: 10.1029/2022GL099583.

G. M. Atkinson, D. W. Eaton, and N. Igonin. Developments in understanding seismicity triggered by hydraulic fracturing. *Nature Reviews Earth & Environment*, 1(5):264–277, 2020. doi: 10.1038/s43017-020-0049-7.

L. Audin, J.-P. Avouac, M. Flouzat, and J.-L. Plantet. Fluid-driven seismicity in a stable tectonic context: The Remiremont fault zone, Vosges, France. *Geophysical Research Letters*, 29(6):13–1–13–4, 2002. doi: 10.1029/2001GL012988.

J.-P. Avouac. From geodetic imaging of seismic and aseismic fault slip to dynamic modeling of the seismic cycle. *Annual Review of Earth and Planetary Sciences*, 43(1):233–271, 2015. doi: 10.1146/annurev-earth-060614-105302.

J.-P. Avouac and S. Leprince. 3.13 - Geodetic imaging using optical systems. In G. Schubert, editor, *Treatise on Geophysics (Second Edition)*, pages 387–424. Elsevier, Oxford, second edition edition, 2015. doi: 10.1016/B978-0-444-53802-4.00067-1.

M. Baiesi and M. Paczuski. Scale-free networks of earthquakes and aftershocks. *Physical Review E*, 69(6):066106, 2004. doi: 10.1103/PhysRevE.69.066106.

S. Baisch, R. Weidler, R. Voros, D. Wyborn, and L. De Graaf. Induced seismicity during the stimulation of a geothermal hfr reservoir in the Cooper Basin, Australia. *Bulletin of the Seismological Society of America*, 96(6):2242–2256, 2006. doi: 10.1785/0120050255.

S. Barbot, N. Lapusta, and J.-P. Avouac. Under the hood of the earthquake machine: Toward predictive modeling of the seismic cycle. *Science*, 368(6082):707–710, 2012. doi: 10.1126/science.1218796.

O. Barnea Cohen, S. Cesca, T. Dahm, A. Hofstetter, Y. Hamiel, and A. Agnon. Seismicity induced at the Northern Dead Sea Transform Fault, Kinneret (Sea of Galilee) Basin, by shallow creep involving a salt body. *Tectonics*, 41(10): e2022TC007247, 2022. doi: 10.1029/2022TC007247.

N. M. Bartlow, D. A. Lockner, and N. M. Beeler. Laboratory triggering of stick-slip events by oscillatory loading in the presence of pore fluid with implications for physics of tectonic tremor. *Journal of Geophysical Research: Solid Earth*, 117 (B11):B11411, 2012. doi: 10.1029/2012JB009452.

T. Baumberger. Contact dynamics and friction at a solid-solid interface: Material versus statistical aspects. *Solid State Communications*, 102(2-3):175–185, 1997. doi: 10.1016/S0038-1098(96)00710-7.

N. M. Beeler and D. A. Lockner. Why earthquakes correlate weakly with the solid earth tides: Effects of periodic stress on the rate and probability of earthquake occurrence. *Journal of Geophysical Research: Solid Earth*, 108(B8): 2001JB001518, 2003. doi: 10.1029/2001JB001518.

N. M. Beeler, T. E. Tullis, and J. D. Weeks. The roles of time and displacement in the evolution effect in rock friction. *Geophysical Research Letters*, 21(18): 1987–1990, 1998. doi: 10.1029/94GL01599.

N. M. Beeler, A. Rubin, P. Bhattacharya, B. Kilgore, and T. Tullis. Apparent age dependence of the fault weakening distance in rock friction. *Journal of Geophysical Research: Solid Earth*, 127(1):e2021JB022772, 2022. doi: 10.1029/2021JB022772.

O. Ben-David, S. M. Rubinstein, and J. Fineberg. Slip-stick and the evolution of frictional strength. *Nature*, 463(7277):76–79, 2010. doi: 10.1038/nature08676.

Y. Ben-Zion and V. Lyakhovsky. Analysis of aftershocks in a lithospheric model with seismogenic zone governed by damage rheology. *Geophysical Journal International*, 165(1):197–210, 2006. doi: 10.1111/j.1365-246X.2006.02878.x.

H. Benioff. Earthquakes and rock creep, part 1. *Bulletin of the Seismological Society of America*, 41:31–62, 1951.

P. Berthoud, T. Baumberger, C. G'Sell, and J.-M. Hiver. Physical analysis of the state- and rate-dependent friction law: Static friction. *Physical Review B*, 59(22): 14313–14327, 1999. doi: 10.1103/PhysRevB.59.14313.

P. Bettinelli, J.-P. Avouac, M. Flouzat, L. Bollinger, G. Ramillien, S. Rajaure, and S. Sapkota. Seasonal variations of seismicity and geodetic strain in the Himalaya induced by surface hydrology. *Earth and Planetary Science Letters*, 266(3-4): 332–344, 2008. doi: 10.1016/j.epsl.2007.11.021.

M. Bevis and A. Brown. Trajectory models and reference frames for crustal motion geodesy. *Journal of Geodesy*, 88(3):283–311, 2014. doi: 10.1007/s00190-013-0685-5.

P. Bhattacharya and R. C. Viesca. Fluid-induced aseismic fault slip outpaces pore-fluid migration. *Science*, 364(6439):464–468, 2019. doi: 10.1126/science.aaw7354.

P. Bhattacharya, A. M. Rubin, T. E. Tullis, N. M. Beeler, and K. Okazaki. The evolution of rock friction is more sensitive to slip than elapsed time, even at near-zero slip rates. *Proceedings of the National Academy of Sciences*, 119(30): e2119462119, 2022. doi: 10.1073/pnas.2119462119.

R. Bilham, N. Suszek, and S. Pinkney. California creepmeters. *Seismological Research Letters*, 75(4):481–492, 2004. doi: 10.1785/gssrl.75.4.481.

P. Bird. An updated digital model of plate boundaries. *Geochemistry, Geophysics, Geosystems*, 4(3), 2003. doi: 10.1029/2001GC000252.

M. L. Blanpied, D. A. Lockner, and J. D. Byerlee. Frictional slip of granite at hydrothermal conditions. *Journal of Geophysical Research: Solid Earth*, 100 (B7):13045–13064, 1995. doi: 10.1029/95JB00862.

G. Blewitt. 3.11 - GPS and space-based geodetic methods. In G. Schubert, editor, *Treatise on Geophysics (Second Edition)*, pages 307–338. Elsevier, Oxford, second edition edition, 2015. doi: 10.1016/B978-0-444-53802-4.00060-9.

G. Blewitt, W. Hammond, and C. Kreemer. Harnessing the GPS data explosion for interdisciplinary science. *Eos*, 99, 2018. doi: 10.1029/2018EO104623.

L. Bollinger, F. Perrier, J. Avouac, S. Sapkota, U. Gautam, and D. R. Tiwari. Seasonal modulation of seismicity in the Himalaya of Nepal. *Geophysical Research Letters*, 34(8):2006GL029192, 2007. doi: 10.1029/2006GL029192.

M. Bornert, F. Brémand, P. Doumalin, J.-C. Dupré, M. Fazzini, M. Grédiac, F. Hild, S. Mistou, J. Molimard, J.-J. Orteu, L. Robert, Y. Surrel, P. Vacher, and B. Wattrisse. Assessment of digital image correlation measurement errors: Methodology and results. *Experimental Mechanics*, 49(3):353–370, 2009. doi: 10.1007/s11340-008-9204-7.

M. Bornert, P. Doumalin, J.-C. Dupré, C. Poilâne, L. Robert, E. Toussaint, and B. Wattrisse. Short remarks about synthetic image generation in the context of sub-pixel accuracy of Digital Image Correlation. Porto, Portugal, 2012.

S. J. Bourne and S. J. Oates. Extreme threshold failures within a heterogeneous elastic thin sheet and the spatial-temporal development of induced seismicity within the Groningen gas field. *Journal of Geophysical Research: Solid Earth*, 122(12):10,299–10,320, 2017. doi: 10.1002/2017JB014356.

S. J. Bourne, S. J. Oates, J. Van Elk, and D. Doornhof. A seismological model for earthquakes induced by fluid extraction from a subsurface reservoir. *Journal of Geophysical Research: Solid Earth*, 119(12):8991–9015, 2014. doi: 10.1002/2014JB011663.

S. J. Bourne, S. J. Oates, and J. van Elk. The exponential rise of induced seismicity with increasing stress levels in the groningen gas field and its implications for controlling seismic risk. *Geophysical Journal International*, 213(3):1693–1700, 2018. doi: 10.1093/gji/ggy084.

J. Boussinesq. Équilibre élastique d'un solide isotrope de masse négligeable,soumis à différents poids [Elastic equilibrium of a weightless isotropic solid under various loads]. *Comptes rendus de l'Académie des Sciences*, 86:1260–1263, 1878.

F. P. Bowden and F. H. Thomas. The surface temperature of sliding solids. *Proceedings of the Royal Society of London A*, 223(1152):29–40, 1878. doi: 10.1098/rspa.1954.0098.

Y. Brechet and Y. Estrin. The effect of strain rate sensitivity on dynamic friction of metals. *Scripta Metallurgica et Materialia*, 30(11):1449–1454, 1994. doi: 10.1016/0956-716X(94)90244-5.

E. E. Brodsky and N. J. Van Der Elst. The uses of dynamic earthquake triggering. *Annual Review of Earth and Planetary Sciences*, 42(1):317–339, 2014. doi: 10.1146/annurev-earth-060313-054648.

E. E. Brodsky, E. Roeloffs, D. Woodcock, I. Gall, and M. Manga. A mechanism for sustained groundwater pressure changes induced by distant earthquakes. *Journal of Geophysical Research: Solid Earth*, 108(B8), 2003. doi: 10.1029/2002JB002321.

D. S. Brothers, N. W. Driscoll, G. M. Kent, A. J. Harding, J. M. Babcock, and R. L. Baskin. Tectonic evolution of the Salton Sea inferred from seismic reflection data. *Nature Geoscience*, 2(8):581–584, 2009. doi: 10.1038/ngeo590.

A. Buades, B. Coll, and J.-M. Morel. A non-local algorithm for image denoising. In *2005 IEEE Computer Society Conference on Computer Vision and Pattern Recognition (CVPR'05)*, volume 2, pages 60–65, San Diego, CA, USA, 2005. IEEE. doi: 10.1109/CVPR.2005.38.

A. Buades, B. Coll, and J.-M. Morel. The staircasing effect in neighborhood filters and its solution. *IEEE Transactions on Image Processing*, 15(6):1499–1505, 2006. doi: 10.1109/TIP.2006.871137.

M. Bucholc and S. Steacy. Tidal stress triggering of earthquakes in Southern California. *Geophysical Journal International*, 205(2):681–693, 2016. doi: 10.1093/gji/ggw045.

L. Buijze, P. A. Van Den Bogert, B. B. Wassing, B. Orlic, and J. Ten Veen. Fault reactivation mechanisms and dynamic rupture modelling of depletion-induced seismic events in a Rotliegend gas reservoir. *Netherlands Journal of Geosciences*, 96(5):s131–s148, 2017. doi: 10.1017/njg.2017.27.

U. Burkitov, H. Van Oeveren, and P. Valvatne. Groningen field review 2015 subsurface dynamic modelling report. Technical report, Nederlandse Aardolie Maatschappij, 2016. URL https://namfeitenencijfers.data-app.nl/download/rapport/e683753a-e085-417d-995d-b7ae7a9c820f?open=true.

R. Bürgmann. The geophysics, geology and mechanics of slow fault slip. *Earth and Planetary Science Letters*, 495:112–134, 2018. doi: 10.1016/j.epsl.2018.04.062.

R. Bürgmann and W. Thatcher. Space geodesy: A revolution in crustal deformation measurements of tectonic processes. In *The Web of Geological Sciences: Advances, Impacts, and Interactions*. Geological Society of America, 2013. doi: 10.1130/2013.2500(12).

R. Bürgmann, D. Schmidt, R. M. Nadeau, M. d'Alessio, E. Fielding, D. Manaker, T. V. McEvilly, and M. H. Murray. Earthquake potential along the Northern Hayward Fault, California. *Science*, 289(5482):1178–1182, 2000. doi: 10.1126/science.289.5482.1178.

R. Bürgmann, K. Chanard, and Y. Fu. Climate- and weather-driven solid-earth deformation and seismicity, 2023. URL https://eartharxiv.org/repository/view/6049/.

J. S. Caine, J. P. Evans, and C. B. Forster. Fault zone architecture and permeability structure. *Geology*, 24(11):1025, 1996. doi: 10.1130/0091-7613(1996)024<1025:FZAAPS>2.3.CO;2.

T. Candela, B. Wassing, J. Ter Heege, and L. Buijze. How earthquakes are induced. *Science*, 360(6389):598–600, 2018. doi: 10.1126/science.aat2776.

T. Candela, S. Osinga, J. Ampuero, B. Wassing, M. Pluymaekers, P. A. Fokker, J. Wees, H. A. Waal, and A. G. Muntendam-Bos. Depletion-induced seismicity at the Groningen gas field: Coulomb rate-and-state models including differential compaction effect. *Journal of Geophysical Research: Solid Earth*, 124(7):7081–7104, 2019. doi: 10.1029/2018JB016670.

T. Candela, M. Pluymaekers, J.-P. Ampuero, J.-D. van Wees, L. Buijze, B. Wassing, S. Osinga, N. Grobbe, and A. G. Muntendam-Bos. Controls on the spatio-temporal patterns of induced seismicity in Groningen constrained by physics-based modelling with Ensemble-Smoother data assimilation. *Geophysical Journal International*, 229(2):1282–1308, 2022. doi: 10.1093/gji/ggab497.

F. Cappa, J. Rutqvist, and K. Yamamoto. Modeling crustal deformation and rupture processes related to upwelling of deep CO $_2$ -rich fluids during the 1965–1967 Matsushiro earthquake swarm in Japan. *Journal of Geophysical Research*, 114 (B10):B10304, 2009. doi: 10.1029/2009JB006398.

G. Carlson, M. Shirzaei, S. Werth, G. Zhai, and C. Ojha. Seasonal and long-term groundwater unloading in the Central Valley modifies crustal stress. *Journal of Geophysical Research: Solid Earth*, 125(1):e2019JB018490, 2020. doi: 10.1029/2019JB018490.

C. Cattania, S. Hainzl, L. Wang, B. Enescu, and F. Roth. Aftershock triggering by postseismic stresses: A study based on Coulomb rate-and-state models. *Journal of Geophysical Research: Solid Earth*, 120(4):2388–2407, 2015. doi: 10.1002/2014JB011500.

S. Cesca, D. Stich, F. Grigoli, A. Vuan, J. Ángel López-Comino, P. Niemz, E. Blanch, T. Dahm, and W. L. Ellsworth. Seismicity at the Castor gas reservoir driven by pore pressure diffusion and asperities loading. *Nature Communications*, 12(4):4783, 2021. doi: 10.1038/s41467-021-24949-1.

K. Chan, T.-W. Lee, and T. J. Sejnowski. Variational Bayesian Learning of ICA with missing data. *Neural Computation*, 15(8):1991–2011, 2003. doi: 10.1162/089976603360675116.

K. Chanard, J. P. Avouac, G. Ramillien, and J. Genrich. Modeling deformation induced by seasonal variations of continental water in the himalaya region: Sensitivity to Earth elastic structure. *Journal of Geophysical Research: Solid Earth*, 119(6):5097–5113, 2014. doi: 10.1002/2013JB010451.

K. Chanard, A. Nicolas, T. Hatano, F. Petrelis, S. Latour, S. Vinciguerra, and A. Schubnel. Sensitivity of acoustic emission triggering to small pore pressure cycling perturbations during brittle creep. *Geophysical Research Letters*, 46(13):7414–7423, 2019. doi: 10.1029/2019GL082093.

C. W. Chen and H. A. Zebker. Two-dimensional phase unwrapping with use of statistical models for cost functions in nonlinear optimization. *Journal of the Optical Society of America A*, 18(2):338, 2001. doi: 10.1364/JOSAA.18.000338.

K. H. Chen and R. Bürgmann. Creeping faults: Good news, bad news? *Review of Geophysics*, 55(2):282–286, 2017. doi: 10.1002/2017RG000565.

T. Chen and N. Lapusta. Scaling of small repeating earthquakes explained by interaction of seismic and aseismic slip in a rate and state fault model. *Journal of Geophysical Research: Solid Earth*, 114(B1):B01311, 2009. doi: 10.1029/2008JB005749.

X. Chen and P. M. Shearer. Comprehensive analysis of earthquake source spectra and swarms in the Salton Trough, California. *Journal of Geophysical Research*, 116(B9):B09309, 2011. doi: 10.1029/2011JB008263.

X. Chen, P. M. Shearer, and R. E. Abercrombie. Spatial migration of earthquakes within seismic clusters in Southern California: Evidence for fluid diffusion. *Journal of Geophysical Research: Solid Earth*, 117(B4):B04301, 2012. doi: 10.1029/2011JB008973.

F. M. Chester. Effects of temperature on friction: Constitutive equations and experiments with quartz gouge. *Journal of Geophysical Research: Solid Earth*, 99 (B4):7247–7261, 1994. doi: 10.1029/93JB03110.

F. M. Chester and J. S. Chester. Ultracataclasite structure and friction processes of the Punchbowl fault, San Andreas system, California. *Tectonophysics*, 295(1-2): 199–221, 1998. doi: 10.1016/S0040-1951(98)00121-8.

L. Chiaraluce, L. Valoroso, D. Piccinini, R. D. Stefano, and P. D. Gori. The anatomy of the 2009 L'Aquila normal fault system (central Italy) imaged by high resolution foreshock and aftershock locations. *Journal of Geophysical Research: Solid Earth*, 116(B12):B12311, 2011. doi: 10.1029/2011JB008352.

R. A. Choudrey and S. J. Roberts. Variational mixture of Bayesian Independent Component Analyzers. *Neural Computation*, 15(1):213–252, 2003. doi: 10.1162/089976603321043766.

T. C. Chu, W. F. Ranson, and M. A. Sutton. Applications of digital-image-correlation techniques to experimental mechanics. *Experimental Mechanics*, 25(3):232–244, 1985. doi: 10.1007/BF02325092.

P. Clayton, G. Zalachoris, E. Rathje, T. Bheemasetti, S. Caballero, X. Yu, and S. Bennett. The geotechnical aspects of the September 3, 2016 M 5.8 Pawnee, Oklahoma earthquake. Technical Report G69885, GEER Association, Berkeley, California, 2016.

E. S. Cochran, J. E. Vidale, and S. Tanaka. Earth tides can trigger shallow thrust fault earthquakes. *Science*, 306(5699):1164–1166, 2004. doi: 10.1126/science.1103961.

E. S. Cochran, Z. E. Ross, R. M. Harrington, S. L. Dougherty, and J. L. Rubinstein. Induced earthquake families reveal distinctive evolutionary patterns near disposal wells. *Journal of Geophysical Research: Solid Earth*, 123(9):8045–8055, 2018. doi: 10.1029/2018JB016270.

E. S. Cochran, A. Wickham-Piotrowski, K. B. Kemna, R. M. Harrington, S. L. Dougherty, and A. F. Peña Castro. Minimal clustering of injection-induced earthquakes observed with a large-n seismic array. *Bulletin of the Seismological Society of America*, 110(5):2005–2017, 2020. doi: 10.1785/0120200101.

C. Cofaru, W. Philips, and W. Van Paepegem. Evaluation of digital image correlation techniques using realistic ground truth speckle images. *Measurement Science and Technology*, 21(5):055102, 2010. doi: 10.1088/0957-0233/21/5/055102.

Correlated Solutions Inc. VIC-2D Version 6.2 Software Manual. Technical report, 2019.

C. A. Coulomb. Sur une application des regles de maximise minimis a quelques problemes de statique, relatifs a i' architecture (On an application of the rules of maximum and minimum to some statical problems, relevant to architecture). *Memoires de Mathematique de Physique, presentes a I' Academie. Royale des Sciences par divers Savans, Ius dans ses Assemblees*, 7:343–382, 1773.

C. A. Coulomb. *Theorie des machines simple (Theory of simple machines)*. Paris, Bachelier, 1821.

T. J. Craig, K. Chanard, and E. Calais. Hydrologically-driven crustal stresses and seismicity in the New Madrid Seismic Zone. *Nature Communications*, 8(1):2143, 2017. doi: 10.1038/s41467-017-01696-w.

B. W. Crowell, Y. Bock, D. T. Sandwell, and Y. Fialko. Geodetic investigation into the deformation of the Salton Trough. *Journal of Geophysical Research: Solid Earth*, 118(9):5030–5039, 2013. doi: 10.1002/jgrb.50347.

T. Dahm and S. Hainzl. A Coulomb stress response model for time-dependent earthquake forecasts. *Journal of Geophysical Research: Solid Earth*, 127(9): e2022JB024443, 2022. doi: 10.1029/2022JB024443.

T. Dahm, S. Hainzl, and T. Fischer. Bidirectional and unidirectional fracture growth during hydrofracturing: Role of driving stress gradients. *Journal of Geophysical Research*, 115(B12):B12322, 2010. doi: 10.1029/2009JB006817.

P. Danré, L. De Barros, F. Cappa, and J. Ampuero. Prevalence of aseismic slip linking fluid injection to natural and anthropogenic seismic swarms. *Journal of Geophysical Research: Solid Earth*, 127(12):e2022JB025571, 2022. doi: 10.1029/2022JB025571.

E. G. Daub and J. M. Carlson. A constitutive model for fault gouge deformation in dynamic rupture simulations. *Journal of Geophysical Research: Solid Earth*, 113(B12):2007JB005377, 2008. doi: 10.1029/2007JB005377.

L. De Barros, F. Cappa, A. Deschamps, and P. Dublanchet. Imbricated aseismic slip and fluid diffusion drive a seismic swarm in the Corinth Gulf, Greece. *Geophysical Research Letters*, 47(9), 2020. doi: 10.1029/2020GL087142.

J. de Jager and C. Visser. Geology of the Groningen field – An overview. *Netherlands Journal of Geosciences*, 96(5):s3–s15, 2017. doi: 10.1017/njg.2017.22.

J. A. de Waal, A. G. Muntendam-Bos, and J. P. A. Roest. Production induced subsidence and seismicity in the Groningen gas field – can it be managed? *Proceedings of the International Association of Hydrological Sciences*, 372:129–139, 2015. doi: 10.5194/piahs-372-129-2015.

R. T. Deane and D. K. Lynch. A moving mud spring threatening critical infrastructure, Imperial county, California. In *Geo-Congress 2020*, pages 717–727, Minneapolis, Minnesota, 2020. American Society of Civil Engineers. doi: 10.1061/9780784482797.070.

D. Dempsey and J. Riffault. Response of induced seismicity to injection rate reduction: Models of delay, decay, quiescence, recovery, and Oklahoma. *Water Resources Research*, 55(1):656–681, 2019. doi: 10.1029/2018WR023587.

D. Dempsey and J. Suckale. Physics-based forecasting of induced seismicity at Groningen gas field, the Netherlands. *Geophysical Research Letters*, 44(15): 7773–7782, 2017. doi: 10.1002/2017GL073878.

J. Dieterich. A constitutive law for rate of earthquake production and its application to earthquake clustering. *Journal of Geophysical Research: Solid Earth*, 99(B2): 2601–2618, 1994. doi: 10.1029/93JB02581.

J. H. Dieterich. Modeling of rock friction: 1. Experimental results and constitutive equations. *Journal of Geophysical Research: Solid Earth*, 84(B5):2161–2168, 1979. doi: 10.1029/JB084iB05p02161.

J. H. Dieterich. Constitutive properties of faults with simulated gouge. In N. L. Carter, M. Friedman, J. M. Logan, and D. W. Stearns, editors, *Geophysical Monograph Series*, pages 103–120. American Geophysical Union, 1981. doi: 10.1029/GM024p0103.

J. H. Dieterich. Applications of rate- and state-dependent friction to models of fault-slip and earthquake occurrence. In *Treatise on Geophysics*, pages 93–110. Elsevier, 2007. ISBN 978-0-444-53803-1. doi: 10.1016/B978-0-444-53802-4.00075-0.

J. H. Dieterich and B. D. Kilgore. Direct observation of frictional contacts: New insights for state-dependent properties. *Pure and Applied Geophysics*, 143(1-3): 283–302, 1994. doi: 10.1007/BF00874332.

J. H. Dieterich, V. Cayol, and P. Okubo. The use of earthquake rate changes as a stress meter at Kilauea volcano. *Nature*, 408(6811):457–460, 2000. doi: 10.1038/35044054.

P. Dong, R. Chen, K. Xia, W. Yao, Z. Peng, and D. Elsworth. Earthquake delay and rupture velocity in near-field dynamic triggering dictated by stress-controlled nucleation. *Seismological Research Letters*, 94(2A):913–924, 2022. doi: 10.1785/0220220264.

P. Dong, K. Xia, Y. Xu, D. Elsworth, and J.-P. Ampuero. Laboratory earthquakes decipher control and stability of rupture speeds. *Nature Communications*, 14(1): 2427, 2023. doi: 10.1038/s41467-023-38137-w.

P. Dong, Y. Xu, R. Xu, K. Xia, and J. Peng. On the unloading-induced fault reactivation: The effect of stress path on failure criterion and rupture dynamics. *Journal of Geophysical Research: Solid Earth*, 129(3):e2023JB028146, 2024. doi: 10.1029/2023JB028146.

Y. Dong and B. Pan. A review of speckle pattern fabrication and assessment for digital image correlation. *Experimental Mechanics*, 57(8):1161–1181, 2017. doi: 10.1007/s11340-017-0283-1.

B. Dost, E. Ruigrok, and J. Spetzler. Development of seismicity and probabilistic hazard assessment for the Groningen gas field. *Netherlands Journal of Geosciences*, 96(5):s235–s245, 2017. doi: 10.1017/njg.2017.20.

B. Dost, B. Edwards, and J. J. Bommer. The relationship between M and ML: A review and application to induced seismicity in the Groningen gas field, The Netherlands. *Seismological Research Letters*, 89(3):1062–1074, 2018. doi: 10.1785/02201700247.

D. Dowson. *History of Tribology*. Addison-Wesley Longman Group Limited, 1979.

P. Dublanchet. Fluid driven shear cracks on a strengthening rate-and-state frictional fault. *Journal of the Mechanics and Physics of Solids*, 132:103672, 2019. doi: 10.1016/j.jmps.2019.07.015.

P. Dublanchet and L. De Barros. Dual seismic migration velocities in seismic swarms. *Geophysical Research Letters*, 48(1), 2021. doi: 10.1029/2020GL090025.

P. Dutilleul, C. W. Johnson, R. Bürgmann, Y. Wan, and Z. Shen. Multifrequential periodogram analysis of earthquake occurrence: An alternative approach to the Schuster spectrum, with two examples in central California. *Journal of Geophysical Research: Solid Earth*, 120(12):8494–8515, 2015. doi: 10.1002/2015JB012467.

B. Efron and C. Stein. The Jackknife estimate of variance. *The Annals of Statistics*, 9(3):586–596, 1981.

J. E. Elkhoury, E. E. Brodsky, and D. C. Agnew. Seismic waves increase permeability. *Nature*, 441:1135–1138, 2006. doi: 10.1038/nature04798.

W. L. Ellsworth. Injection-induced earthquakes. *Science*, 341(6142):1225942, 2013. doi: 10.1126/science.1225942.

W. L. Ellsworth and G. C. Beroza. Seismic evidence for an earthquake nucleation phase. *Science*, 268:6, 1995.

European Space Agency. Sentinel-1 SAR User Guide, 2014. URL https://sentinels.copernicus.eu/web/sentinel/user-guides/sentinel-1-sar.

T. G. Farr, P. A. Rosen, E. Caro, R. Crippen, R. Duren, S. Hensley, M. Kobrick, M. Paller, E. Rodriguez, L. Roth, D. Seal, S. Shaffer, J. Shimada, J. Umland, M. Werner, M. Oskin, D. Burbank, and D. Alsdorf. The Shuttle Radar Topography Mission. *Reviews of Geophysics*, 45(2):RG2004, 2007. doi: 10.1029/2005RG000183.

T. Fischer, J. Horálek, P. Hrubcová, V. Vavryčuk, K. Bräuer, and H. Kämpf. Intra-continental earthquake swarms in West-Bohemia and Vogtland: A review. *Tectonophysics*, 611:1–27, 2014. doi: 10.1016/j.tecto.2013.11.001.

G. Franceschetti and R. Lanari. *Synthetic aperture radar processing*. CRC Press, Boca Raton, Florida, 1st edition, 1999. ISBN 978-0-203-73748-4.

W. B. Frank, P. Poli, and H. Perfettini. Mapping the rheology of the Central Chile subduction zone with aftershocks. *Geophysical Research Letters*, 44(11):5374–5382, 2017. doi: 10.1002/2016GL072288.

A. M. Freed, R. Bürgmann, E. Calais, J. Freymueller, and S. Hreinsdóttir. Implications of deformation following the 2002 Denali, Alaska, earthquake for postseismic relaxation processes and lithospheric rheology. *Journal of Geophysical Research: Solid Earth*, 111(B1):B01401, 2006. doi: 10.1029/2005JB003894.

L. B. Freund. *Dynamic fracture mechanics*. Cambridge University Press, 1990.

L. Frérot, G. Anciaux, V. Rey, S. Pham-Ba, and J.-F. Molinari. Tamaas: a library for elastic-plastic contact of periodic rough surfaces. *Journal of Open Source Software*, 5(51):2121, 2020. doi: 10.21105/joss.02121.

G. S. Fuis, W. D. Mooney, J. H. Healy, G. A. McMechan, and W. J. Lutter. A seismic refraction survey of the Imperial Valley Region, California. *Journal of Geophysical Research: Solid Earth*, 89(B2):1165–1189, 1984. doi: 10.1029/JB089iB02p01165.

V. Gabuchian. *Experimental investigation of thrust fault rupture mechanics*. PhD thesis, California Institute of Technology, Pasadena, CA, 2015.

X. Gao, M. Fraulob, and G. Haïat. Biomechanical behaviours of the bone–implant interface: A review. *Journal of The Royal Society Interface*, 16(156):20190259, 2019. doi: 10.1098/rsif.2019.0259.

Z. Gao, X. Xu, Y. Su, and Q. Zhang. Experimental analysis of image noise and interpolation bias in digital image correlation. *Optics and Lasers in Engineering*, 81:46–53, 2016. doi: 10.1016/j.optlaseng.2016.01.002.

J. K. Gardner and L. Knopoff. Is the sequence of earthquakes in southern california, with aftershocks removed, poissonian? *Bulletin of the Seismological Society of America*, 64(5):1363–1367, 1974. doi: 10.1785/BSSA0640051363.

T. Goebel, M. Weingarten, X. Chen, J. Haffener, and E. Brodsky. The 2016 Mw5.1 Fairview, Oklahoma earthquakes: Evidence for long-range poroelastic triggering at >40 km from fluid disposal wells. *Earth and Planetary Science Letters*, 472: 50–61, 2017. doi: 10.1016/j.epsl.2017.05.011.

Google. Salton Sea, California, USA. URL http://www.earth.google.com.

M. Gori, V. Rubino, A. J. Rosakis, and N. Lapusta. Pressure shock fronts formed by ultra-fast shear cracks in viscoelastic materials. *Nature Communications*, 9(1): 4754, 2018. doi: 10.1038/s41467-018-07139-4.

M. Gori, V. Rubino, A. J. Rosakis, and N. Lapusta. Dynamic rupture initiation and propagation in a fluid-injection laboratory setup with diagnostics across multiple temporal scales. *Proceedings of the National Academy of Sciences*, 118(51): e2023433118, 2021. doi: 10.1073/pnas.2023433118.

J.-L. Got, V. Monteiller, J. Guilbert, D. Marsan, Y. Cansi, C. Maillard, and J.-P. Santoire. Strain localization and fluid migration from earthquake relocation and seismicity analysis in the western Vosges (France). *Geophysical Journal International*, 185(1):365–384, 2011. doi: 10.1111/j.1365-246X.2011.04944.x.

F. Grigoli, S. Cesca, E. Priolo, A. P. Rinaldi, J. F. Clinton, T. A. Stabile, B. Dost, M. G. Fernandez, S. Wiemer, and T. Dahm. Current challenges in monitoring, discrimination, and management of induced seismicity related to underground industrial activities: A European perspective. *Reviews of Geophysics*, 55(2): 310–340, 2017. doi: 10.1002/2016RG000542.

S. Gross and R. Bürgmann. Rate and state of background stress estimated from the aftershocks of the 1989 Loma Prieta, California, earthquake. *Journal of Geophysical Research: Solid Earth*, 103(B3):4915–4927, 1998. doi: 10.1029/97JB03010.

S. Gross and C. Kisslinger. Estimating tectonic stress rate and state with Landers aftershocks. *Journal of Geophysical Research: Solid Earth*, 102(B4):7603–7612, 1997. doi: 10.1029/96JB03741.

D. Gräff and F. Walter. Changing friction at the base of an Alpine glacier. *Scientific Reports*, 11(1):10872, 2021. doi: 10.1038/s41598-021-90176-9.

J.-C. Gu, J. R. Rice, A. L. Ruina, and S. T. Tse. Slip motion and stability of a single degree of freedom elastic system with rate and state dependent friction. *Journal of the Mechanics and Physics of Solids*, 32(3):167–196, 1984. doi: 10.1016/0022-5096(84)90007-3.

A. Gualandi and Z. Liu. Variational Bayesian Independent Component Analysis for InSAR displacement time-series with application to Central California, USA. *Journal of Geophysical Research: Solid Earth*, 126(4):e2020JB020845, 2021. doi: 10.1029/2020JB020845.

A. Gualandi, E. Serpelloni, and M. E. Belardinelli. Blind source separation problem in GPS time series. *Journal of Geodesy*, 90(4):323–341, 2016. doi: 10.1007/s00190-015-0875-4.

A. Gualandi, J.-P. Avouac, J. Galetzka, J. E. Genrich, G. Blewitt, L. B. Adhikari, B. P. Koirala, R. Gupta, B. N. Upreti, B. Pratt-Sitaula, and J. Liu-Zeng. Pre- and post-seismic deformation related to the 2015, M w 7.8 Gorkha earthquake, Nepal. *Tectonophysics*, 714-715:90–106, 2017a. doi: 10.1016/j.tecto.2016.06.014.

A. Gualandi, C. .Nichele, E. Serpelloni, L. Chiaraluce, L. Anderlini, D. Latorre, M. E. Belardinelli, and J.-P. Avouac. Aseismic deformation associated with an earthquake swarm in the northern Apennines (Italy). *Geophysical Research Letters*, 44(15):7706–7714, 2017b. doi: 10.1002/2017GL073687.

A. Gualandi, Z. Liu, and C. Rollins. Post-large earthquake seismic activities mediated by aseismic deformation processes. *Earth and Planetary Science Letters*, 530:115870, 2020. doi: 10.1016/j.epsl.2019.115870.

Y. Guglielmi, F. Cappa, J.-P. Avouac, P. Henry, and D. Elsworth. Seismicity triggered by fluid injection-induced aseismic slip. *Science*, 348(6240):1224–1226, 2015. doi: 10.1126/science.aab0476.

B. Gutenberg and C. F. Richter. Frequency of earthquakes in California. *Bulletin of the Seismological Society of America*, 34(4):185–188, 1944. doi: 10.1785/BSSA0340040185.

S. Gvirtzman and J. Fineberg. Nucleation fronts ignite the interface rupture that initiates frictional motion. *Nature Physics*, 17(9):1037–1042, 2021. doi: 10.1038/s41567-021-01299-9.

H. Haddadi and S. Belhabib. Use of rigid-body motion for the investigation and estimation of the measurement errors related to digital image correlation technique. *Optics and Lasers in Engineering*, 46(2):185–196, 2008. doi: 10.1016/j.optlaseng.2007.05.008.

S. Hainzl. Rate-dependent incompleteness of earthquake catalogs. *Seismological Research Letters*, 87(2A):337–344, 2016. doi: 10.1785/0220150211.

S. Hainzl and T. Fischer. Indications for a successively triggered rupture growth underlying the 2000 earthquake swarm in Vogtland/NW Bohemia. *Journal of Geophysical Research: Solid Earth*, 107(B12):ESE 5–1–ESE 5–9, 2002. doi: 10.1029/2002JB001865.

S. Hainzl, F. Scherbaum, and C. Beauval. Estimating background activity based on interevent-time distribution. *Bulletin of the Seismological Society of America*, 96 (1):313–320, 2006. doi: 10.1785/0120050053.

S. Hainzl, T. Fischer, and T. Dahm. Seismicity-based estimation of the driving fluid pressure in the case of swarm activity in Western Bohemia: Seismicity-based fluid pressure estimation. *Geophysical Journal International*, 191(1):271–281, 2012. doi: 10.1111/j.1365-246X.2012.05610.x.

S. Hainzl, T. Fischer, H. Čermáková, M. Bachura, and J. Vlček. Aftershocks triggered by fluid intrusion: Evidence for the aftershock sequence occurred 2014 in West Bohemia/Vogtland. *Journal of Geophysical Research: Solid Earth*, 121 (4):2575–2590, 2016. doi: 10.1002/2015JB012582.

A. L. Handwerger, A. W. Rempel, R. M. Skarbek, J. J. Roering, and G. E. Hilley. Rate-weakening friction characterizes both slow sliding and catastrophic failure of landslides. *Proceedings of the National Academy of Sciences*, 113(37):10281–10286, 2016. doi: 10.1073/pnas.1607009113.

P. C. Hansen. Analysis of discrete ill-posed problems by means of the L-curve. *SIAM Review*, 34(4):561–580, 1992. doi: 10.1137/1034115.

J. L. Hardebeck and R. A. Harris. Earthquakes in the shadows: Why aftershocks occur at surprising locations. *The Seismic Record*, 2(3):207–216, 2022. doi: 10.1785/0320220023.

J. L. Hardebeck, A. L. Llenos, A. J. Michael, M. T. Page, M. Schneider, and N. J. van der Elst. Aftershock forecasting. *Annual Review of Earth and Planetary Sciences*, 23(3):2.1–2.24, 2024. doi: 10.1146/annurev-earth-040522-102129.

R. A. Harris. Large earthquakes and creeping faults. *Review of Geophysics*, 55(1): 169–198, 2017. doi: 10.1002/2016RG000539.

R. A. Harris and R. W. Simpson. In the shadow of 1857-the effect of the Great Ft. Tejon earthquake on subsequent earthquakes in southern California. *Geophysical Research Letters*, 23(3):229–232, 1996. doi: 10.1029/96GL00015.

R. A. Harris and R. W. Simpson. Suppression of large earthquakes by stress shadows: A comparison of Coulomb and rate-and-state failure. *Journal of Geophysical Research: Solid Earth*, 103(B10):24439–24451, 1998. doi: 10.1029/98JB00793.

R. A. Harris and R. W. Simpson. The 1999 Mw 7.1 Hector Mine, California, earthquake: A test of the stress shadow hypothesis? *Bulletin of the Seismological Society of America*, 92(4):1497–1512, 2002. doi: 10.1785/0120000913.

G. M. Hassan, C. MacNish, and A. Dyskin. Extending digital image correlation to reconstruct displacement and strain fields around discontinuities in geomechanical structures under deformation. In *2015 IEEE Winter Conference on Applications of Computer Vision*, pages 710–717, Waikoloa, HI, USA, 2015. IEEE. doi: 10.1109/WACV.2015.100.

R. L. Hatch, R. E. Abercrombie, C. J. Ruhl, and K. D. Smith. Evidence of aseismic and fluid-driven processes in a small complex seismic swarm near Virginia City, Nevada. *Geophysical Research Letters*, 47(4), 2020. doi: 10.1029/2019GL085477.

E. Hauksson. Average stress drops of southern California earthquakes in the context of crustal geophysics: Implications for fault zone healing. *Pure and Applied Geophysics*, 172(5):1359–1370, 2015. doi: 10.1007/s00024-014-0934-4.

E. Hauksson, W. Yang, and P. M. Shearer. Waveform relocated earthquake catalog for southern California (1981 to June 2011). *Bulletin of the Seismological Society of America*, 102(5):2239–2244, 2012. doi: 10.1785/0120120010.

E. Hauksson, M.-A. Meier, Z. E. Ross, and L. M. Jones. Evolution of seismicity near the southernmost terminus of the San Andreas Fault: Implications of recent earthquake clusters for earthquake risk in southern California. *Geophysical Research Letters*, 44(3):1293–1301, 2017. doi: 10.1002/2016GL072026.

E. R. Heimisson. Constitutive law for earthquake production based on rate-and-state friction: Theory and application of interacting sources. *Journal of Geophysical Research: Solid Earth*, 124(2):1802–1821, 2019. doi: 10.1029/2018JB016823.

E. R. Heimisson and J.-P. Avouac. Analytical prediction of seismicity rate due to tides and other oscillating stresses. *Geophysical Research Letters*, 47(23), 2020. doi: 10.1029/2020GL090827.

E. R. Heimisson and P. Segall. Constitutive law for earthquake production based on rate-and-state friction: Dieterich 1994 revisited. *Journal of Geophysical Research: Solid Earth*, 123(5):4141–4156, 2018. doi: 10.1029/2018JB015656.

E. R. Heimisson, J. D. Smith, J.-P. Avouac, and S. J. Bourne. Coulomb threshold rate-and-state model for fault reactivation: Application to induced seismicity at Groningen. *Geophysical Journal International*, 228(3):2061–2072, 2022. doi: 10.1093/gji/ggab467.

J. Heinicke, T. Fischer, R. Gaupp, J. Götze, U. Koch, H. Konietzky, and K.-P. Stanek. Hydrothermal alteration as a trigger mechanism for earthquake swarms: The Vogtland/NW Bohemia region as a case study. *Geophysical Journal International*, 178(1):1–13, 2009. doi: 10.1111/j.1365-246X.2009.04138.x.

A. Helmstetter and B. E. Shaw. Afterslip and aftershocks in the rate-and-state friction law. *Journal of Geophysical Research: Solid Earth*, 114(B1):B01308, 2009. doi: 10.1029/2007JB005077.

A. Helmstetter and D. Sornette. Diffusion of epicenters of earthquake aftershocks, Omori's law, and generalized continuous-time random walk models. *Physical Review E*, 66(6):061104, 2002a. doi: 10.1103/PhysRevE.66.061104.

A. Helmstetter and D. Sornette. Subcritical and supercritical regimes in epidemic models of earthquake aftershocks. *Journal of Geophysical Research: Solid Earth*, 107(B10):2237, 2002b. doi: 10.1029/2001JB001580.

A. Helmstetter, D. Sornette, J.-R. Grasso, J. V. Andersen, S. Gluzman, and V. Pisarenko. Slider block friction model for landslides: Application to Vaiont and La Clapière landslides. *Journal of Geophysical Research: Solid Earth*, 109(B2): B02409, 2004. doi: 10.1029/2002JB002160.

P. H. Hennings, J.-P. Nicot, R. S. Gao, H. R. DeShon, J.-E. L. Snee, A. P. Morris, M. R. Brudzinski, E. A. Horne, , and C. Breton. Pore pressure threshold and fault slip potential for induced earthquakes in the Dallas-Fort Worth area of North Central Texas. *Geophysical Research Letters*, 48(15):e2021GL093564, 2021. doi: 10.1029/2021GL093564.

F. Heslot, T. Baumberger, B. Perrin, B. Caroli, and C. Caroli. Creep, stick-slip, and dry-friction dynamics: Experiments and a heuristic model. *Physical Review E*, 49(6):4973–4988, 1994. doi: 10.1103/PhysRevE.49.4973.

A. Hicks. *Clustering in multidimensional spaces with applications to statistical analysis of earthquake clustering*. PhD thesis, University of Nevada, Reno, 2011.

D. Hill and S. Prejean. Dynamic triggering. In *Treatise on Geophysics*, pages 273–304. Elsevier, 2015. doi: 10.1016/B978-0-444-53802-4.00078-6.

S. G. Holtkamp and M. R. Brudzinski. Earthquake swarms in circum-Pacific subduction zones. *Earth and Planetary Science Letters*, 305(1-2):215–225, 2011. doi: 10.1016/j.epsl.2011.03.004.

A. Hooper, P. Segall, and H. Zebker. Persistent scatterer interferometric synthetic aperture radar for crustal deformation analysis, with application to Volcán Alcedo, Galápagos. *Journal of Geophysical Research*, 112(B7):B07407, 2007. doi: 10.1029/2006JB004763.

M. C. Hoskins, A. Meltzer, Y. Font, H. Agurto-Detzel, S. Vaca, F. Rolandone, J.-M. Nocquet, L. Soto-Cordero, J. C. Stachnik, S. Beck, C. Lynner, M. Ruiz, A. Alvarado, S. Hernandez, P. Charvis, M. Regnier, S. Leon-Rios, and A. Rietbrock. Triggered crustal earthquake swarm across subduction segment boundary after the 2016 Pedernales, Ecuador megathrust earthquake. *Earth and Planetary Science Letters*, 553:116620, 2021. doi: 10.1016/j.epsl.2020.116620.

S. E. Hough. Shaking intensity from injection-induced versus tectonic earthquakes in the central-eastern United States. *The Leading Edge*, 34(6):690–697, 2015.

M. K. Hubbert and W. W. Rubey. Role of fluid pressure in mechanics of overthrust faulting. *Bulletin of the Geological Society of America*, 70:115–166, 1959. doi: 10.1130/0016-7606(1959)70[115:ROFPIM]2.0.CO;2.

G. Huiskamp. Difference formulas for the surface Laplacian on a triangulated surface. *Journal of Computational Physics*, 95(2):477–496, 1991. doi: 10.1016/0021-9991(91)90286-T.

K. Hutton, J. Woessner, and E. Hauksson. Earthquake monitoring in southern California for seventy-seven years (1932-2008). *Bulletin of the Seismological Society of America*, 100(2):423–446, 2010. doi: 10.1785/0120090130.

Y. Ida. Cohesive force across the tip of a longitudinal-shear crack and Griffith's specific surface energy. *Journal of Geophysical Research*, 77(20):3796–3805, 1973. doi: 10.1029/JB077i020p03796.

S. Ide, G. C. Beroza, D. R. Shelly, and T. Uchide. A scaling law for slow earthquakes. *Nature*, 447(7140):76–79, 2007. doi: 10.1038/nature05780.

M. J. Ikari, B. M. Carpenter, and C. Marone. A microphysical interpretation of rate- and state-dependent friction for fault gouge. *Geochemistry, Geophysics, Geosystems*, 17(5):1660–1677, 2016. doi: 10.1002/2016GC006286.

K. Im and J.-P. Avouac. On the role of thermal stress and fluid pressure in triggering seismic and aseismic faulting at the Brawley Geothermal Field, California. *Geochemistry, Geophysics, Geosystems*, 97:102238, 2021. doi: 10.1016/j.geothermics.2021.102238.

K. Im and J.-P. Avouac. Cascading foreshocks, aftershocks and earthquake swarms in a discrete fault network. *Geophysical Journal International*, 235(1):831–852, 2023. doi: 10.1093/gji/ggad278.

K. Im, D. Elsworth, and Y. Fang. The influence of preslip sealing on the permeability evolution of fractures and faults. *Geophysical Research Letters*, 45(1):166–175, 2018. doi: 10.1002/2017GL076216.

T. Ingleby and T. J. Wright. Omori-like decay of postseismic velocities following continental earthquakes. *Geophysical Research Letters*, 44(7):3119–3130, 2017. doi: 10.1002/2017GL072865.

International Digital Image Correlation Society. A good practices guide for digital image correlation. Technical report, 2018.

J. C. Jaeger, N. G. W. Cook, and R. W. Zimmerman. *Fundamentals of Rock Mechanics*. Blackwell Publishing, London, 4th edition, 2007. ISBN 978-0-632-05759-7.

P. Jeanne, Y. Guglielmi, and F. Cappa. Hydromechanical heterogeneities of a mature fault zone: Impacts on fluid flow. *Groundwater*, 51(6):880–892, 2013. doi: 10.1111/gwat.12017.

Y. Jiang, S. V. Samsonov, and P. J. González. Aseismic fault slip during a shallow normal-faulting seismic swarm constrained using a physically informed geodetic inversion method. *Journal of Geophysical Research: Solid Earth*, 127(7): e2021JB022621, 2022. doi: 10.1029/2021JB022621.

C. E. Johnson and D. P. Hill. Seismicity of the Imperial Valley. In *The Imperial Valley, California, earthquake of October 15, 1979*, volume 1254, pages 15–24. U.S. Geological Survey Professional Paper, 1982.

C. W. Johnson, Y. Fu, and R. Bürgmann. Stress models of the annual hydrospheric, atmospheric, thermal, and tidal loading cycles on California faults: Perturbation of background stress and changes in seismicity. *Journal of Geophysical Research: Solid Earth*, 122(12), 2017a. doi: 10.1002/2017JB014778.

C. W. Johnson, Y. Fu, and R. Bürgmann. Seasonal water storage, stress modulation, and California seismicity. *Science*, 356(6343):1161–1164, 2017b. doi: 10.1126/science.aak9547.

S. Jónsson, H. Zebker, P. Segall, and F. Amelung. Fault slip distribution of the 1999 Mw 7.1 Hector Mine, California, earthquake, estimated from satellite radar and GPS measurements. *Bulletin of the Seismological Society of America*, 92(4): 1377–1389, 2002. doi: 10.1785/0120000922.

Y. Y. Kagan and D. D. Jackson. Long-term earthquake clustering. *Geophysical Journal International*, 104(1):117–134, 1991. doi: 10.1111/j.1365-246X.1991.tb02498.x.

H. Kanamori and D. L. Anderson. Theoretical basis of some empirical relations in Seismology. *Bulletin of the Seismological Society of America*, 65(5):1073–1095, 1975.

Y. Kaneko and N. Lapusta. Variability of earthquake nucleation in continuum models of rate-and-state faults and implications for aftershock rates. *Journal of Geophysical Research*, 113(B12):B12312, 2008. doi: 10.1029/2007JB005154.

S. Kang and R. Knight. Isolating the poroelastic response of the groundwater system in InSAR data from the Central Valley of California. *Geophysical Research Letters*, 50(9):e2023GL103222, May 2023. doi: 10.1029/2023GL103222.

K. Karimi and J. Davidsen. Separating primary and secondary mechanisms for seismicity induced by hydraulic fracturing. *Bulletin of the Seismological Society of America*, 113(5):1982–1991, 2023. doi: 10.1785/0120220200.

A. Kato and K. Obara. Step-like migration of early aftershocks following the 2007 M_w 6.7 Noto-Hanto earthquake, Japan: Kato and Obara: Step-like migration of early aftershocks. *Geophysical Research Letters*, 41(11):3864–3869, 2014. doi: 10.1002/2014GL060427.

K. M. Keranen and M. Weingarten. Induced seismicity. *Annual Review of Earth and Planetary Sciences*, 46:149–174, 2018. doi: 10.1146/annurev-earth-082517-010054.

G. Khazaradze, K. Wang, J. Klotz, Y. Hu, and J. He. Prolonged post-seismic deformation of the 1960 great Chile earthquake and implications for mantle rheology. *Geophysical Research Letters*, 29(22):2050, 2002. doi: 10.1029/2002GL015986.

T. Kim and J. Avouac. Stress-based and convolutional forecasting of injection-induced seismicity: Application to the Otaniemi geothermal reservoir stimulation. *Journal of Geophysical Research: Solid Earth*, 128(4):e2022JB024960, 2023. doi: 10.1029/2022JB024960.

G. King. 4.08 - Fault interaction, Earthquake stress changes, and the Evolution of seismicity. In G. Schubert, editor, *Treatise on Geophysics*, pages 225–255. Elsevier, Amsterdam, 2007. doi: 10.1016/B978-044452748-6.00069-9.

G. C. P. King, R. S. Stein, and J. Lin. Static stress changes and the triggering of earthquakes. *Bulletin of the Seismological Society of America*, 84(3):935–953, 1994.

N. M. Kinkaid, O. M. O'Reilly, and P. Papadopoulos. Automotive disc brake squeal. *Journal of Sound and Vibration*, 267(1):105–166, 2003. doi: 10.1016/S0022-460X(02)01573-0.

J. Kinscher, S. Cesca, P. Bernard, I. Contrucci, A. Mangeney, J. Piguet, and P. Bigarré. Resolving source mechanisms of microseismic swarms induced by solution mining. *Geophysical Journal International*, 206(1):696–715, July 2016. doi: 10.1093/gji/ggw163.

J. Koljonen and J. T. Alander. Deformation image generation for testing a strain measurement algorithm. *Optical Engineering*, 47(10):107202, 2008. doi: 10.1117/1.2993319.

A. P. Kositsky and J.-P. Avouac. Inverting geodetic time series with a principal component analysis-based inversion method. *Journal of Geophysical Research*, 115(B3):B03401, 2010. doi: 10.1029/2009JB006535.

C. Kreemer and I. Zaliapin. Spatiotemporal correlation between seasonal variations in seismicity and horizontal dilatational strain in California. *Geophysical Research Letters*, 45(18):9559–9568, 2018. doi: 10.1029/2018GL079536.

C. Kreemer, G. Blewitt, and E. C. Klein. A geodetic plate motion and Global Strain Rate Model. *Geochemistry, Geophysics, Geosystems*, 15(10):3849–3889, 2014. doi: 10.1002/2014GC005407.

G. Kwiatek, T. Saarno, T. Ader, F. Bluemle, M. Bohnhoff, M. Chendorain, G. Dresen, P. Heikkinen, I. Kukkonen, P. Leary, M. Leonhardt, P. Malin, P. Martínez-Garzón, K. Passmore, P. Passmore, S. Valenzuela, and C. Wollin. Controlling fluid-induced seismicity during a 6.1-km-deep geothermal stimulation in Finland. *Science Advances*, 5(5):eaav7224, 2019. doi: 10.1126/sciadv.aav7224.

C. Kyriakopoulos, M. Chini, C. Bignami, S. Stramondo, A. Ganas, M. Kolligri, and A. Moshou. Monthly migration of a tectonic seismic swarm detected by DInSAR: Southwest Peloponnese, Greece. *Geophysical Journal International*, 194(3):1302–1309, 2013. doi: 10.1093/gji/ggt196.

D. Kühn, S. Hainzl, T. Dahm, G. Richter, and I. Vera Rodriguez. A review of source models to further the understanding of the seismicity of the Groningen field. *Netherlands Journal of Geosciences*, 101:e11, 2022. doi: 10.1017/njg.2022.7.

D. Labonte and W. Federle. Biomechanics of shear-sensitive adhesion in climbing animals: peeling, pre-tension and sliding-induced changes in interface strength. *Journal of The Royal Society Interface*, 13(22):20160373, 2016. doi: 10.1098/rsif.2016.0373.

A. H. Lachenbruch, J. H. Sass, and S. P. Galanis. Heat flow in southernmost California and the origin of the Salton Trough. *Journal of Geophysical Research*, 90(B8):6709, 1985. doi: 10.1029/JB090iB08p06709.

P. Lacroix, A. L. Handwerger, and G. Bièvre. Life and death of slow-moving landslides. *Nature Reviews Earth Environment*, 1(8):404–419, 2020. doi: 10.1038/s43017-020-0072-8.

C. Langenbruch, M. Weingarten, and M. D. Zoback. Physics-based forecasting of man-made earthquake hazards in Oklahoma and Kansas. *Nature Communications*, 9:3946, 2018. doi: 10.1038/s41467-018-06167-4.

N. Lapusta, J. R. Rice, Y. Ben-Zion, and G. Zheng. Elastodynamic analysis for slow tectonic loading with spontaneous rupture episodes on faults with rate- and state-dependent friction. *Journal of Geophysical Research: Solid Earth*, 105 (B10):23765–23789, 2000. doi: 10.1029/2000JB900250.

S. Larochelle, A. Gualandi, K. Chanard, and J. Avouac. Identification and extraction of seasonal geodetic signals due to surface load variations. *Journal of Geophysical Research: Solid Earth*, 123(12):11031–11047, 2018. doi: 10.1029/2018JB016607.

S. Larochelle, N. Lapusta, J. Ampuero, and F. Cappa. Constraining fault friction and stability with fluid-injection field experiments. *Geophysical Research Letters*, 48 (10), 2021. doi: 10.1029/2020GL091188.

S. Larochelle, K. Chanard, L. Fleitout, J. Fortin, A. Gualandi, L. Longuevergne, P. Rebischung, S. Violette, and J. Avouac. Understanding the geodetic signature

of large aquifer systems: Example of the Ozark Plateaus in Central United States. *Journal of Geophysical Research: Solid Earth*, 127(3):e2021JB023097, 2022. doi: 10.1029/2021JB023097.

A. Lattanzi, V. Rubino, M. Rossi, A. Donzelli, A. Rosakis, and N. Lapusta. Uncertainty analysis of dynamic rupture measurements obtained through ultrahigh-speed digital image correlation. *Experimental Mechanics*, 63(3):529–563, 2023. doi: 10.1007/s11340-022-00932-9.

P. Lava, S. Cooreman, S. Coppieters, M. De Strycker, and D. Debruyne. Assessment of measuring errors in DIC using deformation fields generated by plastic FEA. *Optics and Lasers in Engineering*, 47(7-8):747–753, 2009. doi: 10.1016/j.optlaseng.2009.03.007.

D. Lecompte, A. Smits, S. Bossuyt, H. Sol, J. Vantomme, D. Van Hemelrijck, and A. Habraken. Quality assessment of speckle patterns for digital image correlation. *Optics and Lasers in Engineering*, 44(11):1132–1145, 2006. doi: 10.1016/j.optlaseng.2005.10.004.

H. S. Lee and T. F. Cho. Hydraulic characteristics of rough fractures in linear flow under normal and shear load. *Rock Mechanics and Rock Engineering*, 35(4):299–318, 2002. doi: 10.1007/s00603-002-0028-y.

J. R. Leeman, D. M. Saffer, M. M. Scuderi, and C. Marone. Laboratory observations of slow earthquakes and the spectrum of tectonic fault slip modes. *Nature Communications*, 7:11104, 2016. doi: 10.1038/ncomms11104.

X. Lei, Z. Wang, and J. Su. Possible link between long-term and short-term water injections and earthquakes in salt mine and shale gas site in Changning, south Sichuan Basin, China. *Earth and Planetary Physics*, 3(6):510–525, 2019. doi: 10.26464/epp2019052.

W. LePage, J. Shaw, and S. Daly. Optimum paint sequence for speckle patterns in digital image correlation. *Experimental Techniques*, 41(5):557–563, 2017. doi: 10.1007/s40799-017-0192-3.

S. Leprince, F. Ayoub, Y. Klinger, and J.-P. Avouac. Co-Registration of Optically Sensed Images and Correlation (COSI-Corr): An operational methodology for ground deformation measurements. In *2007 IEEE International Geoscience and Remote Sensing Symposium*, pages 1943–1946, Barcelona, Spain, 2007. IEEE. doi: 10.1109/IGARSS.2007.4423207.

B. Q. Li, M. Khoshmanesh, and J.-P. Avouac. Surface deformation and seismicity induced by poroelastic stress at the Raft River Geothermal field, Idaho, USA. *Geophysical Research Letters*, 48(18):e2021GL095108, 2021. doi: 10.1029/2021GL095108.

Y. Li, R. Bürgmann, and T. Taira. Spatiotemporal variations of surface deformation, shallow creep rate, and slip partitioning between the San Andreas and southern Calaveras Fault. *Journal of Geophysical Research: Solid Earth*, 128: e2022JB025363, 2023. doi: 10.1029/2022JB025363.

G. Lin, P. M. Shearer, and E. Hauksson. Applying a three-dimensional velocity model, waveform cross correlation, and cluster analysis to locate southern California seismicity from 1981 to 2005. *Journal of Geophysical Research*, 112 (B12):B12309, 2007. doi: 10.1029/2007JB004986.

E. O. Lindsey and Y. Fialko. Geodetic slip rates in the southern San Andreas Fault system: Effects of elastic heterogeneity and fault geometry. *Journal of Geophysical Research: Solid Earth*, 118(2):689–697, 2013. doi: 10.1029/2012JB009358.

G. Lionello and L. Cristofolini. A practical approach to optimizing the preparation of speckle patterns for digital-image correlation. *Measurement Science and Technology*, 25(10):107001, 2014. doi: 10.1088/0957-0233/25/10/107001.

A. L. Llenos and J. J. McGuire. Detecting aseismic strain transients from seismicity data. *Journal of Geophysical Research*, 116(B6):B06305, 2011. doi: 10.1029/2010JB007537.

D. A. Lockner. A generalized law for brittle deformation of Westerly granite. *Journal of Geophysical Research: Solid Earth*, 103(B3):5107–5123, 1998. doi: 10.1029/97JB03211.

R. B. Lohman and J. J. McGuire. Earthquake swarms driven by aseismic creep in the Salton Trough, California. *Journal of Geophysical Research: Solid Earth*, 112(B4):B04405, 2007. doi: 10.1029/2006JB004596.

X. Lu, N. Lapusta, and A. J. Rosakis. Pulse-like and crack-like ruptures in experiments mimicking crustal earthquakes. *Proceedings of the National Academy of Sciences*, 104(48):18931–18936, 2007. doi: 10.1073/pnas.0704268104.

J.-J. Lévěque, L. Rivera, and G. Wittlinger. On the use of the checker-board test to assess the resolution of tomographic inversions. *Geophysical Journal International*, 115(1):313–318, 1993. doi: 10.1111/j.1365-246X.1993.tb05605.x.

S. Ma, J. Pang, and Q. Ma. The systematic error in digital image correlation induced by self-heating of a digital camera. *Measurement Science and Technology*, 23(2): 025403, 2012. doi: 10.1088/0957-0233/23/2/025403.

S. Mallat. A theory for multiresolution signal decomposition: The wavelet representation. *IEEE Transactions on Pattern Analysis and Machine Intelligence*, 11 (7):674–693, 1989. doi: 10.1109/34.192463.

C. Marone. Laboratory-derived friction laws and their application to seismic faulting. *Annual Review of Earth and Planetary Sciences*, 26(1):643–696, 1998a. doi: 10.1146/annurev.earth.26.1.643.

C. Marone. The effect of loading rate on static friction and the rate of fault healing during the earthquake cycle. *Nature*, 391(6662):69–72, 1998b. doi: 10.1038/34157.

C. Marone, C. H. Scholtz, and R. Bilham. On the mechanics of earthquake afterslip. *Journal of Geophysical Research*, 96(B5):8441, 1991. doi: 10.1029/91JB00275.

D. Marsan and L. O. Extending earthquakes' reach through cascading. *Science*, 319 (5866):1076–1079, 2008. doi: 10.1126/science.1148783.

D. Marsan, E. Prono, and A. Helmstetter. Monitoring aseismic forcing in fault zones using earthquake time series. *Bulletin of the Seismological Society of America*, 103(1):169–179, 2013. doi: 10.1785/0120110304.

P. Martínez-Garzón, I. Zaliapin, Y. Ben-Zion, G. Kwiatek, and M. Bohnhoff. Comparative study of earthquake clustering in relation to hydraulic activities at geothermal fields in California. *Journal of Geophysical Research: Solid Earth*, 123:4041–4062, 2018. doi: 10.1029/2017JB014972.

P. Martínez-Garzón, V. Durand, S. Bentz, G. Kwiatek, G. Dresen, T. Turkmen, M. Nurlu, and M. Bohnhoff. Near-fault monitoring reveals combined seismic and slow activation of a fault branch within the Istanbul–Marmara seismic gap in northwest Turkey. *Seismological Research Letters*, 92(6):3743–3756, 2021. doi: 10.1785/0220210047.

K. Materna, A. Barbour, J. Jiang, and M. Eneva. Detection of aseismic slip and poroelastic reservoir deformation at the North Brawley Geothermal Field from 2009 to 2019. *Journal of Geophysical Research: Solid Earth*, 127(5), 2022. doi: 10.1029/2021JB023335.

G. C. McLaskey. Earthquake initiation from laboratory observations and implications for foreshocks. *Journal of Geophysical Research: Solid Earth*, 124(12): 12882–12904, 2019. doi: 10.1029/2019JB018363.

G. C. McLaskey, B. D. Kilgore, D. A. Lockner, and N. M. Beeler. Laboratory generated M-6 earthquakes. *Pure and Applied Geophysics*, 171(10):2601–2615, 2014. doi: 10.1007/s00024-013-0772-9.

M. Mello. *Identifying the unique ground motion signatures of supershear earthquakes: Theory and experiments*. PhD thesis, California Institute of Technology, 2012.

M. Mello, H. S. Bhat, A. J. Rosakis, and H. Kanamori. Identifying the unique ground motion signatures of supershear earthquakes: Theory and experiments. *Tectonophysics*, 493(3-4):297–326, 2010. doi: 10.1016/j.tecto.2010.07.003.

H. Meyer, J. D. Smith, S. Bourne, and J.-P. Avouac. An integrated framework for surface deformation modelling and induced seismicity forecasting due to reservoir

operations. *Geological Society, London, Special Publications*, 528(1):299–318, 2023. doi: 10.1144/SP528-2022-169.

S. Michel, A. Gualandi, and J.-P. Avouac. Interseismic coupling and slow slip events on the Cascadia megathrust. *Pure and Applied Geophysics*, 176(9):3867–3891, 2019. doi: 10.1007/s00024-018-1991-x.

D. Milbert. Solid, 2018. URL https://geodesyworld.github.io/SOFTS/solid.htm.

S. A. Miller. Aftershocks are fluid-driven and decay rates controlled by permeability dynamics. *Nature Communications*, 11(5787), 2020. doi: 10.1038/s41467-020-19590-3.

T. M. Mitchell and D. R. Faulkner. The nature and origin of off-fault damage surrounding strike-slip fault zones with a wide range of displacements: A field study from the Atacama fault system, northern Chile. *Journal of Structural Geology*, 31(8):802–816, 2009. doi: 10.1016/j.jsg.2009.05.002.

M. J. A. Moein, C. Langenbruch, R. Schultz, F. Grigoli, W. L. Ellsworth, R. Wang, A. P. Rinaldi, and S. Shapiro. The physical mechanisms of induced earthquakes. *Nature Reviews Earth & Environment*, 4(12):847–863, 2023. doi: 10.1038/s43017-023-00497-8.

K. Mogi. Some discussions on aftershocks, foreshocks and earthquake swarm - The fracture of a semi-infinite body caused by an inner stress origin and its relation to the earthquake phenomena (3rd paper). *Bulletin of the Earthquake Research Institute, University of Tokyo*, 41(3):615–658, 1963.

G. Molchan. Interevent time distribution in seismicity: A theoretical approach. *Pure and Applied Geophysics*, 162(6-7):1135–1150, 2005. doi: 10.1007/s00024-004-2664-5.

A. G. Muntendam-Bos. Clustering characteristics of gas-extraction induced seismicity in the Groningen gas field. *Geophysical Journal International*, 221(2):879–892, 2020. doi: 10.1093/gji/ggaa038.

A. G. Muntendam-Bos, J. P. Roest, and H. A. De Waal. The effect of imposed production measures on gas extraction induced seismic risk. *Netherlands Journal of Geosciences*, 96(5):s271–s278, 2017. doi: 10.1017/njg.2017.29.

M. Nakatani. Conceptual and physical clarification of rate and state friction: Frictional sliding as a thermally activated rheology. *Journal of Geophysical Research: Solid Earth*, 106(B7):13347–13380, 2001. doi: 10.1029/2000JB900453.

NCEDC. Northern California Earthquake Data Center, UC Berkeley Seismological Laboratory, 2014.

Nederlandse Aardolie Maatschappij. Groningen Velocity Model 2017 - Groningen full elastic velocity model September 2017. Technical report, 2017. URL https://nam-feitenencijfers.data-app.nl/download/rapport/9a5751d9-2ff5-4b6a-9c25-e37e76976bc1?open=true.

T. L. Nguyen, S. A. Hall, P. Vacher, and G. Viggiani. Fracture mechanisms in soft rock: Identification and quantification of evolving displacement discontinuities by extended digital image correlation. *Tectonophysics*, 503(1-2):117–128, 2011. doi: 10.1016/j.tecto.2010.09.024.

T. Nishikawa and S. Ide. Recurring slow slip events and earthquake nucleation in the source region of the M 7 Ibaraki-Oki earthquakes revealed by earthquake swarm and foreshock activity. *Journal of Geophysical Research: Solid Earth*, 123(9): 7950–7968, 2018. doi: 10.1029/2018JB015642.

H. Noda, N. Lapusta, and H. Kanamori. Comparison of average stress drop measures for ruptures with heterogeneous stress change and implications for earthquake physics. *Geophysical Journal International*, 193(3):1691–1712, 2013. doi: 10.1093/gji/ggt074.

NORSAR. Review of the public KNM induced earthquake catalogue from the Groningen gas field, Project Phase 1, WP1. Technical report, 2018. URL https://kemprogramma.nl/file/download/18f4a605-4bbc-401a-b68e-8bd840b3d05b/1562832346kem11%20norsar_sodm_groningenreview_wp1.pdf.

C. Noël, F. X. Passelègue, C. Giorgetti, and M. Violay. Fault reactivation during fluid pressure oscillations: Transition from stable to unstable slip. *Journal of Geophysical Research: Solid Earth*, 124(11):10940–10953, 2019. doi: 10.1029/2019JB018517.

A. Nur and J. R. Booker. Aftershocks caused by pore fluid flow? *Science*, 175 (4024):885–887, 1972. doi: 10.1126/science.175.4024.885.

S. Oates, A. J. Landman, O. van der Wal, H. Baehr, and H. Piening. Geomechanical, seismological, and geodetic data pertaining to the Groningen gas field: A data package used in the "Mmax II Workshop," on constraining the maximum earthquake magnitude in the Groningen field, 2022.

Y. Ogata. Statistical models for earthquake occurrences and residual analysis for point processes. *Journal of the American Statistical Association*, 83(401):9–27, 1988.

Y. Ogata. Detection of precursory relative quiescence before great earthquakes through a statistical model. *Journal of Geophysical Research*, 97(B13):19845, 1992. doi: 10.1029/92JB00708.

M. Ohnaka. A constitutive scaling law and a unified comprehension for frictional slip failure, shear fracture of intact rock, and earthquake rupture. *Journal of Geophysical Research: Solid Earth*, 108(B2):2000JB000123, 2003. doi: 10.1029/2000JB000123.

Y. Okada. Surface deformation due to shear and tensile faults in a half-space. *Bulletin of the Seismological Society of America*, 75(4):1135–1154, 1985. doi: 10.1785/BSSA0750041135.

Y. Okada. Internal deformation due to shear and tensile faults in a half-space. *Bulletin of the Seismological Society of America*, 82(2):1018–1040, 1992. doi: 10.1785/BSSA0820021018.

F. Omori. On the aftershocks of earthquakes. *Journal of the College of Science, Imperial University of Tokyo*, 7:111–200, 1894.

J.-J. Orteu, D. Garcia, L. Robert, and F. Bugarin. A speckle texture image generator. page 63410H, Nimes, France, 2006. doi: 10.1117/12.695280.

F. Paglialunga, F. Passelègue, S. Latour, A. Gounon, and M. Violay. Influence of viscous lubricant on nucleation and propagation of frictional ruptures. *Journal of Geophysical Research: Solid Earth*, 128(4):e2022JB026090, 2023. doi: 10.1029/2022JB026090.

A. C. Palmer and J. R. Rice. The growth of slip surfaces in the progressive failure of over-consolidated clay. *Proceedings of the Royal Society of London. A. Mathematical and Physical Sciences*, 332(1591):527–548, 1973. doi: 10.1098/rspa.1973.0040.

B. Pan, H. Xie, Z. Wang, K. Qian, and Z. Wang. Study on subset size selection in digital image correlation for speckle patterns. *Optics Express*, 16(10):7037, 2008. doi: 10.1364/OE.16.007037.

Y. Park, S. M. Mousavi, W. Zhu, W. L. Ellsworth, and G. C. Beroza. Machine-learning-based analysis of the Guy-Greenbrier, Arkansas earthquakes: A tale of two sequences. *Geophysical Research Letters*, 47(6):e2020GL087032, 2020. doi: 10.1029/2020GL087032.

M. Parotidis, S. A. Shapiro, and E. Rothert. Back front of seismicity induced after termination of borehole fluid injection. *Geophysical Research Letters*, 31(2), 2004. doi: 10.1029/2003GL018987.

M. Parotidis, S. Shapiro, and E. Rothert. Evidence for triggering of the Vogtland swarms 2000 by pore pressure diffusion. *Journal of Geophysical Research*, 110 (B5):B05S10, 2005. doi: 10.1029/2004JB003267.

L. Passarelli, S. Hainzl, S. Cesca, F. Maccaferri, M. Mucciarelli, D. Roessler, F. Corbi, T. Dahm, and E. Rivalta. Aseismic transient driving the swarm-like

seismic sequence in the Pollino range, Southern Italy. *Geophysical Journal International*, 201(3):1553–1567, 2015. doi: 10.1093/gji/ggv111.

Z. Peng and J. Gomberg. An integrated perspective of the continuum between earthquakes and slow-slip phenomena. *Nature Geoscience*, 3(9):599–607, 2010. doi: 10.1038/ngeo940.

Z. Peng and P. Zhao. Migration of early aftershocks following the 2004 Parkfield earthquake. *Nature Geoscience*, 2(12):877–881, 2009. doi: 10.1038/ngeo697.

C. Penney, K. Sirorattanakul, and J.-P. Avouac. Rheological implications of post-seismic deformation following the 2019 Ridgecrest Earthquakes. *TechRxiv*, 2021. doi: 10.1002/essoar.10506577.1.

H. Perfettini and J.-P. Avouac. Postseismic relaxation driven by brittle creep: A possible mechanism to reconcile geodetic measurements and the decay rate of aftershocks, application to the Chi-Chi earthquake, Taiwan. *Journal of Geophysical Research: Solid Earth*, 109(B2), 2004. doi: 10.1029/2003JB002488.

H. Perfettini and J.-P. Avouac. Modeling afterslip and aftershocks following the 1992 Landers earthquake. *Journal of Geophysical Research*, 112(B7):B07409, 2007. doi: 10.1029/2006JB004399.

H. Perfettini and A. Molinari. A micromechanical model of rate and state friction: 1. Static and dynamic sliding. *Journal of Geophysical Research: Solid Earth*, 122(4):2590–2637, 2017. doi: 10.1002/2016JB013302.

H. Perfettini, J. Schmittbuhl, and A. Cochard. Shear and normal load perturbations on a two-dimensional continuous fault: 1. Static triggering. *Journal of Geophysical Research: Solid Earth*, 108(B9), 2003. doi: 10.1029/2002JB001804.

H. Perfettini, J.-P. Avouac, H. Hernando, A. Kositsky, J.-M. Nocquet, F. Bondoux, M. Chlieh, A. Sladen, L. Audin, D. L. Farber, and P. Soler. Seismic and aseismic slip on the Central Peru megathrust. *Nature*, 465(7294):78–81, 2010. doi: 10.1038/nature09062.

H. Perfettini, W. B. Frank, D. Marsan, and M. Bouchon. A model of aftershock migration driven by afterslip. *Geophysical Research Letters*, 45(5):2283–2293, 2018. doi: 10.1002/2017GL076287.

G. Perrin, J. R. Rice, and G. Zheng. Self-healing slip pulse on a frictional surface. *Journal of the Mechanics and Physics of Solids*, 43(9):1461–1495, 1995. doi: 10.1016/0022-5096(95)00036-I.

B. N. J. Persson. On the theory of rubber friction. *Solid State Communications*, 401 (3):445–454, 1998. doi: 10.1016/S0039-6028(98)00051-X.

J. Poissant and F. Barthelat. A Novel "Subset Splitting" Procedure for Digital Image Correlation on Discontinuous Displacement Fields. *Experimental Mechanics*, 50 (3):353–364, 2010. doi: 10.1007/s11340-009-9220-2.

E. Popova and V. L. Popov. The research works of Coulomb and Amontons and generalized laws of friction. *Friction*, 3(2):183–190, 2015. doi: 10.1007/s40544-015-0074-6.

R. A. J. Post, M. A. J. Michels, J.-P. Ampuero, T. Candela, P. A. Fokker, J.-D. Van Wees, R. W. V. D. Hofstad, and E. R. V. D. Heuvel. Interevent-time distribution and aftershock frequency in non-stationary induced seismicity. *Scientific Reports*, 11(1):3540, 2021. doi: 10.1038/s41598-021-82803-2.

E. Rabinowicz. The nature of the static and kinetic coefficients of friction. *Journal of Applied Physics*, 22(11):1373–1379, 1951. doi: 10.1063/1.1699869.

E. Rabinowicz. Stick and slip. *Scientific American*, 194(5):109–119, 1956.

P. Reasenberg. Second-order moment of central California seismicity, 1969–1982. *Journal of Geophysical Research: Solid Earth*, 90(B7):5479–5495, 1985. doi: 10.1029/JB090iB07p05479.

P. L. Reu. Experimental and numerical methods for exact subpixel shifting. *Experimental Mechanics*, 51(4):443–452, 2011. doi: 10.1007/s11340-010-9417-4.

P. L. Reu, W. Sweatt, T. Miller, and D. Fleming. Camera system resolution and its influence on digital image correlation. *Experimental Mechanics*, 55(1):9–25, 2015. doi: 10.1007/s11340-014-9886-y.

P. L. Reu, E. Toussaint, E. Jones, H. A. Bruck, M. Iadicola, R. Balcaen, D. Z. Turner, T. Siebert, P. Lava, and M. Simonsen. DIC Challenge: Developing images and guidelines for evaluating accuracy and resolution of 2D analyses. *Experimental Mechanics*, 58(7):1067–1099, 2018. doi: 10.1007/s11340-017-0349-0.

P. L. Reu, B. Blaysat, E. Andó, K. Bhattacharya, C. Couture, V. Couty, D. Deb, S. S. Fayad, M. A. Iadicola, S. Jaminion, M. Klein, A. K. Landauer, P. Lava, M. Liu, L. K. Luan, S. N. Olufsen, J. Réthoré, E. Roubin, D. T. Seidl, T. Siebert, O. Stamati, E. Toussaint, D. Turner, C. S. R. Vemulapati, T. Weikert, J. F. Witz, O. Witzel, and J. Yang. DIC Challenge 2.0: Developing images and guidelines for evaluating accuracy and resolution of 2D analyses: Focus on the metrological efficiency indicator. *Experimental Mechanics*, 62(4):639–654, 2022. ISSN 0014-4851, 1741-2765. doi: 10.1007/s11340-021-00806-6.

J. R. Rice. Flash heating at asperity contacts and rate-dependent friction. *Eos, Transactions American Geophysical Union*, 80(46), 1999.

J. R. Rice and A. L. Ruina. Stability of steady frictional slipping. *Journal of Applied Mechanics*, 50(2):343–349, 1983. doi: 10.1115/1.3167042.

J. R. Rice, N. Lapusta, and K. Ranjith. Rate and state dependent friction and the stability of sliding between elastically deformable solids. *Journal of the Mechanics and Physics of Solids*, 49(9):1865–1898, 2001. doi: 10.1016/S0022-5096(01)00042-4.

C. Richter. *Elementary Seismology*. W. H. Freeman and Co, San Francisco, 1958.

G. Richter, S. Hainzl, T. Dahm, and G. Zöller. Stress-based, statistical modeling of the induced seismicity at the Groningen gas field, The Netherlands. *Environmental Earth Sciences*, 79(11):252, 2020. doi: 10.1007/s12665-020-08941-4.

A. P. Rinaldi, L. Improta, S. Hainzl, F. Catalli, L. Urpi, and S. Wiemer. Combined approach of poroelastic and earthquake nucleation applied to the reservoir-induced seismic activity in the Val d'Agri area, Italy. *Journal of Rock Mechanics and Geotechnical Engineering*, 12(4):802–810, 2020. doi: 10.1016/j.jrmge.2020.04.003.

P. T. Robinson and W. A. Elders. Quarternary volcanism in the Salton Sea geothermal field, Imperial Vallue, California. *Geological Society of America Bulletin*, 87: 347–360, 1976.

T. Rockwell, K. Scharer, and T. Dawson. Earthquake geology and paleoseismology of major strands of the San Andreas fault system. In *Applied Geology in California, Association of Environmental and Engineering Geology Special Publication*, volume 26. 2016.

E. Roland and J. J. McGuire. Earthquake swarms on transform faults. *Geophysical Journal International*, 178(3):1677–1690, 2009. doi: 10.1111/j.1365-246X.2009.04214.x.

D. C. Roman and K. V. Cashman. The origin of volcano-tectonic earthquake swarms. *Geology*, 34(6):457, 2006. doi: 10.1130/G22269.1.

A. J. Rosakis, V. Rubino, and N. Lapusta. Recent milestones in unraveling the full-field structure of dynamic shear cracks and fault ruptures in real-time: From photoelasticity to ultrahigh-speed digital image correlation. *Journal of the Mechanics and Physics of Solids*, 87(3):030801, 2020. doi: 10.1115/1.4045715.

Z. E. Ross and E. S. Cochran. Evidence for latent crustal fluid injection transients in Southern California from long-duration earthquake swarms. *Geophysical Research Letters*, 48(12), 2021. doi: 10.1029/2021GL092465.

Z. E. Ross, C. Rollins, E. S. Cochran, E. Hauksson, J.-P. Avouac, and Y. Ben-Zion. Aftershocks driven by afterslip and fluid pressure sweeping through a fault-fracture mesh. *Geophysical Research Letters*, 44(16):8260–8267, 2017. doi: 10.1002/2017GL074634.

Z. E. Ross, D. T. Trugman, E. Hauksson, and P. M. Shearer. Searching for hidden earthquakes in Southern California. *Science*, 364(6442):767–771, 2019a. doi: 10.1126/science.aaw6888.

Z. E. Ross, Y. Yue, M. Meier, E. Hauksson, and T. H. Heaton. PhaseLink: A deep learning approach to seismic phase association. *Journal of Geophysical Research: Solid Earth*, 124(1):856–869, 2019b. doi: 10.1029/2018JB016674.

Z. E. Ross, E. S. Cochran, D. T. Trugman, and J. D. Smith. 3d fault architecture controls the dynamism of earthquake swarms. *Science*, 368(6497):1357–1361, 2020. doi: 10.1126/science.abb0779.

M. Rossi, P. Lava, F. Pierron, D. Debruyne, and M. Sasso. Effect of DIC spatial resolution, noise and interpolation error on identification results with the VFM. *Strain*, 51(3):206–222, 2015. doi: 10.1111/str.12134.

S. Roux and F. Hild. Stress intensity factor measurements from digital image correlation: post-processing and integrated approaches. *International Journal of Fracture*, 140(1-4):141–157, 2006. doi: 10.1007/s10704-006-6631-2.

A. M. Rubin and J.-P. Ampuero. Earthquake nucleation on (aging) rate and state faults. *Journal of Geophysical Research: Solid Earth*, 110(B11), 2005. doi: 10.1029/2005JB003686.

V. Rubino, N. Lapusta, A. J. Rosakis, S. Leprince, and J. P. Avouac. Static laboratory earthquake measurements with the digital image correlation method. *Experimental Mechanics*, 55(1):77–94, 2015. doi: 10.1007/s11340-014-9893-z.

V. Rubino, A. J. Rosakis, and N. Lapusta. Understanding dynamic friction through spontaneously evolving laboratory earthquakes. *Nature Communications*, 8(1): 15991, 2017. doi: 10.1038/ncomms15991.

V. Rubino, A. J. Rosakis, and N. Lapusta. Full-field ultrahigh-speed quantification of dynamic shear ruptures using digital image correlation. *Experimental Mechanics*, 59(5):551–582, 2019. doi: 10.1007/s11340-019-00501-7.

V. Rubino, A. J. Rosakis, and N. Lapusta. Spatiotemporal properties of sub-rayleigh and supershear ruptures inferred from full-field dynamic imaging of laboratory experiments. *Journal of Geophysical Research: Solid Earth*, 125(2): e2019JB018922, 2020. doi: 10.1029/2019JB018922.

V. Rubino, N. Lapusta, and A. J. Rosakis. Intermittent lab earthquakes in dynamically weakening fault gouge. *Nature*, 606(7916):922–929, 2022. doi: 10.1038/s41586-022-04749-3.

S. M. Rubinstein, G. Cohen, and J. Fineberg. Detachment fronts and the onset of dynamic friction. *Nature*, 430(7003):1005–1009, 2004. doi: 10.1038/nature02830.

C. J. Ruhl, R. E. Abercrombie, K. D. Smith, and I. Zaliapin. Complex spatiotemporal evolution of the 2008 M_w 4.9 Mogul earthquake swarm (Reno, Nevada): Interplay of fluid and faulting. *Journal of Geophysical Research: Solid Earth*, 121(11):8196–8216, 2016. doi: 10.1002/2016JB013399.

A. Ruina. Slip instability and state variable friction laws. *Journal of Geophysical Research: Solid Earth*, 88(B12):10359–10370, 1983. doi: 10.1029/JB088iB12p10359.

E. H. Rutter and J. Mecklenburgh. Influence of normal and shear stress on the hydraulic transmissivity of thin cracks in a tight Quartz Sandstone, a Granite, and a Shale. *Journal of Geophysical Research: Solid Earth*, 123(2):1262–1285, 2018. doi: 10.1002/2017JB014858.

J. Réthoré, F. Hild, and S. Roux. Shear-band capturing using a multiscale extended digital image correlation technique. *Computer Methods in Applied Mechanics and Engineering*, 196(49-52):5016–5030, 2007. doi: 10.1016/j.cma.2007.06.019.

J. Réthoré, F. Hild, and S. Roux. Extended digital image correlation with crack shape optimization. *International Journal for Numerical Methods in Engineering*, 73 (2):248–272, 2008. doi: 10.1002/nme.2070.

A. Savitzky and M. J. E. Golay. Smoothing and differentiation of data by simplified least squares procedures. *Analytical Chemistry*, 36(8):1627–1639, 1964. doi: 10.1021/ac60214a047.

SCEDC. Southern California Earthquake Data Center, 2013. URL https://scedc.caltech.edu/.

M. Schoenball, N. C. Davatzes, and J. M. G. Glen. Differentiating induced and natural seismicity using space-time-magnitude statistics applied to the Coso Geothermal field. *Geophysical Research Letters*, 42(15):6221–6228, 2015. doi: 10.1002/2015GL064772.

C. H. Scholz. *The mechanics of earthquakes and faulting*. Cambridge University Press, 3rd edition, 2019.

C. H. Scholz, Y. J. Tan, and F. Albino. The mechanism of tidal triggering of earthquakes at mid-ocean ridges. *Nature Communications*, 10(1):2526, 2019. doi: 10.1038/s41467-019-10605-2.

H. W. Schreier. Systematic errors in digital image correlation caused by intensity interpolation. *Optical Engineering*, 39(11):2915, 2000. doi: 10.1117/1.1314593.

A. Schuster. On lunar and solar periodicities of earthquakes. *Proceedings of the Royal Society of London*, 61:455–465, 1897.

P. Segall. Earthquakes triggered by fluid extraction. *Geology*, 17:942–946, 1989.

P. Segall. *Earthquake and Volcano Deformation*. Princeton University Press, Princeton, NJ, 2010. ISBN 978-0-691-13302-7.

P. Segall and S. Lu. Injection-induced seismicity: Poroelastic and earthquake nucleation effects. *Journal of Geophysical Research: Solid Earth*, 120(7):5082–5103, 2015. doi: 10.1002/2015JB012060.

P. Segall and J. R. Rice. Dilatancy, compaction, and slip instability of a fluid-infiltrated fault. *Journal of Geophysical Research: Solid Earth*, 100(B11):22155–22171, 1995. doi: 10.1029/95JB02403.

P. Segall, J. Grasso, and A. Mossop. Poroelastic stressing and induced seismicity near the Lacq gas field, southwestern France. *Journal of Geophysical Research: Solid Earth*, 99(B8):15423–15438, 1994. doi: 10.1029/94JB00989.

P. Segall, E. K. Desmarais, D. Shelly, A. Miklius, and P. Cervelli. Earthquakes triggered by silent slip events on Kīlauea volcano, Hawaii. *Nature*, 442(7098): 71–74, 2006. doi: 10.1038/nature04938.

E. Serpelloni, F. Pintori, A. Gualandi, E. Scoccimarro, A. Cavaliere, L. Anderlini, M. E. Belardinelli, and M. Todesco. Hydrologically induced Karst deformation: Insights from GPS measurements in the Adria-Eurasia plate boundary zone. *Journal of Geophysical Research: Solid Earth*, 123(5):4413–4430, 2018. doi: 10.1002/2017JB015252.

S. A. Shapiro and C. Dinske. Fluid-induced seismicity: Pressure diffusion and hydraulic fracturing. *Geophysical Prospecting*, 57(2):301–310, 2009. doi: 10.1111/j.1365-2478.2008.00770.x.

S. A. Shapiro, E. Huenges, and G. Borm. Estimating the crust permeability from fluid-injection-induced seismic emission at the KTB site. *Geophysical Journal International*, 131(2):F15–F18, 1997. doi: 10.1111/j.1365-246X.1997.tb01215.x.

S. A. Shapiro, E. Rothert, V. Rath, and J. Rindschwentner. Characterization of fluid transport properties of reservoirs using induced microseismicity. *Geophysics*, 67 (1):212–220, 2002. doi: 10.1190/1.1451597.

V. Sharma, M. Wadhawan, N. Rana, K. M. Sreejith, R. Agrawal, C. Kamra, K. S. Hosalikar, K. V. Narkhede, G. Suresh, and V. K. Gahalaut. A long duration non-volcanic earthquake sequence in the stable continental region of India: The Palghar swarm. *Tectonophysics*, 779:228376, 2020. doi: 10.1016/j.tecto.2020.228376.

J. H. Shaw, A. Plesch, C. Tape, M. P. Suess, T. H. Jordan, G. Ely, E. Hauksson, J. Tromp, T. Tanimoto, R. Graves, K. Olsen, C. Nicholson, P. J. Maechling, C. Rivero, P. Lovely, C. M. Brankman, and J. Munster. Unified Structural Representation of the southern California crust and upper mantle. *Earth and Planetary Science Letters*, 415:1–15, 2015. doi: 10.1016/j.epsl.2015.01.016.

P. M. Shearer. *Introduction to Seismology*. Cambridge University Press, 3rd edition, 2019.

D. R. Shelly and J. L. Hardebeck. Illuminating faulting complexity of the 2017 Yellowstone Maple Creek earthquake swarm. *Geophysical Research Letters*, 46 (5):2544–2552, 2019. doi: 10.1029/2018GL081607.

D. R. Shelly, S. C. Moran, and W. A. Thelen. Evidence for fluid-triggered slip in the 2009 Mount Rainier, Washington earthquake swarm. *Geophysical Research Letters*, 40(8):1506–1512, 2013. doi: 10.1002/grl.50354.

D. R. Shelly, W. L. Ellsworth, and D. P. Hill. Fluid-faulting evolution in high definition: Connecting fault structure and frequency-magnitude variations during the 2014 Long Valley Caldera, california, earthquake swarm: Fluid-faulting evolution in Long Valley. *Journal of Geophysical Research: Solid Earth*, 121(3): 1776–1795, 2016. doi: 10.1002/2015JB012719.

M. Shirzaei. A wavelet-based multitemporal DInSAR algorithm for monitoring ground surface motion. *IEEE Geoscience and Remote Sensing Letters*, 10(3): 456–460, 2013. doi: 10.1109/LGRS.2012.2208935.

M. Shirzaei and R. Bürgmann. Topography correlated atmospheric delay correction in radar interferometry using wavelet transforms. *Geophysical Research Letters*, 39(1), 2012. doi: 10.1029/2011GL049971.

M. Shirzaei and T. R. Walter. Estimating the effect of satellite orbital error using wavelet-based robust regression applied to InSAR deformation data. *IEEE Transactions on Geoscience and Remote Sensing*, 49(11):4600–4605, 2011. doi: 10.1109/TGRS.2011.2143419.

R. H. Sibson. Interactions between temperature and pore-fluid pressure during earthquake faulting and a mechanism for partial or total stress relief. *Nature Physical Science*, 243:66–68, 1973. doi: 10.1038/physci243066a0.

M. Simons and P. Rosen. 3.12 - Interferometric Synthetic Aperture Radar geodesy. In G. Schubert, editor, *Treatise on Geophysics (Second Edition)*, pages 339–385. Elsevier, Oxford, second edition edition, 2015. doi: 10.1016/B978-0-444-53802-4.00061-0.

K. Sirorattanakul, Z. E. Ross, M. Khoshmanesh, E. S. Cochran, M. Acosta, and J. Avouac. Supporting data and codes for The 2020 Westmorland, California earthquake swarm as aftershocks of a slow slip event sustained by fluid flow. *CaltechDATA*, 2022a. doi: 10.22002/658vg-6xn94.

K. Sirorattanakul, Z. E. Ross, M. Khoshmanesh, E. S. Cochran, M. Acosta, and J.-P. Avouac. The 2020 Westmorland, California earthquake swarm as aftershocks of a slow slip event sustained by fluid flow. *Journal of Geophysical Research: Solid Earth*, 127(11):e2022JB024693, 2022b. doi: 10.1029/2022JB024693.

K. Sirorattanakul, S. Larochelle, V. Rubino, N. Lapusta, and A. J. Rosakis. Sliding and healing of frictional interfaces that appear stationary. *Under Review*, 2024.

N. H. Sleep. Application of a unified rate and state friction theory to the mechanics of fault zones with strain localization. *Journal of Geophysical Research: Solid Earth*, 102(B2):2875–2895, 1997. doi: 10.1029/96JB03410.

J. D. Smith, J. Avouac, R. S. White, A. Copley, A. Gualandi, and S. Bourne. Reconciling the long-term relationship between reservoir pore pressure depletion and compaction in the Groningen region. *Journal of Geophysical Research: Solid Earth*, 124(6):6165–6178, 2019. doi: 10.1029/2018JB016801.

J. D. Smith, R. S. White, J.-P. Avouac, and S. Bourne. Probabilistic earthquake locations of induced seismicity in the Groningen region, the Netherlands. *Geophysical Journal International*, 222(1):507–516, 2020. doi: 10.1093/gji/ggaa179.

J. D. Smith, Z. E. Ross, K. Azizzadenesheli, and J. B. Muir. HypoSVI: Hypocentre inversion with Stein variational inference and physics informed neural networks. *Geophysical Journal International*, 228(1):698–710, 2021. doi: 10.1093/gji/ggab309.

J. D. Smith, E. R. Heimisson, S. J. Bourne, and J.-P. Avouac. Stress-based forecasting of induced seismicity with instantaneous earthquake failure functions: Applications to the Groningen gas reservoir. *Earth and Planetary Science Letters*, 594: 117697, 2022. doi: 10.1016/j.epsl.2022.117697.

R. Stein. The role of stress transfer in earthquake occurrence. *Nature*, 402:605–609, 1999. doi: 10.1038/45144.

R. M. Stesky. Rock friction-effect of confining pressure, temperature, and pore pressure. *Pure and Applied Geophysics*, 116:690–704, 1978. doi: 10.1007/BF00876532.

S. M. Stokes, S. Ge, M. R. M. Brown, E. A. Menezes, A. F. Sheehan, and K. F. Tiampo. Pore pressure diffusion and onset of induced seismicity. *Journal of Geophysical Research: Solid Earth*, 128(3):e2022JB026012, 2023. doi: 10.1029/2022JB026012.

A. J. Stäuble and G. Milius. Geology of Groningen Gas Field, Netherlands. In M. Halbouty, editor, *Geology of Giant Petroleum Fields*, volume 14, pages 359–369. American Association of Petroleum Geologists, 1970.

Z. Sun, J. S. Lyons, and S. R. McNeill. Measuring microscopic deformations with digital image correlation. *Optics and Lasers in Engineering*, 27(4):409–428, 1997. doi: 10.1016/S0143-8166(96)00041-3.

U. G. S. a. C. G. Survey. Quaternary fault and fold database for the United States. URL https://www.usgs.gov/programs/earthquake-hazards/faults.

M. Sutton, W. Wolters, W. Peters, W. Ranson, and S. McNeill. Determination of displacements using an improved digital correlation method. *Image and Vision Computing*, 1(3):133–139, 1983. doi: 10.1016/0262-8856(83)90064-1.

M. A. Sutton, J.-J. Orteu, and H. W. Schreier. *Image correlation for shape, motion, and deformation measurements*. Springer, 2009.

I. Svetlizky and J. Fineberg. Classical shear cracks drive the onset of dry frictional motion. *Nature*, 509(7499):205–208, 2014. doi: 10.1038/nature13202.

A. Sáez, B. Lecampion, P. Bhattacharya, and R. C. Viesca. Three-dimensional fluid-driven stable frictional ruptures. *Journal of the Mechanics and Physics of Solids*, 160:104754, 2022. doi: 10.1016/j.jmps.2021.104754.

Y. Tal, V. Rubino, A. J. Rosakis, and N. Lapusta. Illuminating the physics of dynamic friction through laboratory earthquakes on thrust faults. *Proceedings of the National Academy of Sciences*, 117(35):21095–21100, 2020. doi: 10.1073/pnas.2004590117.

Y. Tal, V. Rubino, A. J. Rosakis, and N. Lapusta. Dynamics and near-field surface motions of transitioned supershear laboratory earthquakes in thrust faults. *Journal of Geophysical Research: Solid Earth*, 127(3):e2021JB023733, 2022. doi: 10.1029/2021JB023733.

Y. J. Tan, F. Waldhauser, W. L. Ellsworth, M. Zhang, W. Zhu, M. Michele, L. Chiaraluce, G. C. Beroza, and M. Segou. Machine-learning-based high-resolution earthquake catalog reveals how complex fault structures were activated during the 2016–2017 Central Italy sequence. *The Seismic Record*, 1(1):11–19, 2021. doi: 10.1785/0320210001.

S. Tanaka, M. Ohtake, and H. Sato. Evidence for tidal triggering of earthquakes as revealed from statistical analysis of global data. *Journal of Geophysical Research: Solid Earth*, 107(B10):ESE 1–1–ESE 1–11, 2002. doi: 10.1029/2001JB001577.

C.-C. Tang, C.-H. Lin, and Z. Peng. Spatial-temporal evolution of early aftershocks following the 2010 ML 6.4 Jiashian earthquake in southern Taiwan. *Geophysical Journal International*, 199(3):1772–1783, 2014. doi: 10.1093/gji/ggu361.

M. Y. Thomas, J.-P. Avouac, J. Champenois, J.-C. Lee, and L.-C. Kuo. Spatiotemporal evolution of seismic and aseismic slip on the Longitudinal Valley Fault, Taiwan. *Journal of Geophysical Research: Solid Earth*, 119(6):5114–5139, 2014. doi: 10.1002/2013JB010603.

K. Thøgersen, A. Gilbert, T. V. Schuler, and A. Malthe-Sørenssen. Rate-and-state friction explains glacier surge propagation. *Nature Communications*, 10(1):2823, 2019. doi: 10.1038/s41467-019-10506-4.

S. Toda, R. S. Stein, and T. Sagiya. Evidence from the ad 2000 Izu islands earthquake swarm that stressing rate governs seismicity. *Nature*, 419(6902):58–61, 2002. doi: 10.1038/nature00997.

Z. Tomičevć, F. Hild, and S. Roux. Mechanics-aided digital image correlation. *The Journal of Strain Analysis for Engineering Design*, 48(5):330–343, 2013. doi: 10.1177/0309324713482457.

W. Tong. An evaluation of digital image correlation criteria for strain mapping applications. *Strain*, 41(4):167–175, 2005. doi: 10.1111/j.1475-1305.2005.00227.x.

J. Trampert, R. Benzi, and F. Toschi. Implications of the statistics of seismicity recorded within the Groningen gas field. *Netherlands Journal of Geosciences*, 101:e9, 2022. doi: 10.1017/njg.2022.8.

D. T. Trugman and P. M. Shearer. GrowClust: A hierarchical clustering algorithm for relative earthquake relocation, with application to the Spanish Springs and Sheldon, Nevada, earthquake sequences. *Seismological Research Letters*, 88(2A): 379–391, 2017. doi: 10.1785/0220160188.

D. T. Trugman, P. M. Shearer, A. A. Borsa, and Y. Fialko. A comparison of long-term changes in seismicity at The Geysers, Salton Sea, and Coso geothermal fields. *Journal of Geophysical Research: Solid Earth*, 121:225–247, 2016. doi: 10.1002/2015JB012510.

T. E. Tullis and J. D. Weeks. Constitutive behavior and stability of frictional sliding of granite. *Pure and Applied Geophysics*, 124(3):383–414, 1986. doi: 10.1007/BF00877209.

T. Ueda, A. Kato, C. W. Johnson, and T. Terakawa. Seasonal modulation of crustal seismicity in Northeastern Japan driven by snow load. *Journal of Geophysical Research: Solid Earth*, 129(3):e2023JB028217, 2024. doi: 10.1029/2023JB028217.

T. Utsu. A statistical study on the occurrence of aftershocks. *The Geophysical Magazine*, 30:521–605, 1961.

T. Utsu, Y. Ogata, R. S, and Matsu'ura. The centenary of the Omori formula for a decay law of aftershock activity. *Journal of Physics of the Earth*, 43(1), 1995. doi: 10.4294/jpe1952.43.1.

N. J. van der Elst. *B-Positive* : A robust estimator of aftershock magnitude distribution in transiently incomplete catalogs. *Journal of Geophysical Research: Solid Earth*, 126(2):e2020JB021027, 2021. doi: 10.1029/2020JB021027.

N. J. van der Elst and E. E. Brodsky. Connecting near-field and far-field earthquake triggeringto dynamic strain. *Journal of Geophysical Research: Solid Earth*, 115: B07311, 2021. doi: 10.1029/2009JB006681.

T. van der Elst, J. Zhuang, and M. D. Seismicity declustering. *Community Online Resource for Statistical Seismicity Analysis*, 2012. doi: 10.5078/corssa52382934.

K. van Thienen-Visser and J. Breunese. Induced seismicity of the Groningen gas field: History and recent developments. *Lead. Edge*, 34(6):664–671, 2015. doi: 10.1190/tle34060664.1.

J.-D. Van Wees, S. Osinga, K. Van Thienen-Visser, and P. A. Fokker. Reservoir creep and induced seismicity: Inferences from geomechanical modeling of gas depletion in the Groningen field. *Geophysical Journal International*, 212(3): 1487–1497, 2018. doi: 10.1093/gji/ggx452.

J. E. Vidale and P. M. Shearer. A survey of 71 earthquake bursts across southern California: Exploring the role of pore fluid pressure fluctuations and aseismic

slip as drivers. *Journal of Geophysical Research: Solid Earth*, 111(B5):B05312, 2006. doi: 10.1029/2005JB004034.

J. E. Vidale, W. L. Ellsworth, A. Cole, and C. Marone. Variations in rupture process with recurrence interval in a repeated small earthquake. *Nature*, 368(6472): 624–626, 1994. doi: 10.1038/368624a0.

J. E. Vidale, D. C. Agnew, M. J. S. Johnston, and D. H. Oppenheimer. Absence of earthquake correlation with Earth tides: An indication of high preseismic fault stress rate. *Journal of Geophysical Research: Solid Earth*, 103(B10):24567–24572, 1998. doi: 10.1029/98JB00594.

R. C. Viesca and D. I. Garagash. Ubiquitous weakening of faults due to thermal pressurization. *Nature Geoscience*, 8:875–879, 2015. doi: 10.1038/ngeo2554.

M. Violay, M. J. Heap, M. Acosta, and C. Madonna. Porosity evolution at the brittle-ductile transition in the continental crust: Implications for deep hydro-geothermal circulation. *Scientific Reports*, 7(1):7705, 2017. doi: 10.1038/s41598-017-08108-5.

C. A. Visser and J. L. Solano Viota. Introduction to the Groningen static reservoir model. *Netherlands Journal of Geosciences*, 96(5):s39–s46, 2017. doi: 10.1017/njg.2017.25.

J. Wahr. 3.08 - Time variable gravity from satellites. In G. Schubert, editor, *Treatise on Geophysics*, pages 213–237. Elsevier, Amsterdam, 2007. doi: 10.1016/B978-044452748-6.00176-0.

C. Wang, X. Ding, Q. Li, and M. Jiang. Equation-based InSAR data quadtree downsampling for earthquake slip distribution inversion. *IEEE Geoscience and Remote Sensing Letters*, 11(12):2060–2064, 2014. doi: 10.1109/LGRS.2014.2318775.

H. F. Wang. *Theory of Linear Poroelasticity with Applications to Geomechanics and Hydrogeology*. Princeton University Press, 2000.

W. Wang, P. M. Shearer, J. E. Vidale, X. Xu, D. T. Trugman, and Y. Fialko. Tidal modulation of seismicity at the Coso geothermal field. *Earth and Planetary Science Letters*, 579:117335, 2022. doi: 10.1016/j.epsl.2021.117335.

Y. Q. Wang, M. A. Sutton, H. A. Bruck, and H. W. Schreier. Quantitative error assessment in pattern matching: Effects of intensity pattern noise, interpolation, strain and image contrast on motion measurements. *Strain*, 45(2):160–178, 2009. doi: 10.1111/j.1475-1305.2008.00592.x.

Z. Y. Wang, H. Q. Li, J. W. Tong, and J. T. Ruan. Statistical analysis of the effect of intensity pattern noise on the displacement measurement precision of digital image correlation using self-correlated images. *Experimental Mechanics*, 47(5): 701–707, 2007. doi: 10.1007/s11340-006-9005-9.

B. Wattrisse, A. Chrysochoos, J.-M. Muracciole, and M. Némoz-Gaillard. Analysis of strain localization during tensile tests by digital image correlation. *Experimental Mechanics*, 41(1):29–39, 2001. doi: 10.1007/BF02323101.

S. Wei, J.-P. Avouac, K. W. Hudnut, A. Donnellan, J. W. Parker, R. W. Graves, D. Helmberger, E. Fielding, Z. Liu, F. Cappa, and M. Eneva. The 2012 Brawley swarm triggered by injection-induced aseismic slip. *Earth and Planetary Science Letters*, 422:115–125, 2015. doi: 10.1016/j.epsl.2015.03.054.

C. Werner, U. Wegmüller, T. Strozzi, and A. Wiesmann. Gamma SAR and interferometric processing software. In *Proceedings of the ERS-ENVISAT Symposium*, Gothenburg, Sweden, 2000.

P. Wessel and W. H. F. Smith. A global, self-consistent, hierarchical, high-resolution shoreline database. *Journal of Geophysical Research: Solid Earth*, 101(B4): 8741–8743, 1996. doi: 10.1029/96JB00104.

C. Wicks, W. Thelen, C. Weaver, J. Gomberg, A. Rohay, and P. Bodin. Insar observations of aseismic slip associated with an earthquake swarm in the Columbia River flood basalts. *Journal of Geophysical Research*, 116(B12):B12304, 2011. doi: 10.1029/2011JB008433.

S. Wiemer and M. Wyss. Minimum magnitude of completeness in earthquake catalogs: Examples from Alaska, the Western United States, and Japan. *Bulletin of the Seismological Society of America*, 90(4):859–869, 2000. doi: 10.1785/0119990114.

W. S. D. Wilcock. Tidal triggering of microearthquakes on the Juan de Fuca Ridge. *Geophysical Research Letters*, 28(20):3999–4002, 2001. doi: 10.1029/2001GL013370.

J. D. Wilding, W. Zhu, Z. E. Ross, and J. M. Jackson. The magmatic web beneath Hawai'i. *Science*, 379(6631):462–468, 2023. doi: 10.1126/science.ade5755.

C. Willacy, E. Van Dedem, S. Minisini, J. Li, J.-W. Blokland, I. Das, and A. Droujinine. Full-waveform event location and moment tensor inversion for induced seismicity. *Geophysics*, 84(2):KS39–KS57, 2019. doi: 10.1190/geo2018-0212.1.

L. N. Y. Wong, D. Li, and G. Liu. Experimental studies on permeability of intact and singly jointed meta-sedimentary rocks under confining pressure. *Rock Mechanics and Rock Engineering*, 46(1):107–121, 2013. doi: 10.1007/s00603-012-0251-0.

W. Wu, D. Lu, and D. Elsworth. Fluid injection-induced fault slip during unconventional energy development: A review. *Energy Reviews*, 1(2):100007, Dec. 2022. doi: 10.1016/j.enrev.2022.100007.

N. Wynants-Morel, F. Cappa, L. De Barros, and J.-P. Ampuero. Stress perturbation from aseismic slip drives the seismic front during fluid injection in a permeable

fault. *Journal of Geophysical Research: Solid Earth*, 125:e2019JB01979, 2020. doi: 10.1029/2019JB019179.

K. Xia, A. J. Rosakis, and H. Kanamori. Laboratory earthquakes: The sub-Rayleigh-to-supershear rupture transition. *Science*, 303(5665):1859–1861, 2004. doi: 10.1126/science.1094022.

L. Xue, C. W. Johnson, Y. Fu, and R. Bürgmann. Seasonal seismicity in the Western branch of the East African rift system. *Geophysical Research Letters*, 47(6): e2019GL085882, 2020. doi: 10.1029/2019GL085882.

L. Xue, Y. Fu, C. W. Johnson, J. J. Otero Torres, C. K. Shum, and R. Bürgmann. Seasonal seismicity in the Lake Biwa region of Central Japan moderately modulated by lake water storage changes. *Journal of Geophysical Research: Solid Earth*, 126(12):e2021JB023301, 2021. doi: 10.1029/2021JB023301.

J. Yang, V. Rubino, Z. Ma, J. Tao, Y. Yin, A. McGhee, W. Pan, and C. Franck. SpatioTemporally Adaptive Quadtree Mesh (STAQ) digital image correlation for resolving large deformations around complex geometries and discontinuities. *Experimental Mechanics*, 62(7):1191–1215, 2022. doi: 10.1007/s11340-022-00872-4.

W. Yang and E. Hauksson. The tectonic crustal stress field and style of faulting along the Pacific North America Plate boundary in Southern California. *Geophysical Journal International*, 194(1):100–117, 2013. doi: 10.1093/gji/ggt113.

I. W. Yeo, M. H. D. Freitas, and R. W. Zimmerman. Effect of shear displacement on the aperture and permeability of a rock fracture. *International Journal of Rock Mechanics and Mining Sciences*, 35(8):1051–1070, 1998. doi: 10.1016/S0148-9062(98)00165-X.

L. W. Younker, P. W. Kasameyer, and J. D. Tewhey. Geological, geophysical, and thermal characteristics of the Salton Sea Geothermal Field, California. *Journal of Volcanology and Geothermal Research*, 12(3-4):221–258, 1982. doi: 10.1016/0377-0273(82)90028-2.

Y. Yukutake, H. Ito, R. Honda, M. Harada, T. Tanada, and A. Yoshida. Fluid-induced swarm earthquake sequence revealed by precisely determined hypocenters and focal mechanisms in the 2009 activity at Hakone volcano, Japan. *Journal of Geophysical Research*, 116(B4):B04308, 2011. doi: 10.1029/2010JB008036.

Y. Yukutake, K. Yoshida, and R. Honda. Interaction between aseismic slip and fluid invasion in earthquake swarms revealed by dense geodetic and seismic observations. *Journal of Geophysical Research: Solid Earth*, 2022. doi: 10.1029/2021JB022933.

I. Zaliapin and Y. Ben-Zion. Earthquake clusters in southern California I: Identification and stability. *Journal of Geophysical Research: Solid Earth*, 118(6): 2847–2864, 2013a. doi: 10.1002/jgrb.50179.

I. Zaliapin and Y. Ben-Zion. Earthquake clusters in southern California II: Classification and relation to physical properties of the crust. *Journal of Geophysical Research: Solid Earth*, 118(6):2865–2877, 2013b. doi: 10.1002/jgrb.50178.

I. Zaliapin and Y. Ben-Zion. Discriminating characteristics of tectonic and human-induced seismicity. *Bulletin of the Seismological Society of America*, 106(3): 846–859, 2016. doi: 10.1785/0120150211.

I. Zaliapin and Y. Ben-Zion. Earthquake declustering using the nearest-neighbor approach in space-time-magnitude domain. *Journal of Geophysical Research: Solid Earth*, 125(4), 2020. doi: 10.1029/2018JB017120.

I. Zaliapin, A. Gabrielov, V. Keilis-Borok, and H. Wong. Clustering analysis of seismicity and aftershock identification. *Physical Review Letters*, 101(1):018501, 2008. doi: 10.1103/PhysRevLett.101.018501.

G. Zhai, M. Shirzaei, M. Manga, and X. Chen. Pore-pressure diffusion, enhanced by poroelastic stresses, controls induced seismicity in Oklahoma. *Proceedings of the National Academy of Sciences*, 116(33):16228–16233, 2019. doi: 10.1073/pnas.1819225116.

G. Zheng and J. R. Rice. Conditions under which velocity-weakening friction allows a self-healing versus a cracklike mode of rupture. *Bulletin of the Seismological Society of America*, 88(6):1466–1483, 1998. doi: 10.1785/BSSA0880061466.

P. Zhou and K. E. Goodson. Subpixel displacement and deformation gradient measurement using digital image/speckle correlation (DISC). *Optical Engineering*, 40(8):1613, 2001. doi: 10.1117/1.1387992.

Y. Zhou and Z.-M. Huang. Shear deformation of a composite until failure with a debonded interface. *Composite Structures*, 254:112797, 2020. doi: 10.1016/j.compstruct.2020.112797.

W. Zhu and G. C. Beroza. PhaseNet: A deep-neural-network-based seismic arrival time picking method. *Geophysical Journal International*, 126(1):261–273, 2019. doi: 10.1093/gji/ggy423.

W. Zhu, I. W. McBrearty, S. M. Mousavi, W. L. Ellsworth, and G. C. Beroza. Earthquake phase association using a Bayesian Gaussian Mixture Model. *Journal of Geophysical Research: Solid Earth*, 127(5):e2021JB023249, 2022. doi: 10.1029/2021JB023249.

J. Zhuang and S. Touati. Stochastic simulation of earthquake catalogs. *Community Online Resource for Statistical Seismicity Analysis*, 2015. doi: 10.5078/CORSSA-43806322.

J. Zhuang, Y. Ogata, and D. Vere-Jones. Stochastic declustering of space-time earthquake occurrences. *Journal of the American Statistical Association*, 97: 369–380, 2002. doi: 10.1198/016214502760046925.

A. Ziv and A. M. Rubin. Implications of rate-and-state friction for properties of aftershock sequence: Quasi-static inherently discrete simulations. *Journal of Geophysical Research: Solid Earth*, 108(B1), 2003. doi: 10.1029/2001JB001219.

L. K. Zoet and N. R. Iverson. A healing mechanism for stick-slip of glaciers. *Geology*, 46(9):807–810, 2018. doi: 10.1130/G45099.1.